Coupled and multiphysics phenomena

Publisher:
Alert Geomaterials INPG-3SR

Published version:
DOI:

The Alliance of Laboratories in Europe for
Research and Technology

ALERT Doctoral School 2015

Coupled and multiphysics phenomena

Editors:

Bernhard A. Schrefler

Lorenzo Sanavia

Frédéric Collin

Editorial

The ALERT Doctoral School 2015 entitled *Coupled and multiphysics phenomena* is organized by Bernhard Schrefler, Lorenzo Sanavia (both University of Padova) and Frédéric Collin (University of Liège). The commitment of the school organizers and contributors of this printed volume must be highly appreciated!

Going through the contributions of their book, it becomes obvious how far we have proceeded from Terzaghi's theory of consolidation, which is perhaps one of the first works in this field. Nevertheless, looking at curricula of geotechnical courses at most universities, the impression can arise that time stands still and there is no need to teach more than Terzaghi's theory. The presented book demonstrates the opposite. It covers in a comprehensive manner various subjects of physical phenomena coupled together into powerful theories. It is fascinating to see excursions to environmental engineering, medicine or geology and to realize that we can describe those fields with a common language. I am convinced that the book will be useful not only to students attending the Doctoral School but to anybody with interests on modern geosciences. As usual, the pdf file of the book can be downloaded for free from the website of ALERT Geomaterials – `http://alertgeomaterials.eu`.

On behalf of the ALERT Board of Directors I wish all participants a successful ALERT Doctoral School 2015!

Ivo Herle
Director of ALERT Geomaterials
Technische Universität Dresden

Contents

Coupled and multiphysics phenomena: Foreword

The contributions assembled in the present volume proceed from the lectures of the 2015 ALERT Geomaterials Doctoral School devoted to Coupled and Multiphysics Phenomena. The school has been organized and coordinated by Bernhard Schrefler (Università degli Studi di Padova), Lorenzo Sanavia (Università degli Studi di Padova) and Frédéric Collin (Université de Liège).

When dealing with the behaviour of multiphase porous systems, e.g. geomaterials, instances of complexity and interaction are numerous, mainly because of the coexistence of several constituents and phases, their physical and mechanical interactions, their reactivity and their often non-linear behaviour. The study of these coupled processes deals with a large number of applications, e.g. in geomechanics: underground structures (storage, tunnelling), surface structures (earth and concrete dams, embankments) as well as the exploitation of geo-resources (petroleum and gas extraction, mines and quarries).

This volume contains nine chapters in which emphasis is given to the presentation of the fundamental and new concepts that help understanding coupled and multiphysics phenomena in porous systems. The contributions cover experimental, theoretical, as well as numerical aspects. The school is divided into three main parts: the description of the couplings in multiphysics phenomena, including the experimental developments; the mathematical modelling of all these coupled processes, with an introduction to the constitutive modelling taking into account the dilatancy, which characterizes the mechanical behaviour of geomaterials; the numerical implementation of the mathematical models, comprising constitutive equations as well as balance equations and finally numerical modelling through advanced applications.

The experimental aspects of coupled and multiphysics phenomena are described in Chapter one. Pierre Delage introduced the different techniques to measure and control the environmental variables such as suction and temperature. The results obtained through advanced experimental techniques are presented, providing a global overview of the knowledge in this particular field.

Additional coupling phenomena are described by Jacques Huyghe in Chapters two and three, dealing with physical chemistry of mixtures and swelling, discussing mixtures of a liquid with a dissolved substance and considering electrolytic solutions and osmosis in biological tissues. For their mathematical description, theory of mixtures has been summarised. Moreover, Chapter three presents insights in finite deformation poromechanics with application to soil mechanics, poromechanics of the heart muscle and blood perfusion.

Chapter four by William Gray and Cass Miller deals with thermodynamically constrained averaging theory TCAT, which is the most advanced and most general method to develop governing equations of physical problems able to describe the complex system of couplings in the behaviour of multiphase porous systems. This theory is based on thermo-dynamic principles applied at microscale and averages all quantities from the microscale to the macroscale in a consistent and well-defined manner, so that the connection between microscale and macroscale quantities is explicitly known.

Manuel Pastor introduces in Chapter five the constitutive modelling of geomaterials based on Generalized Plasticity Theory. The underlying idea is to show how this general framework for the development of a constitutive law can be extended from a purely mechanical case to hydro-mechanical context. This helps in exhibiting the role of dilatancy in modelling of the most relevant phenomena in soils behaviour such as liquefaction, bonding and de-bonding due to chemical processes or changes in saturation conditions and influence of particle breakage.

The third part of this book is opened by Manuel Pastor with Chapter six, which introduces the numerical implementation of the mathematical models described in the previous chapters. The aim is to provide the reader with an overview both of the techniques and the difficulties encountered when modelling this type of problems. The analysis is restricted to the simplest case where only one fluid filling the pores is considered, as the main difficulties can be more easily explained and understood.

Then, with the last three chapters, the complexity of the problems increases step by step by considering variably saturated problems, thermo-hydro-mechanical problems and, finally, bio- chemo- thermo- hydro-mechanical problems. Hydraulic fracturing, the first numerical modelling of advanced applications, is presented by Bernhard Schrefler. Fluid-driven fracture propagating in porous media is a common problem in geomechanics. It is used, for example, to enhance the recovery of hydrocarbons from underground reservoirs.

Chapter eight by Lorenzo Sanavia presents a fully coupled and non-linear finite element model for the analysis of non-isothermal variably saturated soils in dynamics. Attention is given to the validation step when dealing with the development of numerical models.

In the last chapter, Frédéric Collin introduces the modelling of municipal waste considered as a bio-chemo-thermo-hydro-mechanical model. This latter material is a perfect example of porous media with coupled and multiphysics phenomena. As a consequence of the numerous physical processes, it is proposed to follow a step by step approach where each single aspect is introduced. The couplings are first presented through closed form solutions for simplified cases and then numerically modelled with all their complexity.

We believe that this volume may provide to postgraduate students, researchers and practitioners, a valuable introduction and a sound basis for further progress in the challenging fields of coupled and multiphysics phenomena in porous systems.

Bernhard Schrefler (Università degli Studi di Padova)

Lorenzo Sanavia (Università degli Studi di Padova)

Frédéric Collin (Université de Liège)

Thermo-hydro-mechanical issues in geomaterials: physical mechanisms and experimental determination

P. Delage

Ecole des Ponts ParisTech, Navier/CERMES

Thermo-hydro-mechanical issues in (water) saturated and multi-phase porous geomaterials concern various aspects of civil, environmental engineering as well as energy production, with particular interest devoted to geo-energy issues, to radioactive waste disposal, to conventional and unconventional oil and gas production and also to CO_2 *sequestration. Various geomaterials are concerned, including unsaturated not swelling and swelling soils, porous oil and gas reservoir rocks and also low permeability rocks, with particular interest to claystones and shales that may play a role either as impervious caprocks, geological host for waste disposal, or even reservoir rocks for oil and gas. In this context, this paper presents some physical phenomena related to microstructure, multi-phase pore fluids, and heat effects in soils and rocks and describes how this phenomena can be explored and characterized through experimental determination in the laboratory.*

1 Introduction

Thermo-hydro-mechanical (THM) issues in geomaterials concern either water saturated or multi-phase soils and rocks in which changes in water content and temperature have significant effects. They are related to various aspects of civil, environmental engineering and energy production, including geothermal issues, radioactive waste disposal, conventional and unconventional oil and gas production from porous and low porosity rocks and also CO_2 sequestration. As a consequence, growing attention has been paid to THM issues in geomaterials in the last decades.

The nature and morphology of pores in geomaterials strongly control their THM response. There is a significant difference between water contained in the pores of clays where water molecules are submitted to physico-chemical interactions and where the pore morphology is dependent of the clay microstructure, and water in porous rocks like sandstone or in the cracks of non clayey rocks in which physico-chemical interactions are negligible.

In saturated soils, couplings are satisfactorily accounted for by using Terzaghi's notion of effective stress. By using in soils effective stress analyses that only concerned the granular skeleton, the nature and the complexity of the multi-physics processes involved, particularly in clays, have been somewhat hidden. The importance of hydro-mechanical processes perhaps appeared when researchers considered in soils some situations where coupling could not be properly accounted for by using standard effective stress analysis. Typically, this was illustrated by the impossibility of the Bishop's tentative extended "effective stress" for unsaturated soils to properly account for the phenomenon of collapse that occurs in unsaturated soils when wetted under load. This phenomenon is illustrated in Figure 1 in the case of a low plasticity loess of Northern France.

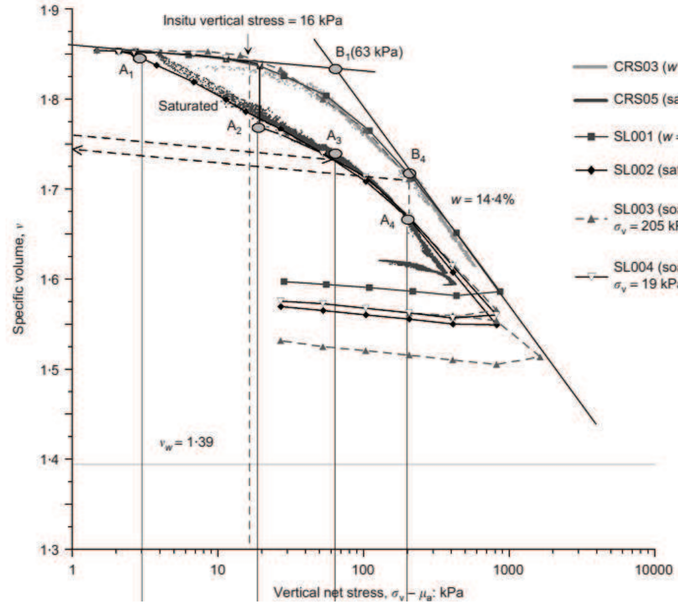

Figure 1 : Collapse of a loess sample under wetting [Muñ11]

In Figure 1, three oedometer compression curves are represented together:

- a compression curve at constant initial water content ($w_i = 14\%$). The unsaturated sample is characterised by a suction s defined by the relation $s = u_a - u_w$ (u_a and u_w respectively being the air and water pressures). This notion will be described in more details further on
- a compression curve obtained after having soaked the sample under 3 kPa and hence reduced the suction down to zero. This curve shows a higher compressibility under a zero suction

- a compression curve where the sample has been first loaded at $w = w_i = 14\%$ up to 200 kPa and then soaked. A 5% collapse is observed and the compression curve at higher stresses after soaking coincides with the soaked curve.

[Bis59] proposed an expression supposed to extend the effective stress to unsaturated soils as follows :

$$\sigma' = \sigma - u_a + \chi\,(u_a - u_w) \qquad (1)$$

with $0 < \chi < 1$, with χ equal to 0 for dry soils and to 1 for saturated soils.

As commented by [Jen62], Bishop's stress should decrease during soaking since $(\sigma - u_a)$ remains constant (u_a being equal to atmospheric pressure) and since the suction $(u_a - u_w)$ decreases during soaking, with also $\chi > 0$. A decrease in effective stress should cause an increase in volume of the sample which is obviously not the case when considering the collapse observed in Figure 1.

Due to this drawback, the necessity of adopting two independent stress variables ([Col64], [Fre77]) to properly describe coupled hydro-mechanical behaviour in unsaturated soils appeared. In other words, the existence of two immiscible fluids (here fluid and air) in geomaterials clearly illustrated the complexity of multiphysics couplings where capillary and physico-chemical processes made necessary the use of more independent stress variables as compared with the better known case of saturated geomaterials where the use of a unique effective stress is satisfactory.

THM couplings were considered in situations where the effects of temperature on geomaterials appeared, in particular in the case of deep geological radioactive waste disposal (see for instance [Hue90]). Beside problems related to the differential thermal expansion of solids and fluids and to the related thermal excess pore pressure (water submitted to temperature elevation dilates 5 times more than minerals), thermal effects appeared to be particularly sensitive in normally consolidated clays. Growing interest was also devoted more recently on the thermal behaviour of claystones and shales in which geological radioactive waste disposal at great depth was considered.

Hydromechanical coupling also appeared in energy production in oil porous reservoir rocks (sandstone, chalk) where three phases co-exist (water, oil and gas). Petroleum engineers are mainly concerned about oil recovery and they mainly considered fluid retention and transfer phenomena in reservoir rocks. However, subsidence effects as those observed in some North Sea reservoir chalks in the past 20 years demonstrated that a process similar to the collapse of unsaturated soils appeared due to chalk waterflooding for enhanced oil recovery [Cha02], [Deg04], [Sch02].

2 Microstructure aspects

2.1 Granular geomaterials

Most often, soils and soft rocks are represented as an assemblage of grains with a given level of bonding between them, with pores delimited by the contours of the grains. This is valid for sands (no inter-grains bonding) and sandstones (with either calcareous or silica bonding agent). This is also true for chalk, where elementary grains are small coccoliths grains (1 μm diameter) with bonding due to calcite crystallisation. The parameter that accounts for microstructure effects in granular assemblage is the porosity, although some more subtle microstructure effects can play a role in grain assemblages at same porosity (see for instance [Ben04], who showed that aggregates of sand grains could affect the susceptibility to liquefaction of loose sands at same porosity). Various considerations on sand structure are also described by [Mit05], among which the preferential sub-horizontal inter-grains contacts orientation that has been observed in natural and pluviated sands. Other important parameters related to the density of granular geomaterials are the grain size distribution and the angularity and surface roughness of the grains. In all these geomaterials, the status of the pore water is described as that of free water, with no mineral-water physico-chemical interactions.

When granular geomaterials contain various immiscible fluids, capillary actions govern most of the interaction between grains and the fluids. In unsaturated sands, the situation is schematically described as shown in Figure 2, where the meniscii created at the interface between the wetting phase and the non-wetting phase are located in the smaller pores close to the inter-grains contacts. In granular geomaterials, the wetting fluid is water. The non-wetting fluid is air in unsaturated soils and oil in reservoir porous rocks.

In the case of a loose assemblage of grains, the scheme of Figure 2 provides a simple interpretation of the collapse phenomenon described in Figure 1.

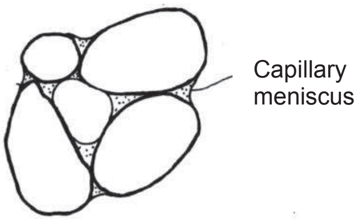

Figure 2 : Schematic view of granular a geomaterial with two fluids

When load is applied on the unsaturated loose assemblage, stability is ensured by the additional normal inter-grains local stress created by the menisci. Up to a point, the strength of this bond increases when suction increases due to drying. When the soil is soaked, the reduction in normal inter-grain stress no longer ensures the assemblage stability because the reduced normal local stresses in some locations are no longer able to sustain the tangential stresses, according to the friction properties of the inter-grains contacts.

In reality, things are less simple, as observed in the SEM photo of an aeolian low porosity loess ($n = 40$-45%) from Northern France presented in Figure 3a (Muñ11). The photo clearly shows the angular shape of the silt grains (10-20 μm diameter) that were produced by erosion by the ice sheet between 15 000 and 20 000 years BP and transported from Southern England by North-West cold, dry and violent winds. Actually, the collapse observed on this loess (see Figure 1) is due only to some local reorganisation in some locations where very large pores (> 10 μm) exist.

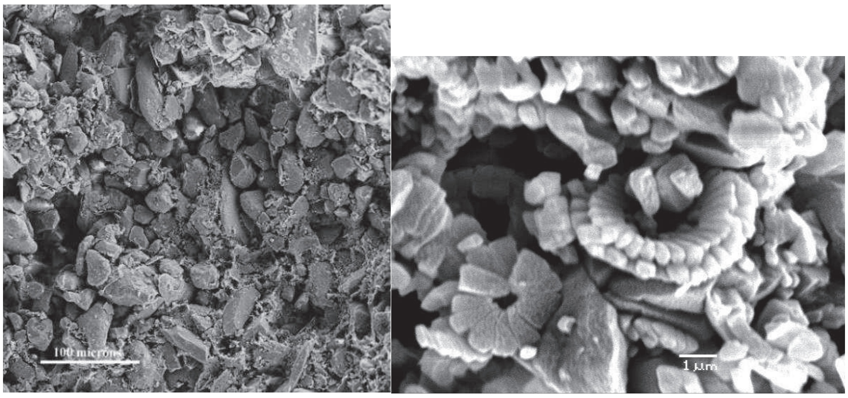

a) b)

Figure 3 : a) SEM photo of a collapsible loess from Northern France (Muñ11); b) SEM photo of Lixhe chalk [Cha02]

Two large pores of this type can be observed in the Figure 3. This loess is also characterised by a heterogeneous repartition of aggregated clay particles. Indeed, some grains appear very clean whereas the inter-grains porosity of others are filled with aggregated clay particles that obviously contribute to the stability of the structure. Apparently, volume decrease due to collapse is due to the local collapse of some largest pores located between clean grains. Similar local collapse phenomenon of largest pores has been observed in the Eastern Canada sensitive clay presented in Figure 6.

Figure 3b presents a SEM photo of the chalk of Lixhe (Belgium) that belongs to the same geological level as the Ekofisk reservoir chalk in which a 20 m subsidence has been observed since enhanced oil recovery by waterflooding started 20 years ago. The high porosity (average value $n = 45\%$) is related to the large pores observed between the elementary 1 μm diameter coccoliths made up of pure calcite that characterise this chalk. Two intact circular arrangements of the unicellular alguae that is typical of this chalk can also be observed. The photo shows that some pores are much larger (5 µm) than the elementary coccolith (1 µm). In the corresponding reservoir chalk full of oil and water, capillarity appears to be the main factor explaining the waterflooding induced collapse.

2.2. Fine-grained soils

Fine grained soils are characterised by a given amount of clay minerals that are quite different in size, shape and nature from the grains represented in the previous Figures. Clay minerals are platy minerals smaller than 2 µm made up of the stacking of various (10 to various hundreds) elementary layers. The mineralogical composition of elementary clay layers is briefly described in Figure 4. The basic components of clay are:

- a tetrahedral layers composed of one atom of silica (Si) surrounded by 4 oxygen ions (O^{--}), with a general chemical composition typical of silica (SiO_2)
- an octahedral layer composed of a metal ion (generally aluminium) located in the centre of the octahedron and surrounded by four OH^- hydroxyls ions.

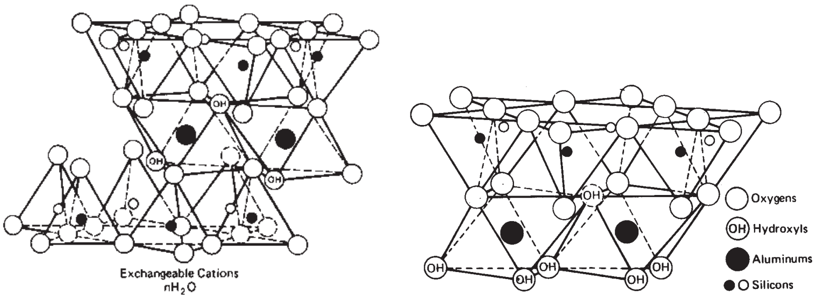

a) b)

Figure 4 : Molecules of montmorillonite (a) and kaolinite (b) [Mit05]

Clays are composed of a combination of these layers together that is made possible by the geometric correspondence between the corners of the tetrahedrons (O^{--}) and the sides of the octahedrons (OH^-). As shown in the Figure, OH^- are replaced by O^{--} at the contacts between the octahedral and the tetrahedral layers:

- Kaolinite is made up of one tetrahedral and one octahedral layer with a 7 Å (0.7 nm) thickness. The link between two elementary layers of kaolinite takes place between a layer of O^{--} (upper tetrahedral layer) and OH^- (bottom OH^-). This link is mainly governed by hydrogen bonding and is rather strong. For this reason, stacks of kaolinite that are composed of 10 to 1000 elementary layers (see [Mit05]) are stable. When kaolinite is hydrated, water does not infiltrate in between the elementary layers;

- Montmorillonite is made up of two tetrahedral and one octahedral layers with a 9 Å (0.9 nm) thickness

Illite is similar to montmorillonite (9 Å thickness) with strong bonds between the elementary layers permitted by fixed potassium cations (K^+). Like in kaolinite, water cannot penetrate the inter-layer space and illite stacks remain stable during hydration. Clays are characterised by an electric charge deficiency resulting from the isomorphic substitution of AL^{+++} by other metals (generally Mg^{++}) inside the octahedral layer. As a result of this electric charge deficiency, an electric field is developed near the clay layer surface, with noticeable effect on the cations dissolved in the pore water that come attracted towards the clay surface (exchangeable cations). This is one of the reasons why an attraction is exerted by clay on water molecules that correspond to the plasticity properties of clay and clay soils.

This is particularly true in the case of montmorillonite where, unlike kaolinite and illite, there are no strong bonds between to elementary layers. During hydration, water molecules can come and adsorb along the elementary layer surfaces. This mechanism is related to the macroscopic swelling that is typical of plastic clays. Due to electrical effects and weak bonds, this interlayer space is also the place where most chemical reactions occur between soluble chemical compounds and clay. Hence, plastic clay with significant amount of smectite (another name for montmorillonite type clays) will be more sensitive to water than lower plastic clays containing kaolinite and illite.

Since they can separate when hydrated, montmorillonite stacks can become quite thin when hydrated to low suction, with less than 10 layers of 9 Å thickness (see [Tes90]). Actually, it has been demonstrated by using X-Ray diffractometry at low angles in various smectites that the hydration of a dry smectite occurs in an ordered manner, as described in Figure 5 [Sai00].

The Figure shows that only one layer of water molecules is adsorbed to the elementary clay layer described in Figure 4 at suction higher than 50 MPa. This corresponds to an internal interlayer distance of 12.6 Å (1.26 nm). When suction is decreased during hydration between 50 and 7 MPa, two layers of water molecules (interlayer distance of 15.6 Å) progressively adsorb. Finally, a third layer (interlayer distance of 18.6 Å) starts adsorbing below 7 MPa and a fourth one at 100 kPa. Simultaneously, the thickness of the stacks reduces with 300 elementary layers above 50 MPa, 150 at 7 MPa. At lower suction, the number stabilises at 10 layers per stack. Inside a saturated aggregate, pores comprised between stacks that reduce in thickness progressively develop, giving rise to three types of pores:

- laminar interlayer pores;
- inter-stacks pores (inside the aggregates);

- inter-aggregates pores.

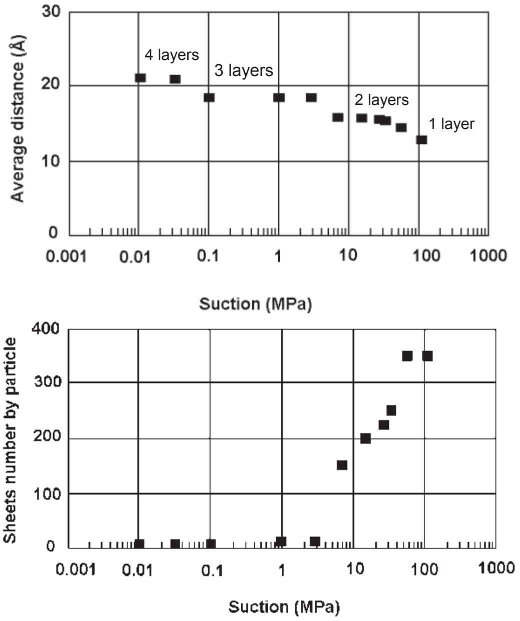

Figure 5 : Hydration mechanism of a dry compacted FoCa clay [Sai00]

In natural soils, it is now admitted that due to higher densities, clays are characterised by aggregates of clay stacks, the aggregation of which being favoured by salt contents higher than 1 mg/l, which is generally the case in Nature.

A theory called the diffuse double layer theory has been developed to model the distribution in water of exchangeable cations generated by the electrical field along the clay layer. As in any electrical field, cations are distributed in the water close to the mineral surface with a concentration that decreases when the distance to the surface decreases. The so-called "diffuse layer" has been described through the Gouy-Chapman Theory (see [Mit05]), which gives the expression of the concentration of cations as a function of the distance from the mineral. More precisely, the diffuse double layer (DDL) is defined by a "thickness" defined by the following relation:

$$x = \sqrt{\frac{DkT}{8\pi n_0 \varepsilon^2 v^2}} \tag{2}$$

where D is the dielectric constant of the medium, k the Boltzmann constant ($k = 1{,}38\ 10^{-16}$ erg/°K), T the absolute temperature, n_0 a reference ionic concentration in a point far from the clay, ε ($\varepsilon = 1{,}6 \times 10^{-19}$ Coulomb) the elementary electronic load, ν the cation valence. This expression shows that the DDL thickness increases with increased dielectric constant and temperature and decreased salt concentration and cation valence.

When two clay layers are close one from another, the effect of the two positively charged DDL is repulsive. The dependency of the DDL thickness versus the valence shows that a montmorillonite suspension made up of the same concentration of soil will have a much larger void ratio in the case of a sodium (Na^+) montmorillonite than in the case of a calcium (Ca^{++}) montmorillonite. For this reason [Mar01] obtained void ratios respectively equal to 11.5 and 3.9 when preparing slurries with Na and Ca clays at a water content $w = 1.1\ w_l$. [Bol56] Bolt (1956) and [Sri82] Sridharan and Jayadeva (1982) proposed a model based on DDL concept to describe the compressibility of smectite suspensions. The DDL theory was also used by [Lam58] to propose a model of the microstructure of compacted soils.

Figure 6a shows the microstructure of a sensitive St Marcel clay from Eastern Canada, mostly composed of illite with no montmorillonite.

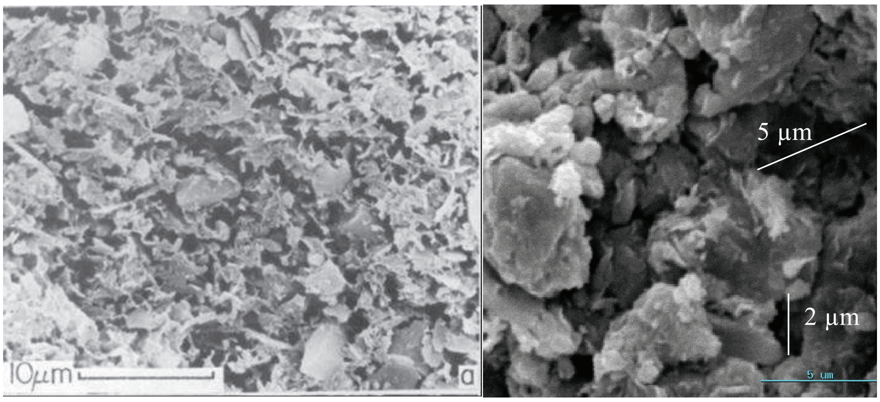

a) b)

Figure 6 : SEM observation of a) Eastern Canada sensitive clay ([Del84]); b) heavily compacted swelling clay for nuclear waste isolation ([Cui02]).

A typical aggregate microstructure is apparent with large inter-aggregates pores (0.5 – 1 µm in diameter) and also some silt grains. It was demonstrated that, in these sensitive clays, aggregates were not affected by remoulding that only concerned inter-aggregates bonds. Figure 6b presents a view of a heavily compacted smectite considered as a possible component of engineered clay barrier for the isolation at great depth of high activity and long life nuclear waste (Japanese Kunigel clay). As in other dry compacted soils ([Ahm74] Ahmed et al. 1974, [Del96] Delage et al. 1996) the photo shows that clay stacks made up of elementary layers are aggregated together. The photo clearly confirms that large pores remain present in compacted clays, even at high specific mass (2 Mg/m^3). Obviously, the microstructure observed in the Figure should play a role in swelling mechanisms that indeed cannot be explained only at the elementary level described in Figure 4. It has been observed that a first stage of hydration and swelling corresponded to the filling of the inter-aggregate voids by aggregate exfoliation. This process progressively conducts to a more homogeneous matrix microstructure in which the inter-stacks actions progressively take place.

Figure 7a presents a SEM photo of the Callovo-Oxfordian (COx) claystone, with a schematic representation of its microstructure also presented in Figure 7b. The COx claystone is considered as a possible host rock for radioactive waste disposal in France. The photo shows the clay matrix (50% clay fraction at 490 m depth in the area of the Bure underground Research Laboratory in the East of France) constituted of a dense assembly of platelets of inter-layered illite-montmorillonite minerals. Detritic grains of quartz and calcite are scattered into the clay matrix. The presence of montmorillonite provides some swelling properties to the COx claystone that exhibits quite interesting self-sealing properties. The main size of the pores is quite small with an average of 30 nm entrance diameter representative of the average thickness of the platelets schematically represented in Figure 7b ([Men14]).

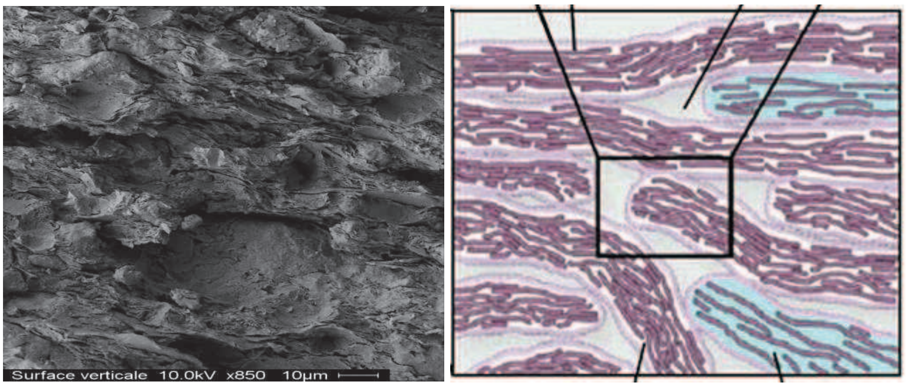

Figure 7: a) SEM photo of the Callovo-Oxfordian claystone [Men14]; b) schematic representation of the COx microstructure ([Yve07])

3 Multiphase geomaterials

Unsaturated granular soils have been briefly described in Figure 2. In fine grained soils, the situation can be schematically represented as shown in Figure 8 ([Del00a]).

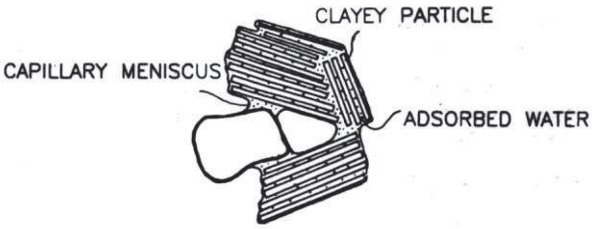

Figure 8. Schematic view of a fine grained unsaturated soil

The unsaturated soil exerts an attraction on water either by capillary action between the grains of the soil or by physico-chemical clay-water interactions. The energy of the water contained in an unsaturated soil is described by a potential, also known as suction or, less satisfactorily, by negative pressure. This suction gives the energy necessary to extract water from the unsaturated soil. For instance, a dense compacted swelling clay used for engineered barriers in nuclear waste confinement will have a suction higher than 10 MPa, which means that the links between the soil and water molecules are very strong. Conversely, a sand, in which only capillary interaction occurs in the smaller pores located at the intergranular contacts, will have maximum suctions not higher than several tens of kPa. If water and air pressures are respectively noted u_a and u_w, the suction (expressed in kPa) is equal to the difference in pressure between air and water:

$$s = u_a - u_w \tag{3}$$

Eq. (3) shows that, if $u_a = 0$ (0 being the atmospheric pressure), a positive value of suction corresponds to a negative value of u_w.

The value of the suction in a soil depends of various parameters, including the water content: a dry soil (high suction) will have a low water content and a low degree of saturation S_r[1], whereas a wet soil will have a low suction and high water content and degree of saturation.

3.1 Water retention properties

The relation suction/water content in a soil is defined by the so-called water retention curve of the soil. The experimental determination of the water retention curve is made using the Richards cell presented in Figure 9.

---

[1] The degree of saturation of a soil is defined by : $S_r = V_w/V_v, = w_{nat}/w_{sat}$, where V_w and V_v are respectively the water and porous volumes and w_{nat} and w_{sat} are the natural (unsaturated) and saturated water contents

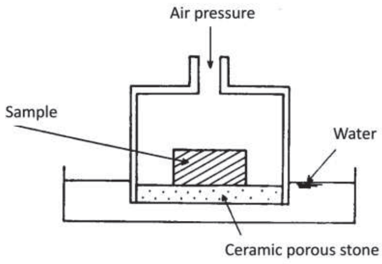

Figure 9. Richards's cell for the determination of water retention curves

This cell permits the control of suction according to the so-called *axis-translation* system [Van08] (Other techniques of controlling suction include the osmotic technique [Del08] and the vapour equilibrium method, [Del98], [Bla08]). The cell is air-pressure proof, and its base is composed of a ceramic low porosity porous stone, called high air entry value (HAEV) porous stone. The principle of the system is that the pores of the ceramic are so small that the air pressures imposed in the cell during the water retention curve remain too small to desaturate it. In other words, the capillary air-water menisci located at the surface of the ceramic can resist to the air pressure, according to Laplace-Jurin law, which writes:

$$u_a - u_w = \frac{2\sigma_s \cos\theta}{r} \tag{4}$$

where r is the pore radius, σ_s the surface air-water tension and θ the contact angle between the meniscus and the solid. For water, σ_s = 72,75 kN/m and $\cos\ \theta = 1$.

Figure 10 [Cro52] shows the retention curve of a clayey sand. The curve was determined by placing the saturated sand in the cell, and by applying increasing air pressures in a step by step progression.

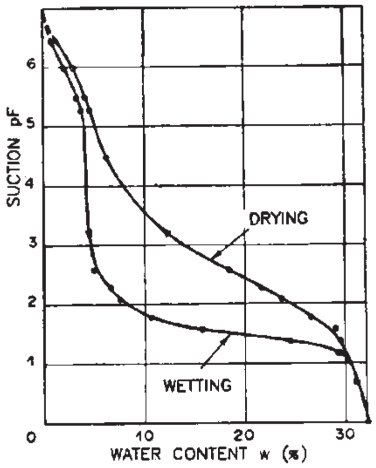

Figure 10. Water retention curve of a clayey sand [Cro52]

For a given applied air pressure, a time period of 4-5 days is waited for to allow for suction equilibration. Then, the sample is quickly withdrawn and weighed to determine the water content. The sample is afterwards placed in the cell so as to increase the pressure, reach a new equilibrium under higher suction and lower water content and degree of saturation, and so on. The curve shows an important characteristic of porous media, i.e. the hysteresis observed in a drying wetting path: at a given suction, the water content obtained when desaturating is still higher than that obtained when wetting the samples. Various explanations of this standard feature are given in [Del00a].

In petroleum engineering, retention curves are called capillary pressure curves, since capillarity is the dominant interaction between the fluids and the solid phase. The retention properties of the oil-water couple of fluids in reservoir rocks (sandstones, chalks) is of utmost importance for oil recovery, particularly in the case of enhanced recovery by waterflooding when seawater is injected in the reservoir rock to help oil extraction. The oil-water retention of Lixhe Chalk from Belgium [Pri04] is presented in Figure 11. Lixhe chalk is belonging to the same geological level as the reservoir chalk of the Ekofisk reservoir that presented subsidence problems that were considered in the Pasachalk European research projects [Pas03].

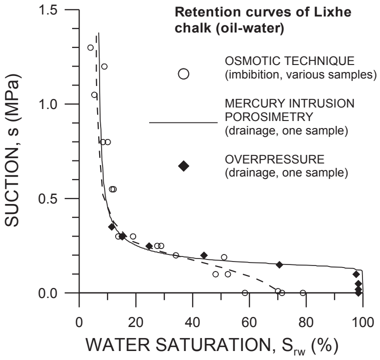

Figure 11. Oil-water retention of Lixhe Chalk [Pri04].

The chalk sample was initially saturated with water and oil was infiltrated under controlled oil-water suction condition (axis translation method). The curve shows that a degree of saturation in water S_{rw} close to 6% is reached at a 1.3 MPa suction. A good similarity is observed between the axis translation water drainage curve obtained from various samples and a curve derived from the mercury intrusion porosimetry test obtained on one sample. Oil was afterwards infiltrated under constant decreasing oil-water suction that was controlled using the osmotic technique. The curve shows that a residual degree of saturation in water close to 70% appears at the end of the oil infiltration phase. This is one of the criteria used when qualifying the wettability of reservoir rocks. A residual degree of saturation of 70% shows that the chalk considered is water wet. Note that some other North Sea reservoir chalks, as the Valhall chalk for instance, are oil wet, due to the adsorption and coating of hydrocarbon components along the surface of the chalk grains. The wettability of reservoir rocks is a key property in petroleum engineering. As further commented later on, interest towards the water retention properties of claystones used as geological host in radioactive waste disposal recently grew due to their significant sensitivity to changes in water content. Figure 12 shows the changes in water content (a) and porosity (b) of the Callovo-Oxfordian claystone with respect to suction starting from an initial state with a porosity of 17%, a water content of 7.2% and a suction of 14 MPa. Claystones exhibit standard features like hysteresis and are also characterised by significant swelling properties and some shrinkage, as indicated in Figure 12b.

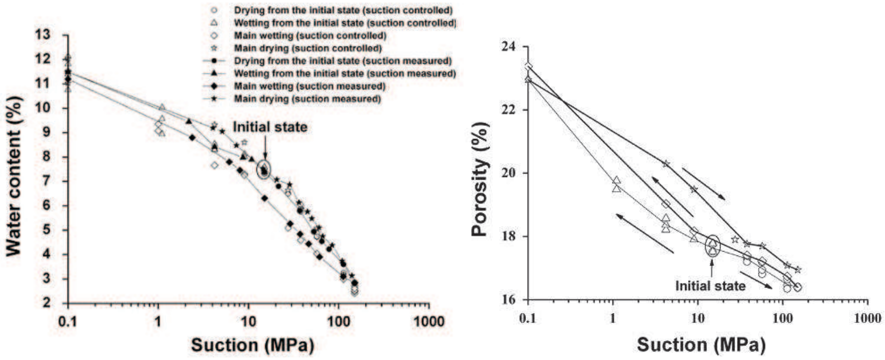

Figure 12. Air-water retention properties of the Callovo-Oxfordian claystone [Wan14]

The concepts of water adsorption in montmorillonites helps interpret the water retention properties of compacted bentonites. Compacted bentonites are considered in radioactive waste disposal to make water proof plugs in cells and galleries. In some options, they are also planned to be placed between the waste canisters and the host rock. This is the case in particular in the Swedish concept of waste disposal in granite. Their initial suction can be very large, up to more than 100 MPa. Figure 13 shows the water retention curve of a FoCa7 compacted bentonite in both free swelling and no volume change conditions. One can then consider, according to the data of Figure 5, that only one layer of water molecules is present at initial state (suction 113 MPa), whereas two layers are adsorbed when hydrating and decreasing suction to 50 MPa. The Figure shows that a significant difference occurs between the free swelling and the constant volume condition close to 9 MPa, i.e. at the suction at which the third layer start to adsorb. This confirms that the hydration energy level of the third layer of water molecules is lower than the previous two layers.

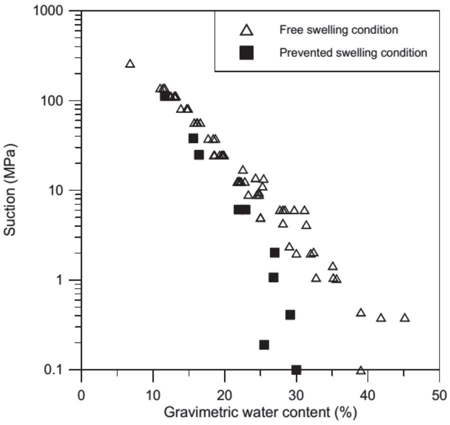

Figure 13. Water retention properties of compacted FoCa7 bentonite [Yah01]

The water retention curves of many compacted bentonites have been investigated, showing the predominant effect of physico-chemical interactions compared to capillary actions. As a consequence, the water retention curves of compacted bentonites are independent of the density.

3.2 Water and gas flows in multiphase geomaterials

In the following, the case of water and air transfer in unsaturated soils is presented. Phenomena are roughly similar in other multiphase geomaterials like reservoir rocks except when considering the compressibility of the non wetting fluid (air in unsaturated soil and oil in reservoir rocks). Actually, various techniques from oil engineering have been adapted to unsaturated soils.

The determination of water transfers in unsaturated soils is necessary to predict infiltration in unsaturated soil masses like in the vadose zone, in unsaturated slopes and in engineered barriers or liners. The water permeability of an unsaturated soil changes with its water content or degree of saturation, which makes permeability determinations more delicate than in saturated soils. Various techniques exist and are described in [Del00a] and [Mas08]. Here, only the so-called instantaneous profile method is described, since it provides at the same time an interesting insight in the mechanism of water infiltration in an unsaturated soil.

Unsaturated water permeability : the instantaneous profile method

The method consists in placing a cylindrical sample of soil in a horizontal column (length L, area A), and in infiltrating water, at a constant flow for instance, in the column from one side [Dan82]. During infiltration, changes in suction with time are monitored at various distances from the infiltration side. Suction is measured using tensiometer for lower suctions ($s < 80$ kPa) in sands or low plasticity silts, and with thermocouple psychrometers in clays ($s < 500$ kPa). In parallel, the wetting path of the water retention curve of the soil is determined. Hence, it is possible to draw the isochrones of suction and water content at various periods of time, as shown in Figure 14.

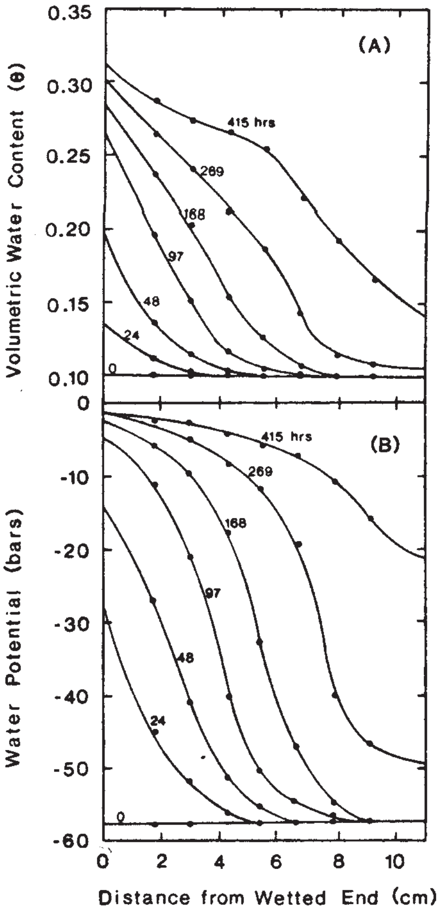

Figure 14. Isochrones of suction and volumetric water content obtained at various periods of time during the infiltration of a column [Dan84]

The calculation of the permeability as a function of water content is based on the calculation of the hydraulic gradient *i* and of the flow *q* in various points of the diagrams of Figure 14 :

- the determination of the gradient *i* is simple, since *i* is given by the slope of the suction vs distance curves, as showed in Figure 14b

- the unit flow is obtained from the water content isochrones of Figure 14a, by integrating the volumetric water content profiles between x_i and L at time $t + \Delta t$ and t. The water volume V passed at a distance x_i is given by :

$$V = A\left(\int_{x_i}^{L} \theta_{t+\Delta t} dx - \int_{x_i}^{L} \theta_t dx \right) \qquad [5]$$

the unit flow q, calculated between t *et* $t+\Delta t$ is equal to :

$$q = A\frac{\int_{x_i}^{L}\theta_{t+\Delta t}dx - \int_{x_i}^{L}\theta_t dx}{\Delta t} \tag{6}$$

The permeability is derived from the unit flow and the average gradient between t and $t + \Delta t$, as follows :

$$K = -\frac{1}{A}\frac{q}{0{,}5\left(i_t + i_{t+\Delta t}\right)} \tag{7}$$

Air permeability

Air permeability measurements can be measured using the device presented in Figure 15 [Yos63]. Basically, the principle is similar to that used in variable head determination of water permeability. A U-tube is connected to an air-tank and to a standard oedometer cell. In a first stage, a small air pressure is imposed in the U-tube, giving rise to a difference in level of water in both sides of the U-tube. In a second step, the U-tube is disconnected from the air reservoir and connected to the cell, and air is circulated through the sample under a decreasing pressure related to the difference in water level in the U-tube. The decreasing level change is monitored as a function of time. According to [Yos63], the intrinsic permeability is given by the following relation:

$$K_a = -\frac{2{,}3Vh\mu_a}{t}\frac{lg\frac{p(t)}{p(0)}}{S\left[p_a + \frac{p(0)}{4}\right]} \tag{8}$$

where V is the reservoir volume, h and S respectively the sample thickness and section, μ_a dynamic viscosity of air, p_a the atmospheric pressure. Experiments show that the air permeability is only depending of the air void ratio $e_a = e\,(1 - S_r)$, according to the two parameters (a, n) following relation:

$$K_a = a\left[e(1 - S_r)\right]^n \tag{9}$$

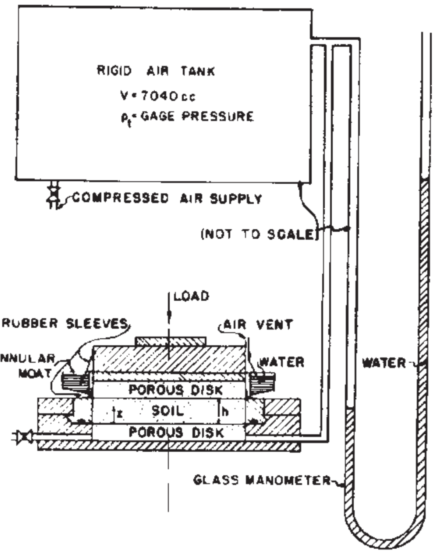

Figure 15. System for air permeability measurements [Yos63]

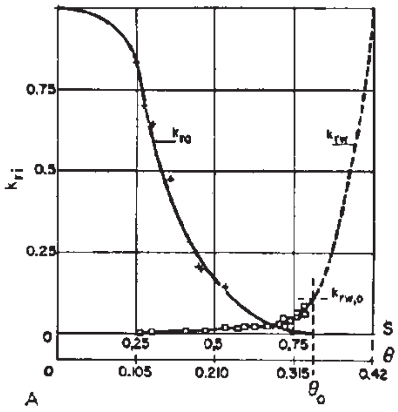

Figure 16. Typical two phase permeabilities in an undeformable porous medium [Vac74]

Typical results in terms of relative permeabilities ($k_r = k(S_r)/k(100\%)$) of air and water permeabilities measured at various degrees of saturation in a sand using the instantaneous profile method are presented in Figure 16 (Vachaud et al. 1974). The figure shows the decreasing air permeability between $S_r = 0$ and 75%, showing that the air is occluded above 75%. Similarly, there is no water continuity between $S_r = 0$ and 25% and most of the water permeability occurs between 75 and 100%. The trends observed in Figure 16 are also valid in the case of reservoir porous rocks (chalks, sandstones) considered in petroleum engineering. In clays, things are less simple due to the clay-water interactions, which induce soil deformations when S_r

changes. The relative permeability curves of reservoir rocks are quite similar to that of Figure 16.

Air and water permeability can also be measured simultaneously [Fle95] using a more sophisticated device initially proposed by [Cor57] where air and water pressures are simultaneously controlled. A similar device can be used for oil reservoir rocks.

3.3 Mechanical testing of unsaturated soils

Figure 17 presents the triaxial suction controlled apparatus developed by [Bis62].

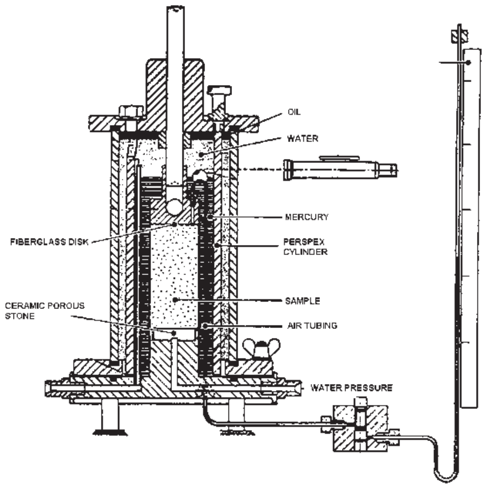

Figure 17. Suction controlled triaxial apparatus Bishop and Donalds (1962)

Oedometers based on the axis translation system were also developed [Esc73]. The sample, cell and pistons are placed inside an air pressure proof cell, and the base porous stone is a ceramic HAEV stone.

Two important behaviour features of the behaviour of unsaturated soils are presented in Figure 18, which presents isotropic (a) and triaxial shear (b) test results performed under controlled suction comprised between 200 and 1500 kPa. Basically, the stiffness and shear resistance of unsaturated soils increase when the soil is dried (decreasing S_r), i.e. when suction is increased. Thus, the compression index decreases and the yield pressure (equivalent to the preconsolidation pressure in saturated soils) increases with increased suction, as quoted initially in the Barcelona Basic Model [Alo90] (Figure 18a). Similarly, the shear modulus and the shear resistance increase with increased suction (Figure 18b).

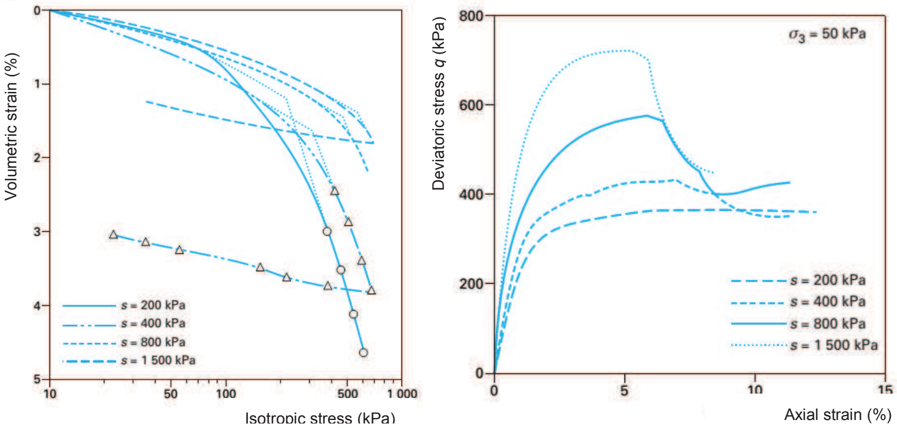

Figure 18a. Compressibility and shear strength of unsaturated soils [Cui96]

4 Thermal issues in clays and claystones

As commented above, the interest devoted to thermal issues in clays and claystones is mainly linked to deep geological disposal of high level exothermic radioactive waste. Investigation initially concerned clays with particular attention to Boom clay, a possible host rock deeply studied in Belgium. More recently, investigation were also carried out in claystones, with particular attention devoted to the Opalinus clay in Switzerland and to the Callovo-Oxfordian claystone in France.

Thermal issues in clays and claystones include the changes in mechanical response with temperature, of significant importance when attempting to predict the response of the host rock in the close field near the disposal cells. This includes thermal volume changes under elevated temperature and the effect of temperature on the shear strength behaviour of clays and claystones (elastoplastic response and failure properties). Another important point is the thermal pressurisation of the pore water in heated clays and claystones that will be commented in more details.

4.1 Thermal testing of clays

Testing clays and claystones at various temperatures between 20 and 100°C is not that difficult, since triaxial cells can easily be heated, for instance, using electrical heating wires placed around the cell. This system was considered in the first thermal triaxial system developed by [Bal85]. Thermocouple sensors placed in the cell fluid provide a simple and accurate way of controlling temperature (0.1°C).

Figure 19 [Del00b] presents an isotropic thermal compression cell developed to investigate the thermal behaviour of the Boom clay. The confining pressure and back pressures are applied through pressure-volume controllers (GDS Brand) that also monitor thermal volume changes, thanks to temperature controlled baths in which the connecting tubes are immersed between the cell and the pressure-volume controllers. A detailed presentation of the systems developed up to now including system using internal heaters is made in [Cek05] in which a novel triaxial system with internal heaters is also presented.

When testing a clay that exhibits some swelling properties like the Boom clay, it is important to impose in-situ stress conditions prior to saturating the specimen. Actually, clay specimens that have been correctly extracted exhibit a suction value close to the average effective stress and a direct contact with water and no stress applied would release the suction and result in some swelling [Del07] that degrades the clay mechanical properties.

When heating a saturated soil, the soil minerals and the pore water thermally expand with different thermal expansion coefficients α_m and α_w, according to:

$$\Delta V_m = \alpha_m V_m \Delta T \quad \text{and} \quad \Delta V_w = \alpha_w V_w \Delta T \tag{10}$$

where α_m is in the order of 10^{-5}°C in clays. For water, [Bal88] proposed to adopt an expression given by Juza, that accounts for the effects of temperature and pore water pressure p_w as follows :

$$\alpha_m (T,p_w) = \alpha_0 + (\alpha_1 + \beta_1 T)\ ln\ mp_w + (\alpha_2 + \beta_2 T)\ (ln\ mp_w)^2 \tag{11}$$

with $\alpha_0 = 4.505\ 10^{-4}$°C, $\alpha_1 = 9.156\ 10^{-5}$°C, $\alpha_2 = 6.381\ 10^{-6}$°C, $\beta_1 = -1.2\ 10^{-6}$°C^{-2}, $\beta_2 = -5.766\ 10^{-8}$°C^{-2}, $m = 15$ MPa^{-1}.

Since the thermal expansion coefficient of water is significantly larger than that of the soil minerals, differential thermal expansion will give rise to significant water pore pressures if heating is too fast with respect to drainage conditions. With standard triaxial specimens (38 mm in diameter and 76 in length), calculations and experiments showed that a heating rate as low as 1°C per hour was necessary to ensure drained conditions with no thermal pore pressure generation during heating.

The subsequent dissipation of pore pressures is called thermal consolidation ([Paa67], [Hou87], [Del00b]). It occurs in clay soils and is fairly similar to standard consolidation. It may be of some importance in saturated host clay rocks in the near field of nuclear waste disposal at great depth, and should affect the gallery stability.

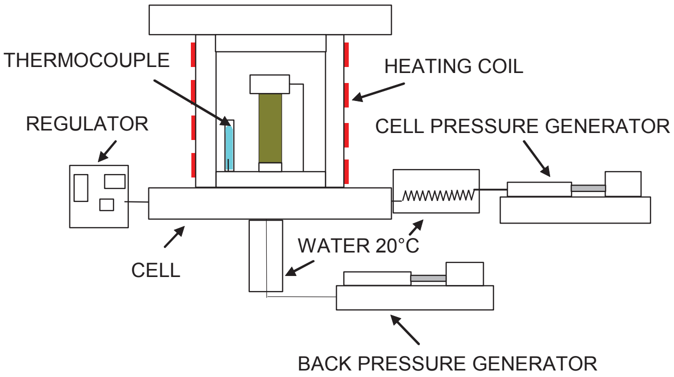

Figure 19. Isotropic compression high pressure thermal cell [Del00b]

At elevated temperature, the viscosity of water decreases resulting in easier movement through the pores of the soil and a decrease in permeability (in m/s) as shown in Figure 20a from data of Boom clay [Del00b]. However the changes in intrinsic permeability (Figure 20b) indicate no significant effect of temperature on the intrinsic permeability. This a simple and important feature when computing water transfers in saturated soils at elevated temperature.

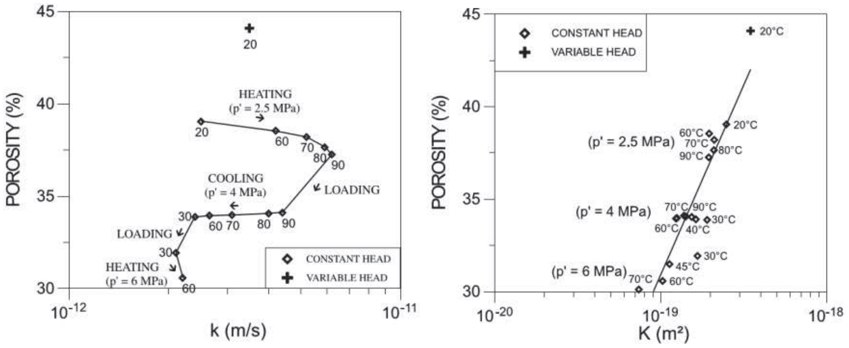

a) b)

Figure 20. Effect of temperature on the permeability of Boom clay [Del00b]

The effect of elevated temperature on the mechanical properties of soils can be considered as opposite to that of suction, i.e. the soil becomes weaker and exhibits smaller shearing resistance. As far as volume changes are concerned, there is little influence on the elastic and plastic compression indexes in clay soils [Cam68], [Cek04]. However, a specific dependence on the overconsolidation ratio has been observed by various authors. Overconsolidated soils behave as any material, i.e. dilates under increased temperature due to the thermal dilation of the components; the thermal dilation occurs up to a maximum temperature which depends on the thermo-mechanical history of the sample. It is followed by a thermal contraction, as seen in Figure 21a [Sul02] where dilation strains are negative. Consolidated soils contract under heating, due to the weakening of clay-water links with temperature, which liberates some layers of water molecules.

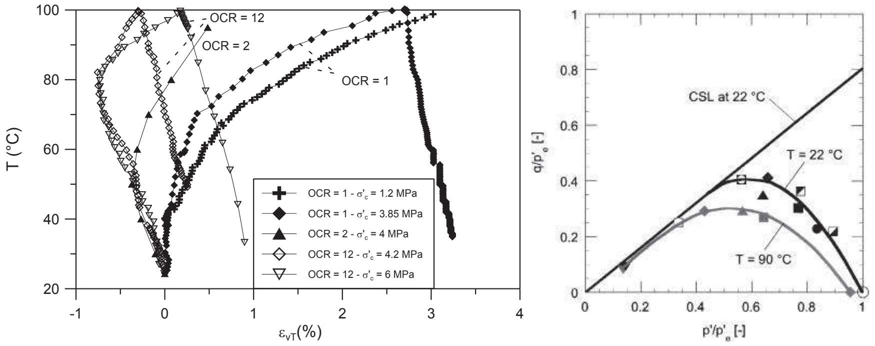

a) b)

Figure 21. a) Volume change response of Boom clay heated under various constant isotropic loads [Sul02]; b) Normalized yield envelope of Kaolin at T = 22 and 90°C [Cek04].

Figure 21b [Cek04] shows the reduction of the normalised yield envelope of a saturated kaolin when the testing temperature is increased from 22 to 90°C. This result confirms earlier findings by [Hue90].

4.2 Thermal testing of claystones and shales

Claystones are one or two order of magnitude less permeable than clays, with intrinsic permeabilities around 10^{-20} - 10^{-21} m^2 corresponding to permeabilities of 10^{-13} - 10^{-14} m/s and the issues of satisfactory drainage conditions and homogeneous pore pressure field conditions are important concerns. Experience also shows that core specimens of claystones and shales are unsaturated once extracted. Actually, unlike clays that in most case remain saturated when extracted because the resulting suction is smaller than the air-entry value [Del07], the larger stress release observed in claystones results in suction once extracted of several tens of MPa, larger than their air-entry value that is close to 10 MPa in the case of the Callovo-Oxfordian (COx) claystone.

Saturation and drainage conditions

Given their significant sensitivity to changes in water content, the saturation procedure adopted (or not adopted) during testing is an important question as well. Like unsaturated soils, they become significantly stronger when desaturated. As shown in Figure 22, [Pha07] observed increases in unconfined compression strength (UCS) from 28 MPa to 58 MPa in samples submitted to desaturation by imposing controlled relative humidities (RHs) of 98% and 32% respectively, with corresponding water contents decreasing from 5.24% to 1.65%. The data of Figure 22 clearly indicate that partial saturation may overestimate the mechanical characteristics of claystones.

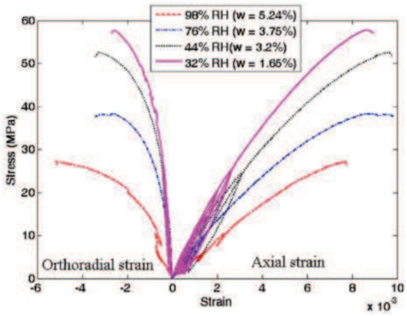

Figure 22. Water sensitivity of COX clay, UCS tests [Pha07].

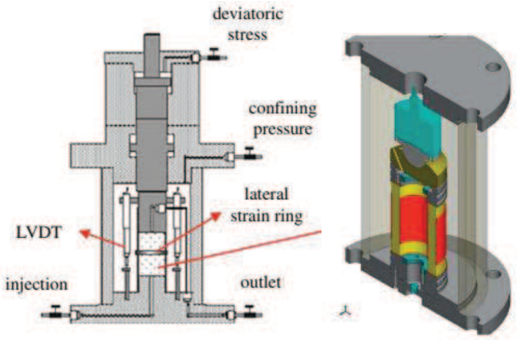

a) b)

Figure 23. Testing devices with short drainage lengths: a) small triaxial device (10 mm in diameter and 20 mm in height, [Hu13]; b) hollow cylinder triaxial (100 mm external, 60 mm internal diameter, 70 mm height, [Mon11a]

In low permeability geomaterials, the resaturation procedure as well as the quality of the drainage and the resulting homogeneity in pore pressure field is conditioned by the drainage length of the testing device. It is known that standard triaxial specimens drained at both bottom and top require excessively long saturation periods or low strain rate when testing. The solution is to adopt small drainage length and various devices have been developed accordingly, as shown in Figure 23.

In the small triaxial device in which the specimen is drained on top and bottom, the drainage length is equal to half the sample height, i.e. 10 mm. In the hollow cylinder where drainage is ensured on top, bottom and on the internal and external faces by means of a geotextile, the drainage length is equal to half the cylinder thickness, i.e. 10 mm. The effect of this enhanced drainage system has been calculated by [Mon11a] and is presented in Figure 24a.

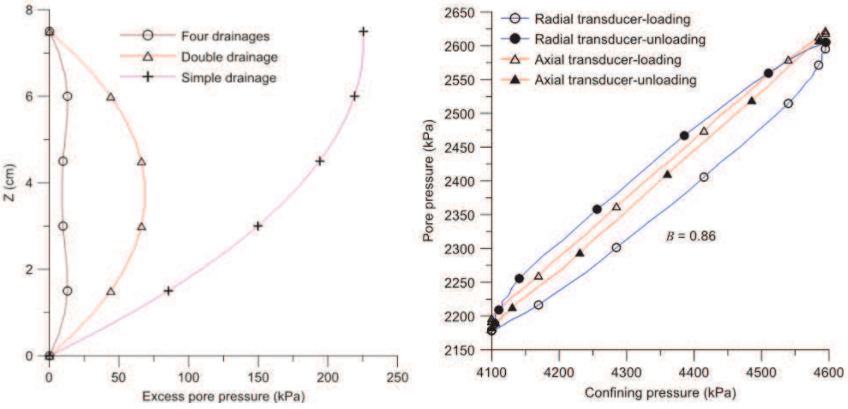

Figure 24. a) Computed excess pore pressure profiles in half the thickness of the sample during isotropic compression under different drainage conditions; b) Undrained loading test to determine the *B* Skempton parameter [Mon11a].

Figure 24b presents the results of an isotropic "undrained" compression test in which the pore pressure increment Δu is presented with respect to the increment in total stress $\Delta\sigma$.

In the framework of poro-elasticity (see for instance [Det93]), the expression of *B* is as follows:

$$B = \frac{\Delta u}{\Delta \sigma} = \frac{c_{\mathrm{d}} - c_{\mathrm{s}}}{c_{\mathrm{d}} - c_{\mathrm{s}} + \phi(c_{\mathrm{w}} - c_{\mathrm{s}})} = \frac{c_{\mathrm{d}} - c_{\mathrm{s}}}{S} \qquad (12)$$

where *S* is the storage coefficient that can be written as:

$$S = c_{\mathrm{d}} - c_{\mathrm{s}} + \phi(c_{\mathrm{w}} - c_{\mathrm{s}}) \qquad (13)$$

where ϕ is the porosity, c_{d} is the drained compressibility of the claystone, c_s is the compressibility of the solid grains, and c_w is the compressibility of water. Parameter c_{s} can be determined by a so-called unjacketed compression test in which the back pressure and the confining stress are simultaneously and equally increased while measuring the volume changes of the specimen.

In soils, good saturation corresponds to *B* values close to one. In porous rocks, this is no longer true given the form of Eq. (2) and the fact that in porous stones c_s is no longer negligible compared to c_d.

Actually, an "undrained" test is in fact a test in which the drainage valves connected to the cell base are closed. In low porosity rocks, it is not fully undrained given that some water exchanges occur between the porosity of the compressed specimen and that of the porous elements surrounding it. This effect has also to be accounted for when comparing the experimental value and the theoretical expression given in Eq. (2). Detailed calculations made in [Mon13] show that a corrected theoretical value of 0.89 is obtained that compares favourably with the slope (B = 0.86) calculated from the data of Figure 24b (with c_w = 0.449 GPa^{-1}, c_d = 0.348 GPa^{-1}, c_s = 0.02 GPa^{-1} for the Opalinus clay).

Thermal volume changes in claystones

The response of a specimen of Opalinus clay to a drained thermal cycle between 25 °C and 80 °C under in situ mean stress conditions (total mean stress p = 4.1 MPa and pore pressure p_w = 2.2 MPa) is presented in Figure 25. The test was conducted at a heating rate of 1°C/h so as to ensure fully drained conditions with the enhanced drainage system (see above).

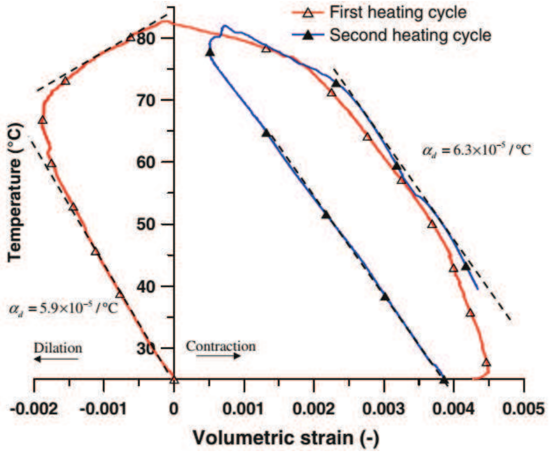

Figure 25. Drained thermal volume changes of Opalinus clay under in-situ mean stress conditions [Mon11b].

The subsequent cooling phase is characterized by a thermo-elastic contraction with a slope approximately parallel to that of the first heating phase, confirming the reversible nature of the response. The corresponding thermal expansion coefficients are $\alpha_d = 5.9 \times 10^{-5}\ ^\circ\mathrm{C}^{-1}$ along the heating phase and $6.3 \times 10^{-5}\ ^\circ\mathrm{C}^{-1}$ along the cooling phase. Note that these thermal expansion coefficients are comparable, although somewhat larger, to those of the solid phases in the claystone (between $1 \times 10^{-5}\ ^\circ\mathrm{C}^{-1}$ and $3.4 \times 10^{-5}\ ^\circ\mathrm{C}^{-1}$).

The thermal irreversible contraction observed during the first heating phase above 65°C is comparable to that observed in normally consolidated plastic clays (e.g. [Bal88] and [Del00] on Boom clay). In fine grained soils, this phenomenon is understood as a thermal consolidation of the sample which corresponds to the rearrangement of the grains after a critical temperature. It seems that the claystone has kept the memory of its maximum supported temperature like over-consolidated soils conserve the memory of the maximum supported load. Once heated up to 83°C after the first cycle, the sample keeps expanding up to 80 °C (the new maximum temperature supported) during the second cycle, forgetting the previous temperature threshold of 65°C. It is interesting to relate this first temperature threshold to the maximum temperature previously experienced by the Opalinus clay. From geological arguments the maximum burial depth of the Opalinus clay at Mont Terri is 1350 m. Assuming a geothermal gradient of about 0.03 °C/m, the value of 65 °C appears as a plausible maximum temperature experienced by the material before our test. The observed behaviour is typical of thermal hardening, with an elastic thermal expansion observed below the maximum supported temperature, followed by a plastic contraction at yielding once the maximum temperature is attained.

Thermal pressurization in claystones

To investigate thermal pressurization, an isotropic thermal compression device with reduced drainage path is presented in Figure 26.

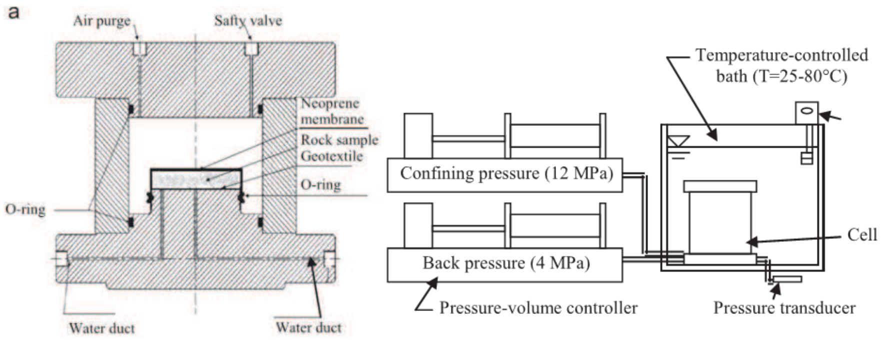

Figure 26. Isotropic compression cell [Moh12].

The aim of the test is to measure the thermal pore pressure developed when the specimen is submitted to temperature elevation under a given stress level. As commented before, this thermal pore pressure generation is due to the fact that the thermal expansion coefficient of water is significantly higher than that of the solid phase.

The cell is presented in Figure 26a and the heating and loading device is shown in Figure 26b. The cell is a standard high pressure isotropic compression cell accommodating a disk-shaped specimen (oedometer type) having a diameter of 70 mm and a height of 10 mm. Drainage is ensured by a geotextile at the base of the sample resulting in a small length of drainage of 10 mm. Two water ducts connect the sample bottom to either a pressure volume controller for back pressure (PVC, GDS brand) or a pressure gauge.

Figure 26b presents the connections to the two PVC and the temperature controlled bath (± 0.1 °C) in which the cell is immersed. Note that the pressure transducer is located outside the bath. Special care was devoted to the saturation procedure that was carried out under stress conditions close to in situ. Given that the drainage length is equal to 10 mm (the height of the specimen drained at bottom), saturation periods comparable to that obtained with the hollow cylinder triaxial were observed. The determination of satisfactory values of the Skempton coefficient *B* was also made.

In a perfect undrained THM test carried out in an elastic porous material, the pore pressure increase is given by the following expression:

$$\Delta u = B\Delta\sigma + \Lambda\Delta T \tag{14}$$

where the thermal pressurization coefficient Λ is defined by the following equation:

$$\Lambda = \frac{\Delta u}{\Delta T} = \frac{\phi(\alpha_{\mathrm{w}} - \alpha_{\mathrm{s}})}{c_{\mathrm{d}} - c_{\mathrm{s}} + \phi(c_{\mathrm{w}} - c_{\mathrm{s}})} \tag{15}$$

As in the case of the determination of the Skempton coefficient *B*, corrections are to be made in the determination of Λ with respect to perturbations due to the effects of the porous elements in contact with the specimen (see [Gha09]; [Moh11]).

The data shown in Figure 27a show the response in pore pressure obtained in a COx sample along a ramp of stepwise progressive temperature elevation between 25 °C and 70 °C. The comparison with the response obtained with a dummy metal sample indicates that the first peak of temperature corresponds in fact to the instantaneous response of the water contained in the permeable porous elements. A period of time has to be waited for to get equilibration between the pore water and that contained in the porous elements, corresponding to the drainage of pore water from the specimen to the porous elements. When considering the equilibration points, one obtains the curve presented in Figure 27b. It can be observed from the results of two tests that the thermal coefficient Λ decreases with temperature from 0.116 to 0.063 MPa/°C between 42 °C and 56 °C in test No. 1 and from 0.145 to 0.107 MPa/°C between 32°C and 62°C in test No. 2.

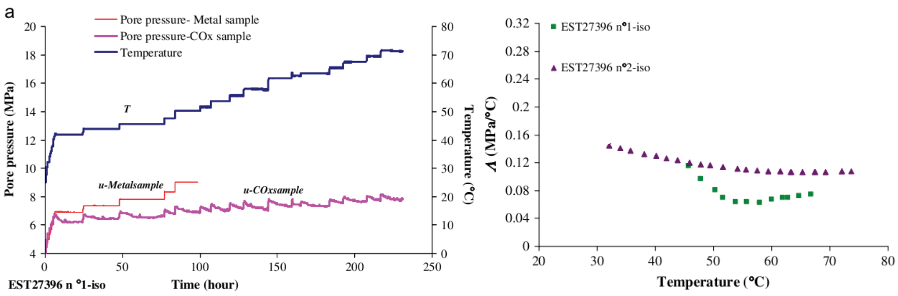

a) b)

Figure 27. a) Comparison between thermally induced pore pressure with a COx claystone and a dummy metal sample; b) Changes in thermal pressurization coefficient with temperature [Moh11].

As commented in more details in [Moh11], the use of Eq. 15 to correctly predict the experimental changes of Λ with respect to temperature observed in Figure 27b requires the adoption of a non-constant value of the drained compressibility changing with either the applied stress or temperature. Indeed, thermal pressurization (in undrained conditions) is a complex combination of increase in pore pressure that results in a corresponding decrease in effective stress. The decrease in effective stress mobilises the specimen's compressibility besides the thermal dilation coefficients of water and of the solid phases.

5 Conclusions

The THM issues dealt with in this text mainly come from the experience gained by the author in problems related with radioactive waste disposal at great depth, with also some insights from standard unsaturated soils and multiphase chalks. The response of both water saturated and multiphase geomaterials to changes in hydric, mechanical and thermal conditions can be roughly summarised as follows:

- Drying (or increasing the non wetting phase) tends to strengthen geomaterials;
- Temperature elevation has the opposite effect of weakening.

In terms of hydric effects, a significant difference arises from the nature of the interaction between the pore fluid and the geomaterials. In non clayey materials like for instance sands, sandstones or chalk, the main interaction comes from capillarity that governs the potential of water (also called suction). In clayey geomaterials, physico-chemical interactions play a dominant role with a level of energy that can be significantly higher. Whereas the order of magnitude of suction is of several to several tens of kPa in granular geomaterials, it can be equal to several hundreds of kPa in clayey materials and finally reach several tens of MPa in plastic soils like for instance compacted bentonites used in radioactive waste disposals to ensure water tightness. In other words, the level of attraction of water molecules along the surfaces of the clay minerals can be very high. In smectites (another name of montmorillonites), the mechanisms of adsorption of water molecules along the minerals are fairly well known and can be useful in interpreting some macroscopic features. Actually, montmorillonite are often present as inter-layered illite-smectite platelets in claystone and their role is essential in terms of radionuclides confinement: active clay minerals are prone to retain radionuclides through physico-chemical interactions; the sealing properties of claystone is also due to smectites minerals that, when hydrated insides cracks, are able to fill the volume of the cracks and to bring back the permeability of the damaged claystone back to that of the intact one.

Thermal issues in geomaterials attracted more and more in the past years for various reasons. Besides the necessity of knowing how the mechanical characteristics change when temperature is elevated, two issues have been also investigated: the volume changes of clays and claystones under elevated temperature and thermal pressurisation. It is well established that normally consolidated clays tend to exhibit plastic contraction when heated, whereas over-consolidated clays dilate with respect to their over-consolidation ratio. Actually, it is not established that claystones behave like over-consolidated clays, given that the long period of diagenesis they have been submitted to (158 millions years for the Callovo-Oxfordian claystone) result in the fact that they don't necessarily kept the memory of the maximum load they supported. As observed here on the Opalinus clay, they may exhibit plastic contraction and thermal hardening.

THM issues in geomaterials remain a topic of wide interest and active researches are still carried out, with on-going researches related to radioactive waste and to sustainable storage of various fluids like CO_2, or of compressed air in caverns or reservoir rocks as an energy storage option. Claystones and shales attract growing interest in unconventional oil and gas recovery. Thermal effects are also essential when interpreting geothermal issues, including thermal piles in which thermo-mechanical coupling concern the long-term stability of buildings founded on piles submitted potentially to many cycles in temperature at the pile/soil interface, a zone supporting high levels of shear. Hydro-mechanics couplings as investigated in unsaturated soils have proven their efficiency to analyse couplings in reservoir rocks as well, providing a sound explanation of the subsidence observed above oil or gas fields.

Besides the developments of sound experimental techniques that enlighten some important mechanisms governing the THM response of geomaterials, constitutive models and numerical codes that have been validated on both in-situ and laboratory experiments now provide some useful and efficient prediction of complex THM problems of growing importance.

References

[Ahm74] Ahmed S., Lovell C.W. and Diamond S. Pore sizes and strength of compacted clay. *Journal of the Geotechnical Engineering Division*, ASCE, 100 (GT4): 407-425, 1974.

[Alo90] Alonso E.E., Gens A. and Josa A. A constitutive model for partially saturated soils. *Géotechnique*, 40(3):405-430, 1990.

[Ave01] Aversa S., Nicotera M.V. A triaxial and oedometer apparatus for testing unsaturated soils. *ASTM Geotechnical Testing Journal*, 25(1): 3-15, 2001.

[Bal85] Baldi G., Borsetto M., Hueckel T. and Tassoni E. Thermal induced strains and pore pressure in clays. *Proceedings of an International Symposium on Environmental Geotechnology*, pages 391-402, 1985.

[Bal88] Baldi G., Hueckel T. and Pelegrini R. Thermal volume changes of mineral-water system in low porosity clays. *Canadian Geotechnical Journal*, 25:807-825, 1988.

[Ben04] Benhamed, N., Canou, J., Dupla, J.-C. Structure initiale et propriétés de liquéfaction statique d'un sable. *Comptes Rendus de l'Académie des Sciences (Mécanique)*, 332(11): 887-894, 2004.

[Bis59] Bishop A.W. The principle of effective stress. *Teknisk Ukeblad* 106(39):859-863, 1959.

[Bis62] Bishop A.W. and Donald I.B. The experimental study of party saturated soil in the triaxial apparatus. *Proc. 5th Conf. On Soil Mechanics and Found Eng.,* 1: 13-21, 1961.

[Bla08] Blatz J.A., Cui Y.J. and Oldecop L. Vapour equilibrium and osmotic technique for suction control. *Geotechnical and Geological Engineering* 26(6): 661-673, 2008.

[Bol56] Bolt G. H. Physico-chemical analysis of the compressibility of pure clays, *Géotechnique*, 6:86-93, 1956.

[Cam68] Campanella, R.G., Mitchell J.K., Influence of temperature variations on soil behaviour. *Journal of Soil Mechanics and Foundation Engineering, ASCE*, 94(SM3): 709-734, 1968.

[Cek04] Cekerevac C., Laloui L. Experimental study of thermal effects on the mechanical behaviour of a clay. *International Journal of Numerical and Analytical Methods in Geomechanics*, 28: 209-228, 2004.

[Cek05] Cekerevac C., Laloui L. and Vulliet L. A novel triaxial apparatus for thermo-mechanical testing of soils. *Geotechnical Testing Journal*, 28(2): 161-170, 2005.

[Cha02] Charlier R., Collin F., Schroeder C., Illing. P., Delage P., Cui Y.J. and De Gennaro V. Constitutive modeling of chalk – Application to waterflooding. *Proc. 2nd Biot Conference*, pages 359-366, Balkema, 2002.

[Col64] Coleman J.D. Stress-Strain relations for partially saturated soils, *Géotechnique*, 12(4): 348-350, 1962.

[Cor57] Corey E.C. Measurement of air and water permeability in unsaturated soil. *Proceedings of the Soil Science Society of America*, vol. 21:7-11, 1957.

[Cro52] Croney D. The movement and distribution of water in soil. *Géotechnique*, 3(1): 1-16, 1952.

[Cui96] Cui Y.J. and Delage P. Yielding and plastic behaviour of an unsaturated compacted silt. *Géotechnique,* 46(2): 291-311, 1996.

[Cui02] Cui Y.J, Loiseau C. and Delage P. Microstructure changes of a confined swelling soil due to suction controlled hydration. *Proceedings of the 3nd International Conference on Unsaturated Soils*, UNSAT'2002 Vol. 2: 593-598, Recife, Brazil, Balkema, 2002.

[Dan82] Daniel D.E. Measurement of hydraulic conductivity of unsaturated soils with thermocouple psychrometers. *Soil Science Society of America Journal*, 20(6): 1125-1129, 1982.

[Deg04] De Gennaro V., Delage P., Priol G., Collin F. Cui Y.J. On the collapse behaviour of oil reservoir chalk. *Géotechnique*, 54(6): 415-420, 2004.

[Del84] Delage P. and Lefebvre G. Study of the structure of a sensitive Champlain clay and its evolution during consolidation. *Canadian Geotechnical Journal*, 21(1):21-35, 1984.

[Del96] Delage P., Audiguier M., Cui Y.J. and Howat M.D. Microstructure of a compacted silt. *Canadian Geotechnical Journal*, 33 (1):150-158, 1996.

[Del98] Delage P., Howat M. and Cui Y.J. The relationship between suction and swelling properties in a heavily compacted unsaturated clay. *Engineering Geology*, 50(1-2): 31-48, 1998.

[Del00] Delage P., Sultan N. and Cui Y.J. On the thermal consolidation of Boom clay. *Canadian Geotechnical Journal*, 37(2): 343-354,2000.

[Del01a] Delage P. and Cui Y. J. L'eau dans les sols non saturés, *Techniques de l'Ingénieur*, article C 301, Eds Techniques de l'Ingénieur, Paris, 2001.

[Del01b] Delage P. and Cui Y. J. Le comportement des sols non saturés. *Techniques de l'Ingénieur*, art. C 302, Eds Techniques de l'Ingénieur, Paris, 2001.

[Del02] Delage P. Experimental unsaturated soil mechanics. *Proceedings of the 3nd International Conference on Unsaturated Soils*, UNSAT'2002, Recife, Brazil, Balkema, 2002.

[Del07] Delage P., Le T.T., Tang A.M., Cui Y.J. and Li X.L. Suction effects in deep Boom clay block samples. *Géotechnique*, 57(1): 239-244, 2007.

[Del08] Delage P. and Cui Y.J. An evaluation of the osmotic method of controlling suction. *Geomechanics and Geoengineering: An International Journal*, 3(1):1-11, 2008.

[Det93] Detournay, E. and Cheng, A. H. Fundamentals of Poroelasticity 1, II, pages 113–171, 1993.

[Esc73] Escario V. and Saez J. Measurement of the properties of swelling and collapsing soils under controlled suction. *Proceedings of the 3rd International Conference of Expansive Soils*, pages 195-200, 1973.

[Fle95] Fleureau J.M. and Taïbi S. Water-air permeabilities for unsaturated soils. *Proceedings of the 1st International Conference on Unsaturated Soils UNSAT'95*, Paris, vol. 2, pages 479 - 484, Balkema/Presses des ponts, 1995.

[Fre77] Fredlund D.G. & Morgenstern N.R. Stress state variables for unsaturated soils. *ASCE J. Geotech. Eng. Div. GT5*, 103:447-466, 1977.

[Gei00] Geiser F., Laloui L. and Vulliet L. On the volume measuerement in unsaturated triaxial test. *Proceedings of the Conference Unsaturated Soils for Asia*, pages 669-674, Balkema, Rotterdam, 2000.

[Gha09] Ghabezloo S. and Sulem J. Stress dependent thermal pressurization of a fluid-saturated rock. *Rock Mechanics and Rock Engineering*, 42(1):1-24, 2009.

[Hou87] Houston , S. L. and Lin, H. D., Thermal consolidation model of pelagic clays. *Marine Geotechnology*, 7:79-98, 1987.

[Hu13] Hu D.W., Zhang F. and Shao J.F. Experimental study of poromechanical behavior of saturated claystone under triaxial compression. *Acta Geotechnica,* 9:207–214, 2014.

[Hue90] Hueckel T. and Baldi G. Thermoplasticity of saturated clays: experimental constitutive study. *Journal of Geotechnical Engineering*, 116(12): 1778-1796, 1990.

[Jen62] Jennings J.E.B. and Burland J.B. Limitations to the use of effective stress in partly saturated soils. *Géotechnique*, 12(2):125-144, 1962.

[Lam58] Lambe T.W. The structure of compacted clay. *Journal of Soil Mechanics and Foundation Engineering*, ASCE 84 (SM2):1-34, 1958.

[Mar01] Marcial D., Delage P. and Cui Y.J. On the high stress compression of bentonites. *Canadian Geotechnical Journal,* 39:812-820, 2002.

[Mas08] Masrouri F., Bicalho K.V. and Kawai K. Laboratory hydraulic testing in unsaturated soils. *Geotechnical and Geological Engineering*, 26(6):691-704, 2008.

[Men14] Menaceur H. Comportement thermo-hydro-mécanique et microstructure de l'argilite du Callovo-Oxfordien. PhD Thesis, Ecole des Ponts ParisTech, Université Paris-Est, 2014.

[Mit05] Mitchell J.K. and Soga K. Fundamentals of soil behaviour. John Wiley and Sons, New-York, 2005.

[Moh11] Mohajerani M., Delage P., Monfared M., Sulem J., Tang A.M. and Gatmiri B. Oedometer compression and swelling behaviour of the Callovo-Oxfordian argillite. *International Journal of Rock Mechanics and Mining Sciences*, 48(4):606-615, 2011.

[Moh12] Mohajerani M., Delage P., Sulem J., Monfared M., Tang A.M. and Gatmiri B. A laboratory investigation of thermally induced pore pressures in the Callovo-Oxfordian Claystone. *International Journal of Rock Mechanics and Mining Sciences*, 52:112-121, 2012.

[Mon11a] Monfared M., Delage P., Sulem J., Mohajerani M., Tang A.M. and De Laure E. A new hollow cylinder triaxal cell to study the behaviour of low permeable materials. *International Journal of Rock Mechanics and Mining Sciences*, 48 (4), 637-649, 2011.

[Mon11b] Monfared M., Sulem J., Delage P., Mohajerani M. A laboratory investigation on the thermal properties of the Opalinus claystone. *Rock Mechanics and Rock Engineering,* 44:735-747, 2011.

[Muñ11] Muñoz-Castelblanco J., Delage P., Pereira J.M., and Cui Y.J. Some aspects of the compression and collapse behaviour of an unsaturated collapsible loess. *Géotechnique Letters*, 1:17-22, 2011.

[Paa67] Paaswell R.E. Temperature effects on clay soil consolidation. *Journal of Soil Mechanics and Foundation Engineering, ASCE*. 93(SM3):9-22, 1967.

[Pas03] Pasachalk 2, “Mechanical Behaviour of PArtially and Multiphase SAturated CHALKs Fluid-skeleton Interaction : Main Factor of Chalk Oil Reservoir Compaction and Related Subsidence - Part 2”. Final report, European Joule III contract no. ENK6-2000-00089.

[Pri04] Priol G., De Gennaro V., Delage P. and Cui Y.J. On the suction and the time dependent behaviour of reservoir chalks of North sea oilfields. *Proc. Second International Workshop on Unsaturated Soils*, Capri (Italy), pages 43-54, 2004.

[Sai00] Saiyouri N., Hicher P.Y. and Tessier D. Microstructural approach and transfer water modelling in highly compacted unsaturated swelling clays, *Mechanics of Cohesive and Frictional Materials*, 5:41-60, 2000.

[Sch02] Schroeder Ch. Du coccolithe au reservoir pétrolier –Approche phénoménologique du comportement mécanique de la craie en vue de sa modélisation à diverses échelles, PhD thesis, Université de Liège, 2002.

[Sri82] Sridharan A. and Jayadeva P. Double layer theory and compressibility of clays. *Géotechnique*, 32: 133-144, 198.

[Sul02] Sultan N., Delage P. and Cui Y.J. Temperature effects on the volume change behaviour of Boom clay. *Engineering Geology*, 64(2-3):135-145, 2002.

[Tes90] Tessier D. Organisation des matériaux argileux en relation avec leur comportement hydrique, in *Matériaux argileux, structure, propriétés et applications*, Decarreau ed., Société Française de Minéralogie et de Cristallographie, pages 387-445, 1990.

[Vac74] Vachaud G., Gaudet J.P. and Kuraz E. Air and water flow during ponded infiltration in a bounded column of soil, *Journal of hydrology*, 22: 89-108, 1974.

[Van08] Vanapalli S.K., Nicotera M.V. and Sharma R. Axis translation and negative water column techniques for suction control. *Geotechnical and Geological Engineering*, 26(6):645-660, 2008.

[Wan14] Wan M., Delage P., Tang A.M., Talandier J. The water retention properties of the Callovo-Oxfordian Claystone. *International Journal of Rock Mechanics and Mining Sciences,* 64:96-104, 2013.

[Whe95] Wheeler S.J. & Sivakumar V. An elasto-plastic critical state framework for unsaturated soil. *Géotechnique*, 45: 35-54, 1995.

[Yah01] Yahia-Aissa M., Delage P. and Cui Y.J. Suction-water relationship in swelling clays. Clay science for engineering, IS-Shizuoka International Symposium on Suction, Swelling, Permeability and Structure of Clays, 65-68, Adachi & Fukue eds, Balkema, 2001.

[Yos63] Yoshimi Y. and Osterberg J.O. Compression of partially saturated cohesive soils. *ASCE Journal of the Soil Mechanics and Foundations Division*, 89(4): 1-24, 1963.

General theory of mixtures. Physical chemistry of mixtures and swelling

J.M. Huyghe

Bernal Institute, University of Limerick, Ireland

We present a description of the mechanical behaviour of mixtures, substances consisting of several components. A component is defined in this context as a set of material constituents that moves jointly in the mixture. In this chapter we will derive a general form of the theory of mixtures. The description has mainly be taken from a publication of Bowen [Bow76]. Then we will discuss mixtures of a liquid with a dissolved substance, also called solutions. As an introduction we will first consider mixtures of ideal gasses. Then we will consider solutions in which the solved particles are electrically neutral: the non-electrolytic solutions. Finally we consider the electrolytic solutions, in which the solved matter falls apart in charged ions and we have to take electroneutrality into account. Particularly concepts like electrochemical potential and (Donnan) osmosis will be discussed. Traditionally this is the field of the physical chemistry. We will follow the procedures that are usual in that field. The relations that are found here however, can also be derived from the general theory of mixtures. The subject matter in this chapter has largely been taken from textbooks about physical chemistry applied to biological systems [Cha81, KC65, Ric80].

1 Quantities of mixtures

Let's consider a general mixture of ν components. Microscopically, only one component is present at a certain moment at a certain place in space. Furthermore, the composition of the mixture will differ in general from one spot to the other. In the theory of mixtures we try not to describe the behaviour of every separate particle. We use a continuum approach instead, in which we spread the properties of the components over a representative volume unit (RVU) ΔV. This volume has to be big enough to provide a good continuum representation of the quantities on microscopic level, but also small enough to avoid averaging of macroscopic variations. If the RVU is displaced through every possible position in the mixture and the average quantities are ascribed to the position of the centre of the RVU, we can determine the average quantities as a function of the position in the mixture (figure 1). A consequence of the averaging concept is that every component, that is present in the mixture, occupies every position x in that mixture. We express the amount of component α in terms of mass m^α or moles n^α.

In the theory of mixtures we usually take the *apparent density* ρ of the components, concerned with the RVU, V, and the present amount of mass, m^α, in it:

$$\rho^\alpha = \frac{m^\alpha}{V}, \qquad \alpha = 1, \ldots, \nu \tag{1}$$

If component α is immiscible with other components, the volume of component α is indicated with V^α. The real *intrinsic density* ρ_i^α of the components of immiscible components is then:

$$\rho_i^\alpha = \frac{m^\alpha}{V^\alpha}, \qquad \alpha = 1, \ldots, \nu \tag{2}$$

We define the *volume fraction* ϕ^α of an immiscible component as:

$$\phi^\alpha = \frac{V^\alpha}{V}, \qquad \alpha = 1, \ldots, \nu \tag{3}$$

in which V^α is the volume occupied by component α within volume V. It will be obvious that:

$$\sum_{\alpha=1}^{\nu} \phi^\alpha = 1 \tag{4}$$

and

$$\rho^\alpha = \phi^\alpha \rho_i^\alpha, \qquad \alpha = 1, \ldots, \nu \tag{5}$$

We define the density ρ of the whole mixture as:

$$\rho = \sum_{\alpha=1}^{\nu} \rho^\alpha \tag{6}$$

2 Kinematics and stress

2.1 Kinematics

We consider the mixture of ν components again. The collection of material points $\underset{\sim}{\xi}$ of a component α ($\alpha = 1, \ldots, \nu$) is indicated with $\mathcal{B}^\alpha$. These points occupy an area $\mathcal{G}^\alpha$ in the three-dimensional space at time t:

$$\mathcal{G}^\alpha(t) = \{x^\alpha = \chi^\alpha(\underset{\sim}{\xi}^\alpha, t) \,|\, \forall \underset{\sim}{\xi}^\alpha \in \mathcal{B}^\alpha\}. \tag{7}$$

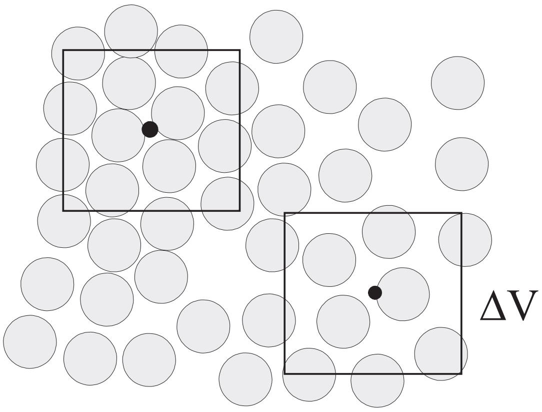

Figure 1: Illustration of the averaging procedure for a mixture of a solid and a fluid.

The areas $\mathcal{G}^\alpha$ $(\alpha = 1,\ldots,\nu)$ coincide according to the theory of mixtures and every position x is occupied by particles of every single component at the same time. Therefore, the following holds:

$$x(t) = x^1(t) = x^2(t) = \cdots = x^\alpha(t) = \cdots = x^\nu(t) \tag{8}$$

We can now define a *deformation tensor* F^α per component:

$$F^\alpha = (\nabla_0^\alpha x^\alpha)^c. \tag{9}$$

In this equation the symbol ∇_0^α represents the gradient operator concerning the state of reference of component α. We define the *Green-Lagrange strain tensor* E^α with respect to component α as:

$$E^\alpha = \frac{1}{2}\left\{(F^\alpha)^c \cdot F^\alpha - I\right\}. \tag{10}$$

The velocity v^α of a material point from component α is defined as:

$$v^\alpha = \left.\frac{\partial \chi^\alpha(\underset{\sim}{\xi}^\alpha, t)}{\partial t}\right|_{\underset{\sim}{\xi}^\alpha}. \tag{11}$$

We define the velocity of the whole mixture v as the mass weighed average of the velocities of the components[1]:

$$v(x,t) = \frac{1}{\rho}\sum_{\alpha=1}^{\nu} \rho^{\alpha} v^{\alpha}(x,t) \tag{12}$$

We can point several velocities in every point of the continuum. Therefore several material time derivatives are defined. Let's consider a quantity a^{α}, a quantity a connected to the component α. We now define two material time derivatives of a^{α}:

$$\dot{a}^{\alpha} = \frac{Da^{\alpha}}{Dt} = \frac{\partial a^{\alpha}}{\partial t} + v \cdot \nabla a^{\alpha} \tag{13}$$

$$\grave{a}^{\alpha} = \frac{D^{\alpha}a^{\alpha}}{Dt} = \frac{\partial a^{\alpha}}{\partial t} + v^{\alpha} \cdot \nabla a^{\alpha} \tag{14}$$

Using time derivative $\dot{a}^{\alpha}$ we move with the average velocity of the mixture, while we move with the component α if we use $\grave{a}^{\alpha}$.

We define the *deformation velocity tensor* D^{α} and the *rotational velocity tensor* Ω^{α} as:

$$D^{\alpha} = \frac{1}{2}\left\{\grave{F}^{\alpha} \cdot (F^{\alpha})^{-1} + (\grave{F}^{\alpha} \cdot (F^{\alpha})^{-1})^{c}\right\} \tag{15}$$

$$\Omega^{\alpha} = \frac{1}{2}\left\{\grave{F}^{\alpha} \cdot (F^{\alpha})^{-1} - (\grave{F}^{\alpha} \cdot (F^{\alpha})^{-1})^{c}\right\} \tag{16}$$

In these definitions we take the material time derivative of the deformation tensor F^{α} while we move with component α.

Finally we define the velocity u^{α} of component α with respect to the velocity of the mixture as:

$$u^{\alpha} = v^{\alpha} - v. \tag{17}$$

---

[1] Already at this point, there is a major distinction between definitions in mixture theory and definition handled in classical small deformation poromechanics. Classical books on strength of materials [GT09], elasticity and poromechanics define quantities such as velocity, pressure, stress or strain as a function of x and t, just like in mixture theory. However, the quantity x has a different meaning. In infinitesimal solid mechanics theory, the x is the position vector in the initial state, not the current state. In fluid mechanics and mixture theory, x refers to the current state. That is why in infinitesimal solid mechanics [GT09, Bio41, Bio56] write for velocity $\frac{\partial u}{\partial t}$ while a fluid mechanics or mixture mechanics textbook never does so. Because, by definition, the partial time derivative $\frac{\partial}{\partial t}$ assumes the variable other than time to be constant, and that the other variable in infintesimal theory is the initial position vector, the partial time derivative in infinitesimal solid mechanics is a material time derivative as in eq. (11). As in our case, the meaning of x in eq. (12) is the current position, a partial time time derivative does not represent a material time derivative but rather a spatial time derivative. To keep the notation consistent throughout the book, we handle the same (fluid mechanics) notation throughout the book, even when infinitesimal deformation is assumed

2.2 Stress

Let's consider a small surface with normal unit vector n_0 and surface area A_0 in this mixture. We can subdivide a force f, that works on this surface, in several contributions f^α, working on each of the components α in the mixture. As a result of the force f the surface deforms, during which it gets a normal unit vector n and a surface area A. We now define the *partial stress vector* t^α as the force working on component α, divided by the *total* surface area:

$$t^\alpha = \frac{f^\alpha}{A} \tag{18}$$

For the choice of size of the averaging surface A the same considerations apply as for the averaging volume V. We now define the *partial Cauchy stress tensor* σ^α:

$$t^\alpha = \sigma^\alpha \cdot n. \tag{19}$$

The tensor σ^α projects the normal unit vector n of a surface to the *partial stress vector* t^α, that represents the force that is applied per unit of surface area of the mixture of component α.

3 Balance of mass, momentum and moment of momentum

3.1 Balance of mass

We consider an arbitrary volume V in space with surface area A. The balance of mass for component α reads in integral form:

$$\frac{\partial}{\partial t}\int_V \rho^\alpha \, dV = -\int_A \rho^\alpha v^\alpha \cdot n \, dA + \int_V \hat{c}^\alpha \, dV. \tag{20}$$

An extra source term is added that accounts for the variation in mass of component α with respect to interactions with other components. The quantity $\hat{c}^\alpha$ is defined as the rate of mass transfer from component α to other components changes per unit volume of mixture. We can think of phase-changes (mass-exchange between liquid and vapour), variation of ionisation (mass-exchange between the ion-component and the solid phase), or chemical reactions. Applying Gauss' theorem yields the *local form of the balance of mass per component* α:

$$\frac{\partial \rho^\alpha}{\partial t} + \nabla \cdot (\rho^\alpha v^\alpha) = \hat{c}^\alpha. \tag{21}$$

The exchange of mass between the mutual components may not influence the total mass:

$$\sum_{\alpha=1}^{\nu} \int\limits_V \hat{c}^\alpha \, dV = 0. \tag{22}$$

At a local level this results in the *local balance of mass for the whole mixture*:

$$\sum_{\alpha=1}^{\nu} \hat{c}^\alpha = 0. \tag{23}$$

3.2 Balance of momentum

We consider the arbitrary, but fixed part of space with volume V and surface area A again. In integral form the balance of momentum for component α is given by:

$$\begin{aligned} \frac{\partial}{\partial t} \int\limits_V \rho^\alpha v^\alpha \, dV &= -\int\limits_A (\rho^\alpha v^\alpha) v^\alpha \cdot n \, dA \\ &\quad + \int\limits_V \rho^\alpha q^\alpha \, dV + \int\limits_A t^\alpha \, dA + \int\limits_V (\hat{p}^\alpha + \hat{c}^\alpha v^\alpha) \, dV. \end{aligned} \tag{24}$$

The integral form for one-phase materials is completed with an interaction-term. The volume force that works upon α is indicated with q^α. The term in t^α represents the force per unit surface area mixture on component α. Based on (18) a contribution of the surface forces has to be calculated by integrating the partial stress vectors t^α over the surface of the mixture A. In the interaction term the volume force $\hat{p}^\alpha$ represents the momentum transfered from other components to component α , counted per unit volume mixture and per unit of time. Transition of momentum occurs for example in friction forces, that are a result of relative movement of the components. The term $\hat{c}^\alpha v^\alpha$ represents momentum transfer associated with the exchange of mass $\hat{c}^\alpha$. It is assumed that the added mass of component α gets the same velocity as the already present mass of component α. Using Gauss' theorem we find the *local form of the balance of momentum per component* α again:

$$\rho^\alpha \left\{ \frac{\partial v^\alpha}{\partial t} + v^\alpha \cdot \nabla v^\alpha \right\} = \rho^\alpha \grave{v}^\alpha = \nabla \cdot (\sigma^\alpha)^c + \rho^\alpha q^\alpha + \hat{p}^\alpha, \tag{25}$$

in which σ^α represents the partial Cauchy stress tensor. The term $\hat{c}^\alpha v^\alpha$ doesn't show up again in this equation, because we used the balance of mass (21). For the total mixture applies that the net conversion of momentum with respect to the interaction terms has to be zero, so the *local balance of momentum for the total mixture* holds:

$$\sum_{\alpha=1}^{\nu} (\hat{c}^\alpha v^\alpha + \hat{p}^\alpha) = \mathbf{0}. \tag{26}$$

3.3 Balance of moment of momentum

The integral form of the balance of moment of momentum for component α is:

$$\begin{aligned}
\frac{\partial}{\partial t}\int_V x^\alpha \times \rho^\alpha v^\alpha \, dV &= -\int_A (x^\alpha \times \rho^\alpha v^\alpha) v^\alpha \cdot n \, dA \\
&+ \int_V x^\alpha \times \rho^\alpha q^\alpha \, dV + \int_A x^\alpha \times t^\alpha \, dA \\
&+ \int_V (x^\alpha \times (\hat{c}^\alpha v^\alpha + \hat{p}^\alpha) + \hat{m}^\alpha) \, dV
\end{aligned} \tag{27}$$

The last term accounts for the transfer of the moment of momentum from other components to component α. The term $x^\alpha \times (\hat{c}^\alpha v^\alpha + \hat{p}^\alpha)$ is the moment of momentum transfer associated with the momentum interaction $(\hat{c}^\alpha v^\alpha + \hat{p}^\alpha)$.The term $\hat{m}^\alpha$ represents the direct moment of momentum transfer to component α by the other components, counted per unit of volume mixture and per unit of time. An example of such direct moment of momentum interaction is the case of friction forces transfered from fluid to solid in flow through helical pore structure with preferential helicity. The local form of the balance of moment of momentum is:

$$\hat{M}^\alpha = (\sigma^\alpha)^c - \sigma^\alpha \tag{28}$$

in which $\hat{M}^\alpha$ is the anti-symmetric tensor corresponding to the axial vector $\hat{m}^\alpha$, defined such that for all vectors a applies:

$$\hat{m}^\alpha \times a = \hat{M}^\alpha \cdot a \tag{29}$$

The reader is referred to specialized literature for the proof of eq.(28). At this moment we consider $\hat{M}^\alpha$ as a quantity, analogous to the terms $\hat{c}^\alpha$ and $\hat{p}^\alpha$.

4 Thermodynamics

4.1 The first law

We formulate the first law of thermodynamics for a component α in the mixture as the first law for a one component continuum, completed with an interaction term :

$$
\begin{aligned}
\frac{\partial}{\partial t}\int_V \rho^\alpha\left(\tilde{U}^\alpha+\tfrac{1}{2}v^\alpha\cdot v^\alpha\right)\,dVdV = \\
-\int_A \rho^\alpha\left(\tilde{U}^\alpha+\tfrac{1}{2}v^\alpha\cdot v^\alpha\right)v^\alpha\cdot n\,dA+\int_V \rho^\alpha q^\alpha\cdot v^\alpha\,dV \\
+\int_A t^\alpha\cdot v^\alpha\,dA+\int_V \rho^\alpha\tilde{r}^\alpha\,dV-\int_A h^\alpha\cdot n\,dA+\int_V \hat{e}^\alpha\,dV \\
+\int_V\left(v^\alpha\cdot\hat{p}^\alpha+\frac{1}{2}\Omega^\alpha:\hat{M}^\alpha+\hat{c}^\alpha(\tilde{U}^\alpha+\tfrac{1}{2}v^\alpha\cdot v^\alpha)\right)\,dV,
\end{aligned}
\tag{30}
$$

in which $\tilde{U}^\alpha$ represents the specific internal energy of component α, h^α represents the heat flux density vector for component α and $\tilde{r}^\alpha$ represents the specific heat supply to component α by heat sources. In the second of these term the symbol $\hat{e}^\alpha$ represents the direct energy transfer from the other components to component α, calculated per unit volume mixture and per unit of time. The last term represents the energy supply caused by interaction effects with respect to the exchange of mass $\hat{c}^\alpha$, the exchange of momentum $\hat{p}^\alpha$ and the exchange of moment of momentum $\hat{M}^\alpha$. Using Gauss' theorem and the balance of mass, momentum and moment of momentum the *local form of the balance of energy per component* α is derived:

$$
\rho\grave{\tilde{U}}^\alpha=\rho^\alpha\tilde{r}^\alpha-\nabla\cdot h^\alpha+\sigma^\alpha:D^\alpha+\hat{e}^\alpha. \tag{31}
$$

Equation (31) shows that only the term $\hat{e}^\alpha$ is added in the mixture. In analogy to the other balance laws, we demand that the balance of energy for the components is consistent with the *balance of energy for the total mixture*:

$$
\sum_{\alpha=1}^{\nu}\left(\hat{e}^\alpha+u^\alpha\cdot\hat{p}^\alpha+\hat{c}^\alpha(\tilde{U}^\alpha+\tfrac{1}{2}u^\alpha\cdot u^\alpha)\right)=0. \tag{32}
$$

Notice that the velocities u^α, defined in (17), are found in this equation, i.e. the component velocities with respect to the mixture velocity.

4.2 The second law

The second law of thermodynamics describes thermodynamic properties of a system. For a mixture it isn't clear how the system has to be defined: is the system formed by the total mixture or forms every component a system on its own? In the last case the entropy production per component has to be greater or equal to zero. In the first case this demand applies for the total mixture, and there can be components for which the entropy production is less than zero. We formulate the second law for the whole mixture as this is the only restriction which is agreed upon by the whole scientific community. We postulate the *local form of the second law for the whole mixture*:

$$\sum_{\alpha=1}^{\nu}\left\{\rho^{\alpha}\grave{\tilde{S}}^{\alpha}-\frac{\rho^{\alpha}\tilde{r}^{\alpha}}{T^{\alpha}}+\nabla\cdot\left(\frac{h^{\alpha}}{T^{\alpha}}\right)+\hat{c}^{\alpha}\tilde{S}^{\alpha}\right\}\geq 0. \tag{33}$$

in which $\tilde{S}^{\alpha}$ is the specific entropy of component α, and T^{α} is the temperature of component α. The term $\sum\hat{c}^{\alpha}\tilde{S}^{\alpha}$ discounts the interaction between the components again. If we eliminate the term $\rho^{\alpha}\tilde{r}^{\alpha}$ using the balance of energy per component (31) and eliminate the term $\sum\hat{e}^{\alpha}$ using the balance of energy for the total mixture (32), it follows that:

$$\begin{aligned}\sum_{\alpha=1}^{\nu}\Bigg\{\rho^{\alpha}\grave{\tilde{S}}^{\alpha}&-\frac{\rho^{\alpha}\grave{\tilde{U}}^{\alpha}}{T^{\alpha}}+\frac{\sigma^{\alpha}:D^{\alpha}}{T^{\alpha}}-\frac{\hat{p}^{\alpha}\cdot u^{\alpha}}{T^{\alpha}}+h^{\alpha}\cdot\nabla\left(\frac{1}{T^{\alpha}}\right)\\&-\frac{\hat{c}^{\alpha}}{T^{\alpha}}(\tilde{U}^{\alpha}+\tfrac{1}{2}u^{\alpha}\cdot u^{\alpha}+T^{\alpha}\tilde{S}^{\alpha})\Bigg\}\geq 0.\end{aligned} \tag{34}$$

If we finally define the Helmholtz free energy per unit mass for component α as,

$$\tilde{F}^{\alpha}=\tilde{U}^{\alpha}-T^{\alpha}\tilde{S}^{\alpha}, \tag{35}$$

we can divert (34) into:

$$\begin{aligned}\sum_{\alpha=1}^{\nu}\frac{1}{T^{\alpha}}\Big\{&-\rho^{\alpha}(\grave{\tilde{F}}^{\alpha}-\tilde{S}^{\alpha}\grave{T}^{\alpha})+\sigma^{\alpha}:D^{\alpha}+\hat{p}^{\alpha}\cdot u^{\alpha}\\&-T^{\alpha}h^{\alpha}\cdot\nabla\left(\frac{1}{T^{\alpha}}\right)-\hat{c}^{\alpha}(\tilde{F}^{\alpha}+\tfrac{1}{2}u^{\alpha}\cdot u^{\alpha})\Big\}\geq 0.\end{aligned} \tag{36}$$

5 Thermodynamic potentials

5.1 Partial quantities

The total mass of a mixture is equal to the sum of the masses of the components of which the mixture consists. The total volume V of a mixture is generally not equal to the sum of the component volume:

$$V\neq\sum_{\alpha=1}^{\nu}V^{\alpha}. \tag{37}$$

This is caused, because the interaction between molecules of the same constituent is generally different from that between molecules of different constituents. To account

Table 1: Balance laws for mixtures.

quantities	balance law for component (c) and mixture (m)	
mass	c	$\grave{\rho}^{\alpha} + \rho^{\alpha} \nabla \cdot v^{\alpha} = \hat{c}^{\alpha}$
	m	$\sum \hat{c}^{\alpha} = 0$
momentum	c	$\rho^{\alpha} \grave{v}^{\alpha} = \nabla \cdot (\sigma^{\alpha})^{c} + \rho^{\alpha} q^{\alpha} + \hat{p}^{\alpha}$
	m	$\sum(\hat{c}^{\alpha} v^{\alpha} + \hat{p}^{\alpha}) = \mathbf{0}$
moment of momentum	c	$\sigma^{\alpha} - (\sigma^{\alpha})^{c} = \hat{M}^{\alpha}$
energy	c	$\rho \grave{\tilde{U}}^{\alpha} = \rho^{\alpha} \tilde{r}^{\alpha} - \nabla \cdot h^{\alpha} + \sigma^{\alpha} : D^{\alpha} + \hat{e}^{\alpha}$
	m	$\sum \left\{ \hat{e}^{\alpha} + u^{\alpha} \cdot \hat{p}^{\alpha} + \hat{c}^{\alpha} (\tilde{U}^{\alpha} + \frac{1}{2} u^{\alpha} \cdot u^{\alpha}) \right\} = 0$
entropy	m	$\sum \left\{ \rho^{\alpha} \grave{\tilde{S}}^{\alpha} - \frac{\rho^{\alpha} \tilde{r}^{\alpha}}{T^{\alpha}} + \nabla \cdot \left(\frac{h^{\alpha}}{T^{\alpha}} \right) + \hat{c}^{\alpha} \tilde{S}^{\alpha} \right\} \geq 0.$

the independence of mixture composition *partial quantities* are used. We define the *partial* molar volume $\bar{V}^{\alpha}$ of component α as:

$$\bar{V}^{\alpha} = \left(\frac{\partial V}{\partial n^{\alpha}} \right)_{p,T,n^{\beta},\beta \neq \alpha}, \qquad \alpha = 1, \ldots, \nu \tag{38}$$

So, $\bar{V}^{\alpha}$ represents the increase of the volume of a mixture as a result of adding a little amount of component α, figured per mol of the added component. Furthermore, the thermodynamic state of the mixture, here characterized by p and T, has to stay constant, as well as the composition of the mixture. If $\bar{V}^{\alpha}$ is independent of the composition of the mixture, then integration of (38), yields:

$$V = \sum_{\alpha=1}^{\nu} n^{\alpha} \bar{V}^{\alpha}. \tag{39}$$

Generally the partial volume of a component in a mixture is not equal to the molar volume of the pure component. If this is the case, we say the mixture is ideal.

5.2 Ideal media

Also for mixtures we can define potentials [KC65]. We will restrict ourselves to an ideal mixture of ν components, in which an amount n^{α} moles of every component α

is present. In the former chapter it turned out that for an ideal medium the Gibbs free energy G is a function of the pressure p and the temperature T. In the mixture, G isalso a function of the mixture composition:

$$G = G(T, p, n^1, \ldots, n^\nu) \tag{40}$$

For variations dG the following differential applies:

$$\begin{aligned} dG &= \left(\frac{\partial G}{\partial T}\right)_{p,n^\alpha} dT + \left(\frac{\partial G}{\partial p}\right)_{T,n^\alpha} dp \\ &+ \sum_{\alpha=1}^{\nu} \left(\frac{\partial G}{\partial n^\alpha}\right)_{p,T,n^\beta,\beta\neq\alpha} dn^\alpha \end{aligned} \tag{41}$$

We now define the *partial molar Gibbs free energy* $\bar{G}^\alpha$ of a component α in a mixture as:

$$\bar{G}^\alpha = \left(\frac{\partial G}{\partial n^\alpha}\right)_{p,T,n^\beta,\beta\neq\alpha} \tag{42}$$

We can consider $\bar{G}^\alpha$ as an increase in free energy of the mixture if we add one mole of component α to that mixture. The partial molar Gibbs free energy is usually called the *chemical potential* μ^α:

$$\mu^\alpha = \bar{G}^\alpha = \left(\frac{\partial G}{\partial n^\alpha}\right)_{p,T,n^\beta,\beta\neq\alpha} \tag{43}$$

Now (41) can be diverted into:

$$dG = \left(\frac{\partial G}{\partial T}\right)_{p,n^\alpha} dT + \left(\frac{\partial G}{\partial p}\right)_{T,n^\alpha} dp + \sum_{\alpha=1}^{\nu} \mu^\alpha dn^\alpha \tag{44}$$

The part of the chemical potential in thermodynamics is comparable with that of the potential energy in mechanics. To illustrate this statement, let's consider a process – for a constant temperature and pressure – in which an amount dn^α of component α is converted from state A to state B. The variation dG in Gibbs free energy then reads:

$$dG = (\mu_B^\alpha - \mu_A^\alpha) dn^\alpha. \tag{45}$$

According to (45) the convertion from A to B will initiate spontaneously if dG is negative, i.e. if $\mu_A^\alpha > \mu_B^\alpha$. If $\mu_A^\alpha < \mu_B^\alpha$, the process will go in the opposite direction. In equilibrium $dG = 0$ applies, such that $\mu_A^\alpha = \mu_B^\alpha$. The chemical potential therefore indicates in what direction the process will go. We will see in section 7 that we can describe processes like osmosis well using the chemical potential.

5.3 Non-ideal media

For mixtures of ideal media we could characterize the state of stress per component with the total pressure of the mixture p and the mixture composition $n^1, \ldots, n^\nu$ (40), because these quantities fix the partial pressures p^α totally. For mixtures of non-ideal media the state of stress has to be described with a whole stress tensor σ^α, that cannot be derived unambiguously from the total mixture stress σ and the mixture composition. Therefore we have to make G explicitly dependent on all component stresses. We characterize the state of stress per component with the second Piola-Kirchhoff stress tensor S^α.

For mixtures of ideal media, like gasses, it is in addition usual to express the amount of a component in moles, indicated with n^α. For non-ideal media it is sometimes more convenient to convert to masses m^α. The Gibbs free energy G for mixtures of non-ideal media can therefore be written as:

$$G = G(T, S^1, \ldots, S^\nu, m^1, \ldots, m^\nu) \tag{46}$$

For the variation of the Gibbs free energy after adding a small amount of component α, counted per unit mass, now applies:

$$\tilde{\mu}^\alpha = \left(\frac{\partial G}{\partial m^\alpha}\right)_{T, P^1, \ldots, P^\nu, m^\beta, \beta \neq \alpha} \tag{47}$$

We call $\tilde{\mu}^\alpha$ the *specific chemical potential* of component α.

6 Mixtures of ideal gasses

We first consider a pure ideal gas. For a constant temperature the differential of the Gibbs free energy of the gas is :

$$dG = V dp \tag{48}$$

in which V is the volume of the gas and p its pressure.

If we now increase the pressure of the gas from p_0 to p, the variation of the Gibbs free energy ΔG is written:

$$\Delta G = G - G_0 = \int_{G_0}^{G} dG = \int_{p_0}^{p} V dp \tag{49}$$

For an ideal gas applies:

$$pV = nRT \tag{50}$$

in which R represents the universal gas constant ($8.314\ J \cdot K^{-1} \cdot \mathrm{mol}^{-1}$) and n is the amount of gas in moles. Substitution of (50) into (49) yields after integration:

$$G - G_0 = nRT \ln \frac{p}{p_0} \tag{51}$$

This equation shows the Gibbs free energy of a gas with respect to the state of reference (p_0, G_0). For the chemical potential of the gas it follows that:

$$\bar{\mu} = \bar{\mu}_0 + RT \ln \frac{p}{p_0} \tag{52}$$

Let's consider a *mixture of ideal gasses*. We take an amount n^I of gas I and an amount n^{II} of a gas II. Both gasses are subjected to a reference pressure p_0, and have the volumes V^I and V^{II}. During mixing of these gasses an ideal mixture with volume V and pressure p is created, for which:

$$V = V^I + V^{II} \tag{53}$$

$$p = p_0 \tag{54}$$

The *partial pressures* p^I and p^{II} of the gasses in the mixture measure:

$$p^I = x^I p_0 \qquad p^{II} = x^{II} p_0, \tag{55}$$

in which the molar fractions x of the components are defined as:

$$x^I = \frac{n^I}{n^I + n^{II}}, \qquad x^{II} = \frac{n^{II}}{n^I + n^{II}} \tag{56}$$

Substitution of the pressures from (55) into (52) now yields for the chemical potential of the gasses:

$$\bar{\mu}^I = \bar{\mu}_0^I + RT \ln x^I, \qquad \bar{\mu}^{II} = \bar{\mu}_0^{II} + RT \ln x^{II} \tag{57}$$

We know that the mixing process as described above occurs spontaneously. We can also see this by calculating the *mixing-energy*. The total Gibbs free energy before mixing amounts:

$$G_{before} = n^I \bar{\mu}_0^I + n^{II} \bar{\mu}_0^{II} \tag{58}$$

For the total Gibbs free energy after mixing applies:

$$G_{after} = n^I \{\bar{\mu}_0^I + RT \ln x^I\} + n^{II} \{\bar{\mu}_0^{II} + RT \ln x^{II}\} \tag{59}$$

We can now derive for the mixture energy ΔG_{mix}:

$$\begin{aligned} \Delta G_{mix} &= G_{after} - G_{before} \\ &= (n^I + n^{II}) RT \{x^I ln x^I + x^{II} ln x^{II}\} \end{aligned} \tag{60}$$

Because x^I as well as x^{II} are smaller than 1, $\Delta G_{mix} < 0$, which means that the mixing process occurs indeed spontaneously.

7 Non-electrolytic solutions

From the former we saw that for mixtures of ideal gasses the chemical potential depends on the composition of the mixture following (57). In general the chemical

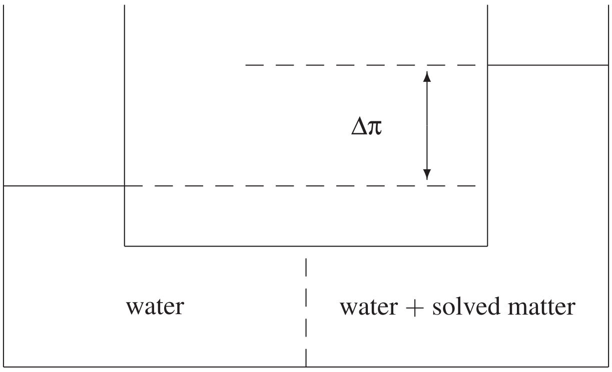

Figure 2: Illustration of the phenomenon osmotic pressure.

potential for mixtures of ideal media depends on the pressure p and the temperature T. We now define an *ideal mixture* as a mixture in which the following relation applies for the chemical potential of the components α:

$$\bar{\mu}^{\alpha}(p,T,x^{\alpha}) = \bar{\mu}_0^{\alpha}(p,T) + RT\ln x^{\alpha} \tag{61}$$

We therefore assume that $\bar{\mu}^{\alpha}$ depends the same way on the composition of the mixture as a mixture of ideal gasses does. For a mixture of ideal gasses we found the concentration dependency through the partial pressures of the gasses. In definition (61) we take the pressure dependency separately into account in the term $\bar{\mu}_0^{\alpha}(p,T)$. If the mixture has an equilibrium, we know that for every component:

$$\nabla\bar{\mu}^{\alpha} = \mathbf{0}. \tag{62}$$

If all components move freely through the mixture, this means, using (61), that there are no gradients in concentration. If this free movement is hampered, a concentration gradient generally will be present in the equilibrium.

This last situation is demonstrated in the experiment, shown in figure 2. In the right compartment there is a solution of n^e moles of a substance e, for example a protein, in n^w moles of a solvent w, for example water. In the solution the protein consists of neutral particles. In the left compartment only the solvent is present, water. The compartments are separated by a semi-permeable membrane, that only allows transport of water. Therefore equation 62 applies across the membrane for water, but not for the protein.

Initially there is no hydrostatic pressure difference between both compartments. For the chemical potential of the water applies:

$$\bar{\mu}_l^w = \bar{\mu}_0^w + RT\ln x_l^w = \bar{\mu}_0^w \qquad (\text{because } x_l^w = 1) \tag{63}$$

$$\bar{\mu}_r^w = \bar{\mu}_0^w + RT\ln x_r^w < \bar{\mu}_0^w \qquad (\text{because } x_r^w < 1) \tag{64}$$

in which we indicate the chemical potential of the water with $\bar{\mu}^w$, in the left (index 1) and the right (index r) compartment and in pure (index 0) state. The chemical potential of the water therefore appears to be lower on the right hand side than that on the left hand side. This difference causes a net transport of water from the left to the right, which results in a hydrostatic pressure difference. The net transport reaches an equilibrium, as soon as the chemical potentials on the left and on the right are equal. In this equilibrium the hydrostatic pressure difference is equal to $\Delta\pi$, the *osmotic pressure difference*. We calculate the size of the osmotic pressure difference. The total differential of the Gibbs free energy G is:

$$dG = \left(\frac{\partial G}{\partial T}\right)_{p,n^\alpha} dT + \left(\frac{\partial G}{\partial p}\right)_{T,n^\alpha} dp + \sum_{\alpha=1}^{\nu} \bar{\mu}^\alpha dn^\alpha, \tag{65}$$

in which the chemical potential $\bar{\mu}^\alpha$ is defined as:

$$\bar{\mu}^\alpha = \bar{G}^\alpha = \left(\frac{\partial G}{\partial n^\alpha}\right)_{p,T,n^\beta,\beta\neq\alpha}. \tag{66}$$

We now state for the volume V and the entropy S of the mixture:

$$V = \left(\frac{\partial G}{\partial p}\right)_{T,n^\alpha} \tag{67}$$

$$S = -\left(\frac{\partial G}{\partial T}\right)_{p,n^\alpha} \tag{68}$$

The partial derivative of the chemical potential with respect to the pressure is:

$$\begin{aligned} \left(\frac{\partial \bar{\mu}^\alpha}{\partial p}\right)_{T,n^\alpha} &= \left(\frac{\partial}{\partial p}\left(\frac{\partial G}{\partial n^\alpha}\right)_{p,T,n^\beta,\beta\neq\alpha}\right)_{T,n^\alpha} \\ &= \left(\frac{\partial}{\partial n^\alpha}\left(\frac{\partial G}{\partial p}\right)_{T,n^\alpha}\right)_{p,T,n^\beta,\beta\neq\alpha}, \end{aligned} \tag{69}$$

which can be rewritten, using (67), into:

$$\left(\frac{\partial \bar{\mu}^\alpha}{\partial p}\right)_{T,n^\alpha} = \left(\frac{\partial V}{\partial n^\alpha}\right)_{T,p,n^\beta,\beta\neq\alpha} = \bar{V}^\alpha \tag{70}$$

in which $\bar{V}^\alpha$ is the partial molar volume of the component α in the mixture. Applied to the water-component in the situation of figure 2, we find:

$$\left(\frac{\partial \bar{\mu}^w}{\partial p}\right)_{T,n^w,n^e} = \bar{V}^w = \bar{V}_0^w \tag{71}$$

The last '='-sign can be justified for a *dilute solution*, in which the partial molar volume of the water is equal to that of pure water. We determine the difference in chemical potential of the water in both compartments, as a result of the pressure difference

$p_r - p_l$, through integration of (71), considering that the partial molar volume of the water is independent of the pressure:

$$\bar{\mu}_r^w - \bar{\mu}_l^w = \int_{p_l}^{p_r} \bar{V}_0^w dp = \bar{V}_0^w (p_r - p_l) \tag{72}$$

In equilibrium the chemical potential of the water left and right is the same:

$$\bar{\mu}_l^w = \bar{\mu}_r^w = \bar{\mu}_0^w + RT \ln x_r^w + \bar{V}_0^w (p_r - p_l) \tag{73}$$

Because $\bar{\mu}_l^w = \bar{\mu}_0^w$, the osmotic pressure difference $\Delta\pi$ is:

$$\Delta\pi = p_r - p_l = -\frac{RT}{\bar{V}_0^w} \ln x_r^w \tag{74}$$

It is usual to relate the osmotic pressure to the concentration of the solution, the protein. For this, we use:

$$\ln x^w = \ln(1 - x^e) \approx -x^e = -\frac{n^e}{n^w + n^e} \approx -\frac{n^e}{n^w} \tag{75}$$

and the following expression for the volume V of the solution:

$$V = n^w \bar{V}^w + n^e \bar{V}^e \approx n^w \bar{V}_0^w. \tag{76}$$

Substitution of these relations in (74) yields:

$$\Delta\pi = \frac{n^e}{V} RT = c^e RT, \tag{77}$$

in which the *concentration* c^e is expressed in moles·m^{-3}. This relation has also been discovered empirically by *Van't Hoff*, indicating that the basic assumption for an ideal mixture, defined in (61), applies for dilute solutions. We define the osmotic pressure of a solution as:

$$\pi = -\frac{RT}{\bar{V}_0^w} \ln x^w, \tag{78}$$

which is well approximated by van 't Hoff's equation in a dilute solution:

$$\pi = c\, RT. \tag{79}$$

in which c is the concentration of the solved substances. Further, we specify expression (61) for the chemical potential of a component α, using (73):

$$\bar{\mu}^\alpha = \bar{\mu}_0^\alpha(T) + RT \ln x^\alpha + p\bar{V}^\alpha. \tag{80}$$

with particularly for water:

$$\bar{\mu}^w = \bar{\mu}_0^w(T) + RT \ln x^w + \bar{V}_0^w p = \bar{\mu}_0^w(T) + \bar{V}_0^w (p - \pi) \tag{81}$$

In other words, the chemical potential consists of a pressure dependent part (the pressure potential) and a concentration-dependent part (the osmotic potential) for isothermal conditions. Deviations of the ideal situations are taken into account using the so called *activity coefficient* γ^α. The molar fraction x^α is corrected to an 'active molar fraction', or *activity* a^α:

$$a^\alpha = \gamma^\alpha x^\alpha, \tag{82}$$

The expression for the chemical potential then becomes:

$$\bar{\mu}^\alpha = \bar{\mu}_0^\alpha(T) + RT \ln a^\alpha + p\bar{V}^\alpha. \tag{83}$$

8 Electrolytic solutions

In biology we often have to deal with solutions of ionized high-molecular proteins. In this paragraph we will consider solutions of a protein, (component e) and a low-molecular salt (component z) in water (component w). We will indicate the protein with PX_z. We assume that in a solution of this protein an equilibrium will be established in which a protein molecule falls apart in a high molecular negative ion P^{z-} and z small positive ions X^+:

$$PX_z \rightleftharpoons P^{z-} + zX^+. \tag{84}$$

In general there are also ions present of a low-molecular electrolyte in such a protein solution, indicated with MZ. We assume that a solution of this electrolyte results in monovalent positive and negative ions:

$$MX \rightleftharpoons M^- + X^+. \tag{85}$$

In this situation the M^-- and the X^+-ion are called the 'co-ion' and the 'counter-ion' respectively.

Since the time constant, corresponding to the establishment of a local electrostatic equilibrium, is very short, we can assume that at every moment electroneutrality applies.

8.1 The electrochemical potential of an ionic component

In the former the chemical potential of a component α was defined as the partial molar Gibbs free energy. This means that we considered the change of the Gibbs free energy if we added one mole of component α to the mixture, during wich we kept the amounts of the other components constant. For a solution of an electrolyte, for example the salt MZ, the movement of cations or anions is not exclusively controled by the chemical potential, as was the case for the water in the porous medium [HB03]. Reason for this is, that the charged particle is also sensitive for an electric-potential field. One mole of a monovalent ion has a charge equal to the constant of Faraday, F. The force that works on an ion in an electric-potential field ξ is:

$$F\nabla\xi \tag{86}$$

Therefore, we do not use the chemical potential for an ionic component but the electrochemical potential, of which the gradient does not only contain the mechanical and chemical forces, but also the electric forces:

$$\bar{\mu}^{\alpha} = \bar{\mu}_0^{\alpha} + RT ln a^{\alpha} + p\bar{V}^{\alpha} + z^{\alpha} F \xi \quad \alpha = +, - \tag{87}$$

Here, z^{α} is the valence of the ion, from which it follows that for a salt in water the chemical potential is:

$$\bar{\mu}^{z} = \bar{\mu}_0^{z} + RT \ln a^{z} + p\bar{V}^{z}, \tag{88}$$

We see that the *activity of the salt* is,

$$a^{z} = a^{+} a^{-}, \tag{89}$$

that the reference-potential is,

$$\bar{\mu}_0^{z} = \bar{\mu}_0^{+} + \bar{\mu}_0^{-}, \tag{90}$$

and that the partial molar volume is,

$$\bar{V}^{z} = \bar{V}^{+} + \bar{V}^{-}. \tag{91}$$

We now define the activity coefficients for the ions γ^{+} and γ^{-}, in analogy to (82), as:

$$a^{+} = \gamma^{+} x^{+}, \qquad a^{-} = \gamma^{-} x^{-}, \tag{92}$$

in which x^{+} and x^{-} represent the (equal) molar fractions of the anion and the cation. We can now derive the activity of the salt a^{z}:

$$a^{z} = \gamma^{+} x^{+} \gamma^{-} x^{-} = (\gamma^{\pm} x)^{2}, \tag{93}$$

in which we defined the *average activity coefficient* of the salt $\gamma^{\pm}$ as:

$$\gamma^{\pm} = (\gamma^{+} \gamma^{-})^{1/2}, \tag{94}$$

and used $x^{+} = x^{-} = x$. The activity coefficients can be determined experimentally from electro-chemical experiments. A theoretical foundation of the relations above is provided for strongly diluted solutions by Debye and Hückel in 1923 [DH23]. In this course we consider the relations as empirical ones. It is obvious that the relations for the chemical potential of a salt as mentioned above do not apply for a pair of ions, present in a porous medium with fixed charges, because in that case the co-ionic charge and the counter-ionic charge do not neutralize one another and therefore one cannot speak of a salt (=electric neutral molecule) in a solution.

8.2 The Donnan-effect

The Donnan-effect occurs in a saturated electrically charged porous solid. We consider two neighbouring points in the charged porous medium. Between these two points there is a difference in fixed charge concentration. The two points are now considered to be two containers, between which water and ions (M^{-} en X^{+}) can move freely. The fixed charges (P^{z-}), however, cannot move from one container to the other. In other

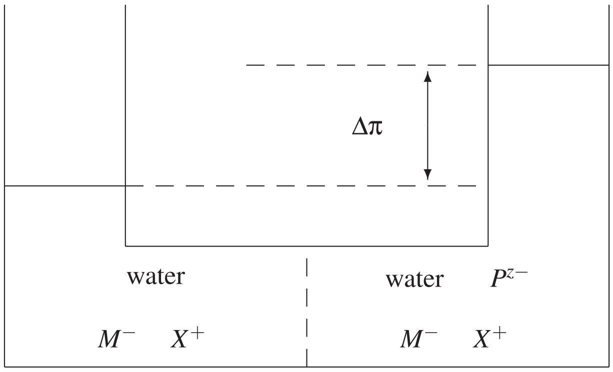

Figure 3: Illustration of the Donnan-effect.

words, the containers communicate through a semi-permeable medium (figure 3). To fix our thoughts and without loss of generality, we assume that the left container has no fixed charge. An equilibrium is established, in which no net transport of particles through the membrane takes place. This equilibrium is characterized by the condition, that the (electro)-chemical potential for substances, that are able to pass the medium freely, is equal in the left as well as the right container:

$$\begin{aligned} \bar{\mu}_l^w &= \bar{\mu}_r^w && (95) \\ \bar{\mu}_l^\alpha &= \bar{\mu}_r^\alpha \quad \alpha = +,- && (96) \end{aligned}$$

Using (83) we can write these relations as:

$$\bar{\mu}_0^w + RT \ln a_l^w + p_l \bar{V}^w = \bar{\mu}_0^w + RT \ln a_r^w + p_r \bar{V}^w, \tag{97}$$

$$\begin{aligned} &\bar{\mu}_0^\alpha + RT \ln a_l^\alpha + p_l \bar{V}^\alpha + z^\alpha F \xi_l = \\ &\qquad \bar{\mu}_0^\alpha + RT \ln a_r^\alpha + p_r \bar{V}^\alpha + z^\alpha F \xi_r \quad \alpha = +,-. \end{aligned} \tag{98}$$

Now, we first consider the ionic equilibrium. As the solution is dilute, the contribution $p\bar{V}^\alpha$ is negligible with respect to the term $RT \ln a^\alpha$. With this the summation of (98), for $\alpha = +,-$, reduces to the condition:

$$a_l^+ a_l^- = a_r^+ a_r^- \tag{99}$$

Using (93) this leads, after conversion to concentrations, to:

$$(\gamma^\pm)_l^2 c_l^+ c_l^- = (\gamma^\pm)_r^2 c_r^+ c_r^- \tag{100}$$

Beside this condition, the condition of electroneutrality for the solution in the left as well as the right compartment should be kept. Deviation from electroneutrality would lead to - relative strong - electric forces, restoring electroneutrality almost immediately. Therefore:

$$c_l^+ = c_l^- \tag{101}$$

$$c_r^+ = c_r^- + zc_r^e, \tag{102}$$

in which c^e is the concentration of the macromolecule to which z fixed charges are attached. For the concentrations of M^-- and X^+-ions in the left and right compartment a combination of (100) – (102) yields:

$$c_r^+ = \frac{1}{2}\left(zc_r^e + \sqrt{(zc_r^e)^2 + 4\frac{(\gamma_l^\pm)^2(c_l^-)^2}{(\gamma_r^\pm)^2}} \right) \tag{103}$$

$$c_r^- = \frac{1}{2}\left(-zc_r^e + \sqrt{(zc_r^e)^2 + 4\frac{(\gamma_l^\pm)^2(c_l^-)^2}{(\gamma_r^\pm)^2}} \right) \tag{104}$$

In a dilute solution we are allowed to equate the activity coefficients $\gamma_l^\pm$ and $\gamma_r^\pm$. We now see that the concentration c^+ of the X^+-ions is different between left and right, as is the concentration c^- of the M^--ions (Fig. 6). This difference in concentration is called the *Donnan-effect*. We also see, that the Donnan-effect decreases for an increasing salt concentration. The osmotic pressure difference between the left and the right compartment $\Delta\pi$ can now be determined from the equilibrium for the water. Therefore, we rewrite (98) as:

$$\Delta\pi = p_r - p_l = -\frac{RT}{\bar{V}^w}\ln\frac{a_r^w}{a_l^w}, \tag{105}$$

If we suppose that the activity coefficients for water are equal left and right, we can switch to molar fractions:

$$x_l^w = \frac{c_l^w}{c_l^w + c_l^+ + c_l^-} = 1 - \frac{c_l^+ + c_l^-}{c_l^w + c_l^+ + c_l^-} \tag{106}$$

$$x_r^w = \frac{c_r^w}{c_r^w + c_r^+ + c_r^- + c_r^e} = 1 - \frac{c_r^+ + c_r^- + c_r^e}{c_r^w + c_r^+ + c_r^- + c_r^e} \tag{107}$$

Because the water concentration is much higher than the other concentrations, we can use the first order approximation $\ln(1+x) \approx x$ and we will find:

$$\frac{\Delta\pi\bar{V}^w}{RT} = \frac{c_r^+ + c_r^- + c_r^e}{c_r^w} - \frac{c_l^+ + c_l^-}{c_l^w}, \tag{108}$$

This expression can be simplified further, because $c_l^w \approx c_r^w = 1/\bar{V}^w \approx 1/\bar{V}_0^w$, which gives:

$$\Delta\pi = RT(c_r^+ - c_l^+ + c_r^- - c_l^- + c_r^e) \tag{109}$$

In many cases the valence z of the protein is very high and therefore the contribution of the protein concentration c^e is negligible, compared to the concentrations of the small ions. If we define the osmotic pressure, in this case, as:

$$\pi = RT(c^{+} + c^{-}) \tag{110}$$

we find the former expression for the osmotic pressure difference back. In the non-ideal situation equation (110) is extended with an osmotic coefficient Γ:

$$\pi = \Gamma RT(c^{+} + c^{-}) \tag{111}$$

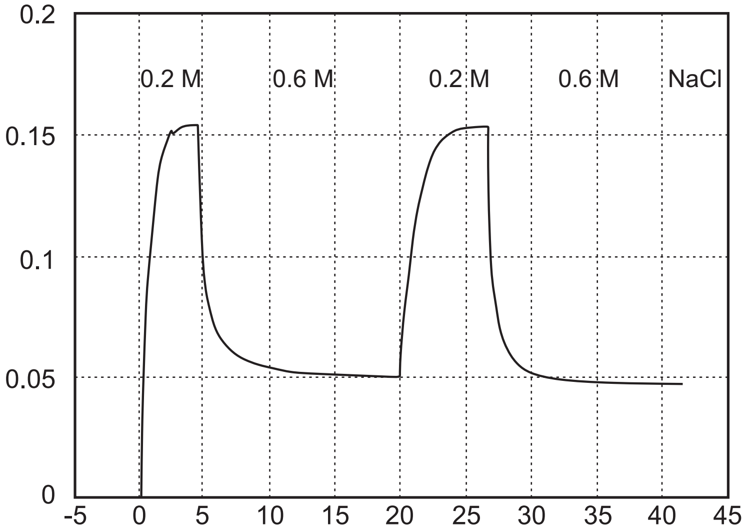

Figure 4: Measured swelling pressure in a copolymer of acrylic acid and acrylamid during step-wise changes in external salt concentration. The equilibrium values at a given external salt concentration are reproducible. The transient from one swelling pressure to the next is a measure of the diffusion speed of ions through the gel [OdHH^{+}95].

From equation (98) also the Donnan-potential difference between the left and right compartment follows:

$$\xi_r - \xi_l = \frac{RT}{F} ln \frac{a_l^{+}}{a_r^{+}} = \frac{RT}{F} ln \frac{a_r^{-}}{a_l^{-}} \tag{112}$$

8.3 Donnan osmosis in biological tissues

The semi-permeable membrane exists in many forms in nature: for example as a cell membrane, as a layer endothelial cells (covering the inner side of blood vessels), or as elastic lamina (a layer that is found in the wall of arteries). The transmembrane potential observed across the membrane of a living cell is a Donnan-potential. However,

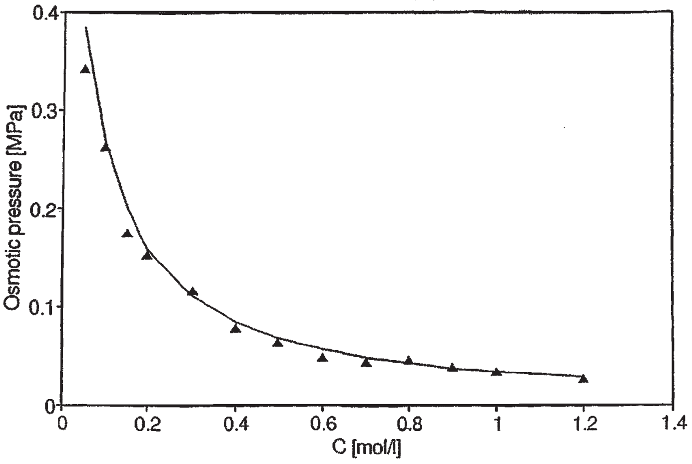

Figure 5: Measured relation between the equilibrium swelling pressures and external salt concentration ($\triangle$) in the synthetic material discussed in Fig. 4. The drawn line represents relation (114), with parameter values $\Phi = \Phi^* = 0.93$, $f = 1$ and $c^{fc} = 0.24 \cdot 10^3 \mathrm{mol{\cdot}m^{-3}}$.

one should realize that many biological tissues function as a semipermeable medium leading to the Donnan-effect (and to osmosis) as a continuous osmotic pressure gradient across the tissue. Therefore the Donnan-effect occurs in, for example, cartilage, where the huge, ionized proteoglycan molecules are tangled in a network of collagen and elastine fibers. The charge of the proteoglycan molecules is caused by the negative carboxyl groups (COO^-) and sulphate groups (SO_3^-). Hence, it is not the concentration of big molecules c^e, but the concentration of negatively combined charge zc^e, that characterizes the material. This concentration is often called *fixed charge density* c^{fc}. We come across several small ions in biological tissues like Na^+, K^+, Ca^{2+} en Cl^-.

For studying the properties of biological tissues, synthetic model materials are developed, consisting of ionised polymer chains [dH94].

The Donnan-osmotic effect can be used to determine the fixed charge density c^{fc} in these materials. The model material ('the right compartment') is therefore exposed to an external solution of a known concentration ('the left compartment') (Fig. 3), after which the osmotic pressure in the material is measured. In figure 5 the measured equilibrium osmotic pressure is plotted against the external salt concentration. From a combination of the relations (100) – (104) and (109) we can eliminate the concentration of free ions in the model material, which will result in:

$$\Delta\pi = RT\{{c^{fc}}^2 + 4f^2c^2\}^{1/2} - 2cRT, \tag{113}$$

in which $c = c_l^+ = c_l^-$ is the (known) concentration of ions in the external solution, and f is a short notation for the relation between the activity of salt in the external solution

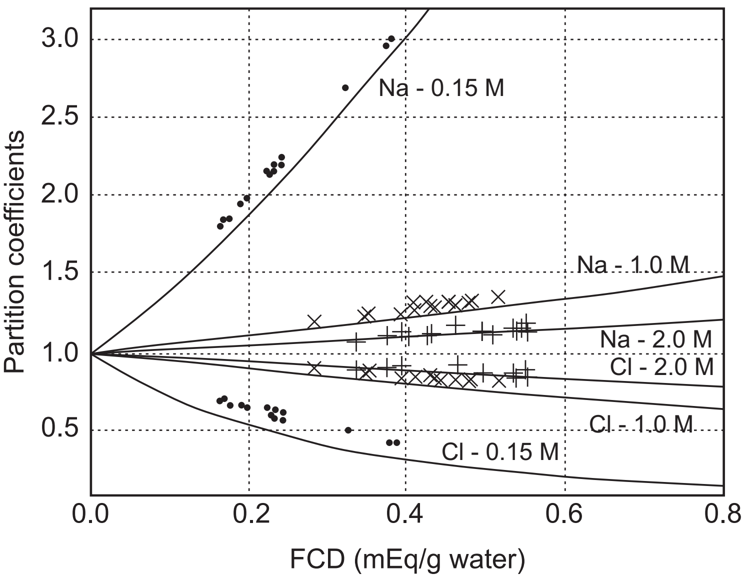

Figure 6: The partition coefficients $\frac{c_r^+}{c_l^+}$ and $\frac{c_r^-}{c_l^-}$ of Na^+ and Cl^- is measured in a copolymer of acrylic acid and acrylamid gel. The continuous line is the prediction by eq. (104-104) for ideal Donnan ($\gamma_r^\pm = \gamma_l^\pm$) [LSSH98].

and that in the material $f = \gamma_l^\pm / \gamma_r^\pm$. We have to realize, that several approximations have been introduced when deriving expression (109). A more elaborate derivation leads to:

$$\Delta\pi = \Phi RT (c^{fc^2} + 4f^2c^2)^{1/2} - 2\Phi^* cRT, \tag{114}$$

with *osmotic coefficients* Φ and Φ^*. The unknowns in this relation can be determined by fitting the experimental data. From figure 5, we see that the relation between the measured concentration and the osmotic pressure can be described well using relation (114).

9 Chemical potential and mass transport

In the former it is stated, that the direction in which thermodynamic processes go, is dependent of differences in chemical potential. We will now specify this statement for the flow of a dissolved substance in a solution. The 'derivation' is meant to give better insight and not to be mathematically precise.

As an introduction we consider a simple one dimensional system, characterized by a mass m and a friction coefficient k, to which a force f is applied, that is related to a potential $\bar{\mu}$. The system model for such a system reads:

$$f = \nabla\bar{\mu} = ma + kv, \tag{115}$$

in which v and a are the velocity and the acceleration of the system. Some time after the force is applied to the system a stationary state will be established, in which the acceleration equals zero, so the velocity v is proportional to the gradient of the potential $\bar{\mu}$:

$$v = \frac{1}{k}\nabla\bar{\mu} \tag{116}$$

Similarly the flow of a constituent α in a solution can also be considered. If we state again, that the friction term is linear in velocity, we find:

$$v^{\alpha} = L^{\alpha} \cdot \nabla\bar{\mu}^{\alpha}, \tag{117}$$

in which L^{α} is a second order tensor. Substitution of expression (80) for the chemical potential yields:

$$v^{\alpha} = D^{\alpha} \cdot \nabla x^{\alpha} + K^{\alpha} \cdot \nabla p \tag{118}$$

If a pressure gradient is absent, we recognize the *law of Fick* for diffusion of constituents caused by a concentration gradient. In the absence of a concentration gradient the equation reduces to the *law of Darcy* for flow of a fluid through a porous medium caused by the influence of a pressure gradient. The tensor K^{α} therefore represents a *permeability tensor*, while D^{α} is a *diffusion tensor*. If we deal with an isotropic system, these tensors reduce to $K^{\alpha}\, I$ and $D^{\alpha}\, I$, respectively.

References

[Bio41] M.A. Biot. General theory of three-dimensional consolidation. *Journal of Applied Physics*, 12(2):155–164, 1941.

[Bio56] M.A. Biot. General solutions of the equations of elasticity and consolidation. *Journal of Applied Mechanics*, 78:91–96, 1956.

[Bow76] R.M. Bowen. *Theory of Mixtures. Part I. Continuum Physics*. Academic Press, 1976.

[Cha81] R. Chang. *Physical chemistry with applications to biological systems*. MacMillan Publishing, 1981.

[DH23] P. Debye and E. Hückel. The theory of electrolytes. i. lowering of freezing point and related phenomena. *Physikalische Zeitschrift*, 24:185–206, 1923.

[dH94] H.J. de Heus. *Verification of mathematical models describing soft charged hydrated tissue behaviour*. PhD thesis, Eindhoven University of Technology, Department of Mechanical Engineering, 1994.

[GT09] J.M. Gere and S.P. Timoshenko. *Mechanics of materials*. Springer, 2009.

[HB03] J.M. Huyghe and P.H.M. Bovendeerd. Biological mixtures. In J. Kubik, M. Kaczmarek, and I. Murdoch, editors, *Modelling coupled phenomena in saturated porous materials : advanced course*, pages 227–278, Warschau, Poland, 2003.

[KC65] A. Katchalsky and P.F. Curran. *Nonequilibrium thermodynamics in biophysics*. Harvard University Press, 1965.

[LSSH98] Y. Lanir, J. Seybold, R. Schneiderman, and J.M. Huyghe. Partition and diffusion of sodium and chloride ions in soft charged foam : the effect of external salt concentration and mechanical deformation. *Tissue Engineering*, 4(4):365–378, 1998.

[OdHH$^+$95] C.W.J. Oomens, H.J. de Heus, J.M. Huyghe, L. Nelissen, and J.D. Janssen. alidation of the triphasic mixture theory for a mimic of intervertebral disc tissue. *Biomimetics*, (3):171–185, 1995.

[Ric80] E.G. Richards. *An introduction to the physical properties of large molecules in solution*. Cambridge University Press, 1980.

Finite deformation poromechanics, with application to heart muscle and blood perfusion

J.M. Huyghe

Bernal Institute, University of Limerick, Ireland

In this chapter we analyse a mixture of an incompressible liquid and an incompressible porous solid. This type of saturated porous medium is a good model for numerous types of soil mechanics problems and is therefore studied since many years in civil engineering. It can also be used in the field of biomechanics to model the coupling between fluid flow and mechanical loading in e.g. cartilage or skin. We will highlight this subject in a somewhat gradual fashion. The equations are first derived in the engineering style of Terzaghi for a simple one-dimensional infinitesimal strain case. This, together with a number of illustrating exercises, ensures that the reader first keeps his/her attention on the physics of the phenomenon. In a subsequent derivation we use the rigorous approach from the mixture theory for the case of three-dimensional finite deformation. As a application, a multiporosity description of finite deformation of a porous solid is developed using the theory of mixtures. Unlike existing multiporosity models from the literature this formulation includes anisotropy of interfaces between porosities. Each porosity is dealt with as a separate component. Fluid flow between porosities are mass exchange term between components. Rather than accounting for a discrete number of porosities a continuous spectrum of intercommunicating compartments is introduced. Conservation laws for mass and momentum have been derived and additionally appropriate formulations for the constitutive behaviour of the constituents are proposed. A finite element description of the hierarchical mixture model has been implemented. 2-D, axi-symmetric and 3-D elements can be used in finite deformation analysis. An example of application is blood perfused biological tissue. A simulation of a blood perfused contracting skeletal muscle is presented.

1 The concepts

1.1 Permeability

The French engineer Darcy initiated a number of experiments in the context of the design of fontains in the city of Dijon. These experiments aimed at quantifying the permeation of water through sand beds [Dar56]. In the experiments water saturated cylindrical sand samples were subjected to a constant pressure gradient. The flow through the specimens was measured for varying pressure difference, cross-sections and lengths of the specimens (Figure 1).

These experiments showed that the flow is proportional to the pressure difference $p_1 - p_2$ and the cross-section A of the sample and inversely proportional to the length L of the sample:

$$Q = \frac{K(p_1 - p_2)A}{L} \tag{1}$$

The proportionality constant K is the *permeability*. Experiments showed that biological tissues complies with Darcy's law reasonably well [MB68, Mar79] when the fluid is a physiological salt solution. In soil mechanics Darcy's law has been shown valid for sand and coarse lime. For clays a conclusive experiment has never been done. When different Newtonian fluids are used in the same sand samples, the permeability of the sample has been shown to be inversely proportional to the viscosity of the fluid. The permeability depends on the size and the structure of the pores of the sample also. If the sample is compressed, the permeability drops. Different relationships between permeability and fluid volume fraction are proposed in the literature. In very deformable porous media, like soft biological tissues, only the viscous forces of the flowing liquid is sufficient to cause compression of the porous medium and thus a reduction of the permeability.

1.2 Effective stress

Consider a mixture of an incompressible solid and an incompressible liquid (figure 2).

We assume that the solid is composed of grains - to focus the attention and without loss of generality. The dimensions of the grains and the pores between the grains are small relative to the macroscopic dimensions of the material. Every grain is subject to two types of external load: (1) the liquid pressure (2) the contact forces with neighbouring grains. The liquid pressure is an isotropic load which cannot result into deformation of the grains as they are incompressible. Only the contact forces with neighbouring grains result into a stress field in the grains and thus deformation of the solid skeleton. The latter stress field, averaged over a large number of grains and measured per unit mixture surface is the effective stress. The effective stress in a mixture

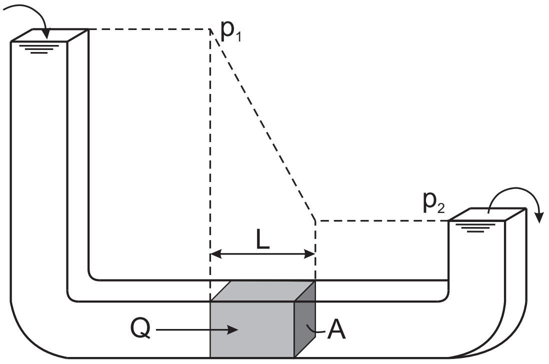

Figure 1: Darcy's experiment

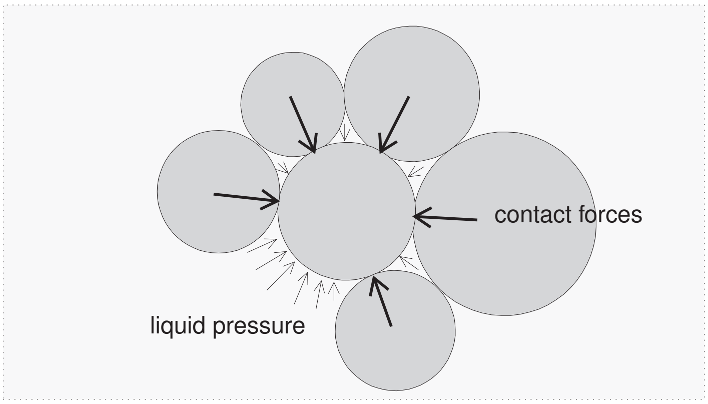

Figure 2: The mechanical stress in a fluid solid mixture.

of an incompressible solid and an incompressible liquid is that part of the stress that causes deformation. The total stress σ is given by the sum of the effective stress σ_e and the hydrostatic pressure $-pI$:

$$\sigma = \sigma_e - pI \tag{2}$$

In this example we assumed that only the pressure of the liquid contributes to the total stress. In principle every component - and therefore also the liquid component - can contribute to the effective stress in a mixture. Therefore it is wrong to consider (2) a division of the stress in an effective stress caused by the solid and a pressure caused by the liquid. In general both components contribute to both terms. In soil and rock mechanics, the fields from which the effective stress concept originates, the effective stress is often called the grain stress, because for lots of soil mixtures contribution of the liquid to the the effective stress is negligible.

In the former chapter we saw that in the more recent theory of mixtures, it is common practise to subdivide the total stress in a mixture in partial stresses, in analogy to the much older concept of partial pressure from the kinetic theory of gasses. These partial stresses can be associated with every individual component. For the porous medium this means:

$$\sigma = \sigma^s + \sigma^f \tag{3}$$

The stress-strain relation becomes a relation between the effective stress and the pressure in a porous medium. Notice that in force equilibrium the total stress appears.

2 Theory of consolidation of Terzaghi

During this presentation of porous media mechanics the historical development will be followed, because that is the easiest way to comprehend it.

One of the major enemies of civil engineering is the phenomenon of consolidation. After constructing a big building or a bridge the foundation of the construction appears to sink several inches into the ground. As long as this sinking is distributed homogeneously over the total area of the foundation consequences are not yet disastrous. If there is differential sinking, the consequences can be catastrophic. Cracks in the construction, leakage in case of a dam or pulling a building out of position (tower of Pisa). Consolidation can usually be attributed to the construction pushing the fluid beneath the foundation aside. Therefore, this problem can only be studied with porous media mechanics.

The problem of consolidation has been studied by Terzaghi in the nineteen twenties. Terzaghi restricted himself to a one dimensional consolidation, in which the liquid flow and the displacement of the solid occur in only one direction. This situation is reasonable for a very wide foundation plate where the sideward outflow of fluid is only a local boundary effect. We can create this situation on purpose in a one dimensional

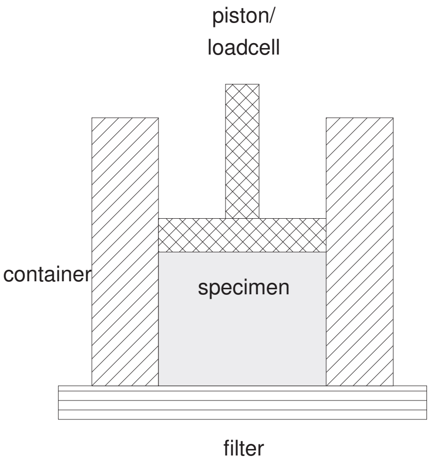

Figure 3: Setup for a one dimensional consolidation test.

consolidation experiment (figure 3), which is often used to study cartilage. In this experiment a cylindrical specimen is placed in a fitting rigid cylinder. The bottom of the specimen has contact with a porous filter in which the permeability is much higher than the permeability in the specimen itself. The top of the cylinder has contact with an impermeable piston with surface area A, that is loaded with an axial force P. For an incremental increase of the force P, this force will first be intercepted by the hydrostatic pressure (2), because no deformation of the solid has taken place yet.

$$p = \frac{P}{A} \qquad\qquad 0 < z < h, \quad t = 0^{+} \tag{4}$$

At $z = 0$ a steep pressure gradient appears that causes the liquid to flow out of the specimen. This outflow of liquid results in a smooth downward motion of the piston. The deformation of the sample causes an effective stress within the sample that gradually will take over the load from the hydrostatic pressure.

We now consider Terzaghi's way to derive the equations that describe this process. We restrict ourselves to small deformations. Consider a layer $[z, z + dz]$ of a one dimensional medium that is subjected to consolidation. The medium consists of a porous, incompressible, elastic solid saturated with an incompressible fluid. Analogue to (1) we subdivide the total stress σ in a hydrostatic pressure p, present in the liquid + solid (pressure positive, see figure 2) and an elastic stress caused by deformation σ_e, measured per unit surface area (extension positive). The liquid flux per unit mixture area is indicated with a q (z-direction positive). If we neglect the forces of inertia and the volume forces, we can write the balance of momentum as:

$$\sigma_e(z + dz) - \sigma_e(z) - p(z + dz) + p(z) = 0 \tag{5}$$

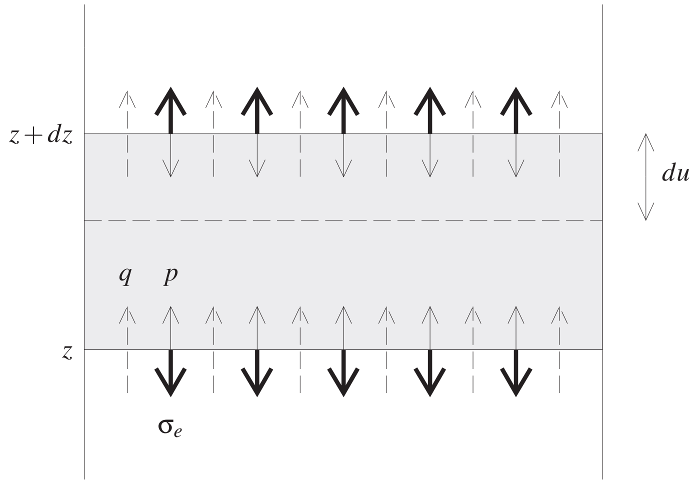

Figure 4: One dimensional consolidation of a porous medium.

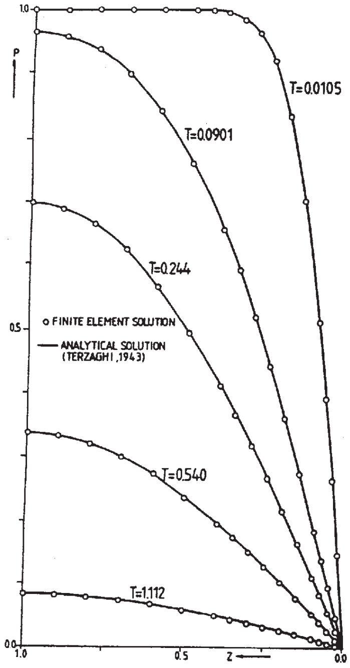

Figure 5: Dimensionless pressure *P* versus dimensionless position *Z* at different times during linear, one dimensional consolidation.

After dividing by dz, we find:

$$\frac{\partial \sigma_e}{\partial z} - \frac{\partial p}{\partial z} = 0 \tag{6}$$

Because of incompressibility the balance of mass reduces to the balance of volume:

$$du(t+dt) - du(t) - q(z)dt + q(z+dz)dt = 0 \tag{7}$$

After division by $dzdt$, we find:

$$\frac{D^s}{Dt}\frac{\partial u}{\partial z} + \frac{\partial q}{\partial z} = 0 \tag{8}$$

In addition to the balance laws we need two constitutive equations. The first is the Darcy equation :

$$q = -K\frac{\partial p}{\partial z} \tag{9}$$

in which we consider the permeability K a constant. Substitution of (9) in (8) yields:

$$\frac{D^s}{Dt}\frac{\partial u}{\partial z} - \frac{\partial}{\partial z}K\frac{\partial p}{\partial z} = 0 \tag{10}$$

The second constitutive relation is the law of Hooke:

$$\sigma_e = H\frac{\partial u}{\partial z} \tag{11}$$

in which H is the compressive modulus. We consider H a constant, i.e. linear elasticity. The compressive modulus is related to the modulus of elasticity, E, and Poisson's ratio, ν, for an isotropic medium:

$$H = E\frac{1-\nu}{(1+\nu)(1-2\nu)} \tag{12}$$

The equations (6), (8), (9) and (11) form a complete set of partial differential equations. Integration of equation (6) yields:

$$\sigma(z,t) - p(z,t) = -p_0(t) \tag{13}$$

with $p_0(t)$ the top load. For a classical consolidation test the top load is a step function: $p_0 = \frac{P}{A}\ for\ t > 0$ otherwise zero. After applying this step the function is constant in time, so[1]:

$$\frac{D^s\sigma_e}{Dt} - \frac{D^s p}{Dt} = 0 \qquad \text{for} \qquad t > t_0 \tag{14}$$

Substitution of (11) in (14), yields

$$H\frac{D^s}{Dt}\frac{\partial u}{\partial z} - \frac{D^s p}{Dt} = 0 \qquad \text{for} \qquad t > t_0 \tag{15}$$

---

[1] In standard infinitesimal solid mechanics notation, we would use $\frac{\partial}{\partial t}$ in stead of $\frac{D^s}{Dt}$

Substitution of (15) and (9) in (8) yields the consolidation equation of Terzaghi:

$$\frac{D^s p}{Dt} - KH\frac{\partial^2 p}{\partial z^2} = 0 \tag{16}$$

Notice the analogy with the diffusion equation. The characteristic time that is needed to start the consolidation process of a porous layer with thickness Δz, permeability K and compressive modulus H, follows from (16):

$$\frac{\Delta p}{\Delta t} = KH\frac{\Delta p}{(\Delta z)^2} \tag{17}$$

or:

$$\Delta t = \frac{(\Delta z)^2}{KH} \tag{18}$$

The consolidation time t is therefore inversely proportional to the permeability K and the stiffness H, and proportional to the square of the thickness of the layer Δz. The analytical solution for the consolidation equation (13) for a specimen with thickness h holds:

$$P = \sum_{n=0}^{\infty} \frac{2}{M}\sin(MZ)e^{-M^2T} \tag{19}$$

with

$$P = \frac{p}{p_0} \tag{20}$$

$$M = \frac{\pi}{2}(2n+1) \tag{21}$$

$$Z = \frac{z}{h} \tag{22}$$

$$T = \frac{KHt}{h^2} \tag{23}$$

Notice that for $T > 1$ the consolidation process of the specimen is largely completed (see figure 5).

3 Mixture description of saturated porous media

We shall derive equations applicable to the behaviour of elastic incompressible fluid saturated porous media from mixture theory. The resulting equations are a special case of Biot's finite porous media theory [Bio72].

3.1 Assumptions

We consider the porous medium as a two-component mixture, composed of a solid (superscript s) and a fluid component (superscript f):

$$\phi^s + \phi^f = 1. \tag{24}$$

Eq. (24) is the saturation condition. We assume that no mass-exchange occurs between the components. Each component is assumed incompressible :

$$\rho_i^\alpha = \frac{\rho^\alpha}{\phi^\alpha} = \text{constant}, \qquad \alpha = s, f. \tag{25}$$

The apparent densities ρ^α however do change as a function of time. We consider processes which are sufficiently slow so as to ensure that inertia forces are negligible. Volume forces are neglected as well. We assume that all components have the same temperature and no gradients in temperature are present either in time or space.

3.2 Conservation laws

3.2.1 Conservation of mass

In the absence of mass exchange the local law of conservation of mass of component α reduces to :

$$\frac{\partial \rho^\alpha}{\partial t} + \nabla \cdot (\rho^\alpha v^\alpha) = 0, \qquad \alpha = s, f. \tag{26}$$

Using eq. (25) we can rewrite (26) :

$$\frac{\partial \phi^\alpha}{\partial t} + \nabla \cdot (\phi^\alpha v^\alpha) = 0, \qquad \alpha = s, f. \tag{27}$$

Summation of the eqs. (27) yields the local mass balance of the mixture :

$$\nabla \cdot (\phi^s v^s) + \nabla \cdot (\phi^f v^f) = 0, \tag{28}$$

or :

$$\nabla \cdot v^s + \nabla \cdot \left(\phi^f (v^f - v^s)\right) = 0. \tag{29}$$

The first term of (29) represents the rate of volume increase of a unit volume of mixture. The second term represents the fluid flux from this unit volume. Eq. (29) states that every volume-increase or decrease of the mixture is associated with an equal amount of in- or outflux of liquid. At this point it is useful to refer current descriptors of the mixture with respect to an initial state of the porous solid. As is usual in continuum mechanics, we define the deformation gradient tensor F mapping an infinitesimal material line segment in the initial state onto the corresponding infinitesimal line segment in the current state. The relative volume change from the initial to the current state is the determinant of the deformation gradient tensor $J = detF$. If we introduce volume fractions

$$\Phi^\alpha = J\phi^\alpha \tag{30}$$

per unit initial volume, we can rewrite the mass balance equation (27) as follows:

$$\frac{D^s \Phi^\alpha}{Dt} + J\nabla \cdot [\phi^\alpha (v^\alpha - v^s)] = 0 \tag{31}$$

or:

$$\frac{D^s}{Dt} J = J\nabla \cdot v^s \tag{32}$$

3.2.2 Conservation of momentum

Considering the assumptions stated earlier momentum balance reduces to :

$$\nabla \cdot (\sigma^{\alpha})^{c} + \hat{p}^{\alpha} = \mathbf{0}, \qquad \alpha = s, f. \tag{33}$$

The momentum interaction $\hat{p}^{\alpha}$ arises e.g., as a consequence of friction between the fluid and the solid. We assume no moment of momentum interaction between fluid and solid. Therefore we tacitly assumed the symmetry of the partial Cauchy stress tensor in (33). Summation of the equations (33) yields the local momentum balance for the mixture as a whole :

$$\nabla \cdot \sigma^{s} + \nabla \cdot \sigma^{f} = \nabla \cdot \sigma = \mathbf{0}, \tag{34}$$

if we use :

$$\hat{p}^{s} + \hat{p}^{f} = \mathbf{0}, \tag{35}$$

3.2.3 The entropy inequality

The local form of the entropy inequality applied to the mixture as a whole, reduces to:

$$\sum_{\alpha=s,f} \left(-\rho^{\alpha} \grave{\tilde{F}}^{\alpha} + \sigma^{\alpha} : D^{\alpha} - \hat{p}^{\alpha} \cdot u^{\alpha} \right) \geq 0. \tag{36}$$

We introduce the strain energy function

$$W = J \sum_{\alpha=s,f} \rho^{\alpha} \tilde{F}^{\alpha} = J \sum_{\alpha=s,f} \psi^{\alpha} \tag{37}$$

as the Helmholtz free energy of a mixture volume which in the *initial* state of the solid equals unity. ψ^{α} is the Helmholz free energy of constituent α per unit mixture volume. Rewriting the inequality (36) for the entropy production per initial mixture volume - i.e. we multiply inequality (36) by the relative volume change J - we find:

$$-\frac{D^{s}}{Dt} W + J\sigma : \nabla v^{s} + J\nabla \cdot \ [(v^{f} - v^{s}) \cdot \sigma^{f} - (v^{f} - v^{s})\psi^{f}] \geq 0. \tag{38}$$

3.3 Constitutive restrictions

We use the entropy inequality to derive constitutive restrictions for the mixture. The entropy inequality should hold for an arbitrary state of the mixture, complying with the balance laws and with incompressibility. There are two ways to comply with these restrictions. One is substitution of the restriction into the inequality, resulting in elimination of a field variable. The other is by introduction of a Lagrange multiplier. The mass balance of the mixture (29) is accounted for by means of a Lagrange multiplier.

Other balance laws and the incompressibility conditions (25) are accounted for by means of substitution. From the inequality 38 we see that the apparent density and the momentum interaction $\hat{p}^{\alpha}$ is already eliminated from the inequality. In other words the conditions of incompressibility and the momentum balance of the constituents have already been substituted into the second law. The divergence of the partial stress tensor of the solid $\nabla \cdot \sigma^s$ and the heat supplies r^{α} also are absent from 38. Thus the momentum balance of the mixture and the energy balance have already been substituted in the second law. Therefore, restrictions still to be fulfilled are the mass balances of the constituents (26) and mass balance of the mixture (29). The latter is substituted by means of a Lagrange multiplier p:

$$\begin{aligned}
&-\frac{D^s}{Dt}W + J\sigma_e : \nabla v^s \\
&+J[\sigma^f + (p\phi^f - \psi^f)I] : \nabla(v^f - v^s) \\
&+J(v^f - v^s)\cdot(-\nabla\psi^f + p\nabla\phi^f + \nabla\cdot\sigma^f) \geq 0.
\end{aligned} \tag{39}$$

in which the effective stress σ_e is defined as

$$\sigma_e = \sigma + pI \tag{40}$$

3.3.1 Choice of independent and dependent variables

We choose as dependent variables the dynamic variables appearing in inequality 39 : W, ψ^f, σ_e, $\sigma^f + p\phi^f I$, $\nabla \cdot \sigma^f + p\nabla\phi^f$. Their number should equate the number of unknown variables appearing in the balance equations minus the number of balance equations. The number of dependent variables should be as small as possible to describe the state of the tissue well. Their choice is a key *assumption* of the continuum theory and is based on insight in the physical phenomena involved in the behaviour of the material. If the dependent variables include only variables describing the local state of the tissue (e.g. E), the theory is a local theory. If the dependent variables include variables describing the state of the tissue some distance away from the point of consideration (e.g. ∇E), the theory is a non-local theory. Throughout this book we consider only local dependent variables. We choose as independent variables the kinematic variables : the Green strain of the solid E^s, the fluid volume fraction Φ^f and the fluid velocity relative to the solid $v^f - v^s$. For reasons of objectivity we need to transform all the vectors and tensors among the dependent and independent variables back to the initial state. This yields for the constitutive relationships:

$$\begin{aligned}
W &= W(E^s, \Phi^f, v^{fs}), \\
\psi^f &= \psi^f(E^s, \Phi^f, v^{fs}), \\
\sigma_e &= F\cdot S_e(E^s, \Phi^f, v^{fs})\cdot F^c, \\
\sigma^f - \phi^f pI &= F\cdot S^f(E^s, \Phi^f, v^{fs})\cdot F^c \\
\hat{p}^f - p\nabla\phi^f &= F\cdot \hat{P}^f(E^s, \Phi^f, v^{fs})
\end{aligned} \tag{41}$$

with

$$v^{fs} = F^{-1} \cdot (v^f - v^s) \tag{42}$$

The principle of equipresence requires that all dependent variables appear in each of the constitutive relationships. The choice of the independent variables is paramount for the form of the constitutive relationships that are derived. E.g., including for the solid Green strain only and no measure of strain rate, implies elasticity of the solid. In mixture mechanics it is also important to realise that each of the variables is an averaged value of a physical quantity over an averaging volume. It may seem surprising that the shear rate of the fluid is not included in the list of independent variables, although the viscosity of the fluid is absolutely essential for the behaviour of the mixture. The reason for this is that in a porous medium the shear rate at one side of the pore has a sign opposite to the shear rate at the other side of the pore. The expectation value of the shear rate in a representative elementary volume is therefore the shear rate of the solid, i.e. a generally very low value, not representative for the dissipation in the fluid. It is therefore more obvious to use the fluid velocity relative to the solid as a macroscopic measure of the microvalues of the shear rate. The fluid volume fraction Φ^f is not independent of the Green strain because of incompressibility :

$$\Phi^f = \det F - 1 + \phi_0^f = \sqrt{\det(2E^s + I)} - 1 + \phi_0^f \tag{43}$$

Because of the strong non-linearity of equation (43), elimination of one of the variables is tedious. In fact, the way we deal with the interdependence of these two variables is by means of the Lagrange multiplier p. The condition 29 is in fact a differentated form of eq. (43). This legitimises the use of E^s and Φ^f as independent variables.

3.3.2 Constitutive relationships

Applying the chain rule for time differentiation of W :

$$\frac{D^s W}{Dt} = \frac{\partial W}{\partial E^s} : \frac{D^s E^s}{Dt} + \frac{\partial W}{\partial \Phi^f}\frac{D^s \Phi^f}{Dt} + \frac{\partial W}{\partial v^{fs}} \tag{44}$$

and substituting the mass balance of the constituents (31) for the elimination of $\frac{D^s \Phi^f}{Dt}$ from the inequality 39 :

$$\begin{aligned}
&(J\sigma_e - F \cdot \frac{\partial W}{\partial E} \cdot F^c) : \nabla v^s + \\
&\frac{\partial W}{\partial v^{fs}} \cdot \frac{D^s}{Dt} v^{fs} \\
&+J[\sigma^f + (\mu^f \phi^f - \psi^f) I] : \nabla(v^f - v^s) \\
&+J(v^f - v^s) \cdot (-\nabla\psi^f + \mu^f \nabla\phi^f + \nabla \cdot \sigma^f) \geq 0.
\end{aligned} \tag{45}$$

in which μ^f is the chemical potential of the fluid:

$$\mu^f = \frac{\partial W}{\partial \Phi^f} + p \tag{46}$$

Eq. (45) should be true for any value of the state variables. Close inspection of the choice of independent variables and the inequality (45), reveals that the first term of (45) is linear in the solid velocity gradient ∇v^s, the second term linear in $\frac{D^s}{Dt} v^{fs}$ and the third term linear in the relative velocity gradients $\nabla(v^f - v^s)$. Therefore, by a standard argument, we find:

$$\sigma_e = \frac{1}{J} F \cdot \frac{\partial W}{\partial E} \cdot F^c \tag{47}$$

$$\frac{\partial W}{\partial v^{fs}} = \mathbf{0} \tag{48}$$

$$\sigma^f = (\psi^f - \mu^f \phi^f) I \tag{49}$$

leaving as inequality:

$$J(v^f - v^s) \cdot (-\nabla \psi^f + \mu^f \nabla phi^f + \nabla \cdot \sigma^f) \geq 0. \tag{50}$$

Eq. (47) indicates that the effective stress of the mixture can be derived from a strain energy function W which represents the free energy of the mixture. Eq. (48) shows that the strain energy function cannot depend on the relative velocity of fluid versus solid. Thus, the effective stress of a biphasic medium can be derived from a regular strain energy function, which physically has the same meaning as in single phase media . According to eq. (49) the partial stress of the fluid and the ions are scalars. Transforming the relative velocities to their Lagrangian equivalents, we find in stead of (50):

$$v^{fs} \cdot [-\nabla_0 \psi^f + \mu^f \nabla_0 \phi^f + \nabla_0 \cdot \sigma^f] \geq 0. \tag{51}$$

in which $\nabla_0 = F^c \cdot \nabla$ is the gradient operator with respect to the initial configuration. Note that as $\mu^f \nabla_0 \phi^f + \nabla_0 \cdot \sigma^f$ depends on v^{fs} according to the constituive relationships (41), the lefthandside of inequality (51) is not a linear function of v^{fs} and therefore it is incorrect to equate the factor $-\nabla_0 \psi^f + \mu^f \nabla_0 \phi^f + \nabla_0 \cdot \sigma^f$ to zero. From a physical point of view it is obvious that unlike the elastic deformation of the solid the flow of fluid relative the solid results in an entropy production. If we assume that the system is not too far from equilibrium, we can express the dissipation (51) associated with relative flow of fluid and ions as a quadratic function of the relative velocities:

$$-\nabla_0 \psi^f + \mu^f \nabla_0 \phi^f + \nabla_0 \cdot \sigma^f = B \cdot v^{fs} \tag{52}$$

B is a semi-positive definite matrix of frictional coefficients. Substituting eq. (49) into eq. (52) yields the Lagrangian form of Darcy's law :

$$-\phi^f \nabla_0 \mu^f = B \cdot v^{fs} \tag{53}$$

The constitutive behaviour of the fluid-solid mixture is thus described by a strain energy function W and frictional tensor B. From the strain energy function we derive both the effective stress and the chemical potential of the fluid.

3.4 Physical interpretation of the constitutive variables

Comparing eq. (40) with eq. (2) reveals that the Lagrange multiplier p should be interpreted as the hydrostatic pressure in fluid.

$$\nabla \cdot \sigma_e - \nabla p = \mathbf{0}. \tag{54}$$

If we define the permeability tensor K as:

$$K = (\phi^f)^2 B^{-1} \tag{55}$$

eq. (53) becomes:

$$\phi^f (v^f - v^s) = -K \cdot \nabla (p + \frac{\partial W}{\partial \Phi^f}). \tag{56}$$

Eq. (56) is the threedimensional form of Darcy's law (9). The difference between the chemical potential μ^f and the pressure p is the *matric* potential. The matric potential accounts for adsorption and capillary forces. It can be quantified experimentally using capillary rising heights (figure 6). In Terzaghi's consolidation theory the matric potentisal is neglected, not because it is negligible in absolute terms but because its gradient is negligible in an homogenous medium with limited variation of fluid volume fraction and coarse pore structure.

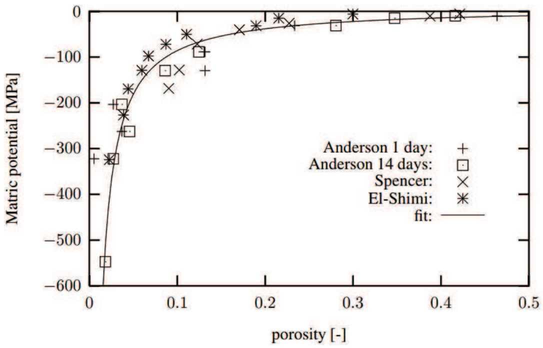

Figure 6: Matric potential as a function of fluid volume fraction ϕ^f for stratum corneum

3.5 Resulting equations

The resulting equations are: Momentum balance of the mixture:

$$\nabla \cdot \sigma_e - \nabla p = \mathbf{0} \tag{57}$$

Mass balance of the mixture:

$$\nabla \cdot v^s - \nabla \cdot (\phi^f (v^f - v^s)) = 0 \tag{58}$$

Darcy's law:

$$v^f - v^s = \phi^f B^{-1} \cdot \nabla \mu^f \tag{59}$$

Stress-strain relationship:

$$\sigma_e = (\det F)^{-1} F \cdot \frac{\partial W}{\partial E^s} \cdot F^c, \tag{60}$$

Constitutive law for the chemical potential of the fluid:

$$\mu^f = p + \frac{\partial W}{\partial \Phi^f} \tag{61}$$

The total stress in the mixture is composed of an effective stress and a hydrodynamic pressure: $\sigma = \sigma_e - pI$. The effective stress σ_e is derived from the strain energy function of the mixture W. In eq. (60) F is the deformation gradient tensor of the solid and E^s the Green strain tensor of the solid. The strain energy W in a function of the solid strain E. In one dimensional space eq. (57) reduces to eq. (6) from Terzaghi's confined compression theory.

Dynamic boundary conditions are:

$$[(\sigma_e - pI) \cdot n] = \mathbf{0} \tag{62}$$

with n the outer normal along the boundary and the square brackets represent the difference between the value at either side of the boundary.

$$[\overline{V}^f \mu^f] = 0, \tag{63}$$

with as a special case the evaporation boundary condition:

$$\overline{V}^f \mu^f = RT ln \frac{p^d}{p^d_s} \tag{64}$$

Eq. (63) and eq. (64) enforces continuity of molar chemical potential. Discontinuity of chemical potential would lead to an infinite fluid flux which is physically impossible. For this reason we can claim that even if the material properties are sharply discontinuous the chemical potential should be continuous. This is not true for the pressure p. E.g. at the interface between a sand layer and a clay layer the pressure is not continuous, at least if capillary effects are not neglected. Similarly interstititial pressure along the surface of the skin is not equal to atmospheric pressure. We use the molar chemical potential in stead of the volumetric chemical potential because the volumetric chemical potential can be used only for incompressible media. Although the medium we consider is incompressible, the medium outside the boundary need not be incompressible as is the case for evaporation. Kinematic boundary conditions are:

$$[u] = \mathbf{0} \tag{65}$$

$$[(v^f - v^s) \cdot n] = 0 \tag{66}$$

4 Remarks

We derived the equations, that describe the behaviour of a porous medium, in two different ways. The traditional approach of Terzaghi has the advantage that we know the physical meaning of the parameters from the start. It is a disadvantage that we have little insight in the assumptions that we - often unconsciously - took. For example, it appears from comparison of the resulting equations with mixture theory equations that we neglected the capillary forces.

In the second approach, using the theory of mixtures, all effects are taken into account, and simplifications have to be done explicitly. It is done by neglecting specific terms in the balance laws or by the choice of the independent variables. This approach is also suitable for generalisation to mixtures with more components, like we will see in chapter 6. A disadvantage of this approach is the complexity of the derivation.

5 Unconfined compression

In the beginning of the chapter, we showed that Terzaghi's problem - known as linear one-dimensional consolidation or confined compression - has an analytical solution 19. The experiment of confined compression requires a sample that fits tightly into a cylinder. Typically, collagen fibres in a confined compression test are never stretched: the radial strain is zero and the axial strain is negative. Therefore only the compressive properties of the proteoglycan gel are tested in this experiment. An analytical solution of a different test is available [Man53], known as unconfined compression, where the cylindrical sample is squeezed between two impervious plates. This experiment is generally more easy to perform, because it does not require the sample to fit exactly into a cylinder. It measures a different set of properties, because under axial compression the radially oriented collagen fibers are stretched. The fluid flow in an uncomfined compression test is radially oriented while the compressive load is axial. The test is therefore intrinsically two-dimensional. The stiffness is typically higher than in comfined compression because linear elasticity does not hold for cartilaginous tissues. Under tension cartilaginous tissues are stiffer than under compression.

6 Finite element formulation of poroelasticity without matric potential.

In this section a set of equations is derived suitable for a FE implementation. To describe the poroelastic medium, the balance of momentum (57), and the mass balance (58) are used. To obtain the weak formulation the equations are multiplied by arbitrary, time independent weighing functions and integrated over the volume of the mixture

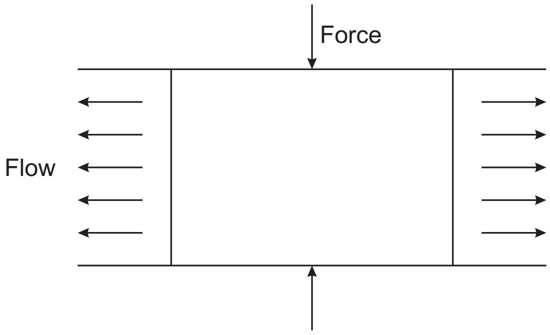

Figure 7: The cartilage sample is sueezd between two impervious plates. The fluid flow is radially oriented

(Ω). The momentum equation is multiplied by a weighing function $\vec{w}_x$. The mass equation is multiplied by the weighing functions w_p. After partial integration and applying the divergence theorem, we find,

$$\begin{aligned} \int_{\Omega} (\nabla \vec{w}_x)^c : \sigma \, d\Omega &= \int_{\Gamma} \vec{w}_x \cdot (\sigma \cdot \vec{n}) \; d\Gamma \, , \\ \int_{\Omega_0} w_p \dot{J} \, d\Omega_0 + \int_{\Omega_0} (K^* \nabla_0 p) \cdot \nabla_0 w_p \; d\Omega_0 &= \int_{\Gamma_0} w_p \, (K^* \nabla_0 p) \cdot \vec{n}_0 \; d\Gamma_0 \, , \end{aligned} \tag{67}$$

in which Γ is the current outer surface of the medium and Γ_0 is the initial outer surface of the medium . Since the model is time dependent and concerning future applications, we chose to use a total Lagrange formulation. The gradient operator is transformed according to,

$$\nabla = F^{-c} \cdot \nabla_0 \tag{68}$$

For the mass balance a time discretization scheme is applied,

$$\vec{\chi} = \theta \vec{\chi}(t_n + \Delta t) + (1 - \theta) \vec{\chi}_n \tag{69}$$

The scalar, θ, can be varied between 0 and 1. This way, the time discretization scheme can be varied easily from implicit Euler ($\theta = 1$) to explicit Euler ($\theta = 0$).

6.1 Linearization

The set of equations equations are nonlinear with respect to the unknown position field and pressure field. Therefore an iteration scheme needs to be adopted to find a solution. The Newton-Raphson iteration procedure is used to determine a sequence of approximate solutions until the balance equation is satisfied up to a given accuracy. If the exact solution of the position field is $\hat{\vec{x}}$, and $\vec{x}$ is an estimate of the exact solution, then we can write,

$$\hat{\vec{x}} = \vec{x} + \delta\vec{x} \tag{70}$$

with $\delta\vec{x}$ the error in the estimate. All quantities appearing in the balance equations can be expressed in a similar way.

6.2 Discretization

A separate interpolation for the error in the position field $\delta\vec{x}$ and pressure δp are introduced within one element Ω_e:

$$\begin{aligned} \delta\vec{x}|_{\Omega_e} &= \sum_{i=1}^{n} \Phi_i(x,y,z)\delta\vec{x}_{ei} = \underset{\sim}{\Phi}^T \delta\underset{\sim}{\hat{\vec{x}}}_e \\ \delta p|_{\Omega_e} &= \sum_{i=1}^{m} \Psi_i(x,y,z)\delta p_{ei} = \underset{\sim}{\Psi}^T \delta\underset{\sim}{p}_e \end{aligned} \tag{71}$$

Quadratic interpolation functions ($\underset{\sim}{\Phi}$) are used for the position field and weighing function $\vec{w}_w$. Linear interpolation functions ($\underset{\sim}{\Psi}$) are taken for the discretization of the pressure and its corresponding weighing function w_p. The components $\delta\underset{\sim}{\hat{\vec{x}}}_e$ are gathered in the column $\delta\underset{\sim}{\vec{x}}_e$. Substitution of these expressions into the linearized equations results in a set of linearized equations for a single element Ω_e, which is written as,

$$\begin{bmatrix} \underline{S} & -\underline{L} \\ -\underline{L}^T & -\underline{K} \end{bmatrix} \begin{bmatrix} \delta\underset{\sim}{u} \\ \delta\underset{\sim}{p} \end{bmatrix} = \begin{bmatrix} -\underset{\sim}{R} \\ \underset{\sim}{U} - \underset{\sim}{T}_1 + \underset{\sim}{T}_2 \end{bmatrix}$$

$$\begin{aligned} \underline{S} &= \int_{\Omega_0} [(\vec{\nabla}_0 \Phi\vec{e})^{-C} : S \cdot \vec{\nabla}_0 \Phi\vec{e} + (\vec{\nabla}_0 \Phi\vec{e})^C : \tfrac{\partial S}{\partial E} : \vec{\nabla}_0 \Phi\vec{e}]\, d\Omega_0 \\ \underline{L} &= \int_{\Omega_0} F^{-C} \cdot \vec{\nabla}_0 \cdot \Phi\vec{e}pJ\, d\Omega_0 \\ \underline{K}_{\alpha\beta} &= \theta \int_{\Omega_0} \nabla_0\vec{\Psi}^C \cdot K^*_{\alpha\beta} \cdot \nabla_0\vec{\Psi}\Delta t\, d\Omega_0 \\ \underset{\sim}{R} &= -\int_{\Gamma_0} \Phi\vec{e} \cdot F^{-1} \cdot \vec{n}_0 J d\Gamma_0 - \int_{\Omega_0} S_e : F^C \cdot \vec{\nabla}_0 \Phi^I \vec{e}\, d\Omega_0 + \int_{\Omega_0} \vec{\nabla} \cdot \Phi\vec{e}pJ\, d\Omega_0 \\ \underset{\sim}{U} &= \int_{\Omega_0} \underset{\sim}{\Psi}(J - J_n)\, d\Omega_0 \\ \underset{\sim}{T}_1 &= \theta \int_{\Omega_0} (K^* \cdot \vec{\nabla}_0 p) \cdot \vec{\nabla}\underset{\sim}{\Psi}\Delta t\, d\Omega_0 \\ \underset{\sim}{T}_2 &= (1-\theta) \int_{\Omega_0} (K^* \cdot \vec{\nabla}_0 p_n) \cdot \vec{\nabla}\underset{\sim}{\Psi}\Delta t\, d\Omega_0 \end{aligned} \tag{72}$$

7 Application to the modelling of heart muscle

The heart consists of two pumps, the right and the left heart, connected to each other in series and anatomically intimately linked together into one organ (Figure 8). The right heart maintains blood flow in the pulmonary circulation, whereas the left heart maintains blood flow in the systemic circulation. The left heart is by far the strongest of both heart pumps. During each heart cycle it develops a pressure of about 16 kPa, which is four to five times the pressure developed by the right heart. Consequently more musculature is developed in the left than in the right ventricular myocardium. The initial stages of cardiac disfunction are found generally in the left ventricle. Because of the functional and clinical importance of the left heart this chapter is mainly devoted to left ventricular modelling, although many aspects could equally well apply to the right ventricle.

The mechanical performance of the left ventricle is the result of a cooperative contractile action of the muscle cells in the left ventricular wall. Therefore, insight into the mechanics at the level of muscle cells is important to understand global left ventricular mechanical performance. For that reason, quantifications of local ventricular wall mechanics have been one of the main concerns in heart research in the past century. This interest was stimulated by the following facts:

- Myocardial wall stress and deformation are some of the primary determinants of myocarcial oxygen consumption.
- Myocardial oxygen supply is dependent upon coronary blood perfusion, which has been shown to depend greatly upon the mechanical state of the myocardical tissue.
- Wall deformation is believed to be the feedback signal that governs myocardial growth. For example, ventricular hypertrophy is the result of excessive loading of the heart.
- Diagnosis of the heart is usually done on the basis of global data of cardiac function. Interpretation of these data in terms of local myocardial disfunction requires a thorough insight into the fundamental principles underlying ventricular mechanics.

Important quantities for the description of local left ventricular mechanics are deformation and stress. At present, local deformation can be measured accurately only at a limited number of sites in the left ventricular wall simultaneously. Reliable measurement of left ventricular wall stress is difficult, because insertion of a force transducer damages the tissue. Because of these experimental limitations, **mechanical models** have been developed in helping to understand left ventricular mechanics. Initially, a simple left ventricular geometry such as a sphere, a cylinder or an ellipsoid, and isotropic linear elastic material properties were used in analytical models. Gradually, more realistic left ventricular geometries and anisotropic nonlinear elastic material properties were introduced, often using the finite element method. Generally these models, predicted maximum stresses (during systole) to occur in the subendocardial (i.e. inner) wall layers *(which is not strange, recalling the solutions for a thick walled cilinder under internal and/or external pressure)*. All models mentioned so far compute stresses and strains from given rheological and geometrical data of the left heart muscle and a given external load (usually the left ventricular pressure). More recent developments allow to account for the influence of intramyocardial coronary blood volume upon the stress distribution in the tissue. In the related models anisotropic contractile material properties, with active stresses depending on time, fiber strain and

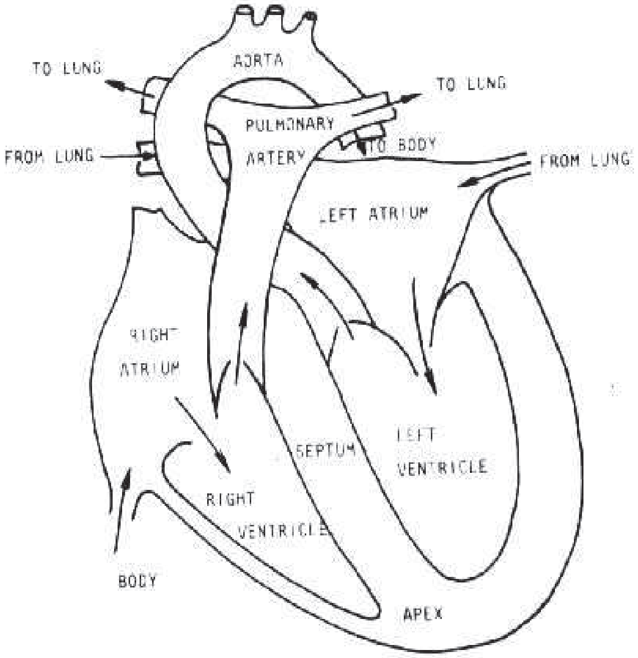

Figure 8: Anatomy and direction of blood flow in the heart

strain rate, were used to describe the mechanics of the systolic left ventricle.

7.1 Poromechanics of the heart muscle

Like most other biological tissues, the heart muscle tissue is a mixture of many different components: muscle fibres, collagen fibres, coronary vessels, coronary blood and interstitial fluid. There are many ways to treat these kinds of complex materials.

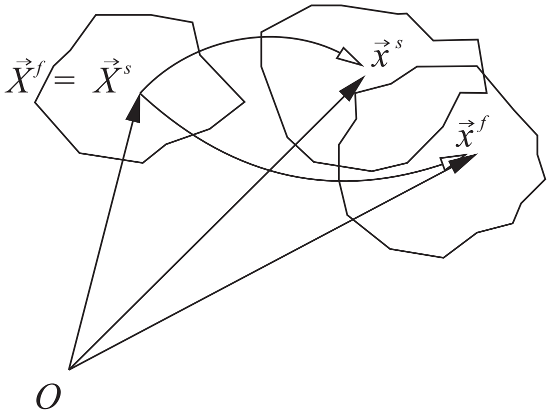

Figure 9: mixture of interacting continua

Assume that in some point *P* in space we want to know the velocity of component α. Normally, some small elementary volume is defined around *P*. The velocities of particles of the component α in that elementary volume can be averaged over this volume and assigned to point *P*, even if in reality this point is occupied by a different component (figure 9). In this way it is possible to define continua that can move through and interact with each other. Theories of this kind are called mixture theories or porous media theories and are also used to describe for instance the mechanical behavior of soil. We will give a global description of two models that were derived for heart muscle. Both models are more or less based on mixture theories. Both theories have been developed in a research cooperation between Eindhoven University of Technology and the University of Maastricht. They will be referred to as the model from Huyghe and the model from Bovendeerd.

7.2 Axisymmetric ventrical model

The tissue is composed of a solid phase and a liquid phase (which is the coronary blood). By introducing an extra variable, which he called the arterio-venous parameter he was able to seperate different coronary microcirculatory components. In this way he could make a distinction between blood in arteries, arterioles, capillaries and venes. In this introductory chapter we ignore this parameter and treat all coronary blood in the same way. For those interested in the model with the spectrum of liquid phases that enables to model the coronary blood flow in more detail we refer to [HOvCH89, HOvC89].

For the time being it is enough to know that it is possible for such a mixture to derive balance equations for the solid, the liquid and for the mixture as a whole. This includes balance of mass, momentum, moment of momentum and energy. These balance equations look very similar to those for one single solid or liquid. The difference is that extra terms are added because the continua interact. For the components, as well as for the interaction terms we need constitutive equations. Together with boundary and initial conditions a solvable set of equations can be derived. With such a mathematical model it is possible to calculate all kinds of local mechanical properties in the tissues, like stresses, strains, pressures and flows. In this course our interest is not the formulation and solution of the balance equations, but our focus is on the constitutive equations for the different components and their interactions.

The first problem we encounter is, that in a mixture we need an adjustment for the definition of the Cauchy stress matrix σ. The stress in the liquid component is described by an intramyocardial pressure p. The stress in the mixture is a full three-dimensional stress matrix σ. The stress in the deformed mixture is best understood as follows. Assume that the solid phase is subjected to the deformation **in the absence of fluid** . The stress σ^s in the solid induced by this deformation and measured per unit bulk surface (= the surface of the total mixture, including the pores) is called effective stress. The word “effective” indicates that this part of the stress is the only part depending directly on deformation. Now we inject fluid at a pressure p into the deformed solid matrix. The pressure p will spread in both the fluid and the solid. So, the total Cauchy stress in the mixture is:

$$\sigma = \sigma^s - pI \tag{73}$$

The negative sign before p arises from the fact that in solid mechanics stress is positive for extension, however in fluid mechanics pressure is positive for compression. A muscle can create an active stress when it contracts. This means that we have to separate the behavior in active and passive behavior. So:

$$\sigma^s = \sigma^p + \sigma^a \tag{74}$$

with σ^p the passive stress and σ^a the active stress.

Passive constitutive behavior

The passive stress matrix σ^p is split into two components, one resulting from an elastic volume change of the myocardial tissue σ^c , the other from a visco-elastic shape change of the myocardial tissue σ^d. The elastic stress σ^c is derived from an isotropic strain energy function. The viscoelastic component σ^d is described in a spectral form of quasi-linear viscoelasticity as proposed by Fung [Fun93].

Because the ventricular wall consists of muscle fibres with different properties in fibre direction than in cross-fibre direction the mechanical behavior is no longer **isotropic**. We have to account for these fibre directions. In the heart muscle the situation is even more complicated. Anatomical studies showed that the fibre direction changes from the endocardium to the epicardium. The material has **inhomogeneous** properties (figure 10). We review some of the consequences of the anisotropy for the mechanical behavior of the heart.

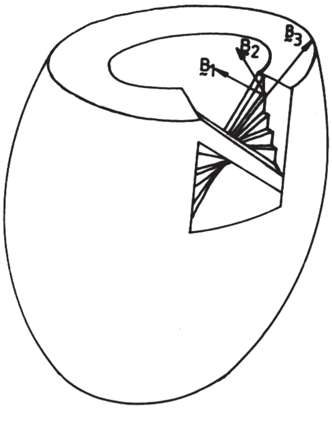

Figure 10: Orthonormal vectors $\vec{B}_1\vec{B}_2,\vec{B}_3$ specifying axes of orthotropy. $\vec{B}_3$ is parrallel to the initial local fibre direction. Vector $\vec{B}_1$ is perpendicular to the wall.

Contractile constitutive behavior

Cardiac muscle is striated across the fibre direction. The sarcomere length is the distance between the striations, and may be used as an objective measure of muscle fibre length during contraction. In experiments it has been found that active stress, generated by cardiac muscle cells, depends on time, sarcomere length and velocity of shortening of the sarcomeres. The active stress generated by the sarcomeres is directed parallel to the fibre orientation. This can be described with phenomenological Hill-type models or with a structural model according to Huxley. These models will be treated in the physiological part of this course.

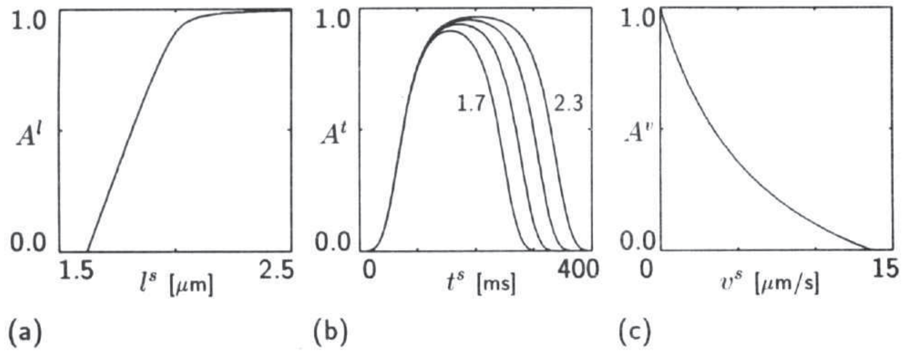

Figure 11: Active material behavior as assumed in the model: (a) length dependence of active stress, (b) time dependence of active stress for sarcomere lengths of 1.7, 1.9, 2.1 and 2.3 μm, (c) stress-velocity relation

The behavior of the liquid

So far we have only discussed the mechanical behavior of the solid. In order to simulate the redistribution of coronary blood in the ventricular wall during deformation, the liquid phase is allowed to flow relative to the solid. It will be clear that there is an interaction between the solid and the liquid. The solid will resist the liquid from flowing. This is described by Darcy's law, i.e. the liquid flow relative to the solid is proportional to the local intramyocardial pressure gradient:

$$\vec{q} = K \nabla p \tag{75}$$

where $\vec{q}$ is the fluid flow vector, representing the difference between the solid velocity and the fluid velocity, K is the permeability matrix and is a material property, depending on pore size, but also on the fluid viscosity. Even with this fairly crude approximation of the liquid phase, important aspects of the influence of coronary blood volume on ventricular mechanics can be demonstrated.

It is not difficult to understand that K also depends on the deformation of the solid. If the solid is compressed the pores will become smaller and thus it will be more difficult for the liquid to move through the solid. This means that K must become smaller:

$$K = \left(\frac{J-1}{\Phi^B} + 1 \right)^2 K^0 \tag{76}$$

K^0 is the permeability of the undeformed tissue. Φ^B is the averaged porosity, i.e. the fluid volume divided by the total volume of the mixture. $J = det(F)$ is the determinant of the deformation matrix, representing the volume change of the material.

The theory described above leads to a set of nonlinear partial differential equations. It is not possible to find closed form solutions for these equations. However, it is possible to solve them numerically. A suitable procedure for this is to use the finite element method. It is not within the scope of this course to discuss this solution process. Huyghe (1992) [HAvCR92] made for his model the assumption that the geometry and the displacements of the left ventricle are axisymmetric. This axisymmetric porous medium finite element model allows for finite torsion about the axis of symmetry and considers redistribution of intracoronary blood in the myocardial wall during deformation. Also, transmural variation of fiber angle is taken into account (10).

The geometry of the left ventricle in an assumed stress-free reference state is derived from eleven cross-sections of a canine diastolic heart obtained by means of X-ray tomography. An average endocardial and epicardial radius are computed for each cross-section, resulting in the geometry shown in figure 12a . The geometry is subdivided in thirty eight-node ring-shaped elements. Quadratic shape functions are used for the cross-sectional geometry, the transmural course of fibre direction, and the radial, axial and circumferential displacements. The shape functions for the isoparametric pressure field are linear. Integration of the volume and surface integrals are obtained by means of 3x3 and three-point Gauss integration, respectively. An implicit-explicit one-step Crank-Nicholson time integration scheme is used.

The upper finite elements (10, 11, 12) in figure 12 represent the annulus fibrosis and are non-contracting elements with a circumferential fibre orientation. For reasons of simplicity a homogeneous distribution of the initial sarcomere length is chosen with $L_s = 1.9\mu m$. At the upper end of the annulus fibrosis, only radial displacement is allowed. The intramyocardial pressure at the nodes of the epicardium (outside wall) are set equal to the pressure in the venous epicardial vessels. At the endocardial surface the intramyocardial pressure is free, whereas no blood is allowed to cross this surface. At the endocardial side of elements 1-9 a uniform intraventricular pressure PLV is applied as an external load (indicated by the arrows). The loads exerted by the papillary muscles and by the pericardium are neglected.

Figure 13 shows a typical course of the electro cardiagram (ECG), the intraventricular pressure PLV and the aortic flow during a cardiac cycle. It is customary to divide the

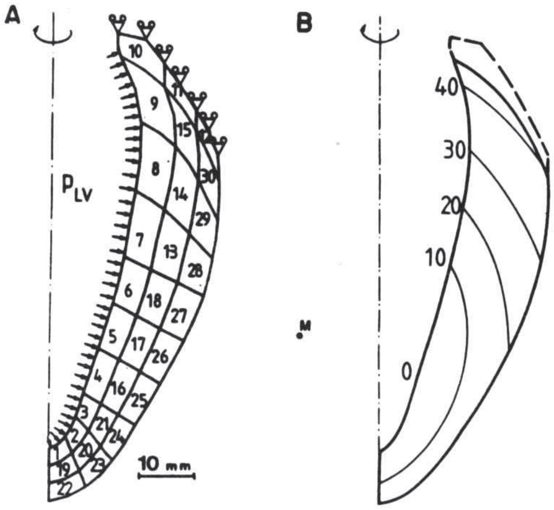

Figure 12: Longitudinal cross-section of axisymmetrix finite element model: (a) finite element mesh; (b) sequence of onset of contraction (simulated to radiate from point M, time in ms).

cardiac cycle into two phases: systole and diastole. Roughly speaking they correspond to contraction and relaxation of the ventricle. Systole can be subdivided into isovolumic contraction, ventricular ejection and isovolumic relaxation. In diastole any active contribution to wall stress is absent by definition. In this phase ventricular filling occurs. Contraction of the heart muscle is caused by a depolarization wave. A typical pattern of the motion of the depolarization wave from the apical subendocardial region to the basal epicardial region is shown in figure 12. The ventricular wall is completely activated after about 50 ms.

In the simulation of a cardiac cycle typically time steps of 5 ms are used. A simulation starts with the diastolic filling phase, during which intraventricular (cavity) pressure PLV is prescribed to increase from 0 kPa to 1 kPa in 150 ms. At this moment the depolarization wave starts and active stress is generated immediately after depolarization. The diastolic phase ends with the closure of the mitral valve, which is assumed to occur at $t = 200ms$. During the following isovolumic contraction phase, cavity pressure is determined iteratively until the cavity volume equals its end-diastolic value. As soon as the cavity pressure exceeds a prescribed aortic pressure level of 10 kPa, the ejection phase starts. During the ejection phase, cavity pressure is determined iteratively until the aortic flow matches the rate of decrease of cavity volume. The ejection phase ends as soon as the calculated flow reverses. The isovolumic relaxation phase is simulated analogously to the isovolumic contraction phase. The simulation of a cycle

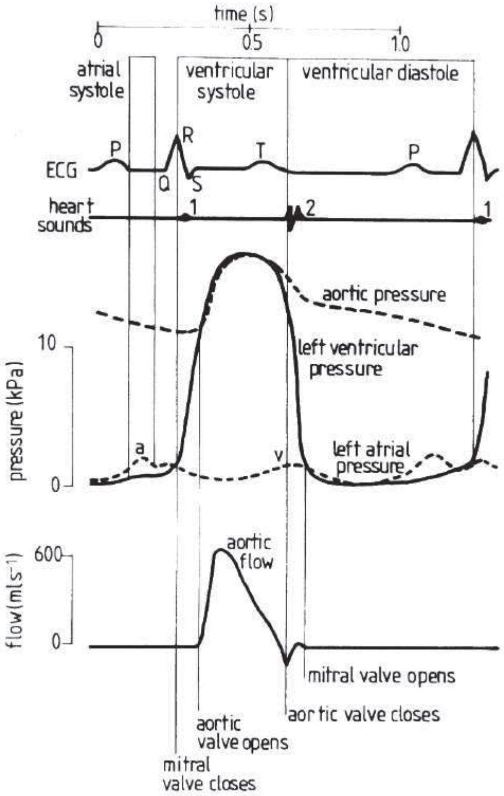

Figure 13: Illustration of the events in the left side of the human heart during a cardiac cycle

ends at a prescribed time of 600 ms.

The hemodynamic coupling of the left ventricle to the aorta is described by a linear three-element aortic input impedance model consisting of an aortic characteristic resistance, placed in series with an arterial compliance which is in parallel to a peripherical resistance.

First, some results are considered of a simulation where the left ventricle was loaded with the end-diastolic pressure (1 kPa), and then three consecutive beats were initiated. The last one of these three cycles was close to the stationary situation. At the beginning of the passive loading a uniform intramyocardial pressure of 0.5 kPa was chosen. The epicardial value of the intramyocardial pressure was kept constant at 0.5 kPa during the whole simulation.

Figure 15 shows a comparison of epicardial deformation parameters as assessed by the above simulation with those obtained in animal experiments by [AVR82]. These investigators measured three epicardial strain components: 1) the circumferential natural strain ε_c, which is the natural logarithm of the ratio of the current radial coordinate to the initial radial coordinate; 2) the axial natural strain ε_z, which is the natural strain in the direction initially perpendicular to the circumference and tangential to the epicardial surface; and 3) the shear angle γ, which is the change of the angle between the circumferential direction and a line on the epicardium initially perpendicular to the circumference. The latter quantity is a measure of torsion of the ventricle. Figure 15 shows a good qualitative agreement between model results and experimental results. Maximal torsion is reached approximately at the end of ejection. Figure 16 shows the distribution of end-systolic values of the three principal strains across the ventricular wall at the interface of the elements 6, 18, 27 and the elements 7, 13, 28. For the sake of comparison with experimental data the principal strains are computed relative to the end-diastolic state.

Heineman and Grayson [HG85] found in aximal experiments that peak systolic intramyocardial pressure, expressed as a ratio relative to peak systolic left ventricular pressure, was linearly distributed across the ventricular wall (figure 17) near the equator region. This is in accordance with findings from the porous medium model. When redistribution of intracoronary blood is suppressed in the model, resulting in incompressible tissue behaviour, a substantial deviation from this behaviour is computed in the equatorial endocardial region. This suggests that redistribution of intracoronary blood in the ventricular wall might play an important role in reducing subendocardial tissue pressure. In addition to the above, due to the porosity effect, the porous medium model is able to simulate the dependence of the ventricular compliance on the intracoronary blood volume as experimentally measured.

Figure 14: Color coded plots of the intramyocardial pressure (top), sarcomere length (middle) and rotation angle (bottom) of the axisymmetric simulation of the beating left ventricle (Fig. 12). The successive states are from left to right, the end of isovolumic contraction, of ejection, of isovolumic relaxation and of diastole.[HAvCR92]

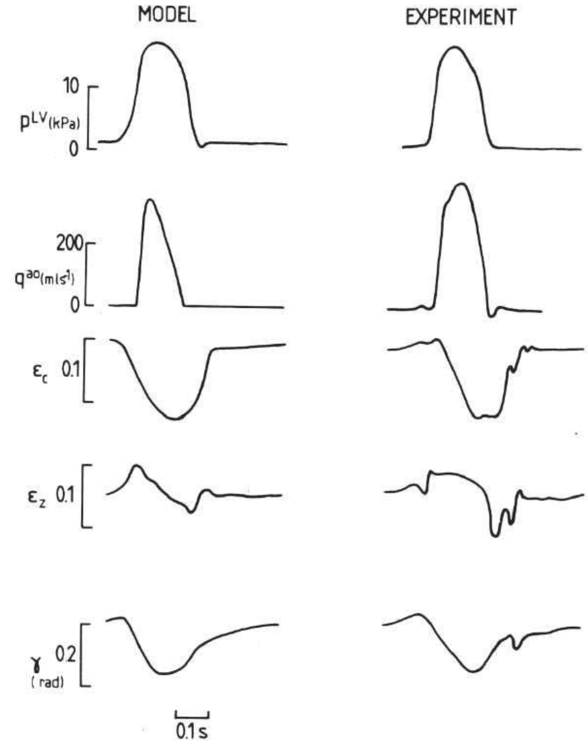

Figure 15: Comparison between results of numerical simulation and experimental data. Model values of $\varepsilon_c, \varepsilon_z$ and γ pertain to epicardial node common to elements 27 and 28 of figure 12 (q^{ao} = aortic flow). Experimental data measured by [AVR82].

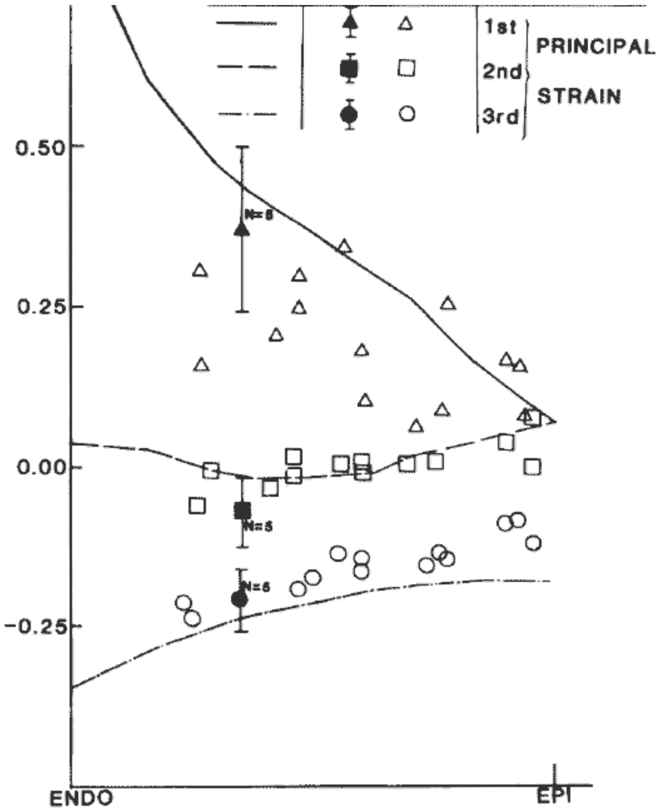

Figure 16: Transmural distribution of end-systolic principal strains as predicted by numerical simulation and as measured by (Waldman et al., 1985).

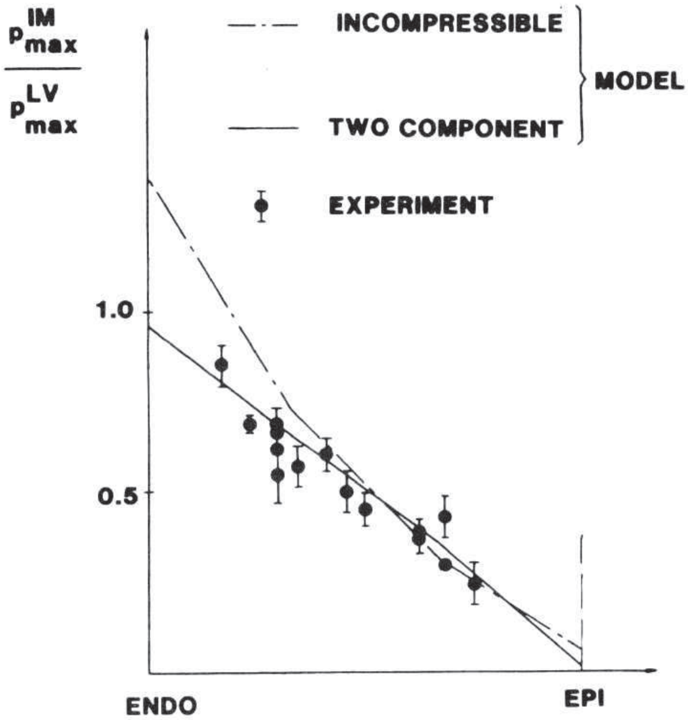

Figure 17: Transmural course of normalized peak intramyocardial pressure near equatorial region as predicted by numerical simulation and as measured by [HG85].

Besides fluid/solid interaction, viscoelasticity contributes to the time dependent behaviour of the passive two-phase mixture. Demer and Yin [DY83] measured biaxial stress-strain relationships of passive myocardial specimens and found large hysteris loops, the size of which was poorly dependent on the rate of loading. The question can be raised whether the observed hysteresis loops are due to viscoelasticity or to poroelasticity. Using the finite element model in which the quasi-linear law has been substituted by its elastic response, the loading/unloading experiments of Demer and Yin have been simulated, while allowing free exchange of fluid between the coronary bed of the specimen and the bathing solution. The resulting stress-strain relationships exhibit hardly any hysteresis loops.

In order to illustrate the effect of viscoelasticity clearly, the passive left ventricular model is repeatedly loaded and unloaded while setting the permeability equal to zero. The model material is then incompressible and not biphasic. On the pressure-volume plot (figure 18) the loading curve is different from the unloading curve. As the cycle of loading and unloading is repeated, the pressure-volume curve tends towards a closed hysteresis loop starting at a higher zero-pressure volume than the original zero-pressure volume. Using faster loading rates shifts the curves towards the pressure axis. After unloading the ventricle exhibits the phenomenon of residual stress (figure 19), although the ventricle was initially stress-free. The subendocardial layers are under compression and subepicardial layers are under tensile stress. The phenomenon of residual stress is consistent with the experimental observation of opening angles seen when the heart is slit open. When the loading cycle is repeated, each cycle yields a distribution of passive myocardial stress which is more uniform than the previous cycle.

8 Introduction to the second application

In this theory the various solid and fluid components of the tissue are modelled as interacting continua. An important fluid component in biological tissue is blood. It is responsible for the nutrition and drainage processes that are essential for the tissue. Blood flows through a hierarchical system of blood vessels: the vascular tree (Fig.20). This tree consists of one or a few large arterial vessels from which smaller vessels bifurcate (Fig.21) and diverge into numerous capillaries which assemble to converging venous vessels. Because of this hierarchical architecture blood flow cannot be adequately described by biphasic mixture theory: the state of the blood strongly depends on the position in the hierarchy. For example, the velocity and pressure of the capillary blood are much lower than of the arterial blood. The pressure difference between arterial and venous vessels is essential as the driving force for the blood flow. Huyghe et al. (1989) [HOvCH89, HOvC89] developed an extended form of Darcy's equation in which this dependency of the fluid flow on hierarchical position was included. In addition the hydraulic permeability matrices are shown to be related quantitatively to

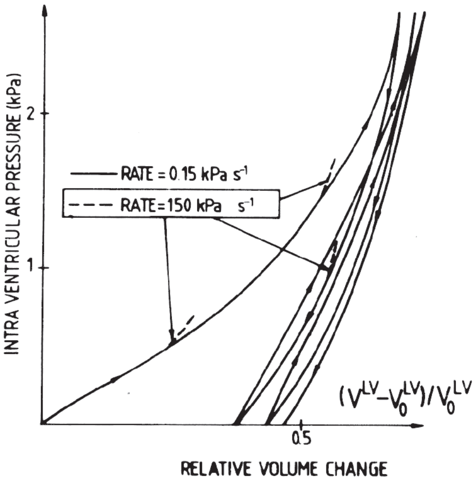

Figure 18: Simulated pressure-volume relationship of the viscoelastic left ventricle at different rates of pressure change. At three sites a departure is shown at a tenfold rate

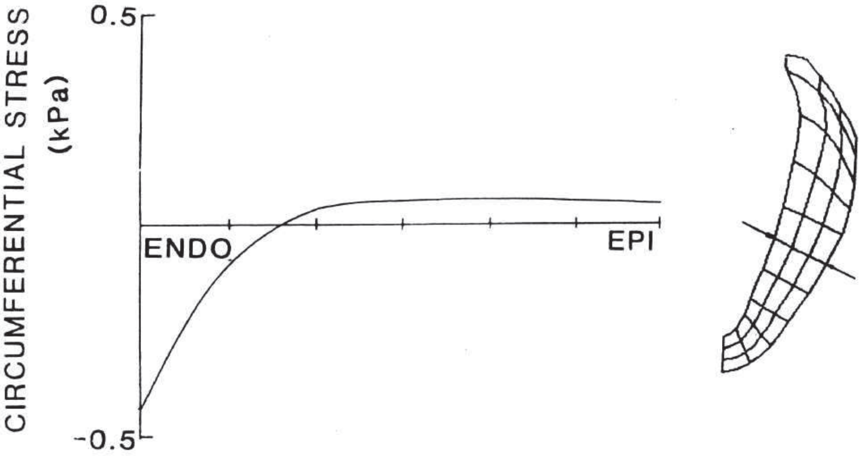

Figure 19: Transmural residual circumferential stress distribution in the unloaded viscoelastic ventricular model after the first loading cycle at the indicated equatorial cross-section

the microstructure of the vessel tree of the tissue. They verified this relationship for Newtonian flow through a rigid vascular tree [HOvCH89, HOvC89, VHJ$^+$97]. Because in biological tissue alterations in blood perfusion can occur due to deformations of the tissue [HS90], the focus of this chapter is to illustrate the concepts developed in [HOvCH89] into a finite deformation theory of saturated porous media. Aifantis (1977) [Aif77] introduced the concept of multiporosity for deforming media that are characterized by several distinct families of flow paths. A special case of this concept, in which only two degrees of diffusivity were included, was applied to fissured rock formations, in which most of the fluid volume is located in the low hydraulic permeability pores of the rock, and most of the hydraulic permeability is associated with the fissures [WA82]. Two different types of permeabilities are included in these models : one is an intracompartmental hydraulic permeability involving flow within a compartment, the other is intercompartmental hydraulic permeability involving flow between compartments. In the present approach mixed terms between intra- and intercompartmental hydraulic permeability occur in addition to those occuring in Aifantis [Aif77]. These mixed terms account for anisotropy of the interface between compartments. In other words, Aifantis [Aif77] implicitly assume the interfaces to be isotropically oriented. The tissue is modelled as a mixture of one solid and one fluid where the fluid represents the blood. The fluid is subdivided into a number of compartments, each of which represents the blood on a different hierarchical position in the vascular tree. Blood flow through the vasculature is described as communication between the fluid compartments, which corresponds with the physiological definition of perfusion: the volume of blood passing a given level in the vascular hierarchy per unit of time and per volume of tissue. Vessel walls, modelled as an elastic solid-fluid interface, are included as a local contribution of the pressure difference between solid and fluid to the mixture's elastic energy. Although this mixture description is specifically developed for biological materials, its applicability to technical materials is not excluded. In the derivation of the mixture model conservation laws of mass and momentum have been formulated and corresponding constitutive behaviour has been derived from constitutive theory [VHJH96b]. Elsewhere the same finite deformation multiporosity equations are derived through averaging of a Poiseuille-type pressure flow relationship at the level of the individual blood vessel [HvC95a, HvC95b]. An integrated finite element description of the total mixture model has been developed and implemented in the DIANA software package [dBKNdW85]. The implementation was subjected to several test procedures, one of which was comparison of the finite element solution with the analytical solution for a confined compression test [VHD$^+$97]. As an illustration of the possibilities of the model a simulation of contraction of a perfused skeletal muscle is performed. Further examples of computations are found in the literature, including 3D analyses [VHJH96a], comparison with animal experiments [VHS$^+$97] and a model study [VHvD$^+$98].

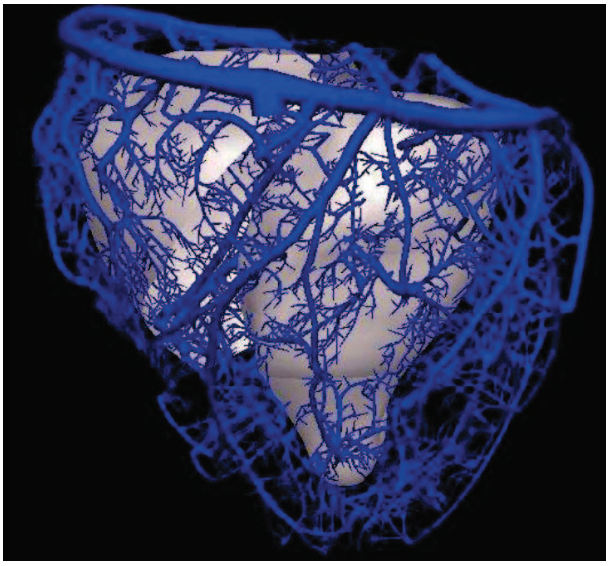

Figure 20: The mayor venous vessels of a human heart. The venous system was injected with a monomer solution too viscous to penetrate the venules. The monomer was allowed to polymerise in the larger veins and tissue was digested away. Note the tree-like structure.

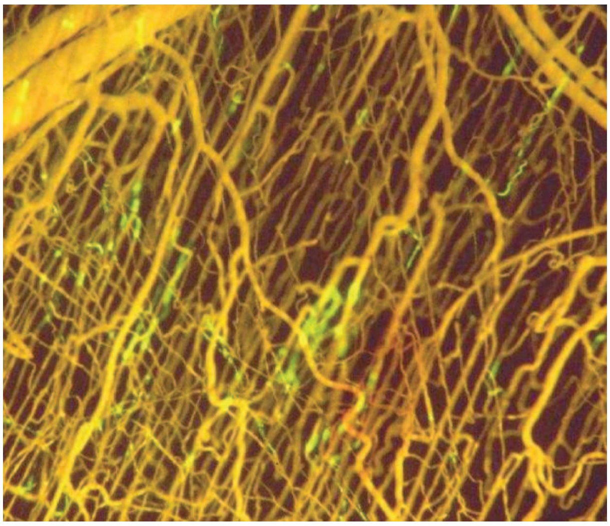

Figure 21: Cardiac capillary vessels. The vessels are mostly parallel to the muscle fibre directions.

9 Conservation Laws

In technical literature we find porous media theories dealing with solids saturated with different fluid constituents [BD83]. Bowen (1980) [Bow80] has derived equations from mixture theory for ν incompressible immiscible fluids saturating one incompressible solid. The equations of conservation of mass are formulated for each constituent and in case of intrinsic incompressibility of each constituent, their quasi-static local form can be denoted as:

$$\frac{\partial \phi^{\alpha}}{\partial t} + \nabla \cdot (\phi \alpha v^{\alpha}) = \theta^{\alpha} \quad , \quad \alpha = 1, ..., \nu \tag{77}$$

in which θ^{α} is the volume transfer from constituent α to the other constituents. Assuming no volume loads and no inertia, the balance of momentum reads :

$$\nabla \cdot \sigma^{\alpha} + \pi^{\alpha} = 0 \quad , \quad \alpha = 1, ..., \nu \tag{78}$$

where ϕ^{α} is the volume fraction, v^{α} the velocity, σ^{α} the Cauchy stress tensor and π^{α} are the momentum interaction of constituent α with other constituents. The exponent α refers to the constituent number and t is time. Balance of mass for the total mixture requires:

$$\sum_{\alpha} \theta^{\alpha} = 0. \tag{79}$$

Likewise for the balance of momentum:

$$\sum_{\alpha} \pi^{\alpha} = \mathbf{0}. \tag{80}$$

Furthermore no moment of momentum interaction between the constituents is assumed, so that σ^{α} is symmetric.

A hierarchical mixture can be thought of to consist of one solid constituent and a fluid constituent that is divided into a continuous series of fluid compartments. Each fluid compartment resides on a specific position in the hierarchy of pores of the solid. The fluid in a compartment flows spatially through the solid (spatial flow) and communicates with compartments on neighbouring hierarchical positions (hierarchical flow). The position in the hierarchy is quantified by a dimensionless parameter x_0, which is assumed to run from 0 to 1, and the communication between the fluid compartments is described by the fluid volume interaction term θ^f appearing in Eq.(77). A fluid compartment defined by the hierarchical range $[x_0, x_0 + dx_0]$ has a volume fraction $\tilde{\phi}^f dx_0$ in which $\tilde{\phi}^f$ represents the fluid volume fraction per unit hierarchical parameter x_0. Generally in this paper a tilde will be used to indicate that a quantity depends on x_0 and, if the quantity is volume specific, is defined per unit x_0. The exponents s and f refer to solid and fluid, respectively. The mass balance for one fluid compartment is:

$$\frac{\partial \tilde{\phi}^f}{\partial t} dx_0 + \nabla \cdot \left(\tilde{\phi}^f \tilde{v}^f \right) dx_0 = \tilde{\phi}^f_{(x_0)} \tilde{v}^f_{0(x_0)} - \tilde{\phi}^f_{(x_0+dx_0)} \tilde{v}^f_{0(x_0+dx_0)} \tag{81}$$

in which the right hand side represents the volume interaction with the neighbouring compartments. $\tilde{v}_0^f$ is a measure of the rate at which fluid flows from one compartment to the next, and is defined as the material time derivative of x_0 with respect to the fluid:

$$\tilde{v}_0^f = \frac{D^f x_0}{Dt}. \tag{82}$$

It can be shown that $\tilde{\phi}^f \tilde{v}_0^f$ corresponds to the traditional, physiological definition of regional blood perfusion [Guy86, HOvCH89]. Dividing Eq. (81) by dx_0 yields for infinitesimal dx_0 the local fluid mass balance:

$$\frac{\partial \tilde{\phi}^f}{\partial t} + \nabla \cdot \left(\tilde{\phi}^f \tilde{v}^f \right) = \tilde{\theta}^f = - \frac{\partial \left(\tilde{\phi}^f \tilde{v}_0^f \right)}{\partial x_0}. \tag{83}$$

Assuming no mass interaction between solid and fluid, the mass balance for the total mixture (79) is rewritten:

$$\theta^s = \int_0^1 \tilde{\theta}^f dx_0 = 0. \tag{84}$$

Because the actual hierarchical fluid volume fraction $\tilde{\phi}^f$ is defined per unit x_0, saturation of the mixture is expressed as:

$$\phi^s + \int_0^1 \tilde{\phi}^f dx_0 = \phi^s + \phi^f = 1, \tag{85}$$

which can be used in combination with Eqs.(83) and (84) to rewrite solid, fluid and total mass conservation as:

$$-\frac{\partial \phi^f}{\partial t} + \nabla \cdot \left(\left(1 - \phi^f\right) v^s \right) = 0 \tag{86}$$

$$\frac{\partial \tilde{\phi}^f}{\partial t} + {}_4\nabla \cdot \left(\tilde{\phi}^f {}_4\tilde{v}^f \right) = 0 \tag{87}$$

$$\nabla \cdot \left(\left(1 - \phi^f\right) v^s \right) + \int_0^1 \left({}_4\nabla \cdot \left(\tilde{\phi}^f {}_4\tilde{v}^f \right) \right) dx_0 = 0, \tag{88}$$

where ${}_4\nabla$ is a four-dimensional operator and ${}_4\tilde{v}^f$ a four-dimensional vector:

$${}_4\nabla = \begin{bmatrix} \frac{\partial}{\partial x_0} \\ \nabla \end{bmatrix}, \quad {}_4\tilde{v}^f = \begin{bmatrix} \tilde{v}_0^f \\ \tilde{v}^f \end{bmatrix}. \tag{89}$$

Because the fluid related quantities depend on x_0, the momentum balance of the total mixture is written as:

$$\nabla\cdot\sigma^s+\int_0^1\nabla\cdot\tilde{\sigma}^f dx_0=0 \tag{90}$$

where the balance condition for momentum interaction, Eq.(80), has been used:

$$\pi^s+\int_0^1\tilde{\pi}^f dx_0=0. \tag{91}$$

10 Constitutive Laws

In the derivation of requirements for the constitutive behaviour the first and second laws of thermodynamics are used. The first law, conservation of total energy, reads under quasi-static conditions - for constituent α of a unit volume of mixture :

$$\dot{U}^\alpha=\dot{W}^\alpha+\dot{Q}^\alpha+\dot{E}^\alpha \tag{92}$$

where $\dot{U}^\alpha$ is the total internal energy, $\dot{W}^\alpha$ is the external work, $\dot{Q}^\alpha$ is the heat supply of phase α and E^α is the energy gain of α due to interaction. The dots above the variables denote their material time derivatives. Assuming intrinsic incompressibility and quasi-stationarity for each constituent, Eq.(92) can be written for the solid and fluid constituents in a volume V of mixture with surrounding surface A:

$$\begin{aligned}\frac{\partial}{\partial t}\left(\int_V\phi^sU^sdV\right)+\int_A\phi^sU^sv^s\cdot\mathbf{n}dA=&\int_A v^s\cdot\sigma^s\cdot\mathbf{n}dA\\&+\int_V\phi^sr^sdV+\int_A\mathbf{h}^s\cdot\mathbf{n}dA+\int_V\varepsilon^sdV+\int_V\pi\cdot v^sdV,\end{aligned} \tag{93}$$

$$\begin{aligned}&\frac{\partial}{\partial t}\left(\int_V\tilde{\phi}^f\tilde{U}^fdV\right)+\int_A\tilde{\phi}^f\tilde{U}^f\tilde{v}^f\cdot\mathbf{n}dA+\int_V\frac{\partial}{\partial x_0}\left(\tilde{\phi}^f\tilde{U}^f\tilde{v}_0^f\right)dV\\&\quad=\int_A\tilde{v}^f\cdot\tilde{\sigma}^f\cdot\mathbf{n}dA+\int_V\frac{\partial}{\partial x_0}\left(\tilde{v}_0^f\tilde{\sigma}_0^f\right)dV+\int_V\tilde{\phi}^f\tilde{r}^fdV+\int_A\tilde{\mathbf{h}}^f\cdot\mathbf{n}dA\\&\qquad+\int_V\frac{\partial}{\partial x_0}\left(\tilde{h}_0^f\right)dV+\int_V\tilde{\varepsilon}^fdV+\int_V\tilde{\pi}^f\cdot\tilde{v}^fdV,\end{aligned} \tag{94}$$

where r^α is the internal heat supply, h^α the external heat supply and ε^α the direct energy supply of constituent α due to interaction. $\tilde{\sigma}_0^f$ is the fluid stress at the interface between neighbouring hierarchical levels and h_0^f the heat supply between neighbouring hierarchical levels. Note that Eq.(94) is expressed per unit of x_0 and that internal energy variation of the fluid due to volume interaction is included in the third term. Applying Gauss' theorem gives for the local conservation of total energy of the solid and the fluid:

$$\frac{\partial}{\partial t}\left(\phi 3U^s\right) = -\nabla\cdot\left(\phi^s U^s v^s\right) + \nabla\cdot\left(v^s\cdot\sigma^s\right) + \phi^s r^s \\ + \nabla\cdot\mathbf{h}^s + \varepsilon^s + \left(\pi^s\cdot v^s\right), \quad (95)$$

$$\frac{\partial}{\partial t}\left(\tilde{\phi}^f\tilde{U}^f\right) = -\nabla\cdot\left(\tilde{\phi}^f\tilde{U}^f\tilde{v}^f\right) - \frac{\partial}{\partial x_0}\left(\tilde{\phi}^f\tilde{U}^f\tilde{v}_0^f\right) + \nabla\cdot\left(\tilde{v}^f\cdot\tilde{\sigma}^f\right) \\ + \frac{\partial}{\partial x_0}\left(\tilde{v}_0^f\tilde{\sigma}_0^f\right) + \tilde{\phi}^f\tilde{r}^f + \nabla\cdot\tilde{\mathbf{h}}^f + \frac{\partial}{\partial x_0}\left(\tilde{h}_0^f\right) + \tilde{\varepsilon}^f + \tilde{\pi}^s\cdot\tilde{v}^f, \quad (96)$$

which is rewritten using the material time derivative of U, and the local mass and momentum balances Eqs.(86) and (87):

$$\phi^s\frac{D^sU^s}{Dt} = \sigma^s : \left(\nabla v^s\right) + \phi^s r^s + \nabla\cdot\mathbf{h}^s + \varepsilon^s, \quad (97)$$

$$\tilde{\phi}^f\frac{D^f\tilde{U}^f}{Dt} \\ = \tilde{\sigma}^f : \left(\nabla\tilde{v}^f\right) + \frac{\partial}{\partial x_0}\left(\tilde{\sigma}_0^f\tilde{v}_0^f\right) + \tilde{\phi}^f\tilde{r}^f + {}_4\nabla\cdot{}_4\tilde{h}^f + \tilde{\varepsilon}^f. \quad (98)$$

In Eq.(98) we made use of the four-dimensional gradient operator ${}_4\nabla$ and fluid velocity ${}_4\tilde{v}^f$ (Eq.(89)) and the analogously defined external heat supply ${}_4\tilde{\mathbf{h}}^f$:

$${}_4\tilde{h}^f = \begin{bmatrix} \tilde{h}_0^f \\ \tilde{h}^f \end{bmatrix}. \quad (99)$$

The local balance condition of the energy interaction of the mixture requires that no energy is created by the interaction:

$$\varepsilon^s + \pi^s\cdot v^s + \int_0^1\left(\tilde{\varepsilon}^f + \tilde{\pi}^f\cdot\tilde{v}^f\right) = 0. \quad (100)$$

The second law of thermodynamics, the entropy inequality, is introduced:

$$dS \geq \frac{dQ}{T} \quad (101)$$

which relates the change of entropy of the mixture, dS, to the supplied heat dQ at a temperature T. For a volume V of mixture with surrounding surface A and constant temperature T in each constituent this is written as:

$$
\begin{aligned}
\frac{\partial}{\partial t}\left(\int_V \phi^s S^s dV\right) + \int_A \phi^s S^s v^s \cdot n dA + \int_0^1 \Bigg[\frac{\partial}{\partial t}\left(\int_V \tilde{\phi}^f \tilde{S}^f dV\right) \\
+ \int_A \tilde{\phi}^f \tilde{S}^f \tilde{v}^f \cdot n dA + \int_V \frac{\partial}{\partial x_0}\left(\tilde{\phi}^f \tilde{S}^f \tilde{v}_0^f\right) dV\Bigg] dx_0 \\
\geq \int_V \frac{\phi^s r^s}{T} dV + \int_A \frac{h^s \cdot n}{T} dA \\
+ \int_0^1 \left[\int_V \frac{\tilde{\phi}^f \tilde{r}^f}{T} + \int_A \frac{\tilde{h}^f \cdot n}{T} dA + \int_V \frac{\partial}{\partial x_0}\left(\frac{\tilde{h}_0^f}{T}\right) dV\right] dx_0. \qquad (102)
\end{aligned}
$$

By applying Gauss' theorem and making use of the material time derivative of S, the local form of Eq.(102) can be written as:

$$
\phi^s \frac{D^s S^s}{Dt} + \int_0^1 \left(\tilde{\phi}^f \frac{D^f \tilde{S}^f}{Dt}\right) dx_0 \geq \frac{1}{T}\left(\phi^s r^s + \nabla \cdot h^s + \int_0^1 \left(\tilde{\phi}^f \tilde{r}^f + {}_4\nabla_4 \tilde{h}^f\right) dx_0\right). \qquad (103)
$$

Substituting the local energy equations for solid and fluid, Eqs.(97) and (98), into the local entropy inequality, Eq.(103), yields:

$$
\begin{aligned}
\phi^s \frac{D^s S^s}{Dt} + \int_0^1 \left(\tilde{\phi}^f \frac{D^f \tilde{S}^f}{Dt}\right) dx_0 \geq \frac{1}{T}\Bigg(\phi^s \frac{D^s U^S}{Dt} - \sigma^s : (\nabla v^s) + \pi^s \cdot v^s \\
+ \int_0^1 \left[\tilde{\phi}^f \frac{D^f \tilde{U}^f}{Dt} - \tilde{\sigma}^f : \left(\nabla \tilde{v}^f\right) - \frac{\partial}{\partial x_0}\left(\tilde{\sigma}_0^f \tilde{v}_0^f\right) + \tilde{\pi}^f \cdot \tilde{v}^f\right] dx_0\Bigg) \qquad (104)
\end{aligned}
$$

in which the total energy interaction $\varepsilon^s + \int_0^1 \tilde{\varepsilon}^f dx_0$ was eliminated by means of Eq.(100). Introducing Helmholtz' free energy $F = U - TS$ for each constituent, and substituting momentum balance Eq.(90) yields:

$$
\begin{aligned}
\frac{1}{T}\Bigg(-\phi^s \frac{D^s F^s}{Dt} + \sigma^s : (\nabla v^s) + v^s \cdot (\nabla \cdot \sigma^s) + \int_0^1 \Bigg[-\tilde{\phi}^f \frac{D^f \tilde{F}^s}{Dt} \\
+ \sigma^f : \left(\nabla \tilde{v}^f\right) + \tilde{v}^f \cdot \left(\nabla \cdot \tilde{\sigma}^f\right) + \frac{\partial}{\partial x_0}\left(\tilde{\sigma}_0^f \tilde{v}_0^f\right)\Bigg] dx_0\Bigg) \geq 0. \qquad (105)
\end{aligned}
$$

Expressing Eq.(105) per unit of undeformed volume of mixture and transforming the material time derivative of F^f yields:

$$
\begin{aligned}
-J\phi^s \frac{D^s F^s}{Dt} + J\nabla \cdot (\sigma^s \cdot v^s) + \int_0^1 \Bigg[-J\tilde{\phi}^f \frac{D^s \tilde{F}^f}{Dt} \\
J_4\nabla \cdot \left({}_4\tilde{\sigma}^f \cdot {}_4\tilde{v}^f\right) - J\tilde{\phi}^f \left({}_4\tilde{v}^f - {}_4v^s\right) \cdot {}_4\tilde{\nabla}\tilde{F}^f\Bigg] dx_0 \geq 0. \qquad (106)
\end{aligned}
$$

For compactness of notation, the four-dimensional fluid stress tensor ${}_4\tilde{\sigma}^f$ and solid velocity vector ${}_4v^s$ have been used, which is written in matrix notation:

$$ {}_4\tilde{\sigma}^f = \begin{bmatrix} \tilde{\sigma}_0^f & 0 \\ 0 & \tilde{\sigma}^f \end{bmatrix} \quad ; \quad {}_4v^s = \begin{bmatrix} 0 \\ v^s \end{bmatrix}. \tag{107} $$

Again rewriting the material time derivatives of F gives:

$$ \begin{aligned} -\frac{D^s J\phi^s F^S}{Dt} + F^s \frac{D^s F\phi^s}{Dt} + F\nabla\cdot(\sigma^s\cdot v^s) + \int_0^1 \Bigg[-\frac{D^s G\tilde{\phi}^f \tilde{F}^f}{Dt} \\ + \tilde{F}^f \frac{D^s J\tilde{\phi}^f}{Dt} - J\tilde{\phi}^f \left({}_4\tilde{v}^f - {}_4v^s\right)\cdot{}_4\nabla\tilde{F}^f + J_4\nabla\cdot\left({}_4\tilde{\sigma}^f\cdot{}_4\tilde{v}^f\right)\Bigg] dx_0 \geq 0. \end{aligned} \tag{108} $$

Because of incompressibility of the solid, $\frac{D^s(J\phi^s)}{Dt}$. Substituting the Lagrangian form of the equation of conservation of fluid mass (Eq.(87)):

$$ \frac{D^s\left(J\tilde{\phi}^f\right)}{Dt} + J_4\nabla\cdot\left(\tilde{\phi}^f\left({}_4v^f - {}_4v^s\right)\right) = 0 \tag{109} $$

in Eq.(108) yields:

$$ \begin{aligned} \int_0^1 \Bigg[-\frac{D^s\tilde{W}}{Dt} + J\nabla\cdot(\sigma^s\cdot v^s) - \tilde{F}^f J_4\nabla\left(\tilde{\phi}\left({}_4\tilde{v}^f - {}_4v^s\right)\right) \\ -F\tilde{\phi}^f\left({}_4\tilde{v}^f - {}_4v^s\right)\cdot{}_4\nabla\tilde{F}^f + J_4\nabla\cdot\left({}_4\tilde{\sigma}^f\cdot{}_4\tilde{v}^f\right)\Bigg] dx_0 \geq 0, \end{aligned} \tag{110} $$

where the strain energy function $\tilde{W} = J\phi^s F^s + J\tilde{\phi}^f\tilde{F}^f$ has been introduced. By using the total stress defined as $\sigma = \sigma^s + \int_0^1 \tilde{\sigma}^f dx_0$, Eq.(110) can be written as:

$$ \begin{aligned} J\sigma : (\nabla v^s) + \int_0^1 \Bigg[-\frac{D^s\tilde{W}}{Dt} - J_4\nabla\cdot\left(\left({}_4\tilde{v}^f - {}_4v^s\right)\tilde{F}^f\right) \\ + J\nabla\cdot\left(\left({}_4\tilde{v}^f - {}_4v^s\right)\cdot{}_4\tilde{\sigma}^f\right)\Bigg] dx_0 \geq 0. \end{aligned} \tag{111} $$

Expressing the free energy of the fluid per unit mixture volume as $\tilde{\psi}^f = \tilde{\phi}^f\tilde{F}^f$, introducing the well known effective stress $\sigma^{eff} = \sigma + pI$ [Ter43] and adding the total mass balance Eq.(88) with a Lagrange multiplier p, Eq.(111) can be written as:

$$ \begin{aligned} J\sigma^{eff} : (\nabla v^s) + \int_0^1 \Bigg[-\frac{D^s\tilde{W}}{Dt} \\ + J\left({}_4\tilde{\sigma} - \tilde{\psi}^f{}_4I - p\tilde{\phi}^f{}_4I\right) : {}_4\nabla\left({}_4\tilde{v}^f - {}_4v^s\right) \\ + J\left({}_4\tilde{v}^f - {}_4v^s\right)\cdot\left({}_4\nabla\cdot{}_4\tilde{\sigma}^f - {}_4\nabla\tilde{\psi}^f + p_4\nabla\tilde{\phi}^f\right)\Bigg] dx_0 \geq 0. \end{aligned} \tag{112} $$

where ${}_4I$ represents the four-dimensional unity tensor. We choose as independent variables the Green-Lagrange strain tensor E, the Lagrangian form of the fluid volume fraction $J\tilde{\phi}^f$ and the relative velocity ${}_4\tilde{v}^{fs} = {}_4\tilde{F}^{-1} \cdot \left({}_4\tilde{v}^f - {}_4v^s\right)$. For convenience of notation we introduced the four-dimensional tensor ${}_4F$:

$$
{}_4F = \begin{bmatrix} 1 & 0 \\ 0 & F \end{bmatrix}, \tag{113}
$$

in which F is the deformation tensor. Applying the principle of equipresence and the chain rule for time differentiation of $\tilde{W}$ and defining $W = \int_0^1 \tilde{W} dx_0$, yields the inequality:

$$
\begin{aligned}
\left[J\sigma^{eff} - F \cdot \frac{\partial W}{\partial E} \cdot F^c\right] : \nabla v^s + \int_0^1 \Bigg[& -\frac{\partial \tilde{W}}{\partial {}_4\tilde{v}^{fs}} \frac{D^s {}_4\tilde{v}^{fs}}{Dt} \\
& + J\left({}_4\tilde{\sigma}^f + \left(\tilde{\mu}^f \tilde{\phi}^f - \tilde{\psi}^f\right) {}_4I\right) : {}_4\nabla\left({}_4\tilde{v}^f - {}_4v^s\right) \\
& + J\left({}_4\tilde{v}^f - {}_4v^s\right) \cdot \left(-{}_4\nabla\tilde{\psi}^f + \tilde{\mu}^f {}_4\nabla\tilde{\phi}^f + {}_4\nabla \cdot {}_4\tilde{\sigma}^f\right)\Bigg] \geq 0
\end{aligned} \tag{114}
$$

which should be true for any value of the state variables. The definition of the chemical potential of the fluid

$$
\tilde{\mu}^f = \frac{\partial \tilde{W}}{\partial\left(J\tilde{\phi}^f\right)} + p. \tag{115}
$$

has been used in Ineq.(114)). The fourth term of the left-hand side of Ineq.(114)) represents the dissipation due to fluid flow. The first term is linear in the solid velocity gradient, the second linear in the accelerations and the third linear in the relative velocity gradients. Therefore, by a standard argument, we find the constitutive relations:

$$
\sigma^{eff} = \frac{1}{J} F \cdot \frac{\partial W}{\partial E} \cdot F^c \tag{116}
$$

$$
\frac{\partial \tilde{W}}{\partial {}_4\tilde{v}^{fs}} = {}_40 \tag{117}
$$

$$
{}_4\tilde{\sigma}^f = \left(\tilde{\psi} - \tilde{\mu}^f \tilde{\phi}^f\right) {}_4I \tag{118}
$$

leaving as inequality:

$$
J \int_0^1 \left[\left({}_4\tilde{v} - {}_4v^s\right) \cdot \left(-{}_4\nabla\tilde{\psi}^f + \tilde{\mu}_4\nabla\tilde{\phi}^f + {}_4\nabla \cdot {}_4\tilde{\sigma}^f\right)\right] dx_0 \geq 0. \tag{119}
$$

If we assume that dissipation associated with fluid flow is a quadratic function of the fluid velocities we find:

$$
-{}_4\nabla_0\tilde{\psi}^f + \tilde{\mu}^f {}_4\nabla_0\phi^f + {}_4\nabla_0 \cdot {}_4\tilde{\sigma}^f = {}_4\tilde{B}^f \cdot {}_4\tilde{v}^{fs}. \tag{120}
$$

Substituting the constitutive expression Eq(118) of the fluid stress ${}_4\tilde{\sigma}^f$ into Eq.(120), yields the extended Darcy equation:

$$
-\tilde{\phi}^f {}_4\nabla_0\tilde{\mu}^f = {}_4\tilde{B}^f \cdot {}_4\tilde{v}^{fs} \tag{121}
$$

which can be written in a more common form [1]:

$$\tilde{\phi}^f\,{}_4\tilde{v}^{fs} = -{}_4\tilde{K}\cdot{}_4\nabla_0\tilde{\mu}^f \tag{122}$$

in which the four-dimensional hydraulic permeability tensor ${}_4\tilde{K}$ reads:

$${}_4\tilde{K} = \left(\tilde{\phi}^f\right)^2\,{}_4\tilde{B}^{f^{-1}}\begin{bmatrix}\tilde{k}_{00} & \tilde{k}_0\\ \tilde{k}_0 & \tilde{K}\end{bmatrix} \tag{123}$$

and which is consistent with earlier forms derived by formal averaging [HvC95b].

11 Numerical implementation

The hierarchical mixture model has been implemented in the finite element software package DIANA. The displacement of the solid u_s, the hydrostatic pressure p and the fluid pressure $\tilde{\mu}^f$ have been chosen as the degrees of freedom. Three equations are used: $\underline{1}$ the momentum balance (3), in which the constitutive equation for the effective stress (41) is substituted, $\underline{2}$ the solid mass balance (11), and $\underline{3}$ the fluid mass balance (12), in which the extended Darcy equation (47) is substituted. The weighted residual method has been applied to the resulting system of non-linear coupled differential equations. After spatial discretization of the degrees of freedom the weighting functions are chosen according to Galerkin's method. Special attention was paid to the discretization of the fluid pressure $\tilde{\mu}^f$, which depends on both spatial position x and x_0. Its spatial discretization was achieved analogously to the hydrostatic pressure's discretization, while an extra linear discretization in x_0 direction was used.

The resulting total element matrix equation is:

$$\begin{aligned}&\begin{bmatrix}0 & 0 & 0\\ {}^{u}_{s}B^{JL}_{j} & {}^{p}_{s}B^{JM}_{j} & {}^{\mu^f}_{s}B^{JN}_{n}\\ 0 & {}^{p}_{f}B^{KM}_{k} & {}^{\mu^f}_{f}B^{KN}_{kn}\end{bmatrix}\begin{bmatrix}\delta\dot{u}^L_j\\ \delta\dot{p}^M\\ \delta\dot{\mu}^{fN}_n\end{bmatrix}\\ &\qquad+\begin{bmatrix}{}^{u}_{m}K^{IL}_{ij} & {}^{p}_{m}K^{IM}_{i} & 0\\ 0 & 0 & 0\\ 0 & 0 & {}^{\mu^f}_{f}K^{KN}_{kn}\end{bmatrix}\begin{bmatrix}\delta u^L_j\\ \delta p^M\\ \delta\mu^{fN}_n\end{bmatrix}\\ &\qquad\qquad=\begin{bmatrix}{}_{m}R^{I}_{ex_i}\\ 0^M\\ {}_{f}R^{K}_{ex_k}\end{bmatrix}-\begin{bmatrix}{}_{m}R^{I}_{in_i}\\ {}_{s}R^{J}_{in}\\ {}_{f}R^{K}_{in_k}\end{bmatrix}\end{aligned} \tag{124}$$

with:

- δu^L_j: iterative correction of displacement component in direction j of node L,
- δp^M: iterative correction of hydrostatic pressure in node M,

- $\delta\tilde{\mu}_n^{f^N}$: iterative correction of fluid pressure at hierarchical level n in node N.

and a dot above a variable denotes its material time derivative. In this matrix equation symmetry is found in the submatrices ${}^{p}_{s}B$, ${}^{\mu^f}_{f}B$, ${}^{m}_{u}K$, ${}^{\mu^f}_{f}K$ and moreover ${}^{p}_{f}B_k^{KM} = {}^{\mu^f}_{s}B_k^{MK}$ and ${}^{u}_{s}B_j^{JL} = {}^{p}_{m}K_j^{LJ}$. Thus a fully symmetric matrix equation is obtained after time integration of the damping contribution. This time integration is achieved by a third order Houbolt scheme [Bat82]:

$$\dot{s}(t) = h_0 s(t) + \sum_{i=1}^{3} h_i s(t - \tau_i) \quad ; \quad s = u^s, p, \tilde{\mu}^f. \tag{125}$$

Linear and quadratic two-dimensional, antisymmetric and three-dimensional isoparametric elements of the serendipity family can be used [TNO93a]. The non-linear equations can be solved by several regular and modified Newton-Raphson iteration techniques and a direct Gauss decomposition [TNO93b]. The implementation has been tested for several problems. Rigid body rotations and translations and analytical solutions of a one-dimensional confined compression experiment and a four-dimensional Laplace equation have been successfully computed [VHD$^+$97].

References

[Aif77]	E.C. Aifantis. Multiporosity theories. *Developments in Mechanics*, 8:209, 1977.
[AVR82]	T. Arts, P.C. Veenstra, and R.S. Reneman. Epicardial deformation and left ventricular ejection in the dog. *Am J Physiol*, 243:379–388, 1982.
[Bat82]	K.J. Bathe. *Finite element procedures in engineering analysis*. Prentice Hall Inc, Englewood Cliffs, New Jersey, first edition, 1982.
[BD83]	A. Bedford and D.S. Drumheller. Theories of immiscible and structured mixtures. *Int. J. Engng Sci.*, 21(8):863—-960, 1983.
[Bio72]	M.A. Biot. Theory of finite deformations of porous solids. *Indiana University Mathematics Journal*, 21(7):597–620, 1972.
[Bow80]	R.M. Bowen. Incompressible porous media models by use of the theory of mixtures. *Int. J. Engng Sci.*, 18:1129—-1148, 1980.
[Dar56]	H.P.G. Darcy. *Les fontaines publiques de la ville de Dijon*. Delmont, Paris,France, 1856.
[dBKNdW85]	R. de Borst, G.M.A. Kusters, P. Nauta, and F.C. de Witte. Diana – a comprehensive, but flexible finite element system. In C.A. Brebbia, editor, *Finite element systems: a handbook*, Springer Verlag, Berlin, New York and Tokyo, 1985.

[DY83] L. Demer and F.C.P. Yin. Passive biaxial mechanical properties of isolated canine myocardium. *J. of Physiol. London*, 339:615–630, 1983.

[Fun93] Y.C. Fung. *Biomechanics: Mechanical properties of living tissues*. Springer Verlag, New York, USA, 1993.

[Guy86] A.C. Guyton. *Textbook of medical physiology*. W.B. Saunders Company, Philadelphia, 7th edition, 1986.

[HAvCR92] J.M. Huyghe, T. Arts, D.H. van Campen, and R.S. Reneman. Porous medium finite element model of the beating left ventricle. *Am J Physiol*, 262:1256–1267, 1992.

[HG85] F.W. Heineman and J. Grayson. Transmural distribution of intramyocardial pressure measured by micropipette technique. *Am J Physiol*, 249:1214–1216, 1985.

[HOvC89] J.M. Huyghe, C.W. Oomens, and D.H. van Campen. Low reynolds number steady state flow through a branching network of rigid vessels: Ii. a finite element mixture model. *Biorheology*, 26:73–84, 1989.

[HOvCH89] J.M. Huyghe, C.W. Oomens, D.H. van Campen, and R.M. Heethaar. Low reynolds number steady state flow through a branching network of rigid vessels: I. a mixture theory. *Biorheology*, 26:55–71, 1989.

[HS90] J.I.E. Hoffman and J.A.E. Spaan. Pressure-flow relations in coronary circulation. *Physiol.Rev.*, 70(2):331–90, 1990.

[HvC95a] J.M. Huyghe and D.H. van Campen. Finite deformation theory of hierarchically arranged porous solids: I. balance of mass and momentum. *Int. J. Engng Sci.*, 33(13):1861–1871, 1995.

[HvC95b] J.M. Huyghe and D.H. van Campen. Finite deformation theory of hierarchically arranged porous solids: Ii. constitutive behaviour. *Int. J. Engng Sci.*, 33(13):1873–1886, 1995.

[Man53] J. Mandel. Consolidation des sols (etude mathematique). *Geotechnique*, 3:287–299, 1953.

[Mar79] A. Maroudas. *Physicochemical properties of articular cartilage, chapter 4, pages 215–290*. M A R Freeman, ed. Adult articular cartilage. 2nd ed. Tunbridge Wells, Kent, UK: Pitman medical, 1979.

[MB68] A. Maroudas and P.G. Bullough. Permeability of articular cartilage. *Nature*, 219:1260—-1261, 1968.

[Ter43] K. Terzaghi. *Theoretical soil mechanics*. John Wiley and Sons, New York, 1943.

[TNO93a] TNO. *DIANA User's Manual: Linear Static Analysis, Release 5.1, vol. 1*. TNO Building and Construction Research, Delft, The Netherlands, 1993.

[TNO93b] TNO. *DIANA User's Manual: Non-linear Analysis, Release 5.1, vol. 4*. TNO Building and Construction Research, Delft, The Netherlands, 1993.

[VHD$^+$97] W.J. Vankan, J.M. Huyghe, M.R. Drost, J.D. Janssen, and A. Huson. A finite element mixture model for hierarchical porous media. *Int. J. Num. Meth. Eng.*, 40:193–210, 1997.

[VHJ$^+$97] W.J. Vankan, J.M. Huyghe, J.D. Janssen, A. Huson, W.J.G. Hacking, and W. Schreiner. Finite element analysis of blood flow through biological tissue. *Int. J. Engng Sci.*, 35:375–385, 1997.

[VHJH96a] W.J. Vankan, J.M. Huyghe, J.D. Janssen, and A. Huson. A 3-d finite element model of blood perfused rat gastrocnemius medialis muscle. *Eur. J. Morphology*, 34(1):19–24, 1996.

[VHJH96b] W.J. Vankan, J.M. Huyghe, J.D. Janssen, and A. Huson. Poroelasticity of saturated solids with an application to blood perfusion. *Int. J. Engng Sci.*, 34(9):1019–1031, 1996.

[VHS$^+$97] W.J. Vankan, J.M. Huyghe, D.W. Slaaf, C.C. van Donkelaar, M.R. Drost, J.D. Janssen, and A. Huson. A finite element model of blood perfusion in muscle tissue during compression and sustained contraction. *Am. J. Physiol.*, 273:H1587—-H1594, 1997.

[VHvD$^+$98] W.J. Vankan, J.M. Huyghe, C.C. van Donkelaar, M.R. Drost, J.D. Janssen, and A. Huson. Mechanical blood–tissue interaction in contracting muscles: a model study. *J. Biomechanics*, 31:401—-409, 1998.

[WA82] R.K. Wilson and E.C. Aifantis. On the theory of consolidation with double porosity. *Int. J. Engng Sci.*, 20(9):1009–1035, 1982.

Thermodynamically Constrained Averaging Theory (TCAT) to Model the Coupled Behavior of Multiphase Porous Systems

W.G. Gray, C.T. Miller

University of North Carolina at Chapel Hill

Modeling of flow in porous media and of the deformation of the solid phase is complicated by the morphology and topology of the pore structure. Because the length scale of the porous structure is small, it is necessary to model porous medium systems at a scale that encompasses at least tens of pore diameters. Equations suitable for modeling at this larger scale must be found that are consistent with smaller scale descriptions of the phase and interface movements yet provide meaningful larger scale values of system variables. The needed equations can be obtained by use of mathematical theorems that average processes occurring in phases, at the interfaces between phases, at common curves where three phases meet, and at common points where four or more phase meet. As a result of the averaging, dynamic equations of mass, momentum, energy, and entropy transport at the larger scale are obtained. In addition, the thermodynamic identities that describe small-scale (microscale) processes are also averaged to the larger scale (macroscale). Finally, kinematic equations that describe the evolution of the shape and distribution of phases and interfaces within the system are derived making use of averaging theorems. As a last step, the resulting equations must be closed so that they can be solved to describe a real system. The method employed here is the Thermodynamically Constrained Averaging Theory (TCAT). It is unique relative to other averaging approaches in its averaging of the thermodynamic relations and its recognition of kinematic processes as being distinct from dynamic processes. Because the method averages all quantities from the microscale to the macroscale in a consistent and well-defined manner, the connection between microscale and macroscale quantities is explicitly known. Thus, experimental and computational work performed at the microscale can be used to support TCAT models, in contrast to models obtained from other averaging procedures. Here we motivate and develop the general TCAT approach and obtain governing equations for some particular systems.

1 What is TCAT?

Thermodynamically Constrained Averaging Theory, commonly referred to as TCAT, is a mathematical framework that has been developed to change the scale of continuum equations from a smaller scale to a larger one [GM14]. The TCAT method essentially filters small scale spatial variability to obtain a larger scale measure of variability. In general, TCAT can be used to increase the scale of equations in the context of multiphase porous media systems, a single-fluid-phase system (in the absence of a solid), multi-fluid systems, or solids. Additionally, the change in scale can proceed up to one that describes only average parameters and variables for the system as a whole rather than one that accounts for filtered variability [GM11a]. Variation may also be taken into account in one or two dimensions while averaging over a third dimension, e.g., [GG10].

In the context of porous medium systems, TCAT is most commonly used to change the equation scale from the *microscale* to the *macroscale*. The term microscale is used interchangeably with the phrase pore scale. At this scale, different phases are visualized as being juxtaposed. They are separated by interfaces. Interfaces meet at common curves, and common curves meet at common points. At the microscale the behavior of fluids within the pore space is described by what are often called point continuum equations. For porous media, microscale descriptions must also include the interactions of phases and the deformation and movement of individual solid grains within the system. The deformation of the interfaces between phases must be described in detail at the microscale because these surfaces are the locations where boundary conditions are applied. Depending on the degree of precision required for a model, the kinematics and dynamics of common curves and common points can also be modeled in detail at the microscale.

TCAT makes use of mathematical theorems to upscale microscale equations by averaging these equations. In brief, the method transforms averages of derivatives of microscale quantities to derivatives of averages of these microscale quantities. Since the TCAT approach is applied to microscale mathematical identities, the result of the averaging procedure is larger scale mathematical identities. The macroscale is a scale where spatial variability of average quantities is accounted for, but the variation is smoothed out. The macroscale typically varies between tens and thousands of pore diameters. Ideally, the macroscale is separated from the microscale such that it is much larger than the microscale and provides stable averages at some scale much less than the system scale. The reason this situation is ideal is that the actual value of the macroscale need not be specified in order to obtain reproducible measures of system properties. Note that this separation of scales is not an inherent requirement of the TCAT approach, but it is an important property if one is to make use of deterministic models that do not require significant stochastic elements that account for the variability associated with length-scale-dependent measurements. For systems that are variable at scales above the macroscale, macroscale parameters can vary and these parameters may even be stochastic. Thus, the length-scale constraint at the macroscale is a workable restriction.

As a byproduct of the mathematical transformation of microscale equations that describe a system at the macroscale, one is also altering the way that a system is described physically. Because quantities are averaged, variability within a pore is no longer accounted for. Rather point-to-point changes of variables averaged over the characteristic macroscale length are described. Implications of this fact include the inability to detail the locations of various phases and interfaces. Instead, the amounts of each of these quantities associated with a point are described. For example, at a macroscale point, the system composition is described by the fractional volume of each phase associated with the averaging region centered at the point.

The TCAT method assures that the transformation of a system description to a larger scale is systematic and rigorous. It is applied to all equations that describe the elements of a system. For example, when applied to equations that describe turbulence, it provides spatially averaged measures of velocity, analogously to the time-averaged velocities that are typically developed.

2 Why Is TCAT Useful?

Although it may be reasonable that one could change the scale of governing equations, one might ask why it is necessary, or even desirable to make this change. Furthermore, if an upscaled equation set is warranted, it is important to understand the attributes of TCAT that make it the method of choice. We will address these two issues here.

Porous medium problems have been at the forefront of environmental studies for many years. Subsurface water resources and contamination of that water due to organics and other chemicals has been an important physical problem and a significant health concern for many years [FC79, Bea79, Ger84, SHCC06]. The need to understand oil and gas reservoir dynamics for effective implementation of advanced drilling technologies and novel extraction methods has motivated a broad range of research activity [AS79, CJ86, AL11, JVC$^+$14]. Future needs for sustainable supplies of water for human and animal consumption, agriculture, manufacturing, and recreation promise that better tools to describe subsurface processes will be essential [Pin12, ETJ13]. Geomechanical issues must be well understood to effectively study problems such as earthquakes [JJ14], land subsidence [GB11], and carbon sequestration [RCMR13]. Porous medium analyses are also applied to studies of a range of engineered systems such as filtration systems [EFM00], reactors and fuel cells [PWL13], and natural systems not involving the subsurface domain [RSML05, HvLB$^+$02, SSG$^+$12].

These different porous medium problems are united by the common thread that modeling of the flow within the solid matrix or of the elements making up the matrix imposes an unmanageable and excessive computational burden if one is interested in behavior of the system as a whole rather than of small-scale distributions. The small-scale processes are important for gaining understanding of porous medium systems, but solving problems of societal interest, such as determining how much subsidence will take place as a result of groundwater extraction, does not require detailed information about solid rearrangement. In fact, modeling of systems at a larger scale is not only cheaper from the perspectives of data collection and simulation but also capable of providing the answers to questions of interest. It is not an overstatement to say that the ability to transform the equations that describe a system from the small scale to a larger scale also transforms many problems from being unsolvable to solvable. Thus the ability of TCAT to facilitate the transformation of equations from the small scale, where they are more readily posed, to a larger scale is of significant value.

With knowledge of the importance of upscaling, we now turn to the attributes of TCAT that recommend it for this task. The first feature of TCAT that is important is that all variables that arise are averages of microscale quantities or combinations of microscale quantities. Because of this unique relationship, measurements made at the microscale can be used, after averaging, to inform the parameterization of macroscale equations. Additionally, it is necessary to explicitly identify all assumptions that are made in formulating the larger scale equations. Thus, if a developed equation set proves to be inadequate for modeling a system of interest, the assumptions can be re-examined to determine the source of discrepancies. The TCAT approach also provides macroscale dynamic equations for interfaces, common curves, and common points that capture the physics of the exchange of mass, momentum, and energy of these entities with each other and with phases.

The kinematics of the phases and interfaces as they redistribute within the system are important. At the microscale, these movements are accounted for by moving boundary kinematic expressions. When the equations being solved are macroscopic, the interfaces that bound the phases are now accounted for on average in a region. Thus, the kinematics must also be accounted for on average. The systematic development of appropriate kinematic equations is unique to the full TCAT approach and provides information and equations that are needed to have a well-defined description of a porous medium system. This stands in stark contrast to approaches that fail to recognize the difference between kinematics and dynamics and thus use erroneous equations and misuse data in cobbling together a system description, e.g., as in [KHJNK14].

A final feature of TCAT worth highlighting is the fact that it makes use of averages of microscale thermodynamic quantities. By doing so, it avoids definitions of macroscale quantities that may appear to have mathematical validity but have no physical justification and may, in fact, not be justified on close mathematical analysis. Indeed, the definition of intensive variables at a larger scale can be accomplished by an infinite set of alternative averaging formalisms. Direct definition of these variables at the macroscale makes it impossible to support the definition with data taken at a smaller scale and inserts a disconnect between scales into the analysis. By providing the definitions for averaged microscale thermodynamic quantities such as temperature, pressure, and chemical potential, TCAT preserves the ability to relate these variables to measurements taken across scales. Equations that result from TCAT are dynamically and thermodynamically consistent across scales and properly account for system

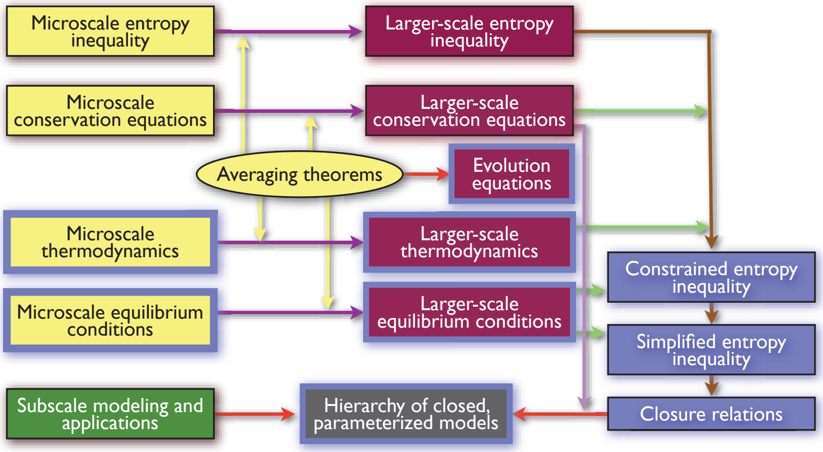

Figure 1: Conceptual representation of the TCAT approach (after [GM14]).

kinematics. These features argue in favor of the TCAT method, at a cost of some significant mathematical analysis.

The equations typically employed to describe flow in porous media are rooted in Darcy's classic experiments for single-fluid-phase flow in a heterogeneous porous media [Dar56]. Extensions based primarily on *ad hoc* extensions to this law have been traditionally employed to obtain equations for multiphase flow in deformable porous media. The opportunities to overlook or misrepresent features related to the interaction between dynamic phases using this approach are numerous and have been exploited! To arrive at a system of equations that is built on fundamental principles and that can be examined thoughtfully in the context of experiments appropriate to the system of interest is a prime objective of TCAT analysis. In the subsequent sections of these notes, we will highlight some of the elements of TCAT and provide tools that will enable the interested reader to formulate models and critique intelligently existing or proposed models.

3 Overview of TCAT

A depiction of the elements of TCAT and their contributions to the TCAT procedure appears in Figure 1. The general flow of the derivation and modeling process can be inferred from the directional arrows on the figure. The end result is a hierarchy of closed, parameterized models, with the values of parameters supported by the subscale modeling and applications.

3.1 Microscale Equations

The starting elements of the TCAT analysis are the standard microscale conservation equations of mass, momentum, angular momentum, and total energy along with the microscale entropy inequality. These equations are posed in a general form without making use of closure relations for quantities such as stress tensor or diffusive flux. Additionally, microscale thermodynamic equations as well as microscale equilibrium conditions are stipulated. It is permissible to begin with any microscale thermodynamic framework, but we will employ classical irreversible thermodynamics (CIT) as formulated in [Bai94, Cal85]. CIT is the simplest formalism among many others, e.g., as found in [GM05, JCV01, JCVL10, LJCV08, Mau99], but has been found to be appropriate for many applications involving dynamic systems.

A key feature of TCAT is that microscale equations are employed not only for phases but also for interfaces, common curves, and common points. For example, the interface conservation equations describe exchanges between adjacent phases and the interface as well as transport processes within the interface. The tangential velocity of material within the interface may be different from the tangential velocity of the interface itself in much the same way that the velocity of flow in a pipe may be different from the velocity of the walls of the pipe. The microscale equations for common curves allow for exchanges with the interfaces as well as for transport along the curve. Microscale thermodynamic equations are employed for interfaces and common curves as well. Of course, equations can also be posed for the common points, but these will not be discussed explicitly here because the equations arise only when considering systems of four or more phases, which is beyond the scope of the present exposition.

3.2 Averaging Theorems and Larger-scale Equations

Once the microscale equations have been stated, they are transformed to a larger scale making use of averaging theorems. These theorems have been derived for phases, interfaces, common curves, and common points [GM14]. Essentially the larger scale equations account for processes within the neighborhood of a point. A point on an interface between two fluid phases will have a particular orientation when viewed at the microscale. However, at the averaged scale, all interfaces within a region are considered as a unit. The orientation at a microscale point cannot be accessed after averaging, but some average measure of orientation within the system will arise. Additionally, because an averaged conservation equation for an interface property describes dynamics of the interface within an integration volume, the equation that results describes spatial transport of interface properties within a three-dimensional system. Thus, in essence, equations that are two-dimensional at the microscale because of their ability to describe processes in a two-dimensional surface become three-dimensional at the macroscale because the macroscale equations describe the dynamic transport of interface properties in a three-dimensional domain. Similar considerations apply to the common curve equations, which are transformed by averaging theorems from one-dimensional entities to three-dimensions.

Based on the preceding considerations, it is reasonable to expect that the macroscale general forms of the equations for phases, interfaces, and common curves will be identical. This is indeed the case for dynamic equations with one notable and important difference. Because of averaging over portions of the domains of the equations, conditions that had to be stated as boundary conditions become conditions within the system. For example, phase equations apply to adjacent "black box" averaging regions and thus exchanges of phase properties with interfaces within that region must be accounted for by the macroscale phase conservation equations. Such terms do arise naturally in the averaging procedure. Similarly, terms arise in the equations for interfaces that account for interactions with phases as well as with common curves. These interaction terms are important as it is the way that the various entities interact with each other that determines system behavior. For example viscous stress between a fluid and solid exerts a drag on the fluid flow that is accounted for and modeled macroscopically. Capillary pressure at interfaces between fluid phases is an important property that significantly impacts the flow behavior in a multi-fluid system. Correctly modeling the exchanges between entities, as well as obtaining closure conditions for macroscale dissipative fluxes with the system entities, provide a large part of the challenge in macroscale modeling of porous media systems.

Larger scale thermodynamic equations are different for different entities, stemming from the fact that they have different forms at the microscale. We note that the averaged Euler forms of thermodynamic expressions are identical in form between the microscale and macroscale. However, because the averaging procedure involves integration of intensive variables, the selection of definitions of these averages is guided by the desire to preserve this identity. However, because thermodynamics provides relations among defined quantities rather than transport equations for these properties, the averages of total time derivatives of thermodynamic identities are entity dependent. This dependence is related to the fact that when an entity, such as an interface or common curve, has an orientation, the orientation impacts the directions in which quantities can change. For example, if the interface in some system are all parallel planes, a difference in temperature between the surfaces can only be eliminated by transport through a phase between the surfaces. Flow within the interface also does not contribute to heat exchange between separated interfaces. If the phase bounded by the surfaces were a perfect insulator, a temperature difference between surfaces would be preserved. However, if the interface in the system is composed of randomly oriented and interconnected elements, the temperature of the interface would relax toward a constant value regardless of the heat transfer properties of the phase bounded by the interface. Thus the rate of change of a thermodynamic property depends on the geometric configuration. This is reflected in the equations for the rate of change of a thermodynamic property as it relates to the rate of change of other thermodynamic properties with the equations for phases being the simplest with increasing complexity arising for interfaces and again for common curves.

In summary, the application of averaging theorems to conservation and thermodynamic equations results in upscaled forms of both equation types. Closure conditions are needed for the dissipative fluxes in these equations. In addition, closure relations are needed for the exchange terms between the various entities. A mathematically intensive, but systematic, method for obtaining the closure relations will be discussed subsequently.

3.3 Evolution Equations for Geometric Densities

In the process of upscaling equations, macroscale representations of variables that have a microscale analogue are encountered. Included among these are quantities such as density, velocity, stress tensor, internal energy, etc. However, in addition to these quantities, variables arise that do not exist at the microscale. These are referred to collectively as geometric densities and include the volume fractions (volume of a phase per volume), specific interfacial area (amount of area between a pair of phases per volume), and specific common curve (length of a common curve where three phases meet per volume). These quantities appear in the conservation equations such that they can be combined with other variables so as to be implicit in the equations. However, in the thermodynamic equations, these additional variables appear such that they must be treated explicitly. This occurrence creates a deficit in the number of equations needed to completely describe the system in addition to the deficit cause by the need to close the dissipative fluxes. Essentially, equations are needed that describe the evolution of the geometric densities.

The needed equations cannot be developed precisely in terms of macroscale variables. It has been pointed out that general relations for deformation of an area at the microscale cannot be obtained [MN85]. At the macroscale, we can obtain equations for the kinematics of geometric densities from the averaging theorems. It is important to understand that the geometric densities and their shapes do not change based on some conservation equation for that variable. Rather, they are described by kinematic equations that describe the effects of movement of parts of the region of interest on its shape. For example, if some nonuniform normal velocity is applied to a plane surface, that surface will deform and take on a new shape. The shape is determined based on the velocity field applied. Thus, the deformation is a kinematic process. That is the deformation depends on the motion of points on the surface but is not concerned with dynamic processes that cause the motion. Kinematic conditions are mathematically determined without consideration of physical constraints. The stretching of a small, finite, planar surface to an extremely large shape can be described mathematically using kinematics. Constructing such a surface may present a physical problem as properties such as elasticity and tearing must be overcome. In a similar way, the deformation of an interface between fluids in a porous medium system can be described kinematically, but physical transport processes associated with the surface are described by dynamic conservation equations.

The kinematics of the geometric densities are described by applying the averaging theorem to a microscopic constant. The result is an equation in terms of averages of microscopic variables. Some of the expressions obtained must be approximated so that the kinematic expression serves as an additional condition without adding additional variables. Although the expressions obtained are approximate, the use of averaging theorems is a reasonable way to proceed. It has been recognized in the boiling literature that kinematic expressions for phase geometries are needed [IKK05, KI05, IKSH09]. In that context, the kinematics are somewhat simpler as the presence of the solid phase in a porous medium causes a wider variety of interface sizes and geometries to exist. Nevertheless, without the use of kinematic closure relations, one cannot properly formulate the dynamics of capillary pressure in a porous medium system.

3.4 Equilibrium Conditions

It is important to know the equilibrium state of a system. When we know conditions of equilibrium, we can often make linearized approximations for fluxes in terms of forces when the system is "near" the equilibrium state. It is then possible to apply the equations developed and determine if the linearized approximation holds or if a more complex formulation is required. In practice, it is found that linearized approximations often are valid and quite useful. Among the well known linear approximations are Fourier's law, which states that heat flux is proportional to temperature gradient, and Fick's law, which states that mass flux is proportional to the gradient of mass fractions.

Some equilibrium conditions are obvious. For example, at equilibrium there is no flow such that the velocities of all entities in a system are zero. We also know that the temperature in an equilibrium system is uniform. The statement that the velocity is zero at equilibrium is a requirement posed to define equilibrium. The fact that the temperature is uniform is a consequence of making the definition of equilibrium. From a thermodynamic perspective, the equilibrium state is achieved when a system reaches its state of minimum energy. With this knowledge, we can perform a variational analysis to determine what conditions must apply to intensive thermodynamic variables if a system will be at equilibrium. The variational analysis for minimization of energy for a microscale CIT formulation can be found in the literature [Bor75, BN77, BRN85, GM14].

The larger scale equilibrium conditions are obtained by simply averaging the microscale conditions. At first blush, it might seem that because the larger scale equilibrium conditions are based on averages, they are not as robust as their microscale counterparts. Subscale variability in a quantity that is required to be constant at equilibrium at the scale of interest can lead to a statement of equilibrium when one is not present. This issue does not arise when the averaging is such that it is independent of variations in the length scale of the averaging region. This is typically taken to be the case when applying a deterministic method, such as TCAT, without building a stochastic framework on top. Thus, the average conditions of equilibrium are taken to be indicative of the state of the system.

3.5 Entropy Inequalities and Closure Relations

The rightmost section of figure 1 provides the steps that need to be taken to obtain useable closed conservation and evolution equations for a system type of interest. The entropy inequality contains the variables entropy, dissipative entropy flux, entropy production by body sources, entropy exchanges between entities, and entropy generation. None of these quantities appear in any of the conservation equations. The task at hand to eliminate these extra terms from the entropy inequality in light of system behavior so that the entropy equation will be useful, particularly, in describing the dissipative fluxes.

To accomplish this, first the exchange terms are removed by summing the entropy equations for each entity over all entities to obtain a system entropy inequality at the scale of analysis. With this process, all the entropy exchange terms cancel out and need not be considered further. Next the conservation equations are each added to the entropy equation after multiplying them by a Lagrange multiplier. By this approach, the conservation equations act as constraints on the entropy inequality. Values for the Lagrange multipliers are selected such that the entropy generation reduces, as far as possible, to a sum of dissipative fluxes multiplied by forces. This equation is called the constrained entropy inequality (CEI).

The general CEI is, in fact, too complex to be used effectively. It contains a number of quantities that relate to averages of microscale values that must be converted to macroscale forms. It is at this point that approximations are introduced with the intention of eliminating small, unimportant terms. The assumptions made to convert the CEI to the simplified entropy inequality (SEI) are the first ones employed in the analysis, other than assumptions regarding the separation of length scale and the thermodynamic form specified. Thus, these assumptions can play a key role if one wishes to examine reasons that a particular final equation set does not adequately model a system. It is prudent to emphasize that simplification of the CEI to an SEI is based on explicit assumptions. Thus one who uses resultant equations can use reexamination of these assumptions as a starting point for finding more accurate models.

The final right side box in figure 1 is the closure relations. These are equalities that model dissipative fluxes in terms of forces. The forces are primarily impetuses to flow or transport that exist because the system is away from equilibrium. The closure relations are typically, and somewhat generally, expressed as fluxes proportional to each of the forces. However, these forms must be studied to ascertain when it is necessary to include the spectrum of forces and if linear dependence is sufficiently general.

3.6 Model Quality and Support

The two remaining boxes at the bottom of figure 1 concern implementation of the derived model. As such, they are concerned with the output from the significant mathematical effort and aim to confirm the utility of that effort. In some sense, these boxes may seem distinct from the other boxes in that they involve model application rather than model development. However, we feel that it is important to list these items as part of the holistic TCAT approach. Without these two boxes, TCAT is reduced to mathematical gymnastics. The prime objective of the rigors of the TCAT approach is to ensure that connections can be retained between variables across scales, that assumptions in models are explicit, and that the results relate well to actual physical systems. This objective can only be realized if the developed models can be subjected to tests and comparisons.

The models developed are referred to as a “hierarchy” because different collections of equations result depending on the characteristics of the system studied. Models can be single-fluid-phase, multi-fluid-phase, species-based, or entity-based. Within each of these types various assumptions can be applied depending on whether the system is isothermal, the presence or absence of turbulence, whether or not concentration gradients are large, the degree of deformation of the solid phase, and so forth. Rather than formulating the ultimate set of general equations, it is prudent to tailor equations to these different possibilities and thereby create a hierarchy of models.

Some small systems can be simulated at the microscale with the results obtained used to support the parameterizations employed in a TCAT model. These systems include idealized collections of pore throats and pore volumes as specified in pore network models [Blu01, BJPV02, Fat56, HGM03, BVC15] or using lattice Boltzmann models for either well-defined sphere packs or natural porous media [DMMG13, GZ02, PLM06, LHLT14, MPM14]. Additionally, laboratory and field-scale studies can contribute to the parameterization of models and analyses of model fidelity to the system of interest, although the experiments can be quite challenging [MG95, WS13, BEAZ15, BSSW14].

4 Mathematical Elements of TCAT

Having provided an overview of the TCAT procedure, we now provide the mathematical elements of the method. It is not possible to go into great detail in these brief notes, so the emphasis will be on usable equations. Those interested in greater understanding and some complete examples are referred to [GM14]. In the current development, we will forego the complexities that are inherent in working with species-based conservation equations for all entities. We will only consider the case where the entities are modeled without considering compositional issues. Because notation may be an obstacle to understanding, we will devote considerable effort making that element of the problem clear.

In the discussion here, we will consider a wetting fluid phase, w, a non-wetting phase, n, and a solid phase, s. The interface between phases is denoted by the pair of subscript associated with the phases in either order. Thus, the interfaces are wn, ws, and ns. For a three-phase system, a common curve may also exist where the three phases meet and is denoted wns. Phases, interfaces, and common curves are referred to collectively as entities. The full index set of entities is designated as $\mathcal{I}$ such that

$$\mathcal{I} = \{w, n, s, wn, ws, ns, wns\} \ . \tag{1}$$

We will also consider the set of entities to which a particular entity is connected. For example, the w phase is connected to the wn interface and the wns common curve. The index set of connected entities α is denoted as $\mathcal{I}_{\mathrm{c}\alpha}$ so that $\mathcal{I}_{\mathrm{cw}}$ is

$$\mathcal{I}_{cw} = \{wn, wns\} \ . \tag{2}$$

It is important to be able to distinguish between connected index sets that are of higher dimensionality than the entity of interest and those of lower dimensionality. This is denoted for entity α as $\mathcal{I}^+_{\mathrm{c}\alpha}$ for entities of higher dimensionality and $\mathcal{I}^-_{\mathrm{c}\alpha}$ for entities of lower dimensionality. For the w phase, both connected entities are of lower dimensionality so that $\mathcal{I}^+_{cw}$ is the null set and $\mathcal{I}^-_{cw} = \mathcal{I}_{cw}$. For the wn interface we can identify the connected sets as

$$\mathcal{I}_{cwn} = \{w, wns\} \ , \tag{3}$$

$$\mathcal{I}^+_{cwn} = \{w\} \ , \tag{4}$$

and

$$\mathcal{I}^-_{cwn} = \{wns\} \ . \tag{5}$$

4.1 Microscale Conservation Equations

Microscale equations are formulated for entities designated as phases, interfaces, and common curves. These are, respectively, three-, two-, and one-dimensional systems. A point within a phase does not interact with any other entities. A point on a surface, however, does interact with a phase, while a point on a common curve interacts with interfaces and, in some cases, phases. Thus the microscale conservation equations have similar forms but differ in there dimensionality and their interaction with other entities. We can take these difference into account and write a general conservation form in m-dimensional space as

$$\begin{aligned}\mathcal{F}_\alpha = \frac{\partial^{(m)} F_\alpha}{\partial t} + \nabla^{(m)}\cdot(\mathbf{v}_\alpha F_\alpha) - S_{\Omega\alpha} - \sum_{\kappa\in\mathcal{I}^+_{c\alpha}} \underset{\kappa\to\alpha}{X} \\ - \mathrm{div}^{(\mathrm{m})}\left(\mathbf{S}_{\Gamma\alpha}\cdot\mathbf{l}^{(m)}_\alpha\right) - G_{\Omega\alpha} = 0 \quad \text{for } \alpha\in\mathcal{I}, \dim\alpha = 3-m \ .\end{aligned} \tag{6}$$

The leftmost quantity is used to designate the property being conserved. We use primes, ′, to indicate that an operator is restricted to a particular dimensionality. In this equation, the quantity (m) appended to operators indicates the number of primes that appear, which restrict the spatial dimensionality that the operator acts in. For example, when $m = 0$, there are no primes and the operators are the usual forms for three-dimensional space. When $m = 1$, the operators are restricted to two-dimensional space ($\mathbf{R}^2$), and when $m = 2$ two primes are used to denote that the operators are restricted to one dimensional space. The subscripts on quantities, as opposed to superscripts, designate that the quantity is a microscale quantity, as opposed to an averaged quantity. The variable F_α is the density of the specific property being conserved in entity α, and $\mathbf{v}_\alpha$ is the microscale velocity. The variable $S_{\Omega\alpha}$ is the body source term; $\underset{\kappa\to\alpha}{X}$ is the transfer term from entity κ to entity α; $\mathbf{S}_{\Gamma\alpha}\cdot\mathsf{I}_\alpha^{(m)}$ is the non-advective source where $\mathsf{I}_\alpha^{(m)}$ is a unit tensor in the domain R^{3-m}; and $G_{\Omega\alpha}$ is a generation term.

With this template for a conservation equation, mass conservation in the wn interface between the w and n phases, for example, is written

$$\mathcal{M}_{wn} = \frac{\partial' \rho_{wn}}{\partial t} + \nabla'\cdot(\rho_{wn}\mathbf{v}_{wn}) - \underset{w\to wn}{M} - \underset{n\to wn}{M} = 0\,. \tag{7}$$

In this equation, M is used to indicate mass exchange. The body source, non-advective source, and generation terms are all zero for mass conservation.

Momentum conservation for the same interface is

$$\begin{aligned}\boldsymbol{\mathcal{P}}_{wn} = \frac{\partial'(\rho_{wn}\mathbf{v}_{wn})}{\partial t} &+ \nabla'\cdot(\rho_{wn}\mathbf{v}_{wn}\mathbf{v}_{wn}) - \rho_{wn}\mathbf{g}_{wn} - \mathbf{v}_w \underset{w\to wn}{M} - \underset{w\to wn}{\mathbf{T}} \\ &- \mathbf{v}_n \underset{n\to wn}{M} - \underset{n\to wn}{\mathbf{T}} - \nabla'\cdot\left(\mathsf{I}'_{wn}\cdot\mathbf{t}_{wn}\right) = 0\,,\end{aligned} \tag{8}$$

where $\mathbf{g}_{wn}$ is the body force per unit of mass (independent of entity if the only body force is gravity), $\mathbf{T}$ accounts for momentum exchange due to non-dissipative (pressure) and dissipative (friction) interactions between the interface and the phases, and $\mathbf{t}_{wn}$ is the stress tensor in the interface. The unit tensor I'_{wn} restricts the stress tensor so that it acts in the interface. The div operator has been replaced by the ∇ operator and the symmetry of the stress tensor has been noted such that the transpose of the stress tensor need not be indicated.

The conservation of total energy for the wn interface is expressed as

$$\begin{aligned}\mathcal{E}_{wn} = &\frac{\partial'}{\partial t}\left[E_{wn} + \rho_{wn}\left(\frac{\mathbf{v}_{wn}\cdot\mathbf{v}_{wn}}{2}\right)\right] \\ &+ \nabla'\cdot\left\{\left[E_{wn} + \rho_{wn}\left(\frac{\mathbf{v}_{wn}\cdot\mathbf{v}_{wn}}{2}\right)\right]\mathbf{v}_{wn}\right\} - \rho_{wn}\mathbf{g}_{wn}\cdot\mathbf{v}_{wn} - h_{wn} \\ &- \left[\left(\frac{E_w}{\rho_w} + \frac{\mathbf{v}_w\cdot\mathbf{v}_w}{2}\right)\underset{w\to wn}{M} + \mathbf{v}_w\cdot\underset{w\to wn}{\mathbf{T}} + \underset{w\to wn}{Q}\right] \\ &- \left[\left(\frac{E_n}{\rho_n} + \frac{\mathbf{v}_n\cdot\mathbf{v}_n}{2}\right)\underset{n\to wn}{M} + \mathbf{v}_n\cdot\underset{n\to wn}{\mathbf{T}} + \underset{n\to wn}{Q}\right] \\ &- \nabla'\cdot\left[\mathsf{I}'_{wn}\cdot(\mathbf{t}_{wn}\cdot\mathbf{v}_{wn} + \mathbf{q}_{wn})\right] = 0\,,\end{aligned} \tag{9}$$

where E_{wn} is the internal energy per unit area, h_{wn} is the body source of energy, if any, Q accounts for heat exchange between the interface and the adjacent phases, and $\mathbf{q}_{wn}$ is the dissipative heat conduction within the interface.

A final balance equation for the interface that we can write is the entropy equation written as

$$\begin{aligned}\mathcal{S}_{wn} = {} & \frac{\partial' \eta_{wn}}{\partial t} + \nabla' \cdot \left(\eta_{wn}\mathbf{v}_{wn}\right) - b_{wn} - \left(\frac{\eta_w}{\rho_w} \underset{w\to wn}{M} + \underset{w\to wn}{\Phi}\right) \\ & - \left(\frac{\eta_n}{\rho_n}\underset{n\to wn}{M} + \underset{n\to wn}{\Phi}\right) - \nabla'\cdot\left(\mathbf{I}'_{wn}\cdot\boldsymbol{\varphi}_{wn}\right) = \Lambda_{wn} \; . \end{aligned} \tag{10}$$

In this equation η_{wn} is the entropy per area, b_{wn} is the entropy body source term, Φ is the entropy exchanged between the interface and the adjacent phases due to processes other than phase change, $\boldsymbol{\varphi}_{wn}$ is the dissipative entropy flux vector, and Λ_{wn} is the entropy generation term. Note that the entropy balance is the only equation that is of conservation form that has a non-zero generation term. The generation term is non-negative, and this property is useful in deriving closure relations.

Although we have not explicitly listed conservation and entropy balance equations for phases and common curves, these should be relatively easily obtained from the general form. The main differences involve choosing subscripts that designate the entity of interest, noting that from a microscale perspective an entity only exchanges properties with entities of higher dimensionality, and the differential operators are adjusted to account for the dimensionality of the space of the entity.

One other equation employed is merely the restatement of an algebraic identity. We will be considering the case where the body force per unit mass, $\mathbf{g}_\alpha$, is obtained as the gradient of a potential function, ψ_α, such that

$$\mathbf{g}_\alpha + \nabla\psi_\alpha = 0 \; . \tag{11}$$

To use this equation in conjunction with surfaces and common curves, we note that we will only differentiate with respect to the surface or lineal coordinates, respectively. Thus we can write, in general

$$\mathbf{I}^{(m)}_\alpha \cdot \mathbf{g}_\alpha = -\nabla^{(m)}\psi_\alpha = 0 \quad \text{for } \alpha \in \mathcal{J}, \dim \alpha = 3 - m \; . \tag{12}$$

Multiplication of the mass conservation equation by ψ_α, rearrangement of the terms, and use of Eqn (11) yields

$$\begin{aligned}\mathcal{G}_\alpha = {} & \frac{\partial^{(m)}\Psi_\alpha}{\partial t} + \nabla^{(m)}\cdot(\mathbf{v}_\alpha\Psi_\alpha) + \rho_\alpha\mathbf{g}_\alpha\cdot\mathbf{v}_\alpha - \sum_{\kappa\in\mathcal{J}^+_{c\alpha}} \underset{\kappa\to\alpha}{M}\psi_\alpha \\ & - \rho_\alpha\frac{\partial^{(m)}\psi_\alpha}{\partial t} - \rho_\alpha\mathbf{g}_\alpha\cdot\left(\mathbf{I} - \mathbf{I}^{(m)}_\alpha\right)\cdot\mathbf{v}_\alpha = 0 \quad \text{for } \alpha \in \mathcal{J}, \dim \alpha = 3 - m \; , \end{aligned} \tag{13}$$

where

$$\Psi_\alpha = \rho_\alpha\psi_\alpha \; . \tag{14}$$

Eqn (13) is useful in conjunction with the conservation equations in obtaining closed models. For example, with $m = 1$ and $\alpha = wn$, it can be added to Eqn (9) to obtain

$$
\begin{aligned}
\mathcal{E}_{wn} + \mathcal{G}_{wn} = {} & \frac{\partial'}{\partial t}\left[E_{wn} + \rho_{wn}\left(\frac{\mathbf{v}_{wn}\cdot\mathbf{v}_{wn}}{2}\right) + \Psi_{wn}\right] \\
& + \nabla'\cdot\left\{\left[E_{wn} + \rho_{wn}\left(\frac{\mathbf{v}_{wn}\cdot\mathbf{v}_{wn}}{2}\right) + \Psi_{wn}\right]\mathbf{v}_{wn}\right\} - h_{wn} \\
& - \left[\left(\frac{E_w}{\rho_w} + \frac{\mathbf{v}_w\cdot\mathbf{v}_w}{2} + \psi_{wn}\right)\underset{w\to wn}{M} + \mathbf{v}_w\cdot\underset{w\to wn}{\mathbf{T}} + \underset{w\to wn}{Q}\right] \\
& - \left[\left(\frac{E_n}{\rho_n} + \frac{\mathbf{v}_n\cdot\mathbf{v}_n}{2} + \psi_{wn}\right)\underset{n\to wn}{M} + \mathbf{v}_n\cdot\underset{n\to wn}{\mathbf{T}} + \underset{n\to wn}{Q}\right] \\
& - \rho_{wn}\frac{\partial'\psi_{wn}}{\partial t} - \rho_{wn}\mathbf{g}_{wn}\cdot\left(\mathbf{l} - \mathbf{l}'_{wn}\right)\cdot\mathbf{v}_{wn} \\
& - \nabla'\cdot\left[\mathbf{l}'_{wn}\cdot\left(\mathbf{t}_{wn}\cdot\mathbf{v}_{wn} + \mathbf{q}_{wn}\right)\right] = 0\ . \qquad (15)
\end{aligned}
$$

4.2 Averaging Relationships

Because it is infeasible to model porous medium systems of any practical size using microscale equations, theorems have been derived that allow for the transition of the equations to a larger scale. In many cases, it is still important to obtain information on how variables depend on spatial location. Thus, it is important to be able to model natural systems, such as aquifers and petroleum reservoirs, as well as laboratory column experiments at scales between the microscale and the system scale. This scale is called the macroscale. Averaging to the macroscale serves as a filter such that some detailed information is sacrificed in favor of being able to obtain information about larger systems.

Conservation and balance equation for a system have been formulated for a system at the microscale in the last subsection. It is appropriate to retain these equations as a bases for the larger scale model rather than abandon them in favor of direct formulation at the larger scale. The latter approach runs the risk of ignoring a process of importance and of developing equations that lose consistency between scales. The transformation of microscale equations to the larger scale is accomplished through averaging theorems. These theorems change the scale of system variables, replace averages of derivatives of microscale quantities with derivatives of larger-scale quantities, and provide explicit accounting for the interaction processes between entities. The averaging theorems to convert from the microscale to the macroscale [AJ67, GH89, GL77, GLKB93, GM13, HW85, Mar67, MG05, Sla67, Whi67] are most readily applied when the length scales of the microscale and macroscale are widely separated. To facilitate implementation of the averaging theorems, it is convenient to introduce notation that defines averages.

4.2.1 Averaging Notation

Roughly speaking, an average involves some sort of summation divided by some normalization function. In averaging microscale properties, we end up with integral expressions for both the numerator and denominator of the averaging operation. Keeping these integrals explicitly in the larger scale conservation equations is clumsy at best and is most certainly inconvenient. To circumvent this problem, we define an averaging operator that accounts for all the elements of integration in abbreviated notation. The averaging operator is defined as a bracketed quantity with subscripts according to

$$\langle \mathcal{P}_\alpha \rangle_{\Omega_\beta,\Omega_\gamma,W} = \frac{\int\limits_{\Omega_\beta} W\mathcal{P}_\alpha \,\mathrm{d}\mathfrak{r}}{\int\limits_{\Omega_\gamma} W \,\mathrm{d}\mathfrak{r}} \qquad \text{for } \dim\Omega_\beta = 1, 2, \text{ or } 3;\ \dim\Omega_\gamma = 1, 2, \text{ or } 3\ . \tag{16}$$

In this equation $\mathcal{P}_\alpha$ is a microscale property of entity α being averaged, W is a weighting function, Ω_β is a domain of integration of the function and Ω_γ is the region of integration used in normalizing the averaging process. If W is not specified, it is assumed to be 1 so that

$$\langle \mathcal{P}_\alpha \rangle_{\Omega_\beta,\Omega_\gamma} = \frac{\int\limits_{\Omega_\beta} \mathcal{P}_\alpha \,\mathrm{d}\mathfrak{r}}{\int\limits_{\Omega_\gamma} \mathrm{d}\mathfrak{r}} \qquad \text{for } \dim\Omega_\beta = 1, 2, \text{ or } 3;\ \dim\Omega_\gamma = 1, 2, \text{ or } 3\ . \tag{17}$$

The dimensions of the averaging domains are the dimensions corresponding to the entities being averaged over in this case.

A microscale function may only be integrated over a domain in which it exists. Thus when a property of one domain is integrated over a different domain, the integration domain must be a boundary. For example, the value of a property of a phase can be integrated over the boundary of the phase or over a common curve that lies on the phase boundary. Thus, we might designate the average of a property f_w of the w phase averaged over the wn interface as $\langle f_w \rangle_{\Omega_{wn},\Omega_{wn}}$. In reality, such notation designates integration over the boundary domain of the w phase and not actually the wn interface.

Although the definition of the averaging operator in Eqn (16) is generally useful and provides an explicit indication of the averaging procedure being undertaken, it is still somewhat notationally awkward. Therefore, three principal averaging notations are introduced to account for the averages that arise. The notation used is abbreviated, and less explicit, but it serves to clarify possible confusion. These averages are referred to as the intrinsic average, the mass average, and uniquely defined averages.

The *general intrinsic average* is the simple case when a quantity is averaged and normalized over the same domain with $W = 1$. A general intrinsic average is denoted by adding an unadorned superscript, referring to the region of integration, to the microscale quantity being averaged such that

$$f_\alpha^\beta = \langle f_\alpha \rangle_{\Omega_\beta,\Omega_\beta} \quad \text{for } \alpha, \beta \in \mathfrak{I};\, . \tag{18}$$

An important special case arises when a quantity is averaged over the full domain where it exists such that $\beta = \alpha$. This can easily be accommodated using the notation of Eqn (18), however for convenience, the lower subscript is not listed such that we obtain the *special intrinsic average*

$$f^{\alpha} = \langle f_{\alpha} \rangle_{\Omega_{\alpha},\Omega_{\alpha}} \quad \text{for } \alpha \in \mathfrak{I} \; . \tag{19}$$

We emphasize that the presence of a superscript, either in combination with or without a complementary subscript, indicates an upscaled quantity. The compressed notation for the general and special intrinsic phase averages conveys a precise meaning for a macroscale variable in terms of a microscale precursor, thereby providing a desirable connection between quantities at different length scales.

The *mass average*, or *mass density weighted average*, is obtained as a special case of Eqn (16) when the mass density of the entity associated with the quantity being averaged is the weighting function, W. The general mass average is indicated as

$$f_{\alpha}^{\overline{\beta}} = \langle f_{\alpha} \rangle_{\Omega_{\beta},\Omega_{\beta},\rho_{\alpha}} \quad \text{for } \alpha, \beta \in \mathfrak{I} \; , \tag{20}$$

where the superscript with an overline denotes a mass average. We can also define the *intrinsic mass average* when β is additionally equal to α. As with the intrinsic average, the subscript is deleted in the general mass average such that

$$f^{\overline{\alpha}} = \langle f_{\alpha} \rangle_{\Omega_{\alpha},\Omega_{\alpha},\rho_{\alpha}} \quad \text{for } \alpha \in \mathfrak{I} \; . \tag{21}$$

The preceding definitions serve the purpose of indicating the averaging used in defining macroscale quantities while simplifying the notation. However, there is an almost unlimited range of averages that arise

The third type of average notation is used to apply to all other averages. We refer to these as *uniquely defined averages* because each average indicated by this notation is some atypical average or particular combination of intrinsic or mass averages with other averages. General uniquely defined averages are indicated by a superscript with a double overbar applied to a subscripted quantity, such as $f_{\alpha}^{\overline{\overline{\beta}}}$, where the superscript typically refers to the domain of averaging and the subscript refers to the domain where the quantities exist. A simpler notation used for a unique average omits the subscript when the averaging pertains to quantities that are averaged over the full domain in which they exist. In these instances, the unique average for a property of entity α is denoted as $f^{\overline{\overline{\alpha}}}$.

The uniquely defined averages can only be related to their precursors by providing the definition in terms of the explicit averaging operator. The double overbar serves as a flag that indicates a unique definition for the upscaled variable is being used. If one wishes to relate that average to the microscale situation, the definition that is provided in a general development must be consulted. The kind of averaging that has occurred is different for different properties that make use of the unique averaging shorthand.

As examples of quantities that are encountered in averaging, we provide the following

$$\rho^{\alpha} = \langle \rho_\alpha \rangle_{\Omega_\alpha,\Omega_\alpha} \qquad \text{for } \alpha \in \mathcal{J} \,, \tag{22}$$

$$\mathbf{v}_\alpha^{\overline{\beta}} = \langle \mathbf{v}_\alpha \rangle_{\Omega_\beta,\Omega_\beta,\rho_\alpha} \qquad \text{for } \alpha \in \mathcal{J}, \beta \in \mathcal{J}_{c\alpha}^{-} \,, \tag{23}$$

$$\mathbf{v}^{\overline{\alpha}} = \langle \mathbf{v}_\alpha \rangle_{\Omega_\alpha,\Omega_\alpha,\rho_\alpha} \qquad \text{for } \alpha \in \mathcal{J} \,, \tag{24}$$

$$\epsilon^{\overline{\overline{\alpha}}} = \langle 1 \rangle_{\Omega_\alpha,\Omega} \qquad \text{for } \alpha \in \mathcal{J} \,, \tag{25}$$

$$E^{\overline{\overline{\alpha}}} = \langle E_\alpha \rangle_{\Omega_\alpha,\Omega} = \epsilon^{\overline{\overline{\alpha}}} E^{\alpha} \qquad \text{for } \alpha \in \mathcal{J} \tag{26}$$

and

$$\mathbf{t}^{\overline{\overline{\alpha}}} = \left\langle \mathbf{I}_\alpha^{(m)} \boldsymbol{\cdot} \mathbf{t}_\alpha - \rho_\alpha (\mathbf{v}_\alpha - \mathbf{v}^{\overline{\alpha}})(\mathbf{v}_\alpha - \mathbf{v}^{\overline{\alpha}}) \right\rangle_{\Omega_\alpha,\Omega_\alpha} \qquad \text{for } \alpha \in \mathcal{J} \,, \tag{27}$$

Note that Eqn (25) provides the definitions for geometric densities with $\epsilon^{\overline{\overline{\alpha}}}$ being the volume fraction when α is a phase, the specific area when α is an interface, and a specific length when α refers to a common curve.

4.3 Averaging Theorems

The differential operators in the microscale equations are all of the same dimensionality as the space in which the property of interest lies. On transformation to the macroscale, all the equations are three-dimensional because the average properties of interest vary from spatial point to spatial point, regardless of how their average values were calculated or which types of entities they characterize. The averaging theorems that are applied to each microscale equation must therefore be able to transform the microscale derivative to a corresponding macroscale derivative and leave extra terms as needed.

The derivation of the averaging theorems can be difficult, but is made somewhat easier by making use of generalized functions. There are three types of averaging theorems needed: one for the divergence operator, one for the gradient operator, and one for the partial time derivative. The gradient theorem follows directly from the divergence theorem, but both forms are provided here.

The averaging theorem for the divergence operator acting on a vector (or tensor) $\mathbf{f}_\alpha$ is given as

$$\begin{aligned} \left\langle \nabla^{(m)} \boldsymbol{\cdot} \mathbf{f}_\alpha \right\rangle_{\Omega_\alpha,\Omega} =& \nabla \boldsymbol{\cdot} \left\langle \mathbf{I}_\alpha^{(m)} \boldsymbol{\cdot} \mathbf{f}_\alpha \right\rangle_{\Omega_\alpha,\Omega} - \left\langle \left(\nabla^{(m)} \boldsymbol{\cdot} \mathbf{I}_\alpha^{(m)} \right) \boldsymbol{\cdot} \mathbf{f}_\alpha \right\rangle_{\Omega_\alpha,\Omega} \\ & + \sum_{\kappa \in \mathcal{J}_{c\alpha}^{-}} \langle \mathbf{n}_\alpha \boldsymbol{\cdot} \mathbf{f}_\alpha \rangle_{\Omega_\kappa,\Omega} \quad \text{for } \alpha \in \mathcal{J}, \dim \alpha = 3 - m \,. \end{aligned} \tag{28}$$

The averaging of a microscale divergence is indicated on the left side of the equation, and the terms on the right are what are used in the macroscale formulation. Roughly, the first term on the right is the divergence of an average, the second accounts for the curvature of a one- or two-dimensional entity, and the third accounts for the boundary processes where the α entity interacts with other entities. This equation is not expressed in terms of simplified averaging notation because the equation itself does not require that any particular type of quantity be averaged, other than a tensor of at least first order. As an example, for the w phase in a system composed of three phases, w, n, and s, the divergence is a three-dimensional operator such that $m = 0$ and Eqn (28) reduces to

$$\begin{aligned}\langle\nabla\cdot\mathbf{f}_w\rangle_{\Omega_w,\Omega} =& \nabla\cdot\langle\mathbf{f}_w\rangle_{\Omega_w,\Omega} + \langle\mathbf{n}_w\cdot\mathbf{f}_w\rangle_{\Omega_{wn},\Omega} \\ &+ \langle\mathbf{n}_w\cdot\mathbf{f}_w\rangle_{\Omega_{ws},\Omega} + \langle\mathbf{n}_w\cdot\mathbf{f}_w\rangle_{\Omega_{wns},\Omega} = 0\ . \qquad (29)\end{aligned}$$

The last term in this equation accounts for interaction between the w phase and the common curve. This interaction is usually negligible and exists only because of a concentrated interaction between the phase and the common curve, such as stress exchange between a common curve and a phase. For our purposes, in fact, this kind of interaction is neglected for flow process and for exchanges other than the stress.

The gradient averaging theorem is obtained when the differential operator acts on a scalar (or tensor of any order) is

$$\begin{aligned}\left\langle\nabla^{(m)}f_\alpha\right\rangle_{\Omega_\alpha,\Omega} =& \nabla\cdot\left\langle\mathsf{I}_\alpha^{(m)}f_\alpha\right\rangle_{\Omega_\alpha,\Omega} - \left\langle\left(\nabla^{(m)}\cdot\mathsf{I}_\alpha^{(m)}\right)f_\alpha\right\rangle_{\Omega_\alpha,\Omega} \\ &+ \sum_{\kappa\in\mathcal{J}_{c\alpha}^{-}}\langle\mathbf{n}_\alpha f_\alpha\rangle_{\Omega_\kappa,\Omega} \quad \text{for } \alpha\in\mathcal{J}, \dim\alpha = 3-m\ . \qquad (30)\end{aligned}$$

The averaging operator is applied to the gradient on the left, and the result is the three terms on the right that have analogous meanings to the terms obtained from the divergence operator. Thus, for example, for the wn interface, $m = 1$ since the dimensionality of the surface is 2. The interaction with an entity of lower order signals interaction with the wns common curve. so that the specific form of the gradient averaging theorem is

$$\begin{aligned}\langle\nabla' f_{wn}\rangle_{\Omega_{wn},\Omega} =& \nabla\cdot\langle\mathsf{I}'_{wn}f_{wn}\rangle_{\Omega_{wn},\Omega} - \langle\left(\nabla'\cdot\mathsf{I}'_{wn}\right)f_{wn}\rangle_{\Omega_{wn},\Omega} \\ &+ \langle\mathbf{n}_{wn}f_{wn}\rangle_{\Omega_{wns},\Omega}\ . \qquad (31)\end{aligned}$$

In this equation, $\mathbf{n}_{wn}$ is a unit vector on the wns common curve that is tangent to the wn surface where it meets the common curve and is also orthogonal to the common curve.

Besides the spatial averaging theorems, a temporal averaging theorem is needed to convert the time derivative of a microscale quantity to the time derivative of a macroscale quantity. The general form of the time averaging theorem can be stated for any entity as

$$\left\langle\frac{\partial^{(m)}f_\alpha}{\partial t}\right\rangle_{\Omega_\alpha,\Omega} = \frac{\partial}{\partial t}\langle f_\alpha\rangle_{\Omega_\alpha,\Omega} + \nabla\cdot\left\langle\left(\mathsf{I}-\mathsf{I}_\alpha^{(m)}\right)\cdot\mathbf{v}_\alpha f_\alpha\right\rangle_{\Omega_\alpha,\Omega}$$

$$+\left\langle \nabla^{(m)}\cdot\mathsf{I}_{\alpha}^{(m)}\cdot\mathbf{v}_{\alpha}f_{\alpha}\right\rangle_{\Omega_{\alpha},\Omega} - \sum_{\kappa\in\mathfrak{I}_{c\alpha}^{-}} \langle \mathbf{n}_{\alpha}\cdot\mathbf{v}_{\kappa}f_{\alpha}\rangle_{\Omega_{\kappa},\Omega}$$

$$\text{for } \alpha\in\mathfrak{I}, \dim\alpha = 3-m\ . \tag{32}$$

For this equation, there are four terms on the right-hand side. The first term is the time derivative of the macroscale quantity, the second term accounts for advective transport of the property within the domain, the third term accounts for changes in the property due to deformation of the region (for interfaces and common curves), and the final term accounts for interactions with domains of lower dimensionality. As an example of a particular form of this theorem, we will write it for a wns common curve in a three-phase system. Thus $m = 2$, and the time averaging theorem becomes

$$\left\langle \frac{\partial'' f_{wns}}{\partial t} \right\rangle_{\Omega_{wns},\Omega} = \frac{\partial}{\partial t}\langle f_{wns}\rangle_{\Omega_{wns},\Omega} + \nabla\cdot\left\langle \left(\mathsf{I}-\mathsf{I}_{wns}''\right)\cdot\mathbf{v}_{wns}f_{wns}\right\rangle_{\Omega_{wns},\Omega} + \left\langle \nabla''\cdot\mathsf{I}_{wns}''\cdot\mathbf{v}_{wns}f_{wns}\right\rangle_{\Omega_{wns},\Omega}\ . \tag{33}$$

For a common curve in a system where no common points exist (i.e. a three-phase system) there are no entities of dimensionality less than that of the common curve, so the interaction term is omitted.

One particular combination of the averaging theorems that is helpful to have at hand is the sum of Eqns (32) and (28) for the case where $\mathbf{f}_{\alpha} = \mathbf{v}_{\alpha}f_{\alpha}$. Addition of the two theorems after making this substitution yields

$$\left\langle \frac{\partial^{(m)} f_{\alpha}}{\partial t} \right\rangle_{\Omega_{\alpha},\Omega} + \left\langle \nabla^{(m)}\cdot\mathbf{v}_{\alpha}f_{\alpha}\right\rangle_{\Omega_{\alpha},\Omega} = \frac{\partial}{\partial t}\langle f_{\alpha}\rangle_{\Omega_{\alpha},\Omega} + \nabla\cdot\langle\mathbf{v}_{\alpha}f_{\alpha}\rangle_{\Omega_{\alpha},\Omega} - \sum_{\kappa\in\mathfrak{I}_{c\alpha}^{-}} \langle \mathbf{n}_{\alpha}\cdot(\mathbf{v}_{\kappa}-\mathbf{v}_{\alpha})f_{\alpha}\rangle_{\Omega_{\kappa},\Omega} \quad \text{for } \alpha\in\mathfrak{I}, \dim\alpha = 3-m\ . \tag{34}$$

Observe that the two terms on the left side of the equation typically appear together in the conservation and balance equations. It is interesting that on the right side of the equation, the terms accounting for geometry of the entities are eliminated as the tensor describing the tangential directions to the one- and two-dimensional entities, $\mathsf{I}_{\alpha}^{(m)}$, cancel out. Thus, although the differential operators on the left side of the equation are dependent on the dimensionality of the entities, no differences exist on the right side except for the exchange term of the α entity with lower-order entities.

5 Macroscale Conservation Equations

The macroscale conservation equations are derived as averages of the microscale equations obtained based on the application of the averaging theorems. Here, we will average the general form of the conservation equation given by Eqn (6) over the domain on which the equation applies to obtain

$$\begin{aligned}\langle \mathcal{F}_\alpha \rangle_{\Omega_\alpha,\Omega} =& \left\langle \frac{\partial^{(m)} F_\alpha}{\partial t} \right\rangle_{\Omega_\alpha,\Omega} + \left\langle \nabla^{(m)} \boldsymbol{\cdot} (\mathbf{v}_\alpha F_\alpha) \right\rangle_{\Omega_\alpha,\Omega} - \langle S_{\Omega\alpha} \rangle_{\Omega_\alpha,\Omega} \\ & - \left\langle \sum_{\kappa \in \mathcal{J}_{c\alpha}^{+}} \underset{\kappa\to\alpha}{X} \right\rangle_{\Omega_\alpha,\Omega} - \left\langle \mathrm{div}^{(\mathrm{m})} \left(\mathbf{S}_{\Gamma\alpha} \boldsymbol{\cdot} \mathbf{I}_\alpha^{(m)} \right) \right\rangle_{\Omega_\alpha,\Omega} \\ & - \langle G_{\Omega\alpha} \rangle_{\Omega_\alpha,\Omega} = 0 \quad \text{for } \alpha \in \mathcal{J}, \dim \alpha = 3 - m \; . \end{aligned} \tag{35}$$

Now we can apply the combined averaging theorem of Eqn (34) to the first two terms after the equal sign and the divergence theorem of Eqn (28) to the second term in the second line so that we exchange the order of differentiation and averaging leaving

$$\begin{aligned}\langle \mathcal{F}_\alpha \rangle_{\Omega_\alpha,\Omega} =& \frac{\partial}{\partial t} \langle F_\alpha \rangle_{\Omega_\alpha,\Omega} + \nabla \boldsymbol{\cdot} \langle \mathbf{v}_\alpha F_\alpha \rangle_{\Omega_\alpha,\Omega} - \sum_{\kappa \in \mathcal{J}_{c\alpha}^{-}} \langle \mathbf{n}_\alpha \boldsymbol{\cdot} (\mathbf{v}_\kappa - \mathbf{v}_\alpha) F_\alpha \rangle_{\Omega_\kappa,\Omega} \\ & - \langle S_{\Omega\alpha} \rangle_{\Omega_\alpha,\Omega} - \left\langle \sum_{\kappa \in \mathcal{J}_{c\alpha}^{+}} \underset{\kappa\to\alpha}{X} \right\rangle_{\Omega_\alpha,\Omega} - \nabla \boldsymbol{\cdot} \left\langle \mathbf{I}_\alpha^{(m)} \boldsymbol{\cdot} \mathbf{S}_{\Gamma\alpha} \right\rangle_{\Omega_\alpha,\Omega} \\ & - \sum_{\kappa \in \mathcal{J}_{c\alpha}^{-}} \langle \mathbf{n}_\alpha \boldsymbol{\cdot} \mathbf{S}_{\Gamma\alpha} \rangle_{\Omega_\kappa,\Omega} - \langle G_{\Omega\alpha} \rangle_{\Omega_\alpha,\Omega} = 0 \quad \text{for } \alpha \in \mathcal{J}, \dim \alpha = 3 - m \; . \end{aligned} \tag{36}$$

In this equation, the two terms involving summations account for interaction of the entity α with entities of lower dimensionality. We observe that

$$\left\langle \sum_{\kappa \in \mathcal{J}_{c\alpha}^{-}} \underset{\kappa\to\alpha}{X} \right\rangle_{\Omega_\alpha,\Omega} = \sum_{\kappa \in \mathcal{J}_{c\alpha}^{-}} \langle \mathbf{n}_\alpha \boldsymbol{\cdot} (\mathbf{v}_\kappa - \mathbf{v}_\alpha) F_\alpha \rangle_{\Omega_\alpha,\Omega} + \sum_{\kappa \in \mathcal{J}_{c\alpha}^{-}} \langle \mathbf{n}_\alpha \boldsymbol{\cdot} \mathbf{S}_{\Gamma\alpha} \rangle_{\Omega_\alpha,\Omega} \tag{37}$$

Therefore, we can combine the exchange terms by making the summation over $\mathcal{J}_{c\alpha}$, the full set of connected entities for entity α so that Eqn (36) becomes

$$\begin{aligned}\langle \mathcal{F}_\alpha \rangle_{\Omega_\alpha,\Omega} =& \frac{\partial}{\partial t} \langle F_\alpha \rangle_{\Omega_\alpha,\Omega} + \nabla \boldsymbol{\cdot} \langle \mathbf{v}_\alpha F_\alpha \rangle_{\Omega_\alpha,\Omega} - \langle S_{\Omega\alpha} \rangle_{\Omega_\alpha,\Omega} \\ & - \left\langle \sum_{\kappa \in \mathcal{J}_{c\alpha}} \underset{\kappa\to\alpha}{X} \right\rangle_{\Omega_\alpha,\Omega} - \nabla \boldsymbol{\cdot} \left\langle \mathbf{I}_\alpha^{(m)} \boldsymbol{\cdot} \mathbf{S}_{\Gamma\alpha} \right\rangle_{\Omega_\alpha,\Omega} - \langle G_{\Omega\alpha} \rangle_{\Omega_\alpha,\Omega} = 0 \\ & \text{for } \alpha \in \mathcal{J}, \dim \alpha = 3 - m \; . \end{aligned} \tag{38}$$

We will also make use of the notation that

$$\left\langle \sum_{\kappa \in \mathcal{J}_{c\alpha}} \underset{\kappa\to\alpha}{X} \right\rangle_{\Omega_\alpha,\Omega} = \sum_{\kappa \in \mathcal{J}_{c\alpha}} \overset{\kappa\to\alpha}{X} \, , \tag{39}$$

where the use of the over-arrow for the exchange indicates that it is a macroscale representation. Because of the averaging procedure, we can calculate this exchange term from available microscale information. However, in actual applications, this exchange term is formulated constitutively as a function of macroscale variables. With substitution of Eqn (39) into Eqn (38), the macroscale equation becomes

$$\begin{aligned}\langle \mathcal{F}_\alpha \rangle_{\Omega_\alpha,\Omega} &= \frac{\partial}{\partial t}\langle F_\alpha \rangle_{\Omega_\alpha,\Omega} + \nabla\cdot\langle \mathbf{v}_\alpha F_\alpha \rangle_{\Omega_\alpha,\Omega} - \langle S_{\Omega\alpha} \rangle_{\Omega_\alpha,\Omega} \\ &- \sum_{\kappa\in\mathfrak{I}_{c\alpha}} \overset{\kappa\to\alpha}{X} - \nabla\cdot\left\langle \mathsf{I}_\alpha^{(m)}\cdot\mathbf{S}_{\Gamma\alpha} \right\rangle_{\Omega_\alpha,\Omega} - \langle G_{\Omega\alpha} \rangle_{\Omega_\alpha,\Omega} = 0 \\ &\text{for } \alpha\in\mathfrak{I}, \dim\alpha = 3-m\ . \qquad (40)\end{aligned}$$

It is useful to write this equation in terms of a material derivative. We can obtain this form by adding and subtracting $\nabla\cdot(\mathbf{v}^{\overline{\alpha}}\langle F_\alpha\rangle_{\Omega_\alpha,\Omega})$ in the left side of the equation and rearranging the result as

$$\begin{aligned}\langle \mathcal{F}_\alpha \rangle_{\Omega_\alpha,\Omega} &= \frac{\mathrm{D}^{\overline{\alpha}}}{\mathrm{D}t}\langle F_\alpha \rangle_{\Omega_\alpha,\Omega} + \langle F_\alpha \rangle_{\Omega_\alpha,\Omega}\mathsf{I}{:}\mathsf{d}^{\overline{\overline{\alpha}}} + \nabla\cdot\left\langle (\mathbf{v}_\alpha - \mathbf{v}^{\overline{\alpha}}) F_\alpha \right\rangle_{\Omega_\alpha,\Omega} - \langle S_{\Omega\alpha} \rangle_{\Omega_\alpha,\Omega} \\ &- \sum_{\kappa\in\mathfrak{I}_{c\alpha}} \overset{\kappa\to\alpha}{X} - \nabla\cdot\left\langle \mathsf{I}_\alpha^{(m)}\cdot\mathbf{S}_{\Gamma\alpha} \right\rangle_{\Omega_\alpha,\Omega} - \langle G_{\Omega\alpha} \rangle_{\Omega_\alpha,\Omega} = 0 \\ &\text{for } \alpha\in\mathfrak{I}, \dim\alpha = 3-m\ , \qquad (41)\end{aligned}$$

where

$$\frac{\mathrm{D}^{\overline{\alpha}}}{\mathrm{D}t} = \frac{\partial}{\partial t} + \mathbf{v}^{\overline{\alpha}}\cdot\nabla \qquad (42)$$

and

$$\mathsf{d}^{\overline{\overline{\alpha}}} = \frac{1}{2}\left[\nabla\mathbf{v}^{\overline{\alpha}} + (\nabla\mathbf{v}^{\overline{\alpha}})^{\mathrm{T}}\right]\ . \qquad (43)$$

Now we turn to some specific instances of this equation as applied to the particular conservation and balance equations.

5.1 Macroscale Mass Conservation

For mass conservation, Eqn (41) applies with $\mathcal{F} = \mathcal{M}$, $F_\alpha = \rho_\alpha$, $\overset{\kappa\to\alpha}{X} = \overset{\kappa\to\alpha}{M}$, $S_{\Omega\alpha} = 0$, $\mathbf{S}_{\Gamma\alpha} = 0$, and $G_{\Omega\alpha} = 0$. Thus we obtain

$$\begin{aligned}\langle \mathcal{M}_\alpha \rangle_{\Omega_\alpha,\Omega} &= \frac{\mathrm{D}^{\overline{\alpha}}}{\mathrm{D}t}\langle \rho_\alpha \rangle_{\Omega_\alpha,\Omega} + \langle \rho_\alpha \rangle_{\Omega_\alpha,\Omega}\mathsf{I}{:}\mathsf{d}^{\overline{\overline{\alpha}}} + \nabla\cdot\left\langle (\mathbf{v}_\alpha - \mathbf{v}^{\overline{\alpha}})\rho_\alpha \right\rangle_{\Omega_\alpha,\Omega} \\ &- \sum_{\kappa\in\mathfrak{I}_{c\alpha}} \overset{\kappa\to\alpha}{M} = 0 \quad \text{for } \alpha\in\mathfrak{I}, \dim\alpha = 3-m\ . \qquad (44)\end{aligned}$$

The leftmost term is an integral over the α entity normalized with respect to the entire domain. Thus, it is a unique average. The average of density can be related to the intrinsic average, and the average involving velocity can be related to a mass average. We therefore make the definitions

$$\langle \mathcal{M}_\alpha \rangle_{\Omega_\alpha,\Omega} = \mathcal{M}_*^{\overline{\overline{\alpha}}} , \tag{45}$$

$$\langle \rho_\alpha \rangle_{\Omega_\alpha,\Omega} = \epsilon^{\overline{\overline{\alpha}}} \rho^\alpha , \tag{46}$$

and

$$\langle \rho_\alpha \mathbf{v}_\alpha \rangle_{\Omega_\alpha,\Omega} = \epsilon^{\overline{\overline{\alpha}}} \rho^\alpha \mathbf{v}^{\overline{\alpha}} . \tag{47}$$

Thus the notation employed for the macroscale mass conservation equation is

$$\mathcal{M}_*^{\overline{\overline{\alpha}}} = \frac{\mathrm{D}^{\overline{\alpha}} (\epsilon^{\overline{\overline{\alpha}}} \rho^\alpha)}{\mathrm{D}t} + \epsilon^{\overline{\overline{\alpha}}} \rho^\alpha \mathsf{l}\mathbf{:}\mathsf{d}^{\overline{\overline{\alpha}}} - \sum_{\kappa \in \mathfrak{I}_{c\alpha}} \overset{\kappa\to\alpha}{M} = 0 \quad \text{for } \alpha \in \mathfrak{I} . \tag{48}$$

5.2 Macroscale Momentum Conservation

Conservation of momentum is a vector equation. For this equation, Eqn (41) applies with $\mathcal{F} = \boldsymbol{\mathcal{P}}$, $F_\alpha = \rho_\alpha \mathbf{v}_\alpha$, $\overset{\kappa\to\alpha}{X} = \mathbf{v}^{\overline{\overline{\alpha},\overline{\kappa}}} \overset{\kappa\to\alpha}{M} + \overset{\kappa\to\alpha}{\mathbf{T}}$, $S_{\Omega\alpha} = \rho_\alpha \mathbf{g}_\alpha$, $\mathbf{S}_{\Gamma\alpha} = \mathbf{t}_\alpha$, and $G_{\Omega\alpha} = 0$. In this identification, we have made use of the notation $\mathbf{v}^{\overline{\overline{\alpha},\overline{\kappa}}}$, which indicates the average of a property of an entity over a lower-dimensional entity on its boundary such that

$$\mathbf{v}^{\overline{\overline{\alpha},\overline{\kappa}}} = \begin{cases} \mathbf{v}_\alpha^{\overline{\kappa}} & \text{if } \kappa \in \mathfrak{I}_{c\alpha}^- \\ \mathbf{v}_\kappa^{\overline{\alpha}} & \text{if } \kappa \in \mathfrak{I}_{c\alpha}^+ \end{cases} . \tag{49}$$

The exchange term is therefore divided into a part associated with phase change and a part related to interaction forces between entities. If we make use of these definitions, the momentum equation is

$$\begin{aligned} \langle \boldsymbol{\mathcal{P}}_\alpha \rangle_{\Omega_\alpha,\Omega} = {} & \frac{\mathrm{D}^{\overline{\alpha}}}{\mathrm{D}t} \langle \rho_\alpha \mathbf{v}_\alpha \rangle_{\Omega_\alpha,\Omega} + \langle \rho_\alpha \mathbf{v}_\alpha \rangle_{\Omega_\alpha,\Omega} \mathsf{l}\mathbf{:}\mathsf{d}^{\overline{\overline{\alpha}}} + \nabla\cdot \left\langle (\mathbf{v}_\alpha - \mathbf{v}^{\overline{\alpha}}) \rho_\alpha \mathbf{v}_\alpha \right\rangle_{\Omega_\alpha,\Omega} \\ & - \langle \rho_\alpha \mathbf{g}_\alpha \rangle_{\Omega_\alpha,\Omega} - \sum_{\kappa \in \mathfrak{I}_{c\alpha}} \mathbf{v}^{\overline{\overline{\alpha},\overline{\kappa}}} \overset{\kappa\to\alpha}{M} - \sum_{\kappa \in \mathfrak{I}_{c\alpha}} \overset{\kappa\to\alpha}{\mathbf{T}} - \nabla\cdot \left\langle \mathsf{l}_\alpha^{(m)} \cdot \mathbf{t}_\alpha \right\rangle_{\Omega_\alpha,\Omega} = 0 \\ & \text{for } \alpha \in \mathfrak{I}, \dim \alpha = 3 - m . \end{aligned} \tag{50}$$

The unique definition for $\mathbf{t}^{\overline{\overline{\alpha}}}$ has been given in Eqn (27). Re-expression of the averages in Eqn (50) in terms of the averaging notation then yields

$$\begin{aligned} \boldsymbol{\mathcal{P}}^{\overline{\overline{\alpha}}} = {} & \frac{\mathrm{D}^{\overline{\alpha}} (\epsilon^{\overline{\overline{\alpha}}} \rho^\alpha \mathbf{v}^{\overline{\alpha}})}{\mathrm{D}t} + \epsilon^{\overline{\overline{\alpha}}} \rho^\alpha \mathbf{v}^{\overline{\alpha}} \mathsf{l}\mathbf{:}\mathsf{d}^{\overline{\overline{\alpha}}} - \epsilon^{\overline{\overline{\alpha}}} \rho^\alpha \mathbf{g}^{\overline{\alpha}} \\ & - \sum_{\kappa \in \mathfrak{I}_{c\alpha}} \mathbf{v}^{\overline{\overline{\alpha},\overline{\kappa}}} \overset{\kappa\to\alpha}{M} - \sum_{\kappa \in \mathfrak{I}_{c\alpha}} \overset{\kappa\to\alpha}{\mathbf{T}} - \nabla\cdot (\epsilon^{\overline{\overline{\alpha}}} \mathbf{t}^{\overline{\overline{\alpha}}}) = 0 \quad \text{for } \alpha \in \mathfrak{I} . \end{aligned} \tag{51}$$

5.3 Macroscale Total Energy Equation

The energy equation is the most complex of the conservation equations and therefore requires some finesse in developing the macroscale form. A driving consideration is that we want to retain the same definition for the macroscale stress and for other macroscale variables that have arisen in the mass and momentum equations. We thus proceed as follows. For energy conservation Eqn (41) applies with

$$\mathcal{F} = \mathcal{E} + \mathcal{G} \tag{52}$$

$$F_\alpha = E_\alpha + \rho_\alpha \frac{\mathbf{v}_\alpha \cdot \mathbf{v}_\alpha}{2} + \Psi_\alpha \tag{53}$$

$$\overset{\kappa\to\alpha}{X} = \left(\overline{E}^{\overline{\overline{\alpha,\kappa}}} + \frac{\mathbf{v}^{\overline{\overline{\alpha,\kappa}}} \cdot \mathbf{v}^{\overline{\overline{\alpha,\kappa}}}}{2} + \psi^{\overline{\overline{\alpha,\kappa}}} + K_E^{\overline{\overline{\alpha,\kappa}}} \right) \overset{\kappa\to\alpha}{M} + \mathbf{v}^{\overline{\overline{\alpha,\kappa}}} \cdot \overset{\kappa\to\alpha}{\mathbf{T}} + \overset{\kappa\to\alpha}{Q} \tag{54}$$

$$S_{\Omega\alpha} = \rho_\alpha \frac{\partial^{(m)} \psi_\alpha}{\partial t} + \rho_\alpha \mathbf{g}_\alpha \cdot \left(\mathsf{I} - \mathsf{I}_\alpha^{(m)} \right) \cdot \mathbf{v}_\alpha + h_\alpha \tag{55}$$

$$\mathbf{S}_{\Gamma\alpha} = \mathbf{t}_\alpha \cdot \mathbf{v}_\alpha + \mathbf{q}_\alpha \tag{56}$$

and

$$G_{\Omega\alpha} = 0\ . \tag{57}$$

Application of the averaging theorems to the general conservation equation with these variables defined gives

$$\begin{aligned}
\langle \mathcal{E}_\alpha + \mathcal{G}_\alpha \rangle_{\Omega_\alpha,\Omega} = {} & \frac{\mathrm{D}^{\overline{\alpha}}}{\mathrm{D}t} \left\langle E_\alpha + \rho_\alpha \frac{\mathbf{v}_\alpha \cdot \mathbf{v}_\alpha}{2} + \Psi_\alpha \right\rangle_{\Omega_\alpha,\Omega} \\
& + \left\langle E_\alpha + \rho_\alpha \frac{\mathbf{v}_\alpha \cdot \mathbf{v}_\alpha}{2} + \Psi_\alpha \right\rangle_{\Omega_\alpha,\Omega} \mathsf{I}:\mathbf{d}^{\overline{\overline{\alpha}}} \\
& + \nabla \cdot \left\langle (\mathbf{v}_\alpha - \mathbf{v}^{\overline{\alpha}}) \left(E_\alpha + \rho_\alpha \frac{\mathbf{v}_\alpha \cdot \mathbf{v}_\alpha}{2} + \Psi_\alpha \right) \right\rangle_{\Omega_\alpha,\Omega} \\
& - \left\langle \rho_\alpha \frac{\partial^{(m)} \psi_\alpha}{\partial t} \right\rangle_{\Omega_\alpha,\Omega} - \left\langle \rho_\alpha \mathbf{g}_\alpha \cdot \left(\mathsf{I} - \mathsf{I}_\alpha^{(m)} \right) \cdot \mathbf{v}_\alpha \right\rangle_{\Omega_\alpha,\Omega} - \langle h_\alpha \rangle_{\Omega_\alpha,\Omega} \\
& - \sum_{\kappa \in \mathfrak{I}_{c\alpha}} \left(\overline{E}^{\overline{\overline{\alpha,\kappa}}} + \frac{\mathbf{v}^{\overline{\overline{\alpha,\kappa}}} \cdot \mathbf{v}^{\overline{\overline{\alpha,\kappa}}}}{2} + \psi^{\overline{\overline{\alpha,\kappa}}} + K_E^{\overline{\overline{\alpha,\kappa}}} \right) \overset{\kappa\to\alpha}{M} \\
& - \sum_{\kappa \in \mathfrak{I}_{c\alpha}} \mathbf{v}^{\overline{\overline{\alpha,\kappa}}} \cdot \overset{\kappa\to\alpha}{\mathbf{T}} - \sum_{\kappa \in \mathfrak{I}_{c\alpha}} \overset{\kappa\to\alpha}{Q} - \nabla \cdot \left\langle \mathsf{I}_\alpha^{(m)} \cdot \mathbf{t}_\alpha \cdot \mathbf{v}_\alpha \right\rangle_{\Omega_\alpha,\Omega} \\
& - \nabla \cdot \left\langle \mathsf{I}_\alpha^{(m)} \cdot \mathbf{q}_\alpha \right\rangle_{\Omega_\alpha,\Omega} = 0 \quad \text{for } \alpha \in \mathfrak{I}, \dim \alpha = 3 - m\ .
\end{aligned} \tag{58}$$

The operators can be eliminated from this equation, for the most part, by judicious definition of variables to obtain

$$\mathcal{E}_*^{\overline{\overline{\alpha}}} + \mathcal{G}_*^{\overline{\overline{\alpha}}} = \frac{\mathrm{D}^{\overline{\alpha}}}{\mathrm{D}t} \left[E^{\overline{\overline{\alpha}}} + \epsilon^{\overline{\alpha}} \rho^\alpha \left(\frac{\mathbf{v}^{\overline{\alpha}} \cdot \mathbf{v}^{\overline{\alpha}}}{2} + K_E^{\overline{\overline{\alpha}}} \right) + \Psi^{\overline{\overline{\alpha}}} \right]$$

$$
\begin{aligned}
&+\left[E^{\overline{\overline{\alpha}}}+\epsilon^{\overline{\overline{\alpha}}}\rho^{\alpha}\left(\frac{\mathbf{v}^{\overline{\alpha}}\boldsymbol{\cdot}\mathbf{v}^{\overline{\alpha}}}{2}+K_E^{\overline{\overline{\alpha}}}\right)+\Psi^{\overline{\overline{\alpha}}}\right]\mathsf{I}\boldsymbol{:}\mathbf{d}^{\overline{\overline{\alpha}}} \\
&-\left\langle\rho_\alpha\frac{\partial^{(m)}\psi_\alpha}{\partial t}\right\rangle_{\Omega_\alpha,\Omega}-\left\langle\rho_\alpha\mathbf{g}_\alpha\boldsymbol{\cdot}\left(\mathsf{I}-\mathsf{I}_\alpha^{(m)}\right)\boldsymbol{\cdot}\mathbf{v}_\alpha\right\rangle_{\Omega_\alpha,\Omega}-\epsilon^{\overline{\overline{\alpha}}}h^{\alpha} \\
&-\sum_{\kappa\in\mathcal{J}_{c\alpha}}\left(\overline{E}^{\overline{\overline{\alpha,\kappa}}}+\frac{\mathbf{v}^{\overline{\overline{\alpha,\kappa}}}\boldsymbol{\cdot}\mathbf{v}^{\overline{\overline{\alpha,\kappa}}}}{2}+\psi^{\overline{\overline{\alpha,\kappa}}}+K_E^{\overline{\overline{\alpha,\kappa}}}\right)\overset{\kappa\to\alpha}{M} \\
&-\sum_{\kappa\in\mathcal{J}_{c\alpha}}\mathbf{v}^{\overline{\overline{\alpha,\kappa}}}\boldsymbol{\cdot}\overset{\kappa\to\alpha}{\mathbf{T}}-\sum_{\kappa\in\mathcal{J}_{c\alpha}}\overset{\kappa\to\alpha}{Q}-\nabla\boldsymbol{\cdot}\left(\mathbf{t}^{\overline{\overline{\alpha}}}\boldsymbol{\cdot}\mathbf{v}^{\overline{\alpha}}\right)-\nabla\boldsymbol{\cdot}\mathbf{q}^{\overline{\overline{\alpha}}}=0 \\
&\qquad\text{for }\alpha\in\mathcal{J},\dim\alpha=3-m\ . \qquad (59)
\end{aligned}
$$

The definitions of the unique variables are

$$E^{\overline{\overline{\alpha}}}=\langle E_\alpha\rangle_{\Omega_\alpha,\Omega}\ , \qquad (60)$$

$$\overline{E}^{\overline{\overline{\alpha,\kappa}}}=\begin{cases}\overline{E}_\alpha^{\overline{\kappa}} & \text{if }\kappa\in\mathcal{J}_{c\alpha}^{-}\\ \overline{E}_\kappa^{\overline{\alpha}} & \text{if }\kappa\in\mathcal{J}_{c\alpha}^{+}\end{cases}\ , \qquad (61)$$

$$K_{E\alpha\kappa}=\begin{cases}\frac{1}{2}\left(\mathbf{v}_\alpha-\mathbf{v}_\alpha^{\overline{\kappa}}\right)\boldsymbol{\cdot}\left(\mathbf{v}_\alpha-\mathbf{v}_\alpha^{\overline{\kappa}}\right) & \text{if }\kappa\in\mathcal{J}_{c\alpha}^{-}\\ \frac{1}{2}\left(\mathbf{v}_\kappa-\mathbf{v}_\kappa^{\overline{\alpha}}\right)\boldsymbol{\cdot}\left(\mathbf{v}_\kappa-\mathbf{v}_\kappa^{\overline{\alpha}}\right) & \text{if }\kappa\in\mathcal{J}_{c\alpha}^{+}\end{cases}\ , \qquad (62)$$

$$K_E^{\overline{\overline{\alpha}}}=\frac{1}{2}\left\langle\left(\mathbf{v}_\alpha-\mathbf{v}^{\overline{\alpha}}\right)\boldsymbol{\cdot}\left(\mathbf{v}_\alpha-\mathbf{v}^{\overline{\alpha}}\right)\right\rangle_{\Omega_\alpha,\Omega_\alpha,\rho_\alpha\omega_{i\alpha}}\ , \qquad (63)$$

$$K_E^{\overline{\overline{\alpha,\kappa}}}=\begin{cases}K_{E\alpha}^{\overline{\overline{\kappa}}}=\langle K_{E\alpha\kappa}\rangle_{\Omega_\kappa,\Omega_\kappa,\rho_\kappa} & \text{if }\kappa\in\mathcal{J}_{c\alpha}^{-}\\ K_{E\kappa}^{\overline{\overline{\alpha}}}=\langle K_{E\alpha\kappa}\rangle_{\Omega_\alpha,\Omega_\alpha,\rho_\alpha} & \text{if }\kappa\in\mathcal{J}_{c\alpha}^{+}\end{cases}\ , \qquad (64)$$

and

$$
\begin{aligned}
\mathbf{q}^{\overline{\overline{\alpha}}}=\Bigg\langle &\mathsf{I}_\alpha^{(m)}\boldsymbol{\cdot}\mathbf{q}_\alpha+\mathsf{I}_\alpha^{(m)}\boldsymbol{\cdot}\mathbf{t}_\alpha\boldsymbol{\cdot}\left(\mathbf{v}_\alpha-\mathbf{v}^{\overline{\alpha}}\right)-\rho_\alpha\Bigg[\overline{E}_\alpha-\overline{E}^{\overline{\alpha}} \\
&+\frac{\left(\mathbf{v}_\alpha-\mathbf{v}^{\overline{\alpha}}\right)\boldsymbol{\cdot}\left(\mathbf{v}_\alpha-\mathbf{v}^{\overline{\alpha}}\right)}{2}-K_E^{\overline{\overline{\alpha}}}\Bigg]\left(\mathbf{v}_{i\alpha}-\mathbf{v}^{\overline{i\alpha}}\right)\Bigg\rangle_{\Omega_\alpha,\Omega_\alpha}\ . \qquad (65)
\end{aligned}
$$

Additionally, we note that $\overline{E}_\alpha=E_\alpha/\rho_\alpha$.

5.4 Macroscale Entropy Balance

In addition to the conservation equations, an entropy balance equation may be formulated for each entity. Application of the averaging operator to the entropy equation yields

$$\langle\mathcal{S}_\alpha\rangle_{\Omega_\alpha,\Omega}=\frac{\mathrm{D}^{\overline{\alpha}}}{\mathrm{D}t}\langle\eta_\alpha\rangle_{\Omega_\alpha,\Omega}+\langle\eta_\alpha\rangle_{\Omega_\alpha,\Omega}\mathsf{I}\boldsymbol{:}\mathbf{d}^{\overline{\overline{\alpha}}}+\nabla\boldsymbol{\cdot}\left\langle(\mathbf{v}_\alpha-\mathbf{v}^{\overline{\alpha}})\eta_\alpha\right\rangle_{\Omega_\alpha,\Omega}-\langle b_\alpha\rangle_{\Omega_\alpha,\Omega}$$

$$-\left\langle \sum_{\kappa\in\mathcal{J}_{c\alpha}^{+}} \frac{\eta_\kappa}{\rho_\kappa} \underset{\kappa\to\alpha}{M} \right\rangle_{\Omega_\alpha,\Omega} - \left\langle \sum_{\kappa\in\mathcal{J}_{c\alpha}^{+}} \underset{\kappa\to\alpha}{\Phi} \right\rangle_{\Omega_\alpha,\Omega}$$
$$-\left\langle \nabla^{(m)}\cdot\left(\mathbf{I}_{\alpha}^{(m)}\cdot\boldsymbol{\varphi}_\alpha\right)\right\rangle_{\Omega_\alpha,\Omega} = \left\langle \Lambda_\alpha \right\rangle_{\Omega_\alpha,\Omega} \quad \text{for } \alpha\in\mathcal{J}; m = 3-\dim\alpha\ . \tag{66}$$

Application of the averaging theorems to this equation yields the macroscale entropy balance given by

$$\mathcal{S}_{*}^{\overline{\overline{\alpha}}} = \frac{\mathrm{D}^{\overline{\alpha}}\eta^{\overline{\overline{\alpha}}}}{\mathrm{D}t} + \eta^{\overline{\overline{\alpha}}}\mathbf{I{:}d}^{\overline{\overline{\alpha}}} - \epsilon^{\overline{\overline{\alpha}}}b^{\alpha} - \sum_{\kappa\in\mathcal{J}_{c\alpha}} \overset{\kappa\to\alpha}{M}\ \overline{\eta}^{\overline{\overline{\alpha,\kappa}}}$$
$$- \sum_{\kappa\in\mathcal{J}_{c\alpha}} \overset{\kappa\to\alpha}{\Phi} - \nabla\cdot\left(\epsilon^{\overline{\overline{\alpha}}}\boldsymbol{\varphi}^{\overline{\overline{\alpha}}}\right) = \Lambda^{\overline{\overline{\alpha}}} \quad \text{for } \alpha\in\mathcal{J}\ . \tag{67}$$

The new variables that appear with unique definitions are

$$\eta^{\overline{\overline{\alpha}}} = \epsilon^{\overline{\overline{\alpha}}}\eta^{\alpha} \tag{68}$$

$$\boldsymbol{\varphi}^{\overline{\overline{\alpha}}} = \left\langle \boldsymbol{\phi}_\alpha - \eta_\alpha(\mathbf{v}_\alpha - \mathbf{v}^{\overline{\alpha}})\right\rangle_{\Omega_\alpha,\Omega_\alpha} \tag{69}$$

$$\overline{\eta}^{\overline{\overline{\alpha,\kappa}}} = \begin{cases} \overline{\eta}_{\alpha}^{\overline{\kappa}} & \text{if } \kappa\in\mathcal{J}_{c\alpha}^{-} \\ \overline{\eta}_{\kappa}^{\overline{\alpha}} & \text{if } \kappa\in\mathcal{J}_{c\alpha}^{+} \end{cases} , \tag{70}$$

and

$$\Lambda^{\overline{\overline{\alpha}}} = \left\langle \Lambda_\alpha \right\rangle_{\Omega_\alpha,\Omega}\ . \tag{71}$$

We observe that the quantities that appear in this balance equation do not appear in the conservation equations. To make use of this equation in conjunction with those conservation equations, two steps are taken. First, summation over all the entities will cause the inter-entity exchange terms to cancel. This leaves

$$\sum_{\alpha\in\mathcal{J}} \mathcal{S}_{*}^{\overline{\overline{\alpha}}} = \sum_{\alpha\in\mathcal{J}} \left[\frac{\mathrm{D}^{\overline{\alpha}}\eta^{\overline{\overline{\alpha}}}}{\mathrm{D}t} + \eta^{\overline{\overline{\alpha}}}\mathbf{I{:}d}^{\overline{\overline{\alpha}}} - \epsilon^{\overline{\overline{\alpha}}}b^{\alpha} - \nabla\cdot\left(\epsilon^{\overline{\overline{\alpha}}}\boldsymbol{\varphi}^{\overline{\overline{\alpha}}}\right)\right] = \sum_{\alpha\in\mathcal{J}} \Lambda^{\overline{\overline{\alpha}}}\ . \tag{72}$$

Additionally, the second law of thermodynamics requires that entropy generation due to irreversible processes at a location will be non-negative. Therefore,

$$\sum_{\alpha\in\mathcal{J}} \Lambda^{\overline{\overline{\alpha}}} \geq 0\ . \tag{73}$$

The second step that is necessary to make the entropy inequality useful in conjunction with the conservation equations is to propose a thermodynamic formalism that relates internal energy to entropy. Here, we will start with classical irreversible thermodynamics postulated to hold at the microscale for each phase, interface, and common curve, and then integrate to the macroscale.

6 Thermodynamic Postulation

The simplest thermodynamic formulation that can be employed is classical irreversible thermodynamics (CIT) [Bai94, Cal85]. Because of its simplicity and the fact that it describes most systems of interest well, we will use it. We will implement CIT by averaging microscale relations to the macroscale. This serves to retain connections between thermodynamic quantities between scales. The CIT approach provides equations with similar structure when applied to fluids, interfaces, and the common curve. We will assume that the solid is elastic and provide the thermodynamic relations consistent with that approach. Note that the thermodynamic formalism is postulated. Thus, any reasonable postulated system can be employed and averaged to the macroscale.

Classical thermodynamics is concerned with the thermodynamic properties of equilibrium systems. The CIT approach as implemented here makes use of a local equilibrium assumption such that the thermodynamic relations that hold at equilibrium for a system are also considered to apply at points in the system. Essentially, this requires that the changes in the system occur slowly enough that thermodynamic variables can be identified and assumes that local point conditions are the same as at equilibrium. This assumption is concerned with rates of change in time as well as with spatial gradients. This is not considered to be a particularly crippling assumption as it has been found to apply in most instances of heating and cooling. Exceptions occur, for example, with a strong explosion where thermodynamic identities might be violated in the short term. We will employ the local equilibrium assumption at the microscale, but it is not required at the larger scale. The averaging of the thermodynamic equations provides information that relates larger to smaller scale variables. Of course, when the local equilibrium assumption applies at the macroscale, the analysis can be simplified.

The thermodynamics of fluid phases, interfaces, and common curves are all defined by the Euler form of the energy equation. This equation is expressed with extensive variables converted to densities relative to the dimensionality of the entity. The thermodynamic expression is

$$E_\alpha = \theta_\alpha \eta_\alpha + \mu_\alpha \rho_\alpha - P_\alpha \quad \text{for } \alpha \in \mathcal{I}_{\setminus s} \ , \tag{74}$$

where θ_α is the microscale temperature of the α entity, μ_α is the chemical potential, and $P_\alpha = p_\alpha$ is pressure when α denotes a fluid phase, $P_\alpha = -\gamma_\alpha$ for an interface where γ_α is the interfacial tension, and $P_\alpha = \gamma_\alpha$ for a common curve where γ_α is the curvilinear tension of the curve. The notation $\mathcal{I}_{\setminus s}$ indicates that we are using this equation for all entities in the system except the solid. The derivative of this equation with respect to time is

$$\frac{\partial^{(m)} E_\alpha}{\partial t} - \theta_\alpha \frac{\partial^{(m)} \eta_\alpha}{\partial t} - \mu_\alpha \frac{\partial^{(m)} \rho_\alpha}{\partial t} = 0 \quad \text{for } \alpha \in \mathcal{I}_{\setminus s}, m = 3 - \text{dim } \alpha \tag{75}$$

and the gradient of Eqn (74) is

$$\nabla^{(m)} E_\alpha - \theta_\alpha \nabla^{(m)} \eta_\alpha - \mu_\alpha \nabla^{(m)} \rho_\alpha = 0 \quad \text{for } \alpha \in \mathcal{I}_{\setminus s}, m = 3 - \text{dim } \alpha \ . \tag{76}$$

Although it is not a thermodynamic condition, the equation for the rate of change of the gravitational potential is handled similarly to the thermodynamic condition. Because $\Psi_\alpha = \rho_\alpha \psi_\alpha$, the temporal and spatial derivatives of this expression are, respectively

$$\frac{\partial^{(m)} \Psi_\alpha}{\partial t} - \psi_\alpha \frac{\partial^{(m)} \rho_\alpha}{\partial t} - \rho_\alpha \frac{\partial^{(m)} \psi_\alpha}{\partial t} = 0 \quad \text{for } \alpha \in \mathfrak{I}_{\backslash s}, m = 3 - \text{dim}\, \alpha \tag{77}$$

and

$$\nabla^{(m)} \Psi_\alpha - \psi_\alpha \nabla^{(m)} \rho_\alpha - \rho_\alpha \nabla^{(m)} \psi_\alpha = 0 \quad \text{for } \alpha \in \mathfrak{I}_{\backslash s}, m = 3 - \text{dim}\, \alpha \; . \tag{78}$$

Averaging theorem Eqn (32) can be applied to Eqns (75) and (77), and Eqn (30) can be applied to Eqns (76) and (78), respectively, to obtain averaged forms. The summation of these results, after dotting the gradient expressions with $\mathbf{v}^{\overline{\alpha}}$, yields the macroscale form of the thermodynamic relation in combination with the gravitational potential given by

$$\begin{aligned}
\mathcal{T}_*^{\overline{\overline{\alpha}}} + \mathcal{T}_{\mathcal{G}*}^{\overline{\overline{\alpha}}} = {} & \frac{\mathrm{D}^{\overline{\alpha}} (E^{\overline{\overline{\alpha}}} + \Psi^{\overline{\overline{\alpha}}})}{\mathrm{D}t} - \theta^{\overline{\overline{\alpha}}} \frac{\mathrm{D}^{\overline{\alpha}} \eta^{\overline{\overline{\alpha}}}}{\mathrm{D}t} - (\mu^{\overline{\alpha}} + \psi^{\overline{\alpha}}) \frac{\mathrm{D}^{\overline{\alpha}} (\epsilon^{\overline{\overline{\alpha}}} \rho^\alpha)}{\mathrm{D}t} \\
& + \sum_{\kappa \in \mathfrak{I}_{c\alpha}^-} \left\langle \mathbf{n}_\alpha \boldsymbol{\cdot} \left(\mathbf{v}_\kappa - \mathbf{v}^{\overline{s}} \right) P_\alpha \right\rangle_{\Omega_\kappa, \Omega} \\
& + \left\langle \eta_\alpha \frac{\mathrm{D}^{(m)\overline{s}} (\theta_\alpha - \theta^{\overline{\overline{\alpha}}})}{\mathrm{D}t} \right\rangle_{\Omega_\alpha, \Omega} + \left\langle \rho_\alpha \frac{\mathrm{D}^{(m)\overline{s}} (\mu_\alpha - \mu^{\overline{\alpha}} - \psi^{\overline{\alpha}})}{\mathrm{D}t} \right\rangle_{\Omega_\alpha, \Omega} \\
& - \left[\eta^{\overline{\overline{\alpha}}} \nabla \theta^{\overline{\overline{\alpha}}} - \nabla \boldsymbol{\cdot} \left\langle \mathsf{I}_\alpha^{(m)} P_\alpha \right\rangle_{\Omega_\alpha, \Omega} + \epsilon^{\overline{\overline{\alpha}}} \rho^\alpha \nabla (\mu^{\overline{\alpha}} + \psi^{\overline{\alpha}}) \right] \cdot \left(\mathbf{v}^{\overline{\alpha}} - \mathbf{v}^{\overline{s}} \right) \\
& - \nabla \boldsymbol{\cdot} \left\langle \left(\mathsf{I} - \mathsf{I}_\alpha^{(m)} \right) \cdot \left(\mathbf{v}_\alpha - \mathbf{v}^{\overline{\alpha}} \right) P_\alpha \right\rangle_{\Omega_\alpha, \Omega} - \left\langle \left(\mathsf{I} - \mathsf{I}_\alpha^{(m)} \right) P_\alpha \right\rangle_{\Omega_\alpha, \Omega} \mathbf{:} \mathsf{\mathbf{d}}^{\overline{\overline{\alpha}}} \\
& - \left\langle \nabla^{(m)} \boldsymbol{\cdot} \mathsf{I}_\alpha^{(m)} \boldsymbol{\cdot} \left(\mathbf{v}_\alpha - \mathbf{v}^{\overline{s}} \right) P_\alpha \right\rangle_{\Omega_\alpha, \Omega} \\
& + \left\langle \eta_\alpha \left(\mathbf{v}_\alpha - \mathbf{v}^{\overline{s}} \right) \cdot \left(\mathsf{I} - \mathsf{I}_\alpha^{(m)} \right) \right\rangle_{\Omega_\alpha, \Omega} \boldsymbol{\cdot} \nabla \theta^{\overline{\overline{\alpha}}} \\
& + \left\langle \rho_\alpha \left(\mathbf{v}_\alpha - \mathbf{v}^{\overline{s}} \right) \cdot \left(\mathsf{I} - \mathsf{I}_\alpha^{(m)} \right) \right\rangle_{\Omega_\alpha, \Omega} \boldsymbol{\cdot} \nabla (\mu^{\overline{\alpha}} + \psi^{\overline{\alpha}}) = 0 \\
& \qquad \text{for } \alpha \in \mathfrak{I}_{\backslash s}, m = 3 - \text{dim}\, \alpha \; ,
\end{aligned} \tag{79}$$

where

$$\Psi^{\overline{\overline{\alpha}}} = \epsilon^{\overline{\overline{\alpha}}} \Psi^\alpha \; , \tag{80}$$

$$\theta^{\overline{\overline{\alpha}}} = \langle \theta_\alpha \rangle_{\Omega_\alpha, \Omega_\alpha, \eta_\alpha} \; , \tag{81}$$

and

$$\frac{\mathrm{D}^{(m)\overline{s}}}{\mathrm{D}t} = \frac{\partial^{(m)}}{\partial t} + \mathbf{v}^{\overline{s}} \boldsymbol{\cdot} \nabla^{(m)} \; . \tag{82}$$

The fact that although the local equilibrium assumption is applied at the microscale but is not required to hold at the macroscale is evident in the appearance of terms involving averages of the difference between microscale and macroscale thermodynamic variables. When macroscale local equilibrium applies, these terms are dropped.

An important area for additional research is the representation of solid phases at the macroscale. In some cases, it is sufficient to treat the solid as a highly viscous fluid. In those cases, the thermodynamic formulation for the solid is as above. Here, we adopt the relatively simple model of the solid as an elastic material, which can be formulated as

$$E_s = \theta_s \eta_s + \boldsymbol{\sigma}_s \mathbf{:} \frac{\mathsf{\mathbf{C}}_s}{j_s} + \mu_s \rho_s \ , \tag{83}$$

where $\boldsymbol{\sigma}_s$ is a stress tensor, $\mathsf{\mathbf{C}}_s$ is Green's deformation tensor, and j_s is the Jacobian. The time and space derivatives of this equation may be written, respectively, as

$$\frac{\partial E_s}{\partial t} = \theta_s \frac{\partial \eta_s}{\partial t} + \boldsymbol{\sigma}_s \mathbf{:} \frac{\partial}{\partial t} \left(\frac{\mathsf{\mathbf{C}}_s}{j_s} \right) + \mu_s \frac{\partial \rho_s}{\partial t} \tag{84}$$

and

$$\nabla E_s = \theta_s \nabla \eta_s + \boldsymbol{\sigma}_s \mathbf{:} \nabla \left(\frac{\mathsf{\mathbf{C}}_s}{j_s} \right) + \mu_s \nabla \rho_s \ . \tag{85}$$

These expressions may each be converted to a macroscale expression by making use of the averaging theorems. With the resultant gradient expression dotted with $\mathbf{v}^{\overline{s}}$ added to the time derivative expression and that equation added to the result of averaging the expressions for the derivatives of the potentials in Eqns (77) and (78), the expression for the relation among the rates of change of macroscale thermodynamic properties of the solid is

$$\begin{aligned}
\mathcal{T}_*^{\overline{\overline{s}}} + \mathcal{T}_{\mathcal{G}*}^{\overline{\overline{s}}} = {} & \frac{\mathrm{D}^{\overline{s}}(E^{\overline{\overline{s}}} + \Psi^{\overline{\overline{s}}})}{\mathrm{D}t} - \theta^{\overline{\overline{s}}} \frac{\mathrm{D}^{\overline{s}} \eta^{\overline{\overline{s}}}}{\mathrm{D}t} - (\mu^{\overline{s}} + \psi^{\overline{s}}) \frac{\mathrm{D}^{\overline{s}}(\epsilon^{\overline{\overline{s}}} \rho^s)}{\mathrm{D}t} \\
& - \sum_{\kappa \in \mathfrak{I}_{\mathrm{cs}}} \left\langle \mathbf{n}_s \boldsymbol{\cdot} (\mathbf{v}_\kappa - \mathbf{v}_s)\, \boldsymbol{\sigma}_s \mathbf{:} \frac{\mathsf{\mathbf{C}}_s}{j_s} \right\rangle_{\Omega_\kappa, \Omega} - \sum_{\kappa \in \mathfrak{I}_{\mathrm{cs}}} \left\langle \mathbf{n}_s \boldsymbol{\cdot} \mathbf{t}_s \boldsymbol{\cdot} \left(\mathbf{v}_s - \mathbf{v}^{\overline{s}} \right) \right\rangle_{\Omega_\kappa, \Omega} \\
& + \left\langle \eta_s \frac{\mathrm{D}^{\overline{s}}(\theta_s - \theta^{\overline{\overline{s}}})}{\mathrm{D}t} \right\rangle_{\Omega_s, \Omega} + \left\langle \rho_s \frac{\mathrm{D}^{\overline{s}}(\mu_s - \mu^{\overline{s}} - \psi^{\overline{s}})}{\mathrm{D}t} \right\rangle_{\Omega_s, \Omega} \\
& - \nabla \boldsymbol{\cdot} \left\langle \left(\mathbf{t}_s - \boldsymbol{\sigma}_s \mathbf{:} \frac{\mathsf{\mathbf{C}}_s}{j_s} \mathsf{\mathbf{I}} \right) \boldsymbol{\cdot} \left(\mathbf{v}_s - \mathbf{v}^{\overline{s}} \right) \right\rangle_{\Omega_s, \Omega} - \epsilon^{\overline{\overline{s}}} \mathbf{t}^s \mathbf{:} \mathbf{d}^{\overline{s}} + \epsilon^{\overline{\overline{s}}} \boldsymbol{\sigma}^{\overline{\overline{s}}} \mathbf{:} \frac{\mathsf{\mathbf{C}}^s}{j^s} \mathsf{\mathbf{I}} \mathbf{:} \mathbf{d}^{\overline{s}} \\
& + \left\langle \left(\nabla \boldsymbol{\cdot} \mathbf{t}_s - \nabla \boldsymbol{\sigma}_s \mathbf{:} \frac{\mathsf{\mathbf{C}}_s}{j_s} \right) \boldsymbol{\cdot} \left(\mathbf{v}_s - \mathbf{v}^{\overline{s}} \right) \right\rangle_{\Omega_s, \Omega} = 0 \ .
\end{aligned} \tag{86}$$

This expression makes use of the microscale local equilibrium approximation and also accounts for the fact that a concentrated force can act on the solid surface and at common curves.

7 Evolution Equations

One additional set of macroscale equations are the kinematic equation that describe the deformation of the space occupied by a phase, the extents of interfaces and the common curve [GM10, GTS02, GM14]. These kinematic equations have received much less attention than the conservation and thermodynamic relations. Nevertheless, they provide some essential auxiliary equation for macroscale analysis of porous media systems.

Kinematics of irregular geometries are difficult to describe in detail, but macroscale descriptions based on averaging theorems, in particular Eqns (30) and (32) with $f_\alpha = 1$, provide exact relations that can be approximated for utilization. With $f_\alpha = 1$, Eqn (30) becomes

$$0 = \nabla\epsilon^{\overline{\overline{\alpha}}} - \nabla\cdot\left\langle \mathsf{I} - \mathsf{I}_\alpha^{(m)} \right\rangle_{\Omega_\alpha,\Omega} - \left\langle \nabla^{(m)}\cdot\mathsf{I}_\alpha^{(m)} \right\rangle_{\Omega_\alpha,\Omega} + \sum_{\kappa\in\mathcal{I}_{c\alpha}^{-}} \langle \mathbf{n}_\alpha \rangle_{\Omega_\kappa,\Omega}$$

$$\text{for } \alpha \in \mathcal{I}, m = 3 - \dim\alpha\ , \qquad (87)$$

while Eqn (32) reduces to

$$0 = \frac{\partial\epsilon^{\overline{\overline{\alpha}}}}{\partial t} + \nabla\cdot\left\langle \left(\mathsf{I} - \mathsf{I}_\alpha^{(m)}\right)\cdot\mathbf{v}_\alpha \right\rangle_{\Omega_\alpha,\Omega} + \left\langle \nabla^{(m)}\cdot\mathsf{I}_\alpha^{(m)}\cdot\mathbf{v}_\alpha \right\rangle_{\Omega_\alpha,\Omega}$$

$$- \sum_{\kappa\in\mathcal{I}_{c\alpha}^{-}} \langle \mathbf{n}_\alpha\cdot\mathbf{v}_\kappa \rangle_{\Omega_\kappa,\Omega} \quad \text{for } \alpha \in \mathcal{I}, m = 3 - \dim\alpha\ . \qquad (88)$$

Broadly speaking, the first term on the right-hand side of these equations provides the change in the specific quantity with space or time. In Eqn (87), the second two terms describe the contributions to the spatial change in $\epsilon^{\overline{\overline{\alpha}}}$ due to orientation effects for surfaces and common curves (for a phase these two terms are zero). The final term accounts for spatial changes encountered due to changes in the amounts of an entity of lower order with space. The only components of the velocity that appear in the second two terms in Eqn (88) are those that are normal to the entity (again, these terms are zero for a phase). The terms describe how the extent of an interface or common curve changes due to the deformation of that interface. The final term in this equation accounts for change in the extent of the interface due to movement of the boundary.

The prime difficulty in working with these kinematic equations is to relate the change in the extent of one entity to the change in the extent of its boundary. For example, the boundary of a phase is easy to model if the phase is spherical and remains spherical as it changes size. The rate of change of surface area is directly related to the rate of change of volume. For complicated phase geometries, phase boundaries, and curve lengths, a simple relation cannot be obtained. Nevertheless, Eqns (87) and (88) provide exact relations. The averages that appear in these equations can be approximated to obtain appropriate macroscale kinematic descriptions. These results are then investigated and applied with all variables written at the macroscale.

Evolution equations are written while moving at the solid velocity. Because the solid deforms slowly, this allows for following an interface within the system relative to the solid. To obtain the needed equation, we take the dot product of Eqn (87) with $\mathbf{v}^{\overline{s}}$ and add this to Eqn (88). After minor rearrangement, this gives

$$\begin{aligned}\frac{\mathrm{D}^{\overline{s}}\epsilon^{\overline{\overline{\alpha}}}}{\mathrm{D}t} &+ \nabla\cdot\left\langle\left(\mathbf{I} - \mathbf{I}_\alpha^{(m)}\right)\cdot\left(\mathbf{v}_\alpha - \mathbf{v}^{\overline{s}}\right)\right\rangle_{\Omega_\alpha,\Omega} + \left\langle\mathbf{I} - \mathbf{I}_\alpha^{(m)}\right\rangle_{\Omega_\alpha,\Omega}\mathbf{:}\mathbf{d}^{\overline{s}} \\ &+ \left\langle\nabla^{(m)}\cdot\mathbf{I}_\alpha^{(m)}\cdot\left(\mathbf{v}_\alpha - \mathbf{v}^{\overline{s}}\right)\right\rangle_{\Omega_\alpha,\Omega} - \sum_{\kappa\in\mathfrak{I}_{c\alpha}^{-}}\left\langle\mathbf{n}_\alpha\cdot\left(\mathbf{v}_\kappa - \mathbf{v}^{\overline{s}}\right)\right\rangle_{\Omega_\kappa,\Omega} = 0 \\ &\text{for } \alpha\in\mathfrak{I}, m = 3 - \dim\alpha\ . \qquad (89)\end{aligned}$$

This description of the evolution of various entities becomes useful when all the quantities in the averaging operators are expressed in terms of macroscale variables, in particular the macroscale variables that already have entered the problem formulation in the development of the conservation and thermodynamic equations. Although the equations for the various geometric densities are difficult to express in terms of the large scale variables, they nevertheless provide important conditions that must not be violated by calculations of model behavior. Nevertheless, these equations are important constraints on the behavior of the system. For the two-fluid-phase system of concern here, we make some approximations that can be revisited if significant errors in subsequent macroscale simulations or insights gained from microscale simulations suggest a need to do so.

The derivation of approximate forms of Eqn (89) for various entities will not be presented here as the identification of potentially useful approximations is rather lengthy. The details may be found in [GM10], or using a more general approach in [GM14]. Here, we provide the approximate equation for the evolution of the wn interface when solid deformation is much slower than fluid redistribution. Elements of the physical processes that can cause $\epsilon^{\overline{\overline{wn}}}$ to evolve are the normal velocity of the interface, interfacial curvature changes, and the movement of the common curve on the solid surface. The governing approximate equation obtained is

$$\begin{aligned}\frac{\mathrm{D}^{\overline{s}}\epsilon^{\overline{\overline{wn}}}}{\mathrm{D}t} &+ \nabla\cdot\left[\epsilon^{\overline{\overline{wn}}}\left(\mathbf{w}^{wn} - \mathbf{G}^{wn}\cdot\mathbf{v}^{\overline{s}}\right)\right] - J_w^{wn}\frac{\mathrm{D}^{\overline{s}}\epsilon^{\overline{\overline{w}}}}{\mathrm{D}t} \\ &- \hat{k}^{wn}\left(\epsilon_{\mathrm{eq}}^{\overline{\overline{wn}}} - \epsilon^{\overline{\overline{wn}}}\right) - \cos\varphi^{\overline{\overline{ws,wn}}}\left(\epsilon^{\overline{\overline{ws}}} + \epsilon^{\overline{\overline{ns}}}\right)\frac{\mathrm{D}^{\overline{s}}\chi_s^{\overline{\overline{ws}}}}{\mathrm{D}t} = 0\ , \qquad (90)\end{aligned}$$

where

$$\mathbf{w}^{wn} = \left\langle\left(\mathbf{I} - \mathbf{I}'_{wn}\right)\cdot\mathbf{v}_{wn}\right\rangle_{\Omega_{wn},\Omega_{wn}}\ , \qquad (91)$$

$$\mathbf{G}^{wn} = \left\langle\mathbf{I} - \mathbf{I}'_{wn}\right\rangle_{\Omega_{wn},\Omega_{wn}}\ , \qquad (92)$$

$$J_w^{wn} = \left\langle\nabla'\cdot\mathbf{n}_w\right\rangle_{\Omega_{wn},\Omega_{wn}}\ , \qquad (93)$$

and

$$\chi_s^{\overline{\overline{ws}}} = \langle 1\rangle_{\Omega_{ws},\Gamma_s}\ . \qquad (94)$$

The terms in Eqn (90) are, in order, the rate of change of wn interface density, the net outward flux of $\epsilon^{\overline{\overline{wn}}}$, increase in $\epsilon^{\overline{\overline{wn}}}$ caused by a change in the volume fraction of fluid phase w, relaxation of $\epsilon^{\overline{\overline{wn}}}$ to an equilibrium configuration, and the change in $\epsilon^{\overline{\overline{wn}}}$ due to movement of the common curve that is the boundary of the interface. The quantity $\mathbf{G}^{wn}$ is an orientation tensor that accounts for the fact that the wn interface may have a preferred orientation direction, J_w^{wn} is the curvature of the interface, and $\chi_s^{\overline{\overline{ws}}}$ is the fraction of the solid surface in contact with the w phase.

The evolution of the ws and ns interfaces as well as the evolution of the wns common curve would seem to be less important than the kinematics of the fluid-fluid interface. Approximations for evolution equations for these entities can be made [GM14], but errors in the approximations are less important than for the fluid-fluid interface.

In conclusion, the kinematic equations are a typically overlooked element of the description of porous medium systems. However, as in the description of boiling processes [IKSH09], useful approximations to the evolution equations are necessary when the interface dynamics are significant. Because multifluid systems are impacted by capillary effects at the fluid-fluid interface and may involve mass transfer across that interface, knowledge of the kinematics of those interfaces are particularly important.

8 Augmented Entropy Inequality

One of the reasons for generating an entropy inequality is that it provides a constraint on allowable processes. In the present case, we need to develop closure relations for exchange terms and for dissipative fluxes such that they do not violate the second law of thermodynamics as expressed in the entropy inequality. The objective of this section is to augment the entropy inequality with conservation and thermodynamic equations in order to isolate the mechanisms that contribute to entropy generation. The augmented entropy inequality, with conservation and thermodynamic equations for all entities added on, is

$$\begin{aligned}\sum_{\alpha\in\mathfrak{I}} \mathcal{S}_*^{\overline{\overline{\alpha}}} + \sum_{\alpha\in\mathfrak{I}} \lambda_{\mathcal{E}}^{\alpha} \left(\mathcal{E}_*^{\overline{\overline{\alpha}}} + \mathcal{G}_*^{\overline{\overline{\alpha}}}\right) + \sum_{\alpha\in\mathfrak{I}} \boldsymbol{\lambda}_{\boldsymbol{\mathcal{P}}}^{\alpha}\cdot\boldsymbol{\mathcal{P}}_*^{\overline{\overline{\alpha}}} + \sum_{\alpha\in\mathfrak{I}} \lambda_{\mathcal{M}}^{\alpha}\mathcal{M}_*^{\overline{\overline{\alpha}}} \\ + \sum_{\alpha\in\mathfrak{I}} \lambda_{\mathcal{T}}^{\alpha}\left(\mathcal{T}_*^{\overline{\overline{\alpha}}} + \mathcal{T}_{\mathcal{G}*}^{\overline{\overline{\alpha}}}\right) = \sum_{\alpha\in\mathfrak{I}} \Lambda^{\overline{\overline{\alpha}}} \geq 0\ . \qquad (95)\end{aligned}$$

In this equation, the coefficients, λ and $\boldsymbol{\lambda}$ that multiply conservation and thermodynamic equations are Lagrange multipliers. The values of these multipliers do not alter the inequality because they each multiply equations that are equal to zero. The selection of the multipliers thus can alter the grouping of terms that sum to equal the generation term, but the value of the sum is independent of the value of the multipliers.

The multipliers are selected such that the material derivatives are eliminated from the equations in favor of retention of the flux and source terms. This is accomplished by examination of the material derivatives that appear in Eqn (95) and ensuring that the multipliers serve to cancel them out. The result of this process gives values of the multipliers such that the entropy inequality is

$$\begin{aligned}
&\sum_{\alpha\in\mathfrak{J}} \mathcal{S}_*^{\overline{\overline{\alpha}}} - \sum_{\alpha\in\mathfrak{J}} \frac{1}{\theta^{\overline{\overline{\alpha}}}} \left(\mathcal{E}_*^{\overline{\overline{\alpha}}} + \mathcal{G}_*^{\overline{\overline{\alpha}}}\right) + \sum_{\alpha\in\mathfrak{J}} \frac{\mathbf{v}^{\overline{\alpha}}}{\theta^{\overline{\overline{\alpha}}}} \cdot \boldsymbol{\mathcal{P}}_*^{\overline{\overline{\alpha}}} \\
&+ \sum_{\alpha\in\mathfrak{J}} \left(\mu^{\overline{\alpha}} + \psi^{\overline{\alpha}} - \frac{\mathbf{v}^{\overline{\alpha}} \cdot \mathbf{v}^{\overline{\alpha}}}{2} + K_E^{\overline{\overline{\alpha}}}\right) \mathcal{M}_*^{\overline{\overline{\alpha}}} \\
&+ \sum_{\alpha\in\mathfrak{J}} \frac{1}{\theta^{\overline{\overline{\alpha}}}} \left(\mathcal{T}_*^{\overline{\overline{\alpha}}} + \mathcal{T}_{\mathcal{G}*}^{\overline{\overline{\alpha}}}\right) = \sum_{\alpha\in\mathfrak{J}} \Lambda^{\overline{\overline{\alpha}}} \geq 0\,. \qquad (96)
\end{aligned}$$

Although this equation is rather innocuous, if one expands out the summations it becomes quite a long equation. Even when terms are cancelled to the degree possible, and identical equation forms are retained in summations, the resulting equation, referred to as the Constrained Entropy Inequality (CEI) is several pages long [GM14]. For conciseness, we will not reproduce that equation here.

Because of its length and complexity, including some averages that require evaluation, the CEI is not in a useful form for analysis of a system of interest. It is, however, a useful equation to serve as an intermediate starting point for analysis of systems without repeating all the algebraic work needed for its derivation. Proceeding from the CEI, which contains no mathematical approximations, we can introduce simplifications based on the processes to be modeled. Introduction of these approximations leads to a simplified entropy inequality (SEI) that applies to a class of systems. To reduce to a specific system of interest, further approximations must be made, for example by restricting the system to be isothermal.

As an example, we can obtain a simplified SEI for an isothermal system with no mass exchange between entities and with the interfaces and common curves specified as massless. Other restrictions apply, but the SEI that results is [GM14]

$$\begin{aligned}
&+ \sum_{\alpha\in\mathfrak{J}_\mathrm{f}} \frac{1}{\theta^{\cdot}} \left(\epsilon^{\overline{\overline{\alpha}}} \mathbf{t}^{\overline{\overline{\alpha}}} + \epsilon^{\overline{\overline{\alpha}}} p^{\alpha} \mathbf{I}\right) \mathbf{:d}^{\overline{\overline{\alpha}}} + \frac{1}{\theta^{\cdot}} \left(\epsilon^{\overline{\overline{s}}} \mathbf{t}^{\overline{\overline{s}}} - \epsilon^{\overline{\overline{s}}} \mathbf{t}^{s}\right) \mathbf{:d}^{\overline{\overline{s}}} \\
&+ \sum_{\alpha\in\mathfrak{J}_\mathrm{I}} \frac{1}{\theta^{\cdot}} \left[\epsilon^{\overline{\overline{\alpha}}} \mathbf{t}^{\overline{\overline{\alpha}}} - \epsilon^{\overline{\overline{\alpha}}} \gamma^{\alpha} \left(\mathbf{I} - \mathbf{G}^{\alpha}\right)\right] \mathbf{:d}^{\overline{\overline{\alpha}}} \\
&+ \frac{1}{\theta^{\cdot}} \left[\epsilon^{\overline{\overline{wns}}} \mathbf{t}^{\overline{\overline{wns}}} + \epsilon^{\overline{\overline{wns}}} \gamma^{wns} \left(\mathbf{I} - \mathbf{G}^{wns}\right)\right] \mathbf{:d}^{\overline{\overline{wns}}} \\
&+ \sum_{\alpha\in\mathfrak{J}_\mathrm{f}} \frac{1}{\theta^{\cdot}} \Bigg\{ \nabla \left(\epsilon^{\overline{\overline{\alpha}}} p^{\alpha}\right) - \epsilon^{\overline{\overline{\alpha}}} \rho^{\alpha} \nabla \left(\mu^{\overline{\alpha}} + K_E^{\overline{\overline{\alpha}}} + \psi^{\overline{\alpha}}\right) - \epsilon^{\overline{\overline{\alpha}}} \rho^{\alpha} \mathbf{g}^{\overline{\alpha}} \\
&\qquad\qquad + \sum_{\kappa\in\mathfrak{J}_{\mathrm{c}\alpha}^{-}} \overset{\alpha\to\kappa}{\mathbf{T}} \Bigg\} \cdot \left(\mathbf{v}^{\overline{\alpha}} - \mathbf{v}^{\overline{s}}\right)
\end{aligned}$$

$$
\begin{aligned}
&- \sum_{\alpha\in\mathcal{J}_\mathrm{I}} \frac{1}{\theta} \Bigg\{ \nabla\cdot \left[\left(\mathsf{I} - \mathsf{G}^{\alpha}\right) \epsilon^{\overline{\overline{\alpha}}} \gamma^{\alpha} \right] + \sum_{\kappa\in\mathcal{J}^{+}_{\mathrm{c}\alpha}} \overset{\kappa\to\alpha}{\mathbf{T}} - \overset{\alpha\to wns}{\mathbf{T}} \Bigg\} \cdot \left(\mathbf{v}^{\overline{\alpha}} - \mathbf{v}^{\overline{s}} \right) \\
&+ \frac{1}{\theta} \Bigg\{ \nabla\cdot \left[\left(\mathsf{I} - \mathsf{G}^{wns}\right) \epsilon^{\overline{\overline{wns}}} \gamma^{wns} \right] - \sum_{\kappa\in\mathcal{J}^{+}_{\mathrm{cwns}}} \overset{\kappa\to wns}{\mathbf{T}} \\
&\qquad\qquad + \left\langle \mathbf{n}_s\cdot\mathbf{t}^{*}_{s}\cdot\mathbf{n}_s\mathbf{n}_s \right\rangle_{\Omega_{wns},\Omega} \Bigg\} \cdot \left(\mathbf{v}^{\overline{wns}} - \mathbf{v}^{\overline{s}} \right) \\
&+ \frac{1}{\theta} \left[\frac{\mathrm{D}^{\overline{s}} \epsilon^{\overline{\overline{w}}}}{\mathrm{D}t} - \chi_s^{\overline{\overline{ws}}} \frac{\mathrm{D}^{\overline{s}} \epsilon}{\mathrm{D}t} - \frac{\gamma^{wn} \hat{k}_1^{wn} \left(\epsilon^{\overline{\overline{wn}}} - \epsilon^{\overline{\overline{wn}}}_{\mathrm{eq}} \right)}{\left(p_w^{wn} - p_n^{wn} \right)} \right] \left(p_w^{wn} - p_n^{wn} - \gamma^{wn} J_w^{wn} \right) \\
&+ \frac{1}{\theta} \frac{\mathrm{D}^{\overline{s}} \epsilon}{\mathrm{D}t} \Bigg[\chi_s^{\overline{\overline{ws}}} p_w^{ws} + \chi_s^{\overline{\overline{ns}}} p_n^{ns} + \chi_s^{\overline{\overline{ws}}} \left(\mathbf{n}_s\cdot\mathbf{t}_s\cdot\mathbf{n}_s \right)^{ws} + \chi_s^{\overline{\overline{ns}}} \left(\mathbf{n}_s\cdot\mathbf{t}_s\cdot\mathbf{n}_s \right)^{ns} \\
&\qquad + \chi_s^{\overline{\overline{ws}}} \gamma^{ws} J_s^{ws} + \chi_s^{\overline{\overline{ns}}} \gamma^{ns} J_s^{ns} \\
&\qquad - \left(\frac{\epsilon^{\overline{\overline{wns}}}}{\epsilon^{\overline{\overline{ws}}} + \epsilon^{\overline{\overline{ns}}}} \right) \left(\gamma_{wn}^{wns} \sin \varphi^{\overline{\overline{ws,wn}}} - \gamma^{wns} \kappa_N^{\overline{\overline{wns}}} - \left(\mathbf{n}_s \cdot \mathbf{t}^{*}_{s}\cdot\mathbf{n}_s \right)^{wns} \right) \Bigg] \\
&- \frac{1}{\theta} \left(\epsilon^{\overline{\overline{ws}}} + \epsilon^{\overline{\overline{ns}}} \right) \frac{\mathrm{D}^{\overline{s}} \chi_{ws}^{ss}}{\mathrm{D}t} \left[\gamma_{wn}^{wns} \cos \varphi^{\overline{\overline{ws,wn}}} + \gamma_{ws}^{wns} - \gamma_{ns}^{wns} + \gamma^{wns} \kappa_G^{\overline{\overline{wns}}} \right] \\
&= \sum_{\alpha\in\mathcal{J}} \Lambda^{\overline{\overline{\alpha}}} \geq 0 \, .
\end{aligned}
\tag{97}
$$

An important feature of this equation is that all terms are products of two quantities, denoted as conjugate fluxes and forces, both of which must be zero at equilibrium. We know that they are zero from the conditions that velocity must be zero and from thermodynamic equilibrium constraints that are derived using variational methods but which are not included here. In this equation, we have written each product with the flux being the first factor and the force being the second factor. By exploiting this property, we can, in general, assume that each flux is a product of all the forces. In the simplest case, which is still applicable in a wide range of systems, we assume that each flux is linearly dependent on all the forces. However this general dependence can then be simplified based on knowledge of system behavior and interactions. Rather than listing these flux-force linearizations, we will proceed directly to the closed model.

9 Closed Conservation Equations

In this section we will present the closed conservation equations that result for slow flow in an isothermal porous medium. The interfaces are considered to be massless, and no phase change occurs between the phases.

9.1 Mass Conservation Equations

When the interfaces and common curves are massless and there is no mass exchange between phases, the only mass conservation equations are those for the phases. These are given by

$$\frac{\mathrm{D}^{\overline{\alpha}}(\epsilon^{\overline{\overline{\alpha}}}\rho^{\alpha})}{\mathrm{D}t} + \epsilon^{\overline{\overline{\alpha}}}\rho^{\alpha}\mathsf{I}{:}\mathsf{d}^{\overline{\overline{\alpha}}} = 0 \quad \text{for } \alpha \in \{w, n, s\} \ . \tag{98}$$

9.2 Fluid Momentum Equations

The momentum conservation equations for the w and n phases make use of the closure relations as linearizations of lines 1 and 4–5 of Eqn (97),

$$\mathsf{t}^{\overline{\overline{\alpha}}} = -p^{\alpha} \quad \text{for } \alpha \in \{w, n\} \ , \tag{99}$$

and

$$\begin{aligned} &\nabla\left(\epsilon^{\overline{\overline{\alpha}}}p^{\alpha}\right) - \epsilon^{\overline{\overline{\alpha}}}\rho^{\alpha}\nabla\left(\mu^{\overline{\alpha}} + \psi^{\overline{\alpha}}\right) - \epsilon^{\overline{\overline{\alpha}}}\rho^{\alpha}\mathbf{g}^{\overline{\alpha}} + \sum_{\kappa\in\mathcal{J}_{\mathrm{c}\alpha}^{-}} \overset{\alpha\to\kappa}{\mathbf{T}} \\ &\qquad = \sum_{\kappa\in\mathcal{J}_{\mathrm{f}}} \hat{\mathsf{R}}^{\alpha}_{\kappa}\cdot\left(\mathbf{v}^{\overline{\kappa}} - \mathbf{v}^{\overline{s}}\right) \quad \text{for } \alpha \in \{w, n\} \ . \end{aligned} \tag{100}$$

Substitution of these two equations into the general momentum equation, Eqn (51), under conditions of no mass exchange yields

$$\begin{aligned} &\frac{\mathrm{D}^{\overline{\alpha}}(\epsilon^{\overline{\overline{\alpha}}}\rho^{\alpha}\mathbf{v}^{\overline{\alpha}})}{\mathrm{D}t} + \epsilon^{\overline{\overline{\alpha}}}\rho^{\alpha}\mathbf{v}^{\overline{\alpha}}\mathsf{I}{:}\mathsf{d}^{\overline{\overline{\alpha}}} + \epsilon^{\overline{\overline{\alpha}}}\rho^{\alpha}\nabla\left(\mu^{\overline{\alpha}} + \psi^{\overline{\alpha}}\right) \\ &\quad + \hat{\mathsf{R}}^{\alpha}_{w}\cdot\left(\mathbf{v}^{\overline{w}} - \mathbf{v}^{\overline{s}}\right) + \hat{\mathsf{R}}^{\alpha}_{n}\cdot\left(\mathbf{v}^{\overline{n}} - \mathbf{v}^{\overline{s}}\right) = 0 \quad \text{for } \alpha \in \{w, n\} \ . \end{aligned} \tag{101}$$

For the case of slow flow, the first two terms in this equation are negligible. The remaining terms provide a Darcy-like expression for flow being proportional to a potential gradient with the added feature of coupling between the two fluid phases,

$$\epsilon^{\overline{\overline{\alpha}}}\rho^{\alpha}\nabla\left(\mu^{\overline{\alpha}} + \psi^{\overline{\alpha}}\right) + \hat{\mathsf{R}}^{\alpha}_{w}\cdot\left(\mathbf{v}^{\overline{w}} - \mathbf{v}^{\overline{s}}\right) + \hat{\mathsf{R}}^{\alpha}_{n}\cdot\left(\mathbf{v}^{\overline{n}} - \mathbf{v}^{\overline{s}}\right) = 0 \quad \text{for } \alpha \in \{w, n\} \ . \tag{102}$$

In many instances, it is convenient to write the driving force for the flow in terms of pressure rather than potential. To achieve this form, we note that the combination of the gradients of macroscale chemical and body force potential can be calculated as

$$\begin{aligned} \epsilon^{\overline{\overline{\alpha}}}\rho^{\alpha}\nabla\left(\mu^{\overline{\alpha}} + \psi^{\overline{\alpha}}\right) &= \epsilon^{\overline{\overline{\alpha}}}\left(\nabla p^{\alpha} - \rho^{\alpha}\mathbf{g}^{\overline{\alpha}}\right) + \langle\nabla\left(p_{\alpha} - p^{\alpha}\right)\rangle_{\Omega_{\alpha},\Omega} \\ &\quad - \left\langle\rho_{\alpha}\nabla\left(\mu_{\alpha} + \psi_{\alpha} - \mu^{\overline{\alpha}} - \psi^{\overline{\alpha}}\right)\right\rangle_{\Omega_{\alpha},\Omega} \quad \text{for } \alpha \in \{w, n\} \ . \end{aligned} \tag{103}$$

When the gradient of volume fraction in the vertical is small (not the case for infiltration problems with a sharp front), and the gradient of the difference term accounting for deviations between point and average values of potentials are also small, the last two terms on the right side of Eqn (103) can be eliminated. Then substitution into Eqn (102) yields

$$\epsilon^{\overline{\overline{\alpha}}}\left(\nabla p^{\alpha}-\rho^{\alpha}\mathbf{g}^{\overline{\alpha}}\right)+\hat{\mathbf{R}}^{\alpha}_{w}\cdot\left(\mathbf{v}^{\overline{w}}-\mathbf{v}^{\overline{s}}\right)+\hat{\mathbf{R}}^{\alpha}_{n}\cdot\left(\mathbf{v}^{\overline{n}}-\mathbf{v}^{\overline{s}}\right)=\mathbf{0}\quad\text{for } \alpha\in\{w,n\}\ . \tag{104}$$

To obtain the usual form of the flow equation, we also would have to drop the cross coupling term. Note that this equation is a simplification of the general form in many aspects. These must all be specifically indicated to obtain the usual form. The fact that the usual equation form for multiphase flow requires that cross-coupling not be considered, that pressure as a driving force is an approximation of potential, and that inertial terms have been eliminated is not known if one simply presumes that Darcy's law for single phase flow with a more complex form of the hydraulic conductivity is applicable.

A final equation needed for this model is obtained from line 9 of Eqn (97). If we linearize this expression and assume that cross-coupling of forces can be neglected, we obtain

$$\frac{\mathrm{D}^{\overline{s}}\epsilon^{\overline{\overline{w}}}}{\mathrm{D}t}-\chi_{s}^{\overline{\overline{ws}}}\frac{\mathrm{D}^{\overline{s}}\epsilon}{\mathrm{D}t}-\frac{\gamma^{wn}\hat{k}_{1}^{wn}\left(\epsilon^{\overline{\overline{wn}}}-\epsilon_{\text{eq}}^{\overline{\overline{wn}}}\right)}{\left(p_{w}^{wn}-p_{n}^{wn}\right)}=\hat{c}^{wn}\left(p_{w}^{wn}-p_{n}^{wn}-\gamma^{wn}J_{w}^{wn}\right)\ . \tag{105}$$

When the solid phase motion is negligible, this equation simplifies to

$$\epsilon\frac{\partial s^{\overline{\overline{w}}}}{\partial t}-\frac{\gamma^{wn}\hat{k}_{1}^{wn}\left(\epsilon^{\overline{\overline{wn}}}-\epsilon_{\text{eq}}^{\overline{\overline{wn}}}\right)}{\left(p_{w}^{wn}-p_{n}^{wn}\right)}=\hat{c}^{wn}\left(p_{w}^{wn}-p_{n}^{wn}+p^{c}\right)\ , \tag{106}$$

where we have also introduced the notation $p^{c}=-\gamma^{wn}J_{w}^{wn}$ into the last term.

Utilization of Eqn (106) provides an interesting challenge. *De facto,* the current typical approach is to assume the left side of the equation is negligible. We say, "*de facto*" because current approaches that are basically heuristic are unaware of the more general equation. Thus, the typical approach is to set

$$p_{w}^{wn}-p_{n}^{wn}+p^{c}=0\ . \tag{107}$$

Then p^{c} is presumed to be a function only of $s^{\overline{\overline{w}}}$, and experimental work is performed to evaluate this function at equilibrium.

A second approach, which arises directly in some formulations and is not understood as a simplification of Eqn (106), intrinsically neglects the second term and proposes that

$$\epsilon\frac{\partial s^{\overline{\overline{w}}}}{\partial t}=\hat{c}^{wn}\left(p_{w}^{wn}-p_{n}^{wn}+p^{c}\right)\ . \tag{108}$$

This formulation attributes the disequilibrium between the pressure difference and the capillary pressure to changing saturation in the system. However, recent work

[GM11b] has suggested that the relaxation of the interfacial area to an equilibrium value is important and must be considered when formulating multiphase flow models. This finding argues in favor of Eqn (106) in that it has the ability to model both changes in saturation and interfacial area. Work is under way to confirm this and to determine the impact of this finding on multiphase flow modeling.

10 Conclusions

These notes are intended to provide a very sparse outline of the TCAT approach. The elements of TCAT have been identified and some of the mathematical tools that are important for the method are identified. Information is omitted particularly with regard to solid phase thermodynamics, the derivation of equilibrium conditions based on variational methods, the full algebraic analysis of the augmented entropy inequality to obtain a simplified entropy inequality, and the exploitation of the SEI to obtain a closed system of equations. Closed flow equations for the fluid phases and a supplementary condition on capillary pressure are developed as examples. Details of the analysis may be found in [GM14]. The last item of a full TCAT analysis, confirmation of the theoretical results through experimental and computational work, is underway. The symbiotic use of theory with experiments and calculations will lead to more robust models than are available today.

Acknowledgments

This work was supported by Army Research Office grant W911NF-14-1-0287, National Science Foundation grant 0941235, and by Department of Energy grant DE-SC0002163.

References

[AJ67] T. B. Anderson and R. Jackson. A fluid mechanical description of fluidized beds. *Industrial and Engineering Chemistry Fundamentals*, 6:527–539, 1967.

[AL11] B. Aadnoy and R. Looyeh. *Petroleum Rock Mechanics: Drilling Operations and Well Design*. Gulf Professional Publishing, 2011.

[AS79] K. Aziz and A. Settari. *Petroleum Reservoir Simulation*. Applied Science Publ., Ltd., London, 1979.

[Bai94] M. Bailyn. *A Survey of Thermodynamics*. American Institute of Physics Press, New York, 1994.

[Bea79] J. Bear. *Hydraulics of Groundwater*. McGraw-Hill, New York, 1979.

[BEAZ15] M. L. Brusseau, A. El Ouni, J. B. Araujo, and H. Zhong. Novel methods for measuring air–water interfacial area in unsaturated porous media. *Chemosphere*, 127:208–213, May 2015.

[BJPV02] M. J. Blunt, M. D. Jackson, M. Piri, and P. H. Valvatne. Detailed physics, predictive capabilities and macroscopic consequences for pore-network models of multiphase flow. *Advances in Water Resources*, 25(8-12):1069–1089, 2002.

[Blu01] M. Blunt. Flow in porous media—Pore-network models and multiphase flow. *Current Opinion in Colloid and Interface Science*, 6(3):197–207, 2001.

[BN77] L. Boruvka and A. W. Neumann. Generalization of the classical theory of capillarity. *Journal of Chemical Physics*, 66(12):5464–5476, 1977.

[Bor75] L. Boruvka. An extension to classical theory of capillarity. Master's thesis, University of Toronto, Toronto, 1975.

[BRN85] L. Boruvka, Y. Rotenberg, and A. W. Neumann. Free energy formulation of the theory of capillarity. *Langmuir*, 1(1):40–44, 1985.

[BSSW14] K. Brown, S. Schl uter, A. Sheppard, and D. Wildenschild. On the challenges of measuring interfacial characteristics of three-phase fluid flow with x-ray microtomography. *Microscopy*, 253(3):171–182, March 2014.

[BVC15] T. Bultreys, L. Van Hoorebeke, and V. Cnudde. Multi-scale, micro-computed tomography-based pore network models to simulate drainage in heterogeneous rocks. *Advances in Water Resources*, 78:36–49, April 2015.

[Cal85] H. B. Callen. *Thermodynamics and an Introduction to Thermostatistics*. Wiley, New York, 1985.

[CJ86] G. Chavent and J. Jaffré. *Mathematical Models and Finite Elements for Reservoir Simulation*. North-Holland, Amsterdam, 1986.

[Dar56] H. Darcy. *Les Fontaines Publiques de la Ville de Dijon*. Dalmont, Paris, 1856.

[DMMG13] A. L. Dye, J. E. McClure, C. T. Miller, and W. G. Gray. Description of non-Darcy flows in porous medium systems. *Physical Review E*, 87(3), 2013.

[EFM00] M. Espedal, A. Fasano, and A. Mikelic. *Filtration in Porous Media and Industrial Applications*. Lecture Notes in Mathematics / C.I.M.E. Foundation Subseries (Book 1734). Springer, 2000.

[ETJ13] S. M. Eberts, M. A. Thomas, and M. L. Jagucki. *The Quality of our Nation's Waters: Factors Affecting Public-Supply-Well Vulnerability to Contamination: Understanding Observed Water Quality and Anticipating Future Water Quality*. Number 1385 in Circular. U. S. Geological Survey, 2013.

[Fat56] I. Fatt. The network model of porous media: I. Capillary pressure characteristics. *Transactions of the AIME*, 207:144–159, 1956.

[FC79] R. A. Freeze and J. A. Cherry. *Groundwater*. Prentice-Hall, Inc., Englewood Cliffs, NJ, 1979.

[GB11] D. L. Galloway and T. J. Burbey. Review: Regional land subsidence accompanying groundwater extraction. *Hydrogeology Journal*, 19:1459–1486, 2011.

[Ger84] J. J. Geraghty. Techniques for protecting groundwater quality. *Journal of the American Water Works Association*, 76(5):34–37, May 1984.

[GG10] W. G. Gray and M. S. Ghidaoui. Thermodynamic analysis of stream flow hydrodynamics. *Journal of Hydraulic Research*, in print, 2010.

[GH89] W. G. Gray and S. M. Hassanizadeh. Averaging theorems and averaged equations for transport of interface properties in multiphase systems. *International Journal of Multiphase Flow*, 15(1):81–95, 1989.

[GL77] W. G. Gray and P. C. Y. Lee. On the theorems for local volume averaging of multiphase systems. *International Journal of Multiphase Flow*, 3:333–340, 1977.

[GLKB93] W. G. Gray, A. Leijnse, R. L. Kolar, and C. A. Blain. *Mathematical Tools for Changing Spatial Scales in the Analysis of Physical Systems*. CRC Press, Boca Raton, 1993.

[GM05] W. G. Gray and C. T. Miller. Thermodynamically constrained averaging theory approach for modeling flow and transport phenomena in porous medium systems: 1. Motivation and overview. *Advances in Water Resources*, 28(2):161–180, 2005.

[GM10] W. G. Gray and C. T. Miller. Thermodynamically constrained averaging theory approach for modeling flow and transport phenomena in porous medium systems: 8. Interface and common curve dynamics. *Advances in Water Resources*, 33(12):1427–1443, 2010.

[GM11a] W. G. Gray and C. T. Miller. On the algebraic and differential forms of Darcy's equation. *Journal of Porous Media*, 14(1):33–50, 2011.

[GM11b] W. G. Gray and C. T. Miller. TCAT analysis of capillary pressure in non-equilibrium, two-fluid-phase, porous medium systems. *Advances in Water Resources*, 34(6):770–778, 2011.

[GM13] W. G. Gray and C. T. Miller. A generalization of averaging theorems for porous medium analysis. *Advances in Water Resources*, 62:227–237, 2013.

[GM14] W. G. Gray and C. T. Miller. *Introduction to the Thermodynamically Constrained Averaging Theory for Porous Medium Systems*. Springer, Switzerland, 2014.

[GTS02] W. G. Gray, A. F. B. Tompson, and W. E. Soll. Closure conditions for two-fluid flow in porous media. *Transport in Porous Media*, 47(1):29–65, 2002.

[GZ02] Z. Guo and T. S. Zhao. Lattice Boltzmann model for incompressible flows through porous media. *Physical Review E*, 66:036304–1–036304–9, 2002.

[HGM03] M. Hilpert, R. Glantz, and C. T. Miller. Calibration of a pore-network model by a pore-morphological analysis. *Transport in Porous Media*, 51(3):267–285, 2003.

[HvLB$^+$02] J. M. R. J. Huyghe, R. van Loon, F. P. T. Baaijens, P. M. van Kemenade, and T. H. Smit. We all are porous media. In J. L. Auriault, C. Geidreau, P. Royer, J. F. Bloch, C. Boutin, and J. Lewandowska, editors, *Poromechanics II*, pages 17–28. Swets and Zeitlinger, Lisse, the Netherlands, 2002.

[HW85] F. A. Howes and S. Whitaker. The spatial averaging theorem revisited. *Chemical Engineering Science*, 40:1387–1392, 1985.

[IKK05] M. Ishii, S. Kim, and J. Kelly. Development of interfacial area transport equation. *Nuclear Engineering and Technology*, 37(6):525–536, 2005.

[IKSH09] M. Ishii, S. Kim, X. Sun, and T. Hibiki. Interfacial area transport equation and implementation into two-fluid model. *Journal of Thermal Science and Engineering Applications*, 1(1), 2009.

[JCV01] D. Jou and J. Casas-Vázquez. Extended irreversible thermodynamics and its relation with other continuum approaches. *Journal of Non-Newtonian Fluid Mechanics*, 96(1–2):77–104, 2001.

[JCVL10] D. Jou, J. Casas-Vázquez, and G. Lebon. *Extended Irreversible Thermodynamics*. Springer, Berlin, 4^{th} edition, 2010.

[JJ14] B. Jha and R. Juanes. Coupled multiphase flow and poromechanics: A computational model of pore pressure effects on fault slip and earthquake triggering. *Water Resources Research*, 50(5):3776–3808, May 2014.

[JVC$^+$14] R. B. Jackson, A. Vengosh, W. Carey, R. J. Davies, T. H. Darrah, F. O'Sullivan, and G. Pétron. The environmental costs and benefits of fracking. *Environment and Resources*, 39:327–362, October 2014.

[KHJNK14] N. K. Karadimitriou, S. M. Hassanizadeh, V. Joekar-Niasar, and P. J. Kleingeld. Micromodel study of two-phase flow under transient conditions: Quantifying effects of specific interfacial area. *Water Resources Research*, 2014.

[KI05] S. Kim and M. Ishii. Dynamic modeling of interfacial structures via interfacial area transport equation. *La Houille Blanche*, 6:105–116, 2005.

[LHLT14] Q. Liu, Y. He, Q. Li, and W. Tao. A multiple-relaxation-time lattice boltzmann model for convection heat transfer in porous media. *International Journal of Heat and Mass Transfer*, 73:761–775, June 2014.

[LJCV08] G. Lebon, D. Jou, and J. Casas-Vázquez. *Understanding Nonequilibrium Thermodynamics*. Springer, Berlin, 2008.

[Mar67] C. Marle. Ècoulements monophasiques en milieu poreux. *Revue de L'Institut Français du Pétrole*, 22(10):1471–1509, 1967.

[Mau99] G. A. Maugin. *The Thermomechanics of Nonlinear Irreversible Behaviors: An Introduction*. World Scientific Press, Singapore, 1999.

[MG95] C. D. Montemagno and W. G. Gray. Photoluminescent volumetric imaging—A technique for the exploration of multiphase flow and transport in porous media. *Geophysical Research Letters*, 22(4):425–428, 1995.

[MG05] C. T. Miller and W. G. Gray. Thermodynamically constrained averaging theory approach for modeling flow and transport phenomena in porous medium systems: 2. Foundation. *Advances in Water Resources*, 28(2):181–202, 2005.

[MN85] C. A. Miller and P. Neogi. *Interfacial Phenomena*. Marcel Dekker, New York, 1985.

[MPM14] J. E. McClure, J. F. Prins, and C. T. Miller. A novel heterogeneous algorithm to simulate multiphase flow in porous media on multicore CPU-GPU systems. *Computer Physics Communications*, 185(7):1865–1874, 2014.

[Pin12] G. F. Pinder. Groundwater hydrology in 2050. In W. Grayman, D. P. Loucks, and L. Saito, editors, *Toward a Sustainable Water Future, Visions for 2050*, pages 277–287. American Society of Civil Engineers, 2012.

[PLM06] C. Pan, L.-S. Luo, and C. T. Miller. An evaluation of lattice Boltzmann schemes for porous medium flow simulation. *Computers & Fluids*, 35(8–9):898–909, 2006.

[PWL13] C. M. A. Parlett, K. Wilson, and A. F. Lee. Hierarchical porous materials: catalytic applications. *Chem Soc Rev*, 42:3876–3893, 2013.

[RCMR13] J. Rutqvist, F. Cappa, A. Mazzoldi, and A. Rinaldi. Geomechanical modeling of fault responses and the potential for notable seismic events during underground CO_2 injection. *Energy Procedia*, 37:4774–4784, 2013.

[RSML05] D. E. B. Reid, U. Silins, c. Mendoza, and V. J. Lieffers. A unified nomenclature for quantification and description of water conducting properties of sapwood xylem based on Darcy's law. *Tree Physiology*, 25(8):993–1000, 2005.

[SHCC06] O. Schmoll, G. Howard, J. Chilton, and I. Chorus, editors. *Protecting Groundwater for Health, Managing the Quality of Drinking-water Sources*. World Health Organization/IWA Publishing, 2006.

[Sla67] J. C. Slattery. Flow of viscoelastic fluids through porous media. *American Institute of Chemical Engineers Journal*, 13(6):1066–1071, 1967.

[SSG$^+$12] G. Sciumé, S. E. Shelton, W. G. Gray, C. T. Miller, F. Hussain, M. Ferrari, P. Decuzzi, and B. A. Schrefler. Tumor growth modeling from the perspective of multiphase porous media mechanics. *Molecular and Cellular Biomechanics*, 202(1):1–20, 2012.

[Whi67] S. Whitaker. Diffusion and dispersion in porous media. *American Institute of Chemical Engineers Journal*, 13(3):420–427, 1967.

[WS13] D. Wildenschild and A. P. Sheppard. X-ray imaging and analysis techniques for quantifying pore-scale structure and processes in subsurface porous medium systems. *Advances in Water Resources*, 51:217–246, 2013.

Generalized Plasticity modelling of geomaterials: the role of dilatancy

D. Manzanal, M. Pastor, J.Fernández-Merodo, P. Mira, M.M. Stikle, Á. Yagüe and Y. Javanmardi

Grupo M2i Modelos Matemáticos en Ingeniería
ETS de Ingenieros de Caminos, Canales y Puertos de Madrid
Universidad Politécnica de Madrid
d.manzanal@upm.es;m.pastor@upm.es

The Chapter is devoted to the constitutive modelling of geo-materials based on Generalized Plasticity Theory presented by Olek Zienkiewicz and Manuel Pastor. The aim is to provide the reader with an overview of the role of dilatancy in the modelling of the most relevant phenomena in soils behaviour such as liquefaction, bonding and de-bonding due to chemical processes or changes in the saturation conditions and influence of particle breakage.

1 Introduction

Constitutive models are a fundamental part of simulations codes, together with mathematical and numerical model. Much effort has been done during the past decades to improve our understanding of how geomaterials in general and soils in particular behave. Experimental techniques, such as tomography or the 3D testing devices [Des84] have provided valuable information which has helped constitutive researchers to improve their models. There are excellent texts and state of art papers devoted to describe constitutive models and their use in geotechnical engineering. We can mention here the classic texts of Cambou and Di Prisco [CdP00], Zienkiewicz et al [ZCP$^+$99] among others, and the references provided therein. In this chapter, we will focus on the Generalized Plasticity models which can reproduce behaviour of geomaterials under both monotonic and cyclic loading.

2 Generalized Plasticity

Generalized Plasticity Theory introduced by [ZM84] and elaborated by Zienkiewicz and Pastor [ZLP85], [PZL85], [PZC90], as it provides a framework within which accurate models can be developed to describe softening and liquefaction under monotonic and cyclic loading. The basic model has been extended to:

(1) Anisotropic materials by Pastor [Pas91]

(2) Bonded geomaterials and collapsible soils by Fernández-Merodo et al. [FMPM$^+$04]

(3)Granular soils incorporating a state parameter by Manzanal et al. [MFMP11]

(4)Non saturated soils by Tamagnini and Pastor [TP04] and Manzanal [MPM11]

Generalized Plasticity Theory introduces the dependence of the constitutive tensor relating increments of stress and strain on the direction of the increment of stress via a unit tensor n which discriminates the states of "loading" and "unloading"

$$\begin{aligned} d\boldsymbol{\varepsilon} &= \mathbf{C}_L : d\boldsymbol{\sigma} \quad for\ \ \mathbf{n} : d\boldsymbol{\sigma}^e > 0 \\ d\boldsymbol{\varepsilon} &= \mathbf{C}_U : d\boldsymbol{\sigma} \quad for\ \ \mathbf{n} : d\boldsymbol{\sigma}^e < 0 \end{aligned} \tag{1}$$

where $\boldsymbol{d\sigma}^e$ is the increment of stress which would be produced if the behaviour were elastic, $\boldsymbol{d\sigma}^e = \mathbf{D}^e : d\boldsymbol{\varepsilon}$, and $\mathbf{D}^e$ is the elastic constitutive tensor.

After imposing the condition of continuity between loading and unloading states, we arrive to

$$\begin{aligned} \mathbf{C}_L &= \mathbf{C}^e + \frac{1}{H_L}\mathbf{n}_{gL} \otimes \mathbf{n} \\ \mathbf{C}_U &= \mathbf{C}^e + \frac{1}{H_U}\mathbf{n}_{gU} \otimes \mathbf{n} \end{aligned} \tag{2}$$

In above equations, subindices L and U refer to "loading" and "unloading". The scalars are referred to as loading and unloading plastic moduli, and unit tensors give the direction of plastic flow during loading and unloading.

The limit case $\mathbf{n} : d\boldsymbol{\sigma}^e = 0$, is called "neutral loading", and with the assumption done in 2, it can be seen that response is continuous as:

$$\begin{aligned} d\boldsymbol{\varepsilon}_L &= \mathbf{C}_L : d\boldsymbol{\sigma} = \mathbf{C}^e : d\boldsymbol{\sigma} \\ d\boldsymbol{\varepsilon}_U &= \mathbf{C}_U : d\boldsymbol{\sigma} = \mathbf{C}^e : d\boldsymbol{\sigma} \end{aligned} \tag{3}$$

The strain increment can be decomposed into two parts, elastic and plastic as:

$$d\boldsymbol{\varepsilon} = d\boldsymbol{\varepsilon}^e + d\boldsymbol{\varepsilon}^p \tag{4}$$

with

$$d\boldsymbol{\varepsilon}^e = \mathbf{C}^e : d\boldsymbol{\sigma} \tag{5}$$

and

$$d\boldsymbol{\varepsilon}^p = \frac{1}{H_{L/U}} \mathbf{n}_{gL/U} \otimes \mathbf{n} \tag{6}$$

The main advantage of Generalized Plasticity Theory is that all ingredients can be postulated without introducing any yield or plastic potential surface. Moreover, it can be seen that both Classical Plasticity and Bounding Surface Plasticity models are special cases of the GPT.

We will describe next a simple model proposed by Pastor, Zienkiewicz , Leung and Chan [PZL85], [PZC90] which is able to reproduce the basic features of sand behaviour under cyclic loading.

3 A basic GP Model for granular soils

The main features of sand behaviour under monotonic and cyclic loading are the following: :

(i) Volumetric deformations depend mainly on the stress ratio $\eta = q/p'$. There is a characteristic value $\eta = M_g$ at which the behaviour changes from contractive to dilative. Ultimate state conditions at constant volume takes place also at this line, referred to as “Characteristic State Line” by Habib and Luong, and it can be interpreted as a Critical State Line for granular soils. The basic idea behind is that the soil, before failure, crosses a state at which there is no volume change, and comes back to it at residual conditions.

(ii) Very loose and loose sands exhibit compaction under shearing, which results on an increase of pore pressures when the loading process is not fully drained. In the limit, liquefaction can happen.

(iii) Dense sands exhibit dilation once the Characteristic State Line has been crossed. Dilation causes softening, and the strength decreases after a peak has been reached. Here, localization of strain in shear bands shadows the experimental results as the specimen is not homogeneous.

(iv) Under cyclic loading we observe the same compaction and dilation patterns. Plastic deformation occurs and the soil compacts progressively or the pore pressure increases. Liquefaction under cyclic loading is just the result of the increase of the pore pressure and the mechanism which is observed in monotonic loading.

(v) Medium dense sands under undrained cyclic loading develop an special type of behaviour which is referred to as ’cyclic mobility’. The difference with liquefaction consists on dilation which causes the pore pressure to decrease, hardening in turn the soil.

Taking into account all experimental facts described above, it is possible to develop a model within the Generalized Plasticity Theory as follows:

First of all, the direction of plastic flow in the (p', q) plane is postulated as:

$$\mathbf{n}_g^T = (n_{gv}, n_{gs}) \tag{7}$$

with

$$n_{gv} = \frac{d_g}{\sqrt{1 + d_g^2}} \tag{8}$$

$$n_{gs} = \frac{1}{\sqrt{1 + d_g^2}} \tag{9}$$

where the dilatancy d_g, which is defined as the ratio between the increments of plastic volumetric and shear strain is given by:

$$d_g = (1 + \alpha)(M_g - \eta) \tag{10}$$

The loading-unloading discriminating relation n is obtained in a similar way:

$$\mathbf{n}^T = (n_v, n_s) \tag{11}$$

with

$$n_v = \frac{d_f}{\sqrt{1 + d_f^2}} \tag{12}$$

$$n_s = \frac{1}{\sqrt{1 + d_f^2}} \tag{13}$$

where

$$d_f = (1 + \alpha)(M_f - \eta) \tag{14}$$

In above equations, M_f, M_g and α are model parameters.

The third ingredient is the plastic modulus H_L, which as to be defined both for loading and unloading. During loading, we will assume:

$$H_L = H_0 p' H_f \{H_v + H_s\} H_{DM} \tag{15}$$

where H_0 is a constitutive parameter, and

$$H_f = \left(1 - \frac{\eta}{\eta_f}\right)^4 \tag{16}$$

In above equations, η_f acts as a limit for the possible states,

$$\eta_f = \left(1 + \frac{1}{\alpha}\right) M_f \tag{17}$$

The volumetric and deviatoric components of the plastic modulus H_v are assumed to be of the form:

$$H_v = \left(1 - \frac{\eta}{M_g}\right) \tag{18}$$

$$H_s = \beta_0 \beta_1 \exp\left(-\beta_0 \xi\right) \tag{19}$$

Finally, H_{DM} keeps track of the maximum stress level reached by the material.

$$H_{DM} = \left(\frac{\zeta_{\max}}{\zeta}\right)^{\gamma} \tag{20}$$

where

$$\zeta = p'.\left\{1 - \left(\frac{1+\alpha}{\alpha}\right)\frac{\eta}{M}\right\}^{1/\alpha} \tag{21}$$

and γ is a new material constant.

Let us now consider each term. The volumetric term is zero at the CSL, and therefore, failure would take place there if H_s were zero. It can be observed in triaxial tests that both in drained and undrained processes, the stress paths are able to cross this line. The role of Hs is to prevent failure at this stage, but to allow it at residual conditions. This is achieved by making H_s to depend on the accumulated deviatoric strain ξ_{dev} defined from

$$d\xi_{dev} = \left(de^p : de^p\right)^{1/2} \tag{22}$$

where de^p is the increment of the plastic deviatoric strain tensor.

This basic model for sands was able to reproduce most salient aspects of sand behaviour under both drained and undrained conditions, the main limitation being the necessity of using different model parameters for different relative densities.

4 Modelling of collapsible soils

An improvement of the Generalized Plasticity model has been recently porposed by the authors to reproduce the mechanical behaviour of bonded soils, weak rocks and other materials of a similar kind.

Following the framework introduced by Gens & Nova [GN93] and Lagioia and Nova [LN95], two basic concepts lie the representation of this mechanical behaviour: the fundamental role played by yield phenomena and the need for considering the observed behaviour of the bonded material in relation with the behaviour of the equivalent unstructured one.

As the amount of bonding increases, the yield surface must grow up. Two parameters define the new enlarged yield locus: p_{c0} that controls the yielding of the bonded soil in isotropic compression and p_t which is related to the cohesion and tensile strength of the material. Both p_{c0} and p_t increase with the magnitude of bonding.

We can assume that the degradation of the material (decrease in bonding) is related to some kind of damage measure, that will in turn depend on plastic strains. Lagioia and Nova proposed simple laws to describe the debonding effect on a calcarenite material. The evolution of p_t is governed by:

$$p_t = p_{t0} \exp\left(-\rho_t \varepsilon^d\right) \tag{23}$$

where p_{t0} and p_t are two constitutive parameters and is the accumulated plastic volumetric strain. It appears reasonable to assume that changes of the yield locus will be controlled by two different phenomena: conventional plastic hardening (or softening) for an unbonded material and bond degradation. In that case, the plastic modulus of the sand model proposed by Pastor et al. [PZC90], can be improved introducing H_b as:

$$H_L = \left(H_0 p^* - H_b\right) H_f^* \left(H_v^* + H_s\right) H_{DM}^* \tag{24}$$

where we have introduced:

$$\begin{aligned} p^* &= p' + p_t \\ H_f^* &= \left(1 - \frac{\eta^*}{\eta_f}\right)^4 \qquad H_v^* = \left(1 - \frac{\eta^*}{M_g}\right) \\ H_b &= b_1 \varepsilon^d \exp\left(-b_2 \varepsilon^d\right) \qquad H_{DM}^* = \left(\frac{\zeta_{\max}^*}{\zeta^*}\right)^{\gamma_{DM}} \\ \eta* &= q/\left(p' + p_t\right) \qquad \zeta^* = \left(p' + p_t\right)\left\{1 - \left(\frac{\alpha_f}{1+\alpha_f}\right)\frac{\eta^*}{M}\right\}^{-1/\alpha} \end{aligned} \tag{25}$$

It can be seen that value of H_b decreases when the volumetric plastic strain increases (i.e. when debonding occurs) and in the limit case, when destructuration is complete, H_b becomes zero. In this case, the new plastic modulus defined above coincides with the original plastic modulus. The assumption of softening depending on plastic volumetric strain is consistent with classical soil hardening and softening, which depends mainly on plastic volumetric strain.

It is possible to reproduce with this improvement the laboratory tests of Lagioia and Nova on the Gravina calcarenite. Figure 1 (Fernández Merodo et al [FMPM$^+$04]) compares experimental data and model predictions for an isotropic compression test.

This type of behaviour -destructuration with an important compaction- is a mechanism which in our opinion plays a paramount role on the generation of pore pressures and catastrophic failure of soils. This is the case of the landslide of Las Colinas (El Salvador), triggered by the first 2001 earthquake. The soil presented cementation and was unsaturated. When sheared, this material can collapse, and if the loading is fast enough, pore pressures can cause the material to liquefy. In order to show qualitatively

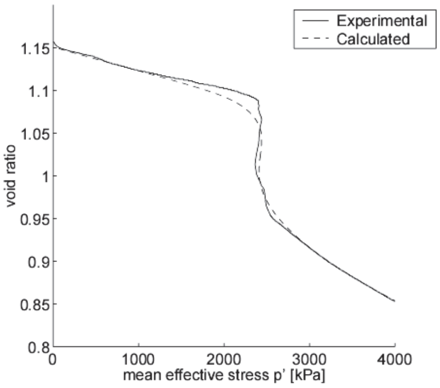

Figure 1: Isotropic compression test: experimental data from Lagioa and Nova and model predictions.

Table 1: Parameters of the constitutive model for Las Colinas landslide.

M_g	M_f	α	β_0	β_1	γ	p_{s0}
1.47	0.3	0.45	1-0	0.2	9.0	120 kPa

p_{m0}	p_{t0}	β_p	ρ_m	ρ_t	ξ
240 kPa	24kPa	0.06	8333	1000	-0.1

the phenomenon, we have performed a simulation on an ideal material, a fine grained soil with cementation. The parameters we have chosen are given in Table I.

Figures 2 show the results of a consolidated undrained triaxial test. We have depicted in Figure 2(left) the stress path and in Figure 2(right) the deviatoric stress vs axial strain for both the bonded and the unbonded materials.

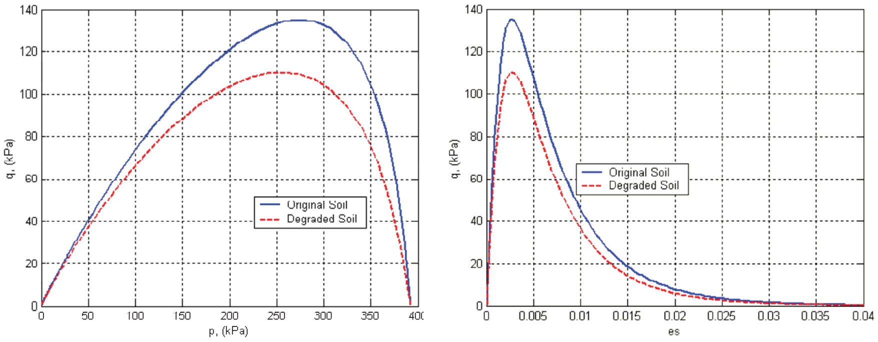

Figure 2: Undrained behaviour of a bonded loose granular soil: stress path (left) and Deviatoric stress versus axial strain (right).

5 A state parameter based Generalized Plasticity model

It is a well known fact that sands have different volumetric and stress – strain responses according to density and mean effective stress level. Contractive behaviour and strain hardening is observed in loose sands while dense sands show dilative behaviour and strain softening during shearing under drained loading. Moreover, for a given density, sands may show strong dilative behaviour at low confining pressures and fully contractive response at high confining pressures. This means that neither density nor confining pressure alone can fully characterize sand behaviour, but a combination of both. The idea of a unified parameter including this double dependency of sand behaviour was studied since the early works of Roscoe and Poorooshasb [RP63], Wroth and Basset [WB65], and Seed and Lee [SK67]. The first constitutive model incorporating a state parameter is the Harmonic Response model of Uriel [Uri75]. In recent years several attempts have been made to deal with the influence of density and confining pressure in soil modelling. It is worth mentioning the work of Jefferies & Shuttle [JA05], Yang and Ling [YL05], Taiebat and Dafalias [TD08], among others. The state parameter, as nowadays is known, has various definitions depending of the different combinations of the current state and critical state [BJ85, Ish93, WDLM02]. The most widely accepted state parameter today is that proposed by Been and Jefferies

[BJ85]. It is defined as the difference of the current voids ratio and the voids ratio at critical state under the same confining pressure. As the state parameter definition is based on the critical state line, we have chosen that proposed by Li [Li97]

$$\psi = e - e_c = e - e_\Gamma + \lambda \left(\frac{p\prime_c}{p\prime_a} \right)^{\zeta_c} \tag{26}$$

where e_Γ is void ratio at a confining pressure of 1 kPa, λ is the slope of critical state line in a plane, e_c and $p\prime_c$ are the void ratio and the confining pressure at critical state, respectively and $p\prime_a$ is the atmospheric pressure. The parameters e_Γ and λ can be determined by fitting the experimental data at critical state in a $e - (p\prime/p\prime_a)^{\zeta_c}$ plane and ζ_c varies between 0.60 to 0.80 as Li [Li97] stated.

One limitation of the basic model for sands described in the preceding sections is that specimens of a given sand with different densities require different set of parameters to reproduce the observed behaviour. The method we will follow to extend the basic generalized plasticity model for sand is based on how the basic ingredients of the model depend on confining pressure and void ratio through the state parameters defined above. The state parameter will enter the definitions of the three main ingredient of a Generalized Plasticity model: the directions $\mathbf{n}_g$ and $\mathbf{n}$ and the plastic modulus H_L.

Concerning the plastic flow direction $\mathbf{n}_g$, we have introduced a new dilatancy law following Li and Dafalias [LD00]

$$d = \frac{d_0}{M_g} \cdot (\eta_{PTS} - \eta) \longrightarrow \eta_{PTS} = M_g \cdot \exp{(m\psi)} \tag{27}$$

where d_0 and m are model constants. ψ is the state parameter; η is the stress ratio and M_g is the Critical State Line in the plot q – p'. Finally, η_{PTS} is the stress ratio at the phase transformation point which depends on the state parameter ψ. Equation (14) shows the existence of a family of stress - dilatancy curves for different densities and confining pressures. The model constants d_0 and m can be obtained from the experimental data in drained or undrained triaxial tests as explained by Li & Dafalias [LD00].

The second ingredient which was found in the basic model to depend on void ratio and confining pressure was the loading- unloading discriminating direction **n**. Here we have kept the same basic structure (see eq. (5)) and we will assume d_f to be of the form:

$$d_f = \frac{d_0}{M_f} \cdot (M_f \cdot (m\psi) - \eta) \tag{28}$$

The proposed expression includes a material parameter M_f which in the basic PZ model is constant. Zienkiewicz, Chan, Pastor, Schrefler and Shiomi [ZCP+99] proposed that the ratio between M_f and M_g was similar to the sand relative density.

Here we propose the following relation which allows determination of M_f once M_g is known:

$$\frac{M_f}{M_g} = h_1 - h_2 \cdot \left(\frac{e}{e_c}\right)^{\beta} \tag{29}$$

where h_1 and h_2 are model constants and β is equal to 1.80. The ratio $\frac{e}{e_c}$ varies between $\frac{e_{min}}{e_{max}}$ and $\frac{e_{max}}{e_{min}}$ as stated by Verdugo and Ishihara [VI96]. When $\frac{e}{e_{CS}}$ reaches its lower limit, M_f/M_g ratio is close to one. Parameters h_1 and h_2 can be calibrated based on the $q - p'$ curve form undrained triaxial test on loose states for different values of M_f/M_g and the ratio $\frac{e}{e_c}$ equal to $e_{\min}/e_{\max}$.

Finally, the third ingredient which was found to depend on the void ratio and the confining pressure was the loading plastic modulus. Here we have kept the same basic structure of the plastic modulus proposed by Pastor, Zienkiewicz and Chan [PZC90], which is expressed as:

$$H_L = H_0 \cdot \sqrt{p\prime \cdot p\prime_a} \cdot H_{DM} \cdot H_f \cdot (H_v + H_s) \tag{30}$$

In above equation H_f, H_s and H_{DM} are defined by equation (7) and M_f is given by equation (16).

H_0 has been assumed to depend on the state parameter. Here we have chosen the law:

$$H_0 = H_0' \cdot \exp\left[-\beta_0' \left(e/e_c\right)^{\beta}\right] \tag{31}$$

where H_0' and β_0' are additional model parameters. It can be seen that we have introduced a dependency of H_0 on void ratio in order to improve the model accuracy in tests run at constant stress ratio, including as a special case the isotropic compression test for which it is zero. The model constants H_0' and β_0' can be determined adjusting the volumetric response of the model with the experimental counterpart of the isotropic triaxial test.

Finally, taking into account that the peak stress ratio η_p depends on the initial conditions of the soil, we have modified H_v by making it dependent on ψ. The proposed expression is:

$$H_v = H_{v0} \cdot [\eta_p - \eta] \longrightarrow \eta_p = M_g \cdot \exp\left(-\beta_v \cdot \psi\right) \tag{32}$$

where H_{v0} and β_v are model parameters. It can be easily verified that $\eta_p < M_g$ for loose states while $\eta_p > M_g$ for dense states. Parameter β_v can be determined at a peak stress in the drained test as shown by Li and Dafalias (2000). Assuming that for saturated soils the model constants β_0 andβ_1 are zero, we can obtain H_{v0} by fitting the model predictions with the experimental results of drained triaxial tests

As in other constitutive models for soils, the proposed model assumes a non-linear reversible response through the expression of the shear modulus proposed by Richart, Hall and Woods [RHW70], and the elastic bulk modulus are assumed to be:

$$\begin{aligned} G &= G_{eso} \cdot \frac{(2.97-e)^2}{(1+e)} \cdot \sqrt{p\prime \cdot p\prime_a} \\ K &= K_{evo} \cdot \frac{(2.97-e)^2}{(1+e)} \cdot \sqrt{p\prime \cdot p\prime_a} \end{aligned} \tag{33}$$

where G_{eso} and K_{evo} are model constants. e is the void ratio, $p\prime\cdot$ is the confining pressure and $p\prime_a$ is the atmospheric pressure in kPa.

In order to assess the model predictive capability, we have reproduced well known experimental results obtained on two different sands, Toyoura and Kurnell. In all these cases, we have obtained a single set of constitutive parameters which have been used for all densities, confining pressures and types of tests –drained and undrained. Details about parameter calibration can be found in Manzanal [Man08].

5.1 Toyoura sand

Verdugo & Ishihara [VI96] have reported a series of drained and undrained controlled deformation triaxial tests on Toyoura Sand, which is a uniform fine quartz – feldspar sand with a mean diameter $D_{50} = 0.17mm$ and a uniformity coefficient $C_u = 1.70$. The specific gravity is 2.65 and minimum and maximum void ratio is 0.977 and 0.597, respectively. All samples have been consolidated isotropically and then sheared under a range of confining pressures between 100 kPa and 3000 kPa and void ratios between 0.735 and 0.996. Figure 4 shows a table displaying the initial conditions of 11 undrained triaxial test (TCU) and 6 drained triaxial test (TCD) used to assess the performance of the proposed model.

The critical state line and the initial state of the tests are shown in 3. All these combinations of densities and confining pressures will be simulated with a single set of constitutive parameters (see Table 2). Figure 4 compares the model predictions and experimental data of undrained triaxial tests in terms of effective stress paths $(q - p')$ and stress - strain behaviour for dense $(e = 0.735 - Dr = 63.7\%)$, medium dense $(e = 0.833 - Dr = 37.9\%)$ and loose $(e = 0.907 - Dr = 18.5\%)$ samples. In Figure 4a, it can be seen that the model captures well the phase transformation in the effective stress path for samples with an initial density $Dr = 63.7\%$ under different confining pressures, ranging from low pressures $(po = 50kPa)$ with a markedly dilative behaviour to high pressures $(po = 3000kPa)$ with a marked phase transformation point which divides contractive to dilative behaviour. The stress - strain behaviour is also predicted with accuracy by the modified model as is shown in Figure 4b. Similar comparisons for medium dense and loose samples are shown in Figures 4c–f. Without losing the good predictive capability of the basic PZ model, the present extension

Test	po´	e
TCU0118	100	0,907
TCU0137	100	0,833
TCU0163	100	0,735
TCU1018	1000	0,907
TCU1037	1000	0,833
TCU1063	1000	0,735
TCU2018	2000	0,907
TCU2037	2000	0,833
TCU2063	2000	0,735
TCU3037	3000	0,833
TCU3063	3000	0,735
TCD01L	100	0,996
TCD01M	100	0,917
TCD01D	100	0,831
TCD05L	500	0,960
TCD05M	500	0,866
TCD05D	500	0.810

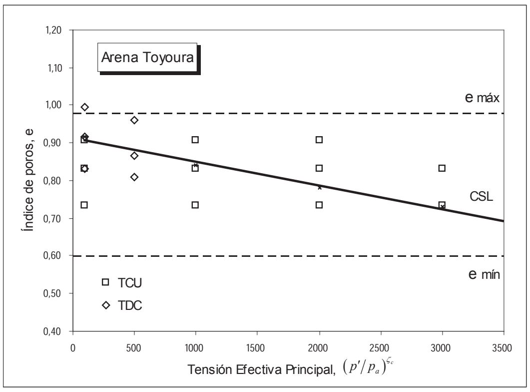

Figure 3: Initial state and Critical State Line for toyoura sand.

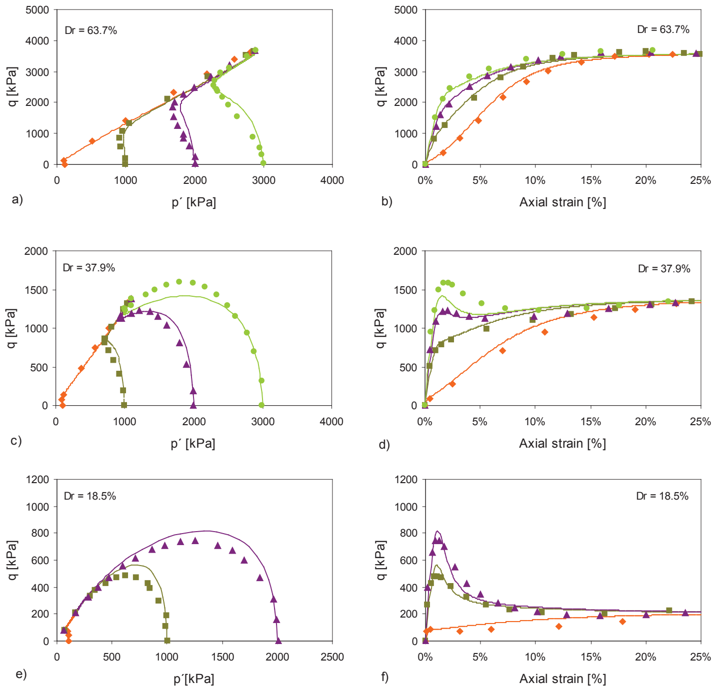

Figure 4: Comparison between model predictions and experimental data undrained triaxial compression test of Toyoura sand.

reproduce static liquefaction in loose samples (Figure 4e-f), the contractive - dilative behaviour in medium dense sands and the dilative behaviour in dense states with a set of 13 model constant as shown Table 1. Figure 5 compares the model predictions

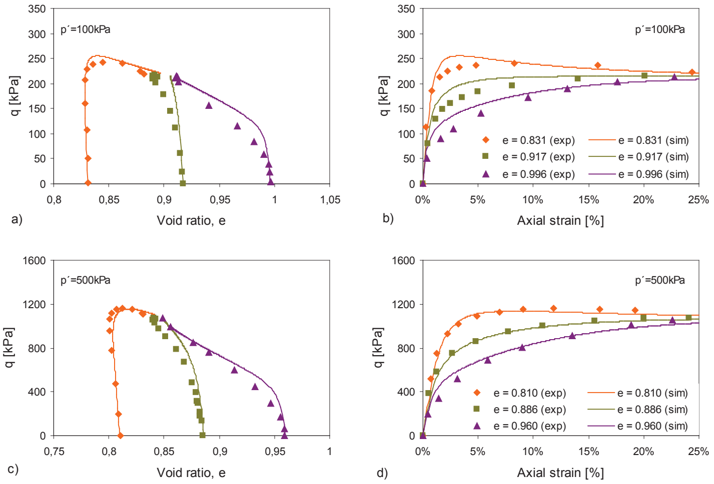

Figure 5: Comparison between model predictions and experimental data drained triaxial compression test of Toyoura sand.

and experimental data of drained triaxial tests on dense ($e = 0.831$), medium dense ($e = 0.917$) and loose ($e = 0.996$) samples of Toyoura sand with an initial confining pressure of 100 kPa. Figure 5a shows the influence of the density on the behaviour of the sand in terms of deviator stress – void ratio. The model simulates the change from contractive to dilative behaviour in dense specimens ($e = 0.831$) and the contractive behaviour in loose specimens ($e = 0.996$). For the three samples, the model reaches an identical critical void ratio at large strain as observed in experimental data. The model accurately predicts the initial peak stress and the strain softening during the deformation history for the dense sample ($e = 0.831$) and also the strain hardening for the loose sample ($e = 0.996$) (Figure 4b). Figures 4c-d show also a good agreement between predicted and measured behaviour of three different samples of different densities sheared at the initial confining pressure of 500kPa.

Table 2: Constitutive model parameters for Toyoura sand.

G_{eso}	K_{eso}	M_g	e_Γ	λ	ζ_c	d_0	m	h_1/h_2
125	167	1.25	0.934	0.019	0.70	0.88	3.50	1.31/0.85

H'_0	β'_0	β	H_{v0}	β_v	β_1	β_0	γ	α
125	1.90	1.80	175	1.50	0	0	0	0.45

5.2 Kurnell sand

Russell & Khalili [RK06] have reported a series of triaxial compression test on saturated samples of Kurnell sand. These tests were carried out at high confining pressures and we will use them to assess the performance of the proposed model. It should be noted that modelling the saturated behaviour of Kurnell sand in saturated conditions is a first step towards modelling its behaviour in unsaturated conditions, which will be described in the second part of this paper. Kurnell sand is a uniform, fine quartzitic sand with a mean diameter $D_{50} = 0,31mm$ and a uniformity coefficient $C_u = 1.83$. Figure 6 shows initial and final states of Kurnell sand samples tested in drained path together with the critical state line in $e - (p\prime/p\prime_a)^{\zeta_c}$ plane. Drained triaxial compression tests with a range of confining pressure from 50kPa to 2395kPa and densities of 58% and 83% were used to assess the model capability. We have presented the tests in two groups, corresponding to initial confining pressures smaller than and greater than 300 kPa. Figure 7 shows the comparisons of experimental data and model simulations for drained triaxial compression tests in terms of deviator stress versus deviator strain $(q - \varepsilon_s)$ and volumetric strain versus deviator strain $(\varepsilon_v - \varepsilon_s)$ for samples tested at confining pressures below and higher than 300kPa. Not only the stress – strain relationship but also the volumetric response is accurately predicted by the proposed model. The isotropic compression test and model simulations for four different void ratio is presented in Figure 8. The overall behaviour of Kurnell sand is well reproduced by the model.

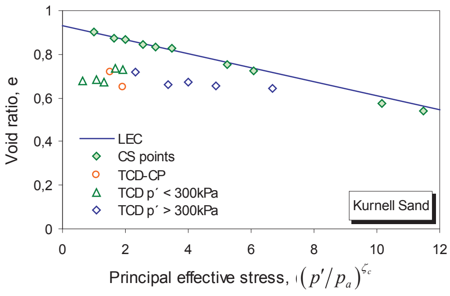

TEST Nº	po [kPa]	eo	Dr [%]
50D	50	0,677	76
115D	114,5	0,685	73
157D	156,5	0,67	78
242D	242	0,735	58
301D	301	0,73	59
200D-CP	200	0,719	63
300D-CP	300	0,652	84
410D	410	0,72	63
760D	760	0,661	81
1010D	1010	0,671	78
1417D	1417	0,654	83
2395D	2395	0,641	87

Figure 6: Initial state and critical state line (CSL) for drained triaxial tests on Kurnell sand.

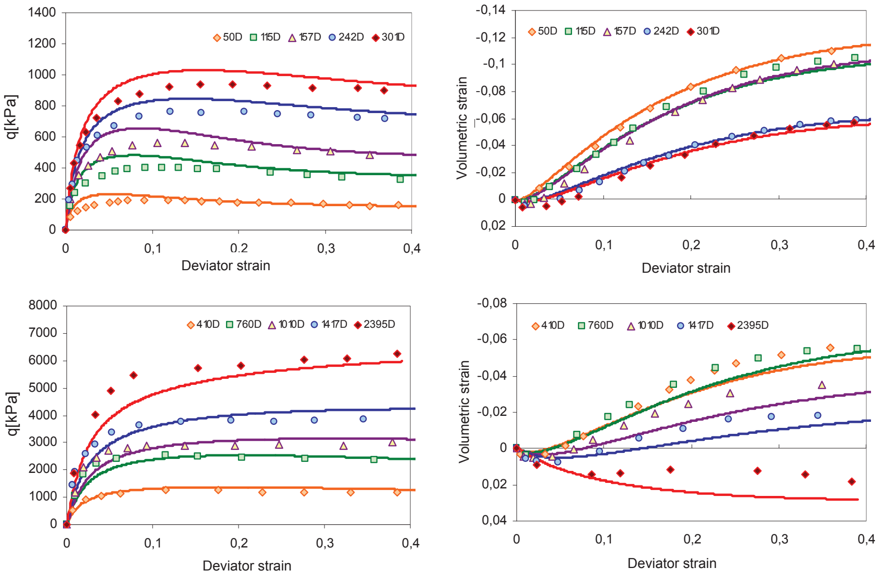

Figure 7: Comparison of drained triaxial test results and model simulations of Kurnell sand.

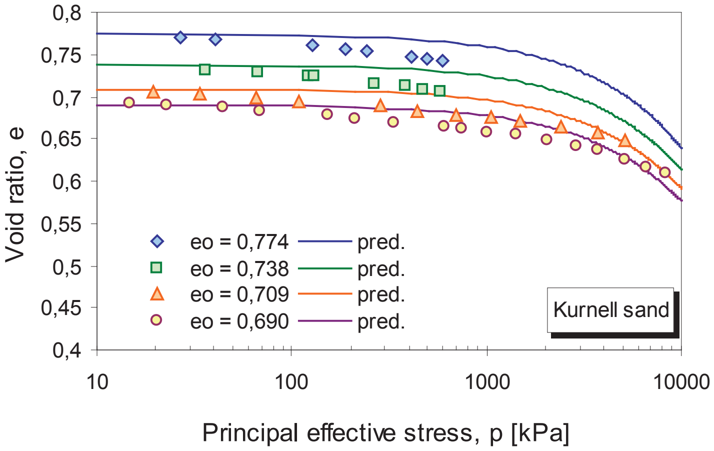

Figure 8: Comparison of isotropic compression tests and model si-mulations of Kurnell sand.

6 Extension to unsaturated materials

In this section we present an extension of the basic Generalized Plasticity constitutive model [PZC90] to reproduce the main features of the behaviour of unsaturated soils from state parameter point of view. The proposed model has been inspired by previous work of Tamagnini and Pastor [TP04] and Tamagnini [Tam04]. Tamagnini and Pastor model was able to reproduce some salient aspects of unsaturated soils, such as the volumetric collapse when the soil is saturated, but presented some limitations which have been addressed by Manzanal et al. [MPM11] and which will be described next.

The model is formulated using two set of stress – strain work conjugated variables [Hou97] coupling the hydraulic and the mechanical behaviour of unsaturated soils within a Generalized Plasticity framework. Stress variables are the effective stress tensor and the matrix suction s, and Strain variables are the soil skeleton strain and the degree of saturation. The effective stress is given by

$$\sigma'_{ij} = \sigma_{ij} - p_a \cdot \delta_{ij} + S_{re} \cdot (p_a - p_w) \cdot \delta_{ij} \tag{34}$$

where σ_{ij} is the total stress tensor, p_a is the pore air pressure, p_w is the pore water pressure, $p_a - p_w$ is the matrix suction s, δ_{ij} is the Kronecker delta and S_{re} is the relative degree of saturation which is given by

$$S_{re} = \frac{S_r - S_{r0}}{1 - S_{r0}} \tag{35}$$

where S_{r0} is the residual degree of saturation. We found an important dispersion on the experimental data even when we used the effective stress definition introduced by Schrefler [Sch84] with a modified scalar factor of Bishop effective stress defined by $\chi = S_r$. The improvement obtained by using S_{re} in the effective stress definition can be seen in Figure 9 which shows the predictive and experimental shear strength with both approaches, $\chi = S_{re}$ and $\chi = S_r$, for the experimental data described in Toll [Tol90] and Sivakumar [Siv93].

The first ingredient of this model is the definition of the state parameter defined on the previous Section, which is based on the critical state line. In the case of unsaturated soils the CSL depends on suction, it is of paramount importance to define the dependence of CSL on suction. Recently, Gallipoli, Gens, Sharma, and Vaunat [GGSV03] proposed a normalization of CSL for non saturated soils by using the bonding variable ξ as:

$$\xi = f(s) \cdot (1 - S_r) \tag{36}$$

where the function $f(s)$ is the ratio between the stabilizing pressure at a given suction s and at zero suction introduced by Haines [Hai25] and Fisher [Fis26] and it is given by

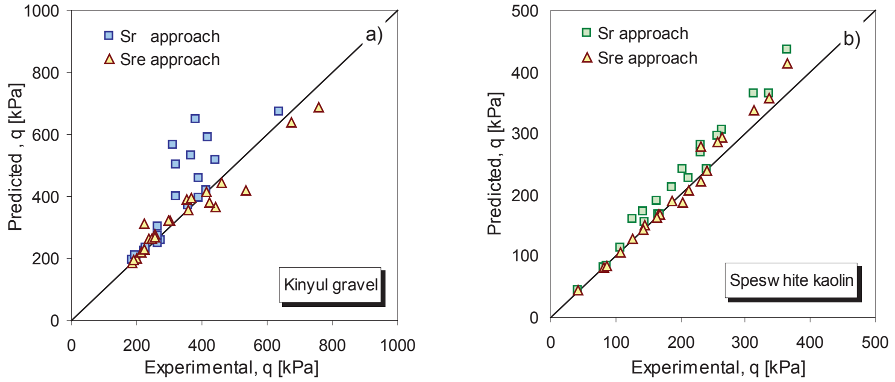

Figure 9: Comparison between predicted and experimental deviatoric stress for a) kinyul gravel (Experimental data from [Tol90] and b) speswhite kaolin (Experimental data from [Siv93].

$$f\left(s\right)=\frac{3}{4}\left\{2-\frac{1}{2s}\left[-\frac{3T_s}{R}+\sqrt{\left(\frac{3T_s}{R}\right)^2+\frac{8T_s}{R}s}\right]\right\} \tag{37}$$

where T_s is the surface tension and R the radius of the spherical particles. There are two limit cases, when suction tends to zero and to infinity. In the former, $f(s) = 1$ and in the latter, when suction tends to infinity $f(s) = 3/2$.

Here, we will use the following alternative relation linking the values of p' at saturation and at a given suction for a fixed void ratio:

$$\frac{p\prime_{CS}^{unsat}}{p\prime_{CS}^{sat}}=1+g\left(\xi\right) \tag{38}$$

where

$$g\left(\xi\right)=a\cdot\left[exp\left(b\cdot\xi\right)-1\right] \tag{39}$$

and ξ is bonding parameter defined by [GGSV03]. The function $g(\xi)$ depends on the degree of saturation and on suction and takes a zero value at saturation. The parameters a and b are calibrated from experimental data as shown by Gallipoli et al [GGSV03]. In fig. 7 we have depicted the CSL for saturated and unsaturated state on the plane and the normalization effect of the function $g(\xi)$ (see eq.(27)).

By combining equation (26) and (27) with a suitable definition of a CSL for saturated states, we will obtain a generalization of the critical state line to unsaturated states.

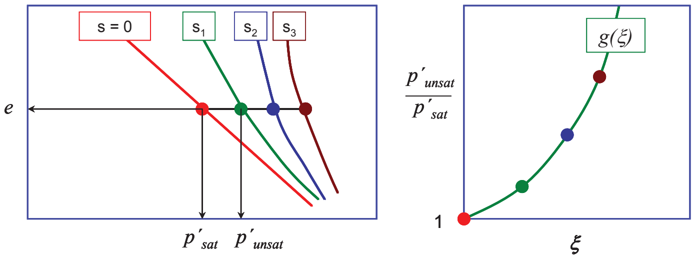

Figure 10: CSLs for saturated and unsaturated state.

We provide in fig. 11 an example using the experimental data described in Sivakumar [Siv93] which illustrate the effectiveness of the proposed approach.

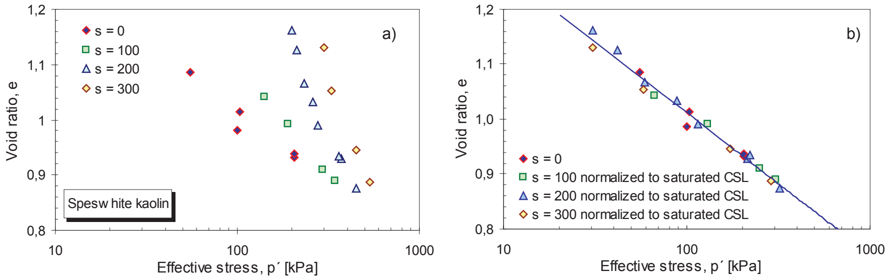

Figure 11: a) Critical state for speswhite kaolin at different suctions b) Normalization of CSLs (Experimental data from [Siv93].

The increment of strain is assumed to be:

$$d\varepsilon = \mathbf{C}^e : d\sigma' + \frac{1}{H_{L/U}} \cdot \mathbf{n}_{gL/U} \otimes : d\sigma' \; + \frac{1}{H_b} \cdot \mathbf{n}_{gL/U} \cdot ds \tag{40}$$

where the two first terms are the elastic and plastic strain which have already been described and the last term is the plastic strain develop during wetting – drying cycles.

The plastic modulus Hb is given by

$$H_b = w\left(\xi\right) \cdot H_0 \cdot \sqrt{p\prime \cdot p_{atm}} \cdot H_{DM} \cdot H_f \tag{41}$$

where

$$H_{DM} = \left(\frac{\zeta_{\max} \cdot J_s}{\zeta}\right)^{\gamma} \tag{42}$$

is a modified discrete memory function incorporating the effect of the suction and degree of saturation,

$$J_s = \exp\left(c.g\left(\xi\right)\right) \tag{43}$$

where c is a model parameter and $g(\xi)$ is defined by equation (27). To illustrate the role of J_s, we will consider the case of a saturated soil which has been consolidated at p_{c0} and then it has been dried, its suction increasing from zero. We have depicted in Figure 12 the variation of $\zeta_{max} \cdot J_s$ with the bonding parameter. It can be interpreted within the framework of classical plasticity as the increase in size of the yield surface with suction. The value of ζ_{max} at saturated conditions can be obtained by $r_0 \cdot p_{cs}^{SAT}$ where r_0 is a material parameter and p_{cs}^{SAT} is the mean effective stress at critical state. Indeed this new parameter in equation 42 is equivalent to the OCR used in classical plasticity models.

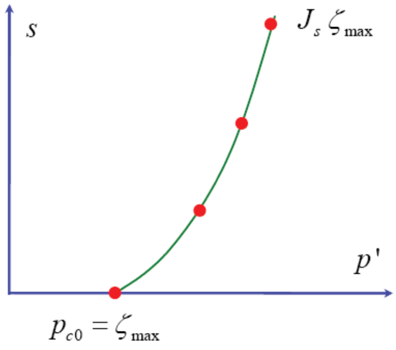

Figure 12: Effect of the bonding parameter on the hardening law.

$w(\xi)$ incorporates the effect of the bonding parameter above defined.

$$w\left(\xi\right) = \left\{ \begin{array}{c} -\left\{1 - \exp\left[g\left(\xi\right)\right]^2\right\}^2 \\ 1 \end{array} \right\} \tag{44}$$

and H_0, H_f, H_v and H_s are the same functions defined for saturated soils.

The model is completed with a suitable hydraulic equation which takes into account both the hydraulic hysteresis during a drying – wetting cycle and its dependency on past history. We have chosen a modified version of the water retention curve proposed by Fredlund & Xing [FX94]:

$$Sr = Sr_0 + (1 - Sr_0) \cdot \left\{ \ln\left[\exp\left(1\right) + \left(\frac{e^{\Omega} \cdot s}{a_w \cdot p_0}\right)^n\right]\right\}^{-m} \tag{45}$$

where Ω, a_w, n and m are model parameters, e is the void ratio and s the matrix suction. The main wetting and drying curves are obtained by assuming different values for a_w,n and m.

Therefore, the non-linear irreversible behaviour of a unsaturated soil can be fully characterized within the Generalized Plasticity framework by adding a plastic modulus in wetting and drying paths H_b and a bonding parameter ξ to the formulation presented in part I [32]. Coupling with a state dependent WRC allows not only reproduce the irreversible response in wetting – drying paths but also the mechanical effect on the hydraulic behaviour (Figure 13).

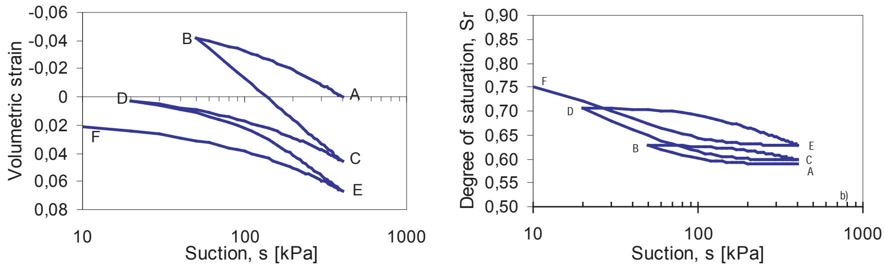

Figure 13: Wetting and drying test.

With the proposed model, it is also possible to reproduce an interesting case, the effect of suction on the undrained behaviour of an unsaturated fine grained soil. We have depicted in Figure 14 constant volume triaxial tests for different suctions. It can be observed the hardening effect due to increasing the suction on a loose sample which in saturated conditions ($s = 0$) arrives to liquefaction. If a soil at a large initial suction (point A) is sheared at constant deviatoric stress decreasing the suction, the stress path will become unstable and fail in a catastrophic manner. This phenomenon has been recently modelled by [BN11]. It is important to remark that this is just a qualitative example, a complete analysis based on the method proposed by Darve et al [DL00, DL01] being necessary to fully understand the process.

Using this state parameter based model, it is possible to reproduce the set of tests on Kurnell sand reported by Russell [Rus04] with a single set of parameters for saturated and non saturated conditions (See Table 3).

Concerning fine soils, we have chosen the experiments performed by Sivakumar [Siv93]. The first example is a series of constant volume triaxial tests on Speswhite Kaolin, denoted as 2A, 3A, 4A and 5A, with net confining pressures of 200, 100, 150 and 300 kPa, and at initial suction of 200 kPa. Figure 16 provides (i) net confining pressure vs deviatoric stress, (ii) axial strain vs deviatoric stress, and (iii) axial strain vs pore pressure change. As in the case of sands, all the simulations were performed with a single set of parameters [MPM11].

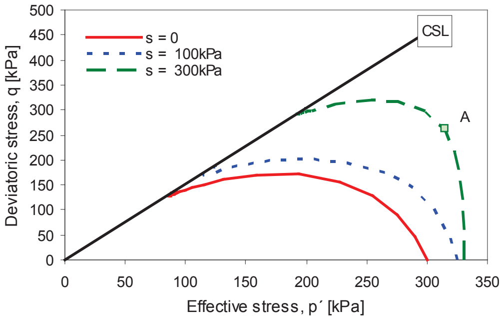

Figure 14: Constant volume triaxial test for different suction.

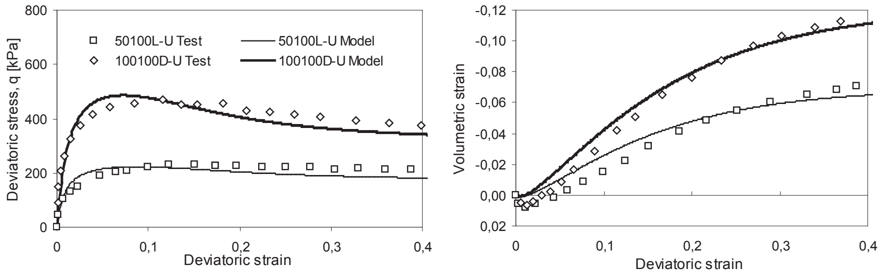

a) s_0 = 100kPa

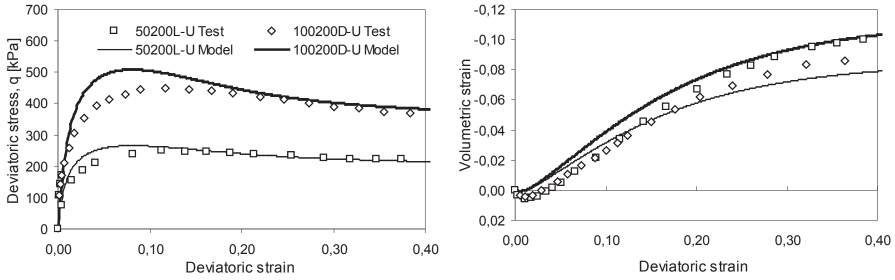

b) s_0 = 200kPa

Figure 15: Comparison between model predictions and experimental data of undrained triaxial compression tests at constant specific water volume on Kurnell sand (Experimental data from [Rus04].

Table 3: Constitutive model parameters for Kurnell sand.

G_{eso}	K_{eso}	M_g	e_Γ	λ	ζ_c	d_0	m	h_1/h_2
135	292	1.475	0.932	0.0328	0.60	0.80	3.32	1 /0.55

H'_0	β'_0	β	H_{v0}	β_v	β_1	β_0	γ	α
125	1.90	1.80	175	1.50	0	0	0	0.45

a	b	c	S_{r0}	Ω	a_w/a_d	n_w/n_d	m_w/m_d	β_w
0.20	2.00	0	0.009	2.10	0.03/0.05	6.00/10	0.80/1.00	2

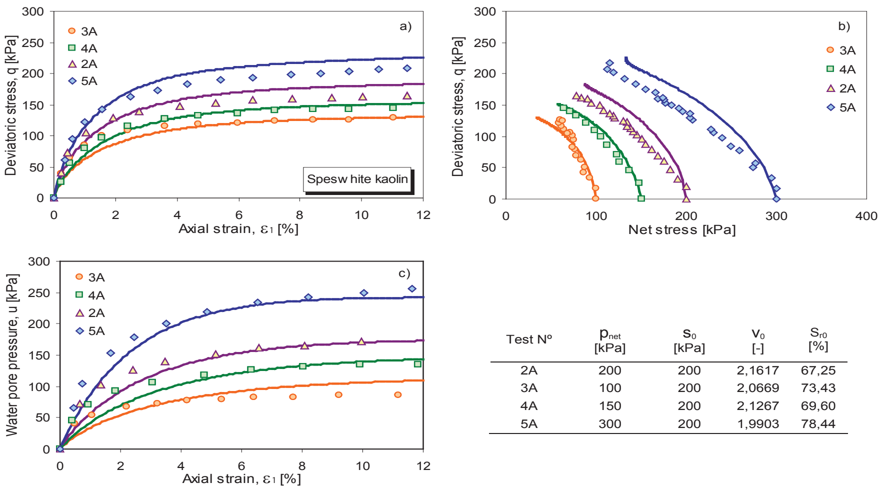

Test Nº	p_{net} [kPa]	s_0 [kPa]	v_0 [-]	S_{r0} [%]
2A	200	200	2,1617	67,25
3A	100	200	2,0669	73,43
4A	150	200	2,1267	69,60
5A	300	200	1,9903	78,44

Figure 16: Comparison between model predictions and experimental data of undrained (constant volume) triaxial compression tests at constant suction on Speswhite kaolin (Experimental data from [Siv93]).

In order to show the influence of the wetting- drying cycle on the mechanical soil behaviour, we have chosen an experiment performed by Sharma [Sha98]. The test consists in a constant suction isotropic compression loading/unloading cycle (a-b-c), followed by wetting – drying cycle (c-d-e) and a second constant suction isotropic reloading and unloading cycle (e-f-g). Figure 17 provides the model predictions and experimental data on compacted bentonite - kaolin sample in (i) net confining pressure vs void ratio, (ii) degree of saturation vs net stress (iii) degree of saturation vs suction, and (iv) stress path followed during the test. The parameters are reported in Manzanal et al (2011).

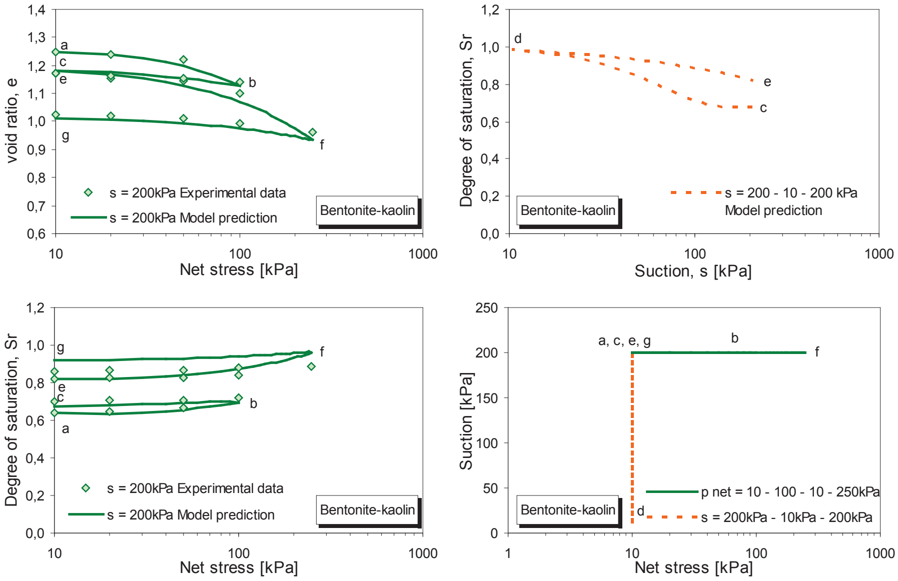

Figure 17: Comparison between model predictions and experimental data of isotropic loading/unloading tests at s = 200kPa with a wetting-drying cycle at pnet = 10kPa on a bentonite - kaolin sample (Experimental data from [Sha98].

7 Dilatancy for flowing materials

In classical soil mechanics, residual conditions are defined as states where the soil is sheared at constant effective stresses, and it is assumed that residual conditions take place on a line on the 3D space (e, p', q) where e is the void ratio, $p' = (1/3)tr(\sigma')$ the mean effective confining stress and $q = \sqrt{3J_2'}]$ where $J_2' = (1/2)tr\left(s^2\right)$ and s

the deviatoric stress. This line is referred to as the Critical state Line (CSL) [Par60]:

$$\begin{aligned} e &= \Gamma - \lambda \ln p\prime \\ q &= M(\theta)\, p\prime \end{aligned} \tag{46}$$

where :

Γ is the void ratio at p'=1

λ is a material parameter characterizing the slope of the CSL on (e, ln p')

$M(\theta)$ is related to friction angle at residual conditions by:

$$M(\theta) = \frac{6 \sin \phi}{3 - \sin \phi \sin 3\theta} \tag{47}$$

In above equation, the Lode's angle θ is given by

$$\theta = -\frac{1}{3} \arcsin \left(\frac{3\sqrt{3}}{2} \frac{J_3}{J_2^{3/2}} \right) \quad \text{with} \ \ J_3 = \frac{1}{3} tr\left(s^3\right) \tag{48}$$

At residual conditions, where

$$\frac{q}{p\prime} = M(\theta) \tag{49}$$

the soil shears at constant volume, and dilatancy, defined as the ratio between volumetric and shear rates of plastic strain $d_g = \frac{d\varepsilon_v^p}{d\varepsilon_s^p}$ is zero Constitutive equations provide suitable expressions for dilatancy. One simple example is obtained by assuming that dilatancy varies linearly with the distance to the CSL as:

$$d_g = \frac{d\varepsilon_v^p}{d\varepsilon_s^p} = (1 + \alpha)\left(M(\theta) - \eta\right) \tag{50}$$

with $\eta = \frac{q/}{p'}$ being the stress ratio.

Obviously, soil dilatancy is not constant when the soil is sheared, as loose soils tend to compact while dense soils dilate. This fact has been considered to play an important role in triggering of landslides and early stages of propagation [PNP08], [Ive05][89], [59]).

Simple plasticity models such as those using a Mohr Coulomb yield surface will predict dilation during plastic shearing of the soil unless a non-associated flow rule is used. Indeed, at residual conditions dilatancy should be zero.

Unfortunately, the implementation of dilatancy rules in depth integrated models present the difficulty of introducing a dilatancy angle which should not be constant, as it depends both on the stress state and the material history.

In the case of landslides, dilatancy laws have to be modified when soil crushing occurs or when the soil flows at shear strain rates much higher than those used in classical soil mechanics tests.

Concerning the latter, laboratory tests performed in rheometers have shown that:

(i) If a granular material is sheared at constant confining pressure, it will dilate when shear strain rate increases (Hanes and Inman [HD85]).

(ii) If shearing is done at constant volume, the pressure will increase with the shear strain rate (Bagnold [Bag54]). Figure 18 depicts the rheometer experiments performed by Bagnold in 1954 [Bag54].

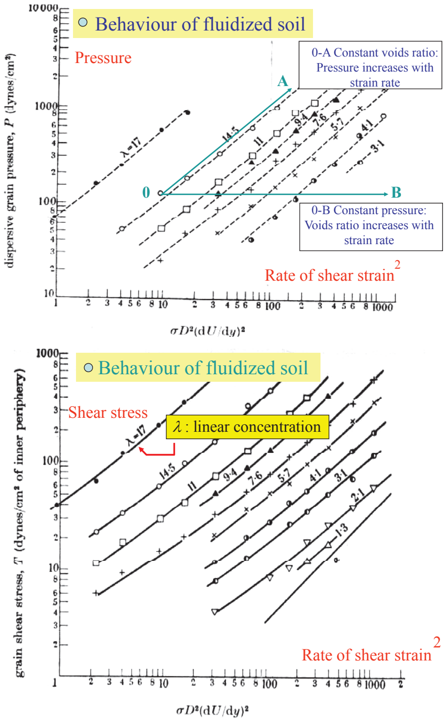

Figure 18: Rheometer experiments performed by Bagnold in 1954.

More elaborated experiments performed by the GDR MiDi [MiD04] have provided considerable insight in the behaviour of granular fluids.

Experimental results on several types of rheometers (Forterre and Pouliquen [FP08], Pailha and Pouliquen [PNP08]) show that volume fraction decreases linearly with the inertia number I as:

$$\Phi_{eq} = \Phi_{\max} + (\Phi_{\min} - \Phi_{\max})\, I \tag{51}$$

which suggests the existence of an unique volume fraction (porosity or void ratio) for a given inertia number I. A similar law has been proposed by George and Iverson [GI11]

The authors (Pastor et al [PBP09]) have proposed the law:

$$e_{CSL,\,dyn} = e_{CSL} + \beta_1\left(I_{2d}\right) \tag{52}$$

where β_1 is a material parameter, e_{CSL} the void ratio at CSL (at the same p') and $e_{CSL,\,dyn}$ the void ratio at the dynamic CSL corresponding to I_{2d}.

In above equation, I_{2d} is the second invariant of the rate of deformation tensor.

Concerning dilatancy, Roux and Radjai [RR88] and Pailha and Pouliquen [PNP08] propose laws of the type:

$$\frac{1}{\Phi}\frac{d\Phi}{dt} = k_3\left(\Phi - \Phi_{eq}\right)\dot{\gamma} \tag{53}$$

where $\dot{\gamma}$ is the 1D rate of shear strain.

Above equation describes the evolution towards the dynamic CSL. Alternatively, Pastor et al [PBP09] proposed

$$d_g = -\beta_2 \frac{e_{CSL,\,dyn} - e}{e_{CSL}} \tag{54}$$

where β_2 is a material parameter. Fig 19 illustrates the idea, interpreting both constant pressure and constant volume rheometer tests.

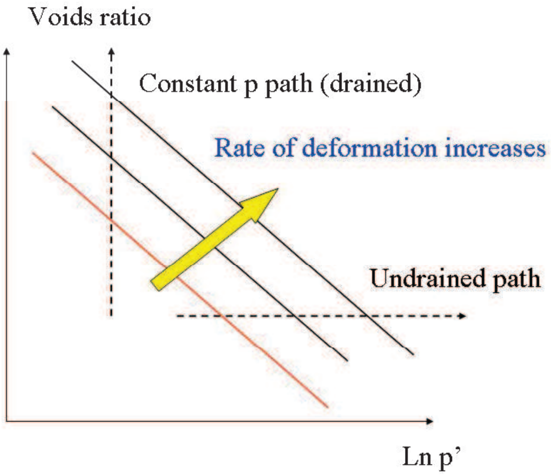

Figure 19: Interpretation of constant p and constant volume rheometer tests.

From above ideas, an alternative could be:

$$e_{CSL,\,dyn} = e_{CSL} + \beta_1 I \tag{55}$$

$$\dot{\varepsilon}_v = -\beta_2\left(e_{CSL,\,dyn} - e\right)\dot{\gamma} \tag{56}$$

8 Dilatancy and modelling of crushing materials

Concerning breaking of soil particles, Iverson et al. [IMI10] have proposed that it can generate pore pressures during landslide propagation. They studied the behaviour of a loamy sand presenting aggregates in a shear ring apparatus, concluding that the breaking of aggregates caused a tendency to compact and, hence, increase of pore pressures. Constitutive and numerical analysis of crushing has been studied by Hicher and Daouadji [DH09], Hu et al [HYDH11], Muir Wood and Maeda [MWM07], and Russell et al. [Rus11]. Several approaches have been developed to quantify particle breakage of a crushable material subjected to different stress path (compression and shearing)[Har85, Mar67, LF67, MBR96]. Hardin [Har85] proposed identify two parameter (i) the Granular Size Distribution (GSD) before loading and (ii) the particle size diameter which represent the fine content (silts and clays) of a representative sample. The total Breakage B_t is obtained from the relative position of Granular Size Distribution (GSD) after loading:

$$B_t = B_p - B_{pl} \tag{57}$$

where B_p is the total potential amount of particle breakage [Har85] and B_{pl} the potential amount of particle breakage after some crushing occur. Since the GSD of a crushable material evolves during loading, B_p and B_{pl} depend on GSD before $d_b y$ and after $d_a y$ loading and are defined as:

$$B_{p,pl} = \int_0^1 \log\left(\frac{d_{a,b}\left(y\right)}{d_{\min}}\right) dy \tag{58}$$

y represents the passing fraction for given diameter varying from 0 to 1, and $d_{min} = 74\ \mu\text{m}$ is the upper limit of silt particles. Figure 1 shows the interpretation of B_p which represents the total area between the initial GSD and the constant cut-off.

The relative breakage is defined as $B_r = B_t/B_p$ and neglects the breakage of particles smaller than 74um.

Marsal [Mar67] proposed a Breakage Factor as the individual particle size difference between initial and final GSD. The lower and upper limits are 0% and 100% which represent no crushing and total crushed materials. Breakage index suggested by Lee and Farhoomand [LF67], is defined as the ratio between diameter passing 15% finer of GSD before and after loading. The fractal distribution of particles has been noted experimentally by [MBR96] and [LC02]. The fractal distribution of particles of final GSD defined by a fractal of a dimension of 2.5 or 2.6 can be adopted as ultimate limit of GSD. Einav [Ein07] proposed a modified Hardin Relative Breakage based on the fractal distribution of particles of final GSD defined by a fractal of a dimension:

$$B_r = \frac{\int\limits_{d_m}^{d_M} \left[F_u\left(d\right) - F_d\left(d\right)\right] d(\log d)}{\int\limits_{d_m}^{d_M} \left[F_u\left(d\right) - F_o\left(d\right)\right] d(\log d)} \tag{59}$$

where F_o, F_d and F_u are the initial, current and ultimate grain size cumulative functions. Similar approach was proposed by Kikumoto et al. [KWMR10].

As noted in the previous sections, sands have different volumetric and stress – strain responses according to density and mean effective stress level. Contractive behaviour and strain hardening is observed in loose sands while dense sands show dilative behaviour and strain softening during shearing. This change from contractive to dilative behavior can be quantified in terms of the state parameter

$$\psi = e - e_\Gamma - \left(e_{\min} - e_{\max}\right) \frac{B_r}{B_r + b_{cr}} + \lambda \left(\frac{p\prime}{p\prime_a}\right)^{\zeta_c} \tag{60}$$

where b_{cr} is a material parameter related to mineral of grain, e_{min} and e_{max} the minimum and maximun void ratio and B_r is the relative breakage parameter given by [DH09]:

$$B_r = \frac{W^P}{W^P + \chi_{cr}} \tag{61}$$

where W^P is accumulated plastic work:

$$W^P = \int \sigma_{ij} \left|d\varepsilon_{ij}^p\right| \tag{62}$$

The model is completed by modifing the plastic modulus as:

$$H_L = (1 - B_r \cdot H_0 \cdot \sqrt{p \cdot p_a} \cdot H_{DM} \cdot f\left(\eta\right) \tag{63}$$

The influence of particle breakage during a undrained triaxial test and the evolution of grain size distribution during shearing are shown in Figure 20 and 21. Small variations in the grain size distribution, show increases in the pressure pores.

9 A note on bounding surface models

Classic elasto-plastic constitutive models are unable to predict the cyclic behavior of materials properly. This is mainly because of the fact that the stress state during unloading and reloading is located inside the yield surface and a pure elastic behavior is

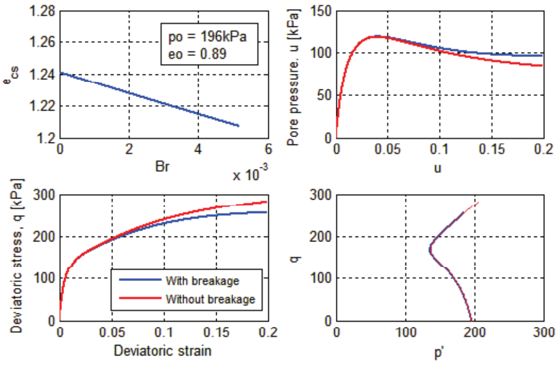

Figure 20: Undrained triaxial simulation with and without breakage.

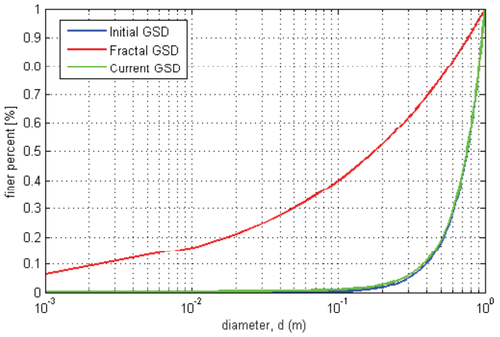

Figure 21: Grain size distribution during shearing.

predicted in this region. Hence, such models cannot capture the accumulation of plastic volumetric strains or pore water pressure during a stress controlled cyclic shearing. To overcome such deficiencies the concept of bounding surface plasticity was developed by [Daf75, Kri75, DE75]. Compared to the multi surface plasticity models, bounding surface plasticity models do not need to define, renew and keep in the memory several yield surfaces. Therefore, generally, the latter models are less complicated and more efficient. Bounding surface is similar to conventional yield surface in many respects, with plastic strains are allowed to occur inside the bounding surface. In fact, if the stress state is located on the bounding surface, the bounding surface model acts similar to a classical elasto-plastic model. Two different approaches in the context of bounding surface plasticity are proposed by [Daf75, DH80]. In the former approach, a loading surface (or yield surface or bubble) is defined in addition to bounding surface. Such models are called two surface models. Loading surface defines an elastic region in the stress space. The stress state can be located inside or on the loading surface and the loading surface should be enclosed by the bounding surface. However, the loading surface can translate inside the bounding surface. In the latter approach, the elastic zone is neglected and a mapping rule is used to correspond the current stress state to an image point on the bounding surface. A plastic potential surface is also associated with this surface. Hence, plastic hardening modulus can be obtained at image point. The plastic hardening modulus at current stress state is a function of this value and the distance between the current stress state and the image point. Unloading can be considered to be pure elastic (MIT-E3 model,[Whi91]) or a separate plastic modulus can be defined for unloading (CASM-c model, [YKW07]). In p-q space (deviatoric stress-mean effective stress) a straight line or an ellipse is usually taken as bounding surface for sands and clays, respectively. More advanced models use a distorted surface as the bounding surface. The size of bounding surface is usually controlled by NCL (or limiting compression curve) [CWD94, PW99]. Furthermore, the concept of state parameter for cohesionless materials has been implemented successfully in the such framework [MD97]. Evaluation of the behaviour of sands with fines has revealed that the state parameter [BJ85] cannot describe completely some aspects of their behaviour [BLW$^+$09]. In such cases, one can define a new reference state curve to define a new state parameter. The new state parameter can effectively incorporate in the formulation of the bounding surface and plastic potential and improve the predictions of the model. Bounding surface plasticity and Generalized Plasticity provide flexible framework to predict soil behaviour under monotonic and cyclic loading.

10 Conclusions

This Chapter presents an overview of the hierarchical and versatile formulation of Generalized Plasticity Theory (GPT) developed by Zienkiewicz and Pastor in the middle of the eighties and the most recent developments:

(i) a state-dependency on soils behaviour has been introduced on GP approach to reproduce the stress – strain response of granular materials under different densities, confining pressures and stress paths.

(ii) in the extension of Generalized Plasticity to unsaturated behaviour, the model adopts the Bishop effective stress and suction as stress variables and the strain of solid skeleton and degree of saturation as deformation variables. The model considers both the void ratio and hydraulic hysteresis effect on hydraulic behaviour.

(iii) a generalization of the critical state for different suctions as function of a bonding parameter is proposed. This allows the extension of the state parameter concept to model the behaviour of partially saturated soil. The model is capable of reproducing stress-strain behaviour of unsaturated soils for different densities, confining pressures and suctions, by using the same materials constants.

(iv) it was introduced the concept of dynamical critical state line (DCSL), depending on shear strain velocity, which generalizes the critical state line (CSL) used in Geomechanics to describe residual conditions at failure. The model consisted on a volumetric part, based on a dilatancy term depending on the distance to the DCSL, and a deviatoric part incorporating coupling with pore pressures. This concepts can allow the use of viscoplastic models for both the prefailure (solid) and post failure (fluidized) behaviour.

(v) the evolution of particle size distribution due to particle breakage was introduced as function of plastic work.

The results show a general good agreement between the models predictions and laboratory experiments. Further details on extended formulation and calibration can be obtained in [FMPM$^+$04, Man08, PMFM$^+$10, MFMP11, MPM11].

Acknowlegment

The authors gratefully acknowledge the financial support granted by the Spanish Ministry of Science and Innovation (Project GEOFLOW BIAS 37020-C02-01).

References

[Bag54] R.A. Bagnold. Experiments on a gravity-free dispersion of large solid spheres in a newtonian fluid under shear. *Proceedings of the Royal Society of London A*, 225:49–63, 1954.

[BJ85] K. Been and M. Jefferies. A state parameter for sand. *Géotechnique*, 35:99–112, 1985.

[BLW$^+$09] D. Bobei, S.R. Lo, D. Wanatowski, C.T. Gnanendran, and M.M. Rahman. Modified state parameter for characterizing static liquefaction of sand with fines. *Can. Geotech. J.*, 46:281–295, 2009.

[BN11] G. Buscarnera and R. Nova. Modelling instabilities in triaxial testing on unsaturated soil specimens. *International Journal for Numerical and Analytical Methods in Geomechanics*, 35(2):179–200, 2011.

[CdP00] B. Cambou and C. di Prisco. *Constitutive Modelling of Geomaterials*. Hermes, 2000.

[CWD94] R.S. Crouch, J.P. Wolf, and Y.F. Dafalias. Unified critical state bounding surface plasticity model for soil. *J. Eng. Mech.*, 120:2251–2270, 1994.

[Daf75] Y.F. Dafalias. *On cyclic and anisotropic plasticity: (i) A general model including material behavior under stress reversals, (ii) Anisotropic hardening for initially orthotropic materials*. PhD thesis, University of California, Berkeley, 1975.

[DE75] Y.F. Dafalias and Popov E.P. A model of nonlinearly hardening materials for complex loadings. *Acta Mech.*, 21:173–192, 1975.

[Des84] J. Desrues. *La localization de la déformation dans les matériaux granulaires*. PhD thesis, USTMG et IMPG, Grenoble, France, 1984.

[DH80] Y.F. Dafalias and L.R. Herrmann. *A bounding surface soil plasticity model*, volume 1. International symposium on soils under cyclic and transient loading. Swansea, U.K., 1980.

[DH09] A. Daouadji and P.Y. Hicher. An enhanced constitutive model for crushable granular materials. *International Journal for Numerical and Analytical Methods in Geomechanics*, pages 555–580, 2009.

[DL00] F. Darve and F. Laouafa. Instabilities in granular materials and application to landslides. *Mechanics of Cohesive-Frictional Materials*, 5:627–652, 2000.

[DL01] F. Darve and F. Laouafa. Modelling of slope failure by a material instability mechanism. *Computer and Geotechnics*, 29:301–325, 2001.

[Ein07] I. Einav. Breakage mechanics—Part I: Theory. *Journal of the Mechanics and Physics of Solids*, 55(6):1274–1297, June 2007.

[Fis26] R.A. Fisher. On the capillary forces in an ideal soil; correction of formulas by w.b. haines. *Journal of Agricultural Science*, 16:492–505, 1926.

[FMPM$^+$04] J. A. Fernandez Merodo, M. Pastor, P. Mira, L. Tonni, M. I. Herreros, E. Gonzalez, and R. Tamagnini. Modelling of diffuse failure mechanisms of catastrophic landslides. *Computer Methods in Applied Mechanics and Engineering*, 193:2911–2939, 2004.

[FP08] Y. Forterre and O. Pouliquen. Flow of dense granular media. *Ann. Rev. Fluid Mech.*, 40:1–24, 2008.

[FX94] D. Fredlund and A. Xing. Equations for the soil-water characteristic curve. *Canadian Geotechnical Journal*, 31:521–532, 1994.

[GGSV03] D. Gallipoli, A. Gens, R. Sharma, and J. Vaunat. An elastoplastic model for unsaturated soil incorporating the effects of suction and degree of sturation on mechanical behaviour. *Géotechnique*, 53:123–135, 2003.

[GI11] D.L. George and R.M. Iverson. *A two-phase debris-flow model that includes coupled evolution of volume fractions, granular dilatancy, and pore-fluid pressure*. Debris-flow Hazards Mitigation, Mechanics, Prediction, and Assessment, 2011.

[GN93] A. Gens and R. Nova. *Conceptual bases for a constitutive model for bonded soils and weak rocks*. Proceedings of international symposium on geotechnical engineering of hard soils-soft rocks, Rotterdam, Balkema, 1993.

[Hai25] W.B. Haines. Studies in the physical properties of soils. a note on the cohesion developed by capillary forces in an ideal soil. *Journal of Agricultural Science*, 15:529–535, 1925.

[Har85] B.O. Hardin. Crushing of soil particles. *J. Geotech. Eng*, 111:1177–1192, 1985.

[HD85] D.L. Hanes D.M., Inman. Observations of rapidly flowing granular fluid materials. *J.Fluid Mech.*, 150:357–380, 1985.

[Hou97] G.T. Houlsby. The work input to an unsaturated granular material. *Géotechnique*, 47:193–196, 1997.

[HYDH11] W. Hu, Z. Yin, C. Dano, and P.Y. Hicher. A constitutive model for granular materials considering grain breakage. *Science China Technological Sciences*, 54(8):2188–2196, 2011.

[IMI10] N.R. Iverson, J.E. Mann, and R.M. Iverson. Effects of soil aggregates on debris-flow mobilization: Results from ring-shear experiments. *Engineering Geology*, 114(1-2):84–92, 2010.

[Ish93] K. Ishihara. Liquefaction and flow failure during earthquakes. *Géotechnique*, 43:351–415, 1993.

[Ive05] R.M. Iverson. Regulation of landslide motion by dilatancy and pore pressure feedback. . *Geophys. Res.*, 110:–, 2005.

[JA05] M. G. Jefferies and Shuttle D. A. Norsand: Features, calibration and use. In *Geo-Frotiers Conference: Soil constitutive models: evaluation, selection and calibration*, pages 204–236. 2005.

[Kri75] R.D. Krieg. A practical two-surface plasticity theory. *J. Appl. Mech.*, 42:641–646, 1975.

[KWMR10] M. Kikumoto, D. Wood Muir, and A. Russell. Particle crushing and deformation behaviour. *Soils and foundations*, 50(4):547–563, 2010.

[LC02] L. Luzziani and M.R. Coop. On the Relationship between Particle Breakage and the Critical State of Sands. *SOILS AND FOUNDATIONS*, 42(2):71–82, 2002.

[LD00] X. S. Li and Y. Dafalias. Dilatancy for cohesionless soils. *Géotechnique*, 50:449–460, 2000.

[LF67] K. L. Lee and I. Farhoomand. Compressibility and crushing of granular soil in anisotropic triaxial compression. *Can. Geotech. J.*, 4(1):68–86, 1967.

[Li97] XS. Li. Modeling of dilative shear failure. *Journal of Geotechnical and Geoenvironmental Engineering*, 123:609–616, 1997.

[LN95] R. Lagioia and R. Nova. An experimental and theoretical study of the behaviour of a calcarenite in triaxial compression. *Géotechnique*, 45:633–648, 1995.

[Man08] D. Manzanal. *Constitutive model based on Generalized Plasticity incorporating state parameter for saturated and unsaturated sand (Spanish).* PhD thesis, School of Civil Engineering, Technical University of Madrid, 2008.

[Mar67] R. J. . Marsal. Large scale testing of rockfill materials. *J. Soil Mech. Found. Div. ASCE*, 93(2):27–44, 1967.

[MBR96] G.R. McDowell, M.D. Bolton, and D. Robertson. The fractal crushing of granular materials. *Journal of the Mechanics and Physics of Solids*, 44(12):2079–2101, December 1996.

[MD97] M. T. Manzari and Y. F. Dafalias. A critical state two-surface plasticity model for sands. 47:255–272, 1997.

[MFMP11] Diego Manzanal, José Antonio Fernández Merodo, and Manuel Pastor. Generalized plasticity state parameter-based model for saturated and unsaturated soils. part 1: Saturated state. *International Journal for Numerical and Analytical Methods in Geomechanics*, 35(12):1347–1362, 2011.

[MiD04] G. D. R. MiDi. On dense granular flows. 14:341, 2004.

[MPM11] Diego Manzanal, Manuel Pastor, and José Antonio Fernández Merodo. Generalized plasticity state parameter-based model for saturated and unsaturated soils. part ii: Unsaturated soil modeling. *International Journal for Numerical and Analytical Methods in Geomechanics*, 35(18):1899–1917, 2011.

[MWM07] D. Muir Wood and K. Maeda. Changing grading of soil: effect on critical states. *Acta Geotechnica*, 3(1):3–14, 2007.

[Par60] R.H.G. Parry. Triaxial compression and extension tests on remoulded saturated clay. *Géotechnique*, 10:166–180, 1960.

[Pas91] M. Pastor. *Modelling of anisotropic sand behaviour*, volume 11. 1991.

[PBP09] M. Pastor, T. Blanc, and M.J Pastor. A depth-integrated viscoplastic model for dilatant saturated cohesive-frictional fluidized mixtures: Application to fast catastrophic landslides. *J. Non-Newtonian Fluid Mech.*, 158:142–153, 2009.

[PMFM$^+$10] M. Pastor, D. Manzanal, J.A. Fernández Merodo, P. Mira, T. Blanc, V. Drempetic, M.J. Pastor, B. Haddad, and M. Sánchez. From solids to fluidized soils: diffuse failure mechanisms in geostructures with applications to fast catastrophic landslides. *Granular Matter*, 12(3):211–228, 2010.

[PNP08] M. Pailha, M. Nicolas, and O. Pouliquen. Initiation of underwater granular avalanches: Influence of the initial volume fraction. *Physics of Fluids (1994-present)*, 20(11):–, 2008.

[PW99] J.M. Pestana and A.J. Whittle. Formulation of a unified constitutive model for clays and sands. *Int. J. Numer. Anal. Meth. Geomech.*, 23:1215–1243, 1999.

[PZC90] M. Pastor, O.C. Zienkiewicz, and A.H.C. Chan. Generalized plasticity and the modelling of soil behaviour. *International Journal for Numerical and Analytical Methods in Geomechanics*, 14:151–190, 1990.

[PZL85] M. Pastor, O. C. Zienkiewicz, and K. H. Leung. Simple model for transient soil loading in earthquake analysis ii: Non-associative models for sands. *International Journal for Numerical and Analytical Methods in Geomechanics*, 9:477–498, 1985.

[RHW70] F.E. Richart, J.R. Hall, and R.D. Woods. *Vibration of soils and foundations*. Prentice-Hall, 1970.

[RK06] A.R. Russell and N Khalili. Cavity expansion in unsaturated soils. *International Journal for Numerical and Analytical Methods in Geomechanics*, 30:181–212, 2006.

[RP63] K. H. Roscoe and H. B Poorooshasb. A fundamental principle of similarity in model test for earth pressure problems. In *Proceeding of 2nd Asian Conference on Soil Mechanics*, pages 134–140. 1963.

[RR88] S. Roux, , and F. Radjai. Texture-dependent rigid plastic behavior. In *Summer school Physics of Dry Granular Media, September 1997, Cargese, France. Proceedings: Physics of Dry Granular Media, HJ Herrmann et al (eds), Kluwer, Dordrecht*, pages 305–311. 1988.

[Rus04] A. R. Russell. *Cavity expansion in unsaturated soils*. PhD thesis, PhD Thesis School of Civil and Enviromental Engineering, University of New South Wales, 2004.

[Rus11] a. R. Russell. A compression line for soils with evolving particle and pore size distributions due to particle crushing. *Géotechnique Letters*, 1(January-March):5–9, March 2011.

[Sch84] B.A. Schrefler. *The finite element method in soil consolidation (with applications to surface subsidence)*. PhD thesis, 1984.

[Sha98] R.S. Sharma. *Mechanical behaviour of unsaturated highly expansive clays*. PhD thesis, 1998.

[Siv93] V. Sivakumar. *A critical state framework for unsaturated soil*. PhD thesis, 1993.

[SK67] H.B. Seed and Lee K.L. Undraind strength characteristics of cohesionless soils. *Journal of the Soil Mechanics and Foundations Division*, 93:333–360, 1967.

[Tam04] R. Tamagnini. An extended cam-clay model for unsaturated soils with hydraulic hysteresis. *Géotechnique*, 54:223–228, 2004.

[TD08] M. Taiebat and Y.F. Dafalias. Sanisand: Simple anisotropic plasticity model. *International Journal for Numerical and Analytical Methods in Geomechanics*, 32:915–948, 2008.

[Tol90] D.G. Toll. A framework for unsaturated soil behaviour. *Géotechnique*, 40:31–44, 1990.

[TP04] R. Tamagnini and M Pastor. *A thermodynamically based model for unsaturated soils: a new framework for generalized plasticity*. 2nd International Workshop on Unsaturated Soils, Mancuso Ed., 2004.

[Uri75] S. Uriel. *Intrinsic dynamic of the quasi-static mechanics of granular soils*. Numerical Methods in Soil and Rock Mechanics, Borm, G. & Meissher, H. Eds, 1975.

[VI96] R. Verdugo and K. Ishihara. The steady state of sandy soils. *Soil and Foundation*, 36:81–91, 1996.

[WB65] C.P. Wroth and N. Bassett. A stress-strain relationship for the shearing behaviour of sand. *Géotechnique*, 15:32–56, 1965.

[WDLM02] Z. Wang, Y. Dafalias, X. S. Li, and F.I. Makdisi. State pressure index for modeling sand behaviour. *Journal of Geotechnical and Geoenvironmental Engineering*, 128:511–519, 2002.

[Whi91] J.R. Whittle. Mit-e3: A constitutive model for overconsolidated clays. In *Comp. Meth. And advances Geomech., Balkema, Rotterdam.* 1991.

[YKW07] H.S. Yu, C. Khong, and J. Wang. A unified plasticity model for cyclic behavior of clay and sand. *Mechanics research communications*, 34:97–114, 2007.

[YL05] S. Yang and H.I. Ling. Calibration of a generalized plasticity model and its application to liquefaction analysis. In *Geo-Frotiers Conference: Soil constitutive models: evaluation, selection and calibration*, pages 483–494. 2005.

[ZCP$^+$99] O.C. Zienkiewicz, A.H. Chan, M. Pastor, B. A. Schrefler, and T. Shiomi. *Computational Geomechanics*. John Wiley & Sons, 1999.

[ZLP85] O. C. Zienkiewicz, K. H. Leung, and M. Pastor. Simple model for transient soil loading in earthquake analysis. i: Basic model and its application. *International Journal for Numerical and Analytical Methods in Geomechanics*, 9:453–476, 1985.

[ZM84] O. C. Zienkiewicz and Z. Mroz. *Generalized plasticity formulation and applications to geomechanics*. John Wiley & Sons, 1984.

An introduction to numerical modelling of coupled problems in geomechanics

M. Pastor, P. Mira, J.A. Fernández-Merodo, M. Martín Stickle, D. Manzanal and A. Yagüe

Grupo M2i Modelos Matematicos en Ingenieria and ETS de Ingenieros de Caminos, Canales y Puertos de Madrid

This Chapter is devoted to present an introduction to numerical modelling of coupled problems in geotechnical engineering. It aims to provide the reader with an overview both of the techniques and the difficulties encountered when modelling this type of problems. We have restricted the analysis to the simplest case where we have only a fluid filling the pores, as the main difficulties can be more easily explained and understood. The paper is limited to finite element techniques, even tough the authors have worked with meshless methods such as the SPH and the MPM. Again, the reason is that the problems found in finite elements are also found in SPH and MPM.

1 Introduction

Soils and rocks are geomaterials with voids which can be filled with water, air, and other fluids. They are, therefore, multiphase materials, exhibiting a mechanical behaviour governed by the coupling between all the phases.

Pore pressures of fluids filling the voids play a paramount role in the behaviour of a soil structure, and indeed, their variations can induce failure. If we consider the soil as a mixture, we will have equations describing: (i) balance of mass for all phases, i.e., solid skeleton, water and air, in the case of non saturated soils (ii) balance of linear momentum for pore fluids and for the mixture, and (iii) constitutive equations. A crucial point is the choice between eulerian and lagrangian formulations. In soil mechanics, the approach followed most often is mixed, lagrangian for the skeleton and eulerian for the relative movement of the pore fluids relative to the soil skeleton. In many occasions, convective terms can be neglected.

The first mathematical model describing the coupling between solid and fluid phases was proposed by Biot [Bio41], [Bio55] for linear elastic materials. This work was followed by further development at Swansea University, where Zienkiewicz and coworkers [Zie80], [Zie84], [Zie90a], [Zie90b], [ZS99] extended the theory to non-linear materials and large deformation problems. It is also worth mentioning the work of Lewis and Schrefler [Lew98], Coussy [Cou95] and de Boer [Boe00].

An alternative description is that of mixture theories, developed by Green & Adkin [Gre60], Green [Gre69] and Bowen [Bow76]. This approach was also studied by Li, Zienkiewicz and Xie [Li90] and Schrefler [Sch95]. The interested reader is referred to the texts by de Boer [Boe00] and Zienkiewicz et al. [ZS99].

This Chapter is devoted to present different alternative models which can be used to describe the coupling between solid skeleton and pore fluids in geomaterials, both in solid and fluidized states. We have chosen an approach closer to mixture theories than to the more classical approach used in computational geotechnics, as it provides a more general description which can be used not only for the initiation of failure but also for propagation of catastrophic landslides.

2 Mathematical models for coupled behaviour of geomaterials

Mathematical models for coupled materials, including the definition of effective pressure have already been presented in this book. Therefore, we will present only a succinct description of the mathematical models which will be discretized.

We will start summarizing the general equations which describe the *hydro-mechanical* coupling of a saturated porous materials.

2.1 The $v_s - v_w - p_w$ Biot Zienkiewicz model for saturated geomaterials

We will introduce:

- The porosity n

  $$n = \frac{e}{1+e} \tag{1}$$

  where e is the void ratio. Alternatively, a solid fraction Φ can be defined as $\Phi = 1 - n$

- Densities of the pore water and solid particles will be denoted as ρ_w and ρ_s, from here phase densities are obtained as:

  $$\begin{aligned} \rho^{(s)} &= (1-n)\,\rho_s \\ \rho^{(w)} &= n\rho_w \end{aligned} \tag{2}$$

- Material derivatives following the solid and the fluid, which move with velocities v_s and v_w:

$$\begin{aligned}\frac{d^{(s)}}{dt} &= \frac{\partial}{\partial t} + {v_s}^T.\,\mathrm{grad} \\ \frac{d^{(w)}}{dt} &= \frac{\partial}{\partial t} + {v_w}^T.\,\mathrm{grad}\end{aligned} \tag{3}$$

  Both derivatives are related by

$$\frac{d^{(w)}}{dt} = \frac{d^{(s)}}{dt} + (v_w - v_s)^T.\,\mathrm{grad} \tag{4}$$

- In classical geomechanics, a relative velocity w (Darcy) is introduced as:

$$v_w = v_s + \frac{w}{n} \tag{5}$$

The balance of mass equations are:

$$\frac{d^{(s)}}{dt}\left((1-n)\,\rho_s\right) + (1-n)\,\rho_s\,\mathrm{div}\ v_s = 0 \tag{6}$$

and

$$\frac{d^{(w)}}{dt}\,(n\rho_w) + n\rho_w\,\mathrm{div}\,v_w = 0 \tag{7}$$

They can be combined as:

$$\frac{(1-n)}{\rho_s}\frac{d^{(s)}\rho_s}{dt} + \frac{n}{\rho_w}\frac{d^{(w)}\rho_w}{dt}\ \mathrm{div}\ v_s + \mathrm{div}\ w = 0 \tag{8}$$

Balance of linear momentum is:

$$n\rho_w\frac{d^{(w)}v_w}{dt} = -\,n\ \mathrm{grad}\ p_w + n\rho_w b + nR_w \quad \text{(fluid)} \tag{9}$$

$$(1-n)\,\rho_s\frac{d^{(s)}v_s}{dt} = \ \mathrm{div}\,\sigma' - (1-n)\,\mathrm{grad}\ p_w + (1-n)\,\rho_s b + (1-n)\,R_s\ \text{(solid)} \tag{10}$$

where σ' is the effective stress, b is the body forces vector, and R_w and R_s characterize the mechanical interaction between phases.

It is important to note that the interaction forces between the solid skeleton and the pore fluid will be described by models such as the Darcy or Anderson et al. [And67]. The set of PDE's given by eqns. 6, 7 and 9, 10 are complemented by suitable constitutive relations describing the effective stress σ', and kinematics relations for both solid and fluid phases.

The general (2 phases) model described by eqns. 6, 7 and 9, 10 can be simplified in many cases of interest assuming that

$$\frac{d^{(w)}}{dt} = \frac{d^{(s)}}{dt} + (v_w - v_s)^T . \mathrm{grad} \approx \frac{d^{(s)}}{dt} \tag{11}$$

In what follows, we will drop the superindexes (s) and (w) assuming that derivatives are taken relative to the solid phase.

In this case, equations 6 and 7 can be combined, resulting in:

$$\frac{(1-n)}{\rho_s}\frac{d\rho_s}{dt} + \frac{n}{\rho_w}\frac{d\rho_w}{dt} + \mathrm{div}\ v_s + \mathrm{div}\ w = 0 \tag{12}$$

From here, introducing the volumetric stiffness of solid particles and the fluid, K_s and K_w, we arrive to:

$$\frac{1}{Q}\frac{dp_w}{dt} + \mathrm{div}\ v_s + \mathrm{div}\ w = 0 \tag{13}$$

where

$$\frac{1}{Q} = \frac{(1-n)}{K_s} + \frac{n}{K_w} \tag{14}$$

The resulting model is cast in terms of v_s, v_w, p_w and σ'. Using a constitutive relation plus the kinematic relations between velocities, strains and stresses, the unknowns of the system reduce to $v_s,\ v_w$ and p_w.

This $v_s - v_w - p_w$ model is of interest in cases such as debris flows.

2.2 The $v_s - p_w$ Biot-Zienkiewicz model

In some cases (Zienkiewicz et al 1990a [Zie90a]), the relative velocity of the pore fluid can be eliminated. The resulting model, known as the $u - p_w$ is the much celebrated model which is found in most geotechnical finite element codes used today.

The equations are:

(i) Balance of linear momentum equations for the solid and pore fluid that, once combined are:

$$\rho\frac{dv}{dt} = \mathrm{div}\,\sigma' - \ \mathrm{div}\ p_w + \rho\, b \tag{15}$$

(ii) Balance of mass and momentum of the pore fluid, which, once combined to eliminate w result on:

$$\frac{1}{Q}\frac{dp_w}{dt} + \mathrm{div}\ v + \mathrm{div}\ (\,k_w\,\mathrm{grad}\ p_w) = 0 \tag{16}$$

In above equation, we have assumed an interaction law between solid and fluid phases given by Darcy's law, k_w being the permeability.

2.3 Boundary and initial conditions

The equations presented so far have to be complemented by suitable boundary and initial conditions for the problem variables. In the $\mathbf{u} - p_w$ the conditions are the following:

(i) $\mathbf{u}$ prescribed on Γ_u;

(ii) tractions prescribed on Γ_t, $\sigma.\mathbf{n} = \bar{t}$, $\Gamma_u \cup \Gamma_t = \Gamma$, $\Gamma_u \cap \Gamma_t = \{\emptyset\}$;

(iii) p_w prescribed on Γ_{pw};

(iv) flux -$k_w \nabla p_w \mathbf{n}$ prescribed along Γ_q,$\Gamma_{pw} \cup \Gamma_q = \Gamma$, $\Gamma_{pw} \cap \Gamma_q = \{\emptyset\}$.

In the case of a non-saturated slope under rain, the boundary conditions to be applied can be simplified to a prescribed pressure (atmospheric) on the surface, but care should be taken as the inflow cannot be larger than the amount of percolating water. In this way, the saturation will increase within the material and the effective stresses will decrease.

The initial conditions will be:

(i) solid displacements and velocities at $t = 0$,

(ii) pore pressures at $t = 0$.

2.4 The incompressible undrained limit

The $u - p_w$ version of Biot equations can be further simplified depending on whether accelerations are small, leading to what is known as "consolidation", or "slow consolidation phenomena", which in the case of saturated materials are:

$$\mathbf{S}^T \sigma + \rho \mathbf{b} = \mathbf{0} \tag{17}$$

where $\mathbf{S}^T$ is the divergence operator and

$$\nabla^T \left\{ k_w \left(-\nabla p_w + \rho_w \mathbf{b} \right) \right\} + \frac{1}{Q} \dot{p}_w + \operatorname{tr}\left(\dot{\varepsilon} \right) = 0 \tag{18}$$

If we now consider a material of very small permeability and very large volumetric stiffness, above equations can be written as:

$$\mathbf{S}^T \left(\sigma' + \mathbf{m}\, p_w \right) + \rho \mathbf{b} = \mathbf{0}$$
$$\nabla^T \dot{\mathbf{u}} = 0$$

where $\mathbf{m} = (1, 1, 1, 0, 0, 0)$ in 3 dimensions, which corresponds in vector notation to the trace operator. These equations are similar to the equations found in solid mechanics for incompressible materials. Here, important difficulties regarding both the interpolation spaces which can be used for displacements and pressures and simulation of failure processes are found, and will be discussed later.

2.5 A note on mixed $\sigma' - v - p_w$

One interesting possibility is to formulate the model using, as nodal variables, effective stresses, velocities and pore pressures. This approach has been shown to provide an excellent accuracy which allows the use of lower order elements, such as linear triangles and tetrahedra.

For the sake of simplicity, we will consider the case of a drained material, for which $p_w = 0$.In 1D, the equations are:

(i) Balance of momentum (convective terms not included)

$$\rho \frac{\partial v}{\partial t} = \frac{\partial \sigma'}{\partial x} \tag{19}$$

(ii) Constitutive equation (elastic material)

$$\frac{\partial \sigma}{\partial t} = E \frac{\partial v}{\partial x} \tag{20}$$

Above equations can be written in a compact manner as

$$\frac{\partial}{\partial t}\begin{pmatrix} \sigma' \\ v \end{pmatrix} + \begin{pmatrix} 0 & E \\ 1/\rho & 0 \end{pmatrix} \frac{\partial}{\partial x}\begin{pmatrix} \sigma' \\ v \end{pmatrix} \tag{21}$$

The equation can be solved using stable FE schemes which will be described later on.

3 Discretization: FEM techniques

3.1 Biot-Zienkiewicz u-p$_w$ finite element formulation

The mathematical model consists on equations 15,16.

This system of partial differential equations can be discretized using standard Galerkin techniques, as described in [Zie90a]. After approximating the fields u and p_w as: $u = \mathbf{N}_u \bar{\mathbf{u}}$, $p_w = \mathbf{N}_p \bar{\mathbf{p}}_w$, it results in two ordinary differential equations:

$$\mathbf{M} \frac{d^2 \bar{\mathbf{u}}}{dt^2} + \int_\Omega \mathbf{B}^T . \sigma' d\Omega - \mathbf{Q} \bar{\mathbf{p}}_w - \mathbf{f}_u = \mathbf{0} \tag{22}$$

where $\mathbf{B} = \mathbf{S}.\mathbf{N}_u$, and

$$\mathbf{Q}^T . \frac{d\bar{\mathbf{u}}}{dt} + \mathbf{H}.\bar{\mathbf{p}}_w + \mathbf{C}.\frac{d\bar{\mathbf{p}}_w}{dt} - \mathbf{f}_p = \mathbf{0} \tag{23}$$

The matrices given above are defined as:

$$
\begin{aligned}
\mathbf{M} &= \textstyle\int_\Omega \rho \mathbf{N}_u^T \mathbf{N}_u d\Omega \\
\mathbf{C} &= \textstyle\int_\Omega \frac{1}{Q} \mathbf{N}_p^T \mathbf{N}_p d\Omega \\
\mathbf{Q} &= \textstyle\int_\Omega S_w \alpha \mathbf{B}^T \mathbf{m} \mathbf{N}_p d\Omega \\
\mathbf{H} &= \textstyle\int \nabla \mathbf{N}_p^T \mathbf{k}_w \nabla \mathbf{N}_p d\Omega
\end{aligned}
\tag{24}
$$

where S_w is the degree of saturation and α the ratio between the volumetric stiffnesses of the soil skeleton and that of solid particles, and

$$
\mathbf{f}_u = \textstyle\int_\Omega \mathbf{N}_u^T \mathbf{b} d\Omega + \int_{\Gamma_t} \mathbf{N}_u^T \,\bar{\mathbf{t}} d\Gamma
$$

$$
\mathbf{f}_p = \textstyle\int_{\Gamma_q} \mathbf{N}_p^T \mathbf{k}_w \dfrac{\partial p}{\partial n} d\Gamma + \int_\Omega \nabla \mathbf{N}_p^T \mathbf{k}_w \rho_w \mathbf{b} d\Omega - \left(\int_\Omega \nabla \mathbf{N}_p \mathbf{k}_w \mathbf{N}_u d\Omega \right) \ddot{\mathbf{u}} - \int_\Omega \mathbf{N}_p^T s_0 d\Omega
\tag{25}
$$

The term including accelerations in $\mathbf{f}_p$ is usually disregarded.

The time derivatives of $\mathbf{u}$ and $\mathbf{p}_w$are approximated in a typical step of computation using the Generalized Newmark GN22 scheme for displacements and a GN11 for the water pressure [MO55], [OZ91].

If we introduce the following notation [MO55]:

$$
\begin{aligned}
\Delta \ddot{\mathbf{u}}^n &= \ddot{\mathbf{u}}^{n+1} - \ddot{\mathbf{u}}^n \\
\Delta \dot{p}_w^n &= \dot{p}_w^{n+1} - \dot{p}_w^n
\end{aligned}
$$

$$
\begin{aligned}
\dot{\mathbf{u}}^{n+1} &= \dot{\mathbf{u}}^{p,n+1} + \beta_1 \Delta t \Delta \ddot{\mathbf{u}}^n \\
\mathbf{u}^{n+1} &= \mathbf{u}^{p,n} + \tfrac{1}{2} \beta_2 \Delta t^2 \Delta \ddot{\mathbf{u}}^n \\
p_w^{n+1} &= p_w^{p,n+1} + \theta \Delta t \Delta \dot{p}_w^n
\end{aligned}
\tag{26}
$$

where

$$
\begin{aligned}
\dot{\mathbf{u}}^{p,n+1} &= \dot{\mathbf{u}}^n + \Delta t \ddot{\mathbf{u}}^n \\
\mathbf{u}^{p,n+1} &= \mathbf{u}^n + \Delta t \dot{\mathbf{u}}^n + \tfrac{1}{2} \Delta t^2 \ddot{\mathbf{u}}^n \\
p_w^{p,n+1} &= p_w^n + \Delta t \dot{p}_w^n
\end{aligned}
\tag{27}
$$

we obtain the discretized system of equations valid in each time step:

$$
\mathbf{M} \Delta \ddot{\mathbf{u}}^n + \int \mathbf{B}^T \sigma'^{n+1} - \theta \Delta t \mathbf{Q} \Delta \dot{\mathbf{p}}_w^n - \mathbf{F}_u^{n+1} = \mathbf{\Phi}_u = \mathbf{0}
\tag{28}
$$

$$\beta_1 \Delta t \mathbf{Q}^T \Delta \ddot{\mathbf{u}}^n + (\Delta t \theta \mathbf{H} + \mathbf{C}) \Delta \dot{\mathbf{p}}_w^n - \mathbf{F}_p^{n+1} = \mathbf{\Phi}_p = \mathbf{0} \tag{29}$$

where the unknown values are $\Delta \ddot{\mathbf{u}}^n$ and $\Delta \dot{\mathbf{p}}_w^n$

If this system is non-linear, it can be solved by using a Newton Raphson method with a suitable jacobian matrix:.

$$\begin{bmatrix} \dfrac{\partial \mathbf{\Phi}_u}{\partial \Delta \ddot{\mathbf{u}}} & \dfrac{\partial \mathbf{\Phi}_u}{\partial \Delta \dot{\mathbf{p}}} \\ \dfrac{\partial \mathbf{\Phi}_p}{\partial \Delta \ddot{\mathbf{u}}} & \dfrac{\partial \mathbf{\Phi}_p}{\partial \Delta \dot{\mathbf{p}}} \end{bmatrix}^{(i)} \begin{bmatrix} \delta(\Delta \ddot{\mathbf{u}}) \\ \delta(\Delta \dot{\mathbf{p}}) \end{bmatrix}^{(i+1)} = - \begin{bmatrix} \mathbf{\Phi}_u \\ \mathbf{\Phi}_p \end{bmatrix}^{(i)} \tag{30}$$

Using equations 28 and 29 we can write the above step as:

$$\begin{bmatrix} \mathbf{M} + \frac{1}{2} \Delta t^2 \beta_2 \mathbf{K}_T & -\theta \Delta t \mathbf{Q} \\ \beta_1 \Delta t \mathbf{Q}^T & \Delta t \theta \mathbf{H} + \mathbf{S} \end{bmatrix}^{(i)} \begin{bmatrix} \delta(\Delta \ddot{\mathbf{u}}) \\ \delta(\Delta \dot{\mathbf{p}}) \end{bmatrix}^{(i+1)} = - \begin{bmatrix} \mathbf{\Phi}_u \\ \mathbf{\Phi}_p \end{bmatrix}^{(i)} \tag{31}$$

where $\mathbf{K}_T$ is the tangent stiffness matrix. $\mathbf{K}_T = \int \mathbf{B}^T \mathbf{D}_{ep} \mathbf{B} d\Omega$

3.2 Application: Liquefaction failure of a dyke under earthquake action

The case we will consider next is that of an earthquake induced flowslide in very loose saturated sand. The problem consists on a dike 10 m in height with slopes 2:1, founded on a sand layer which extends 10 m in depth and lies on a rigid rockbed. The material of both the dike and the foundation is a very loose saturated sand.

Initial conditions correspond to geostatic equilibrium under gravity forces. Pore pressure at the surface has been assumed to be equal to -20 kPa. The finite element mesh can be seen in Fig.1 and consists on 500 quadrilaterals with 8 nodes for displacements and 4 for pore pressures. A reduced integration rule has been used in the solid part to avoid locking. The number of nodes is 1611, with 3535 degrees of freedom.

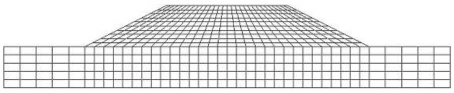

Figure 1: Finite element mesh

Loading is applied by prescribing horizontal accelerations at the base. We have used the horizontal accelerations of the *NS* component of El Centro earthquake. A simplified absorbing boundary condition has been applied at lateral boundaries. Concerning pore pressures, it has been assumed that no flux occurs at artificial boundaries, and the constant value of -20 kPa has been kept at the surface.

The behaviour of the loose material, $D_R = 27^o$, is represented, using the Pastor-Zienkiewicz model for sand.

The results can be seen in Fig.2, 3, 4, 5, where the contours of pore pressure, plastic strain, p'/p'_0 and displacements are given at different times. Plastic strain accumulates in two zones, with much higher values at the right hand slope. The ratio between the mean effective confining pressure and its initial value p'/p'_0 has been used as an indicator of the extent of the liquefied zones. From these results, it can be concluded that failure of the dike is caused by liquefaction of the outer liquefied zone.

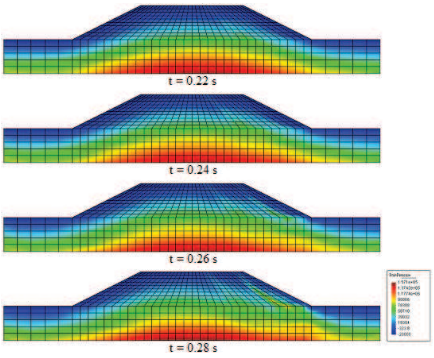

Figure 2: Pore pressure contour (Pa)

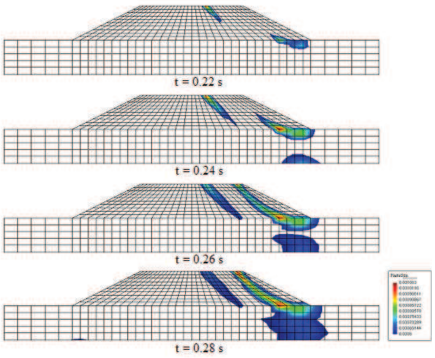

Figure 3: Plastic deformation contour

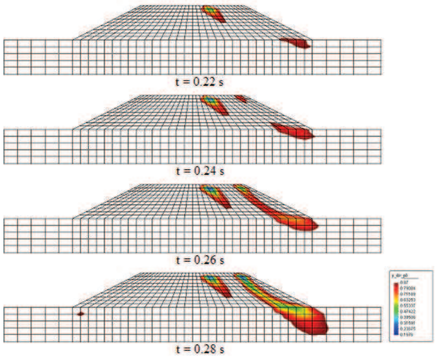

Figure 4: p'/p'_0 contour

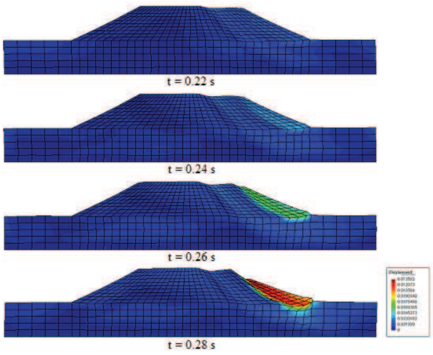

Figure 5: Deformation contour

3.2.1 A note on air liquefaction failure

If the soil is partially saturated, its behaviour depends on the coupling between the solid skeleton and the pore air and water. In the limit case of a dry soil, the air has to flow out from the pores for the material to consolidate, but typical air consolidation times are much smaller than those of the water. Therefore, in practical cases, the role of air pressures is neglected, as the characteristic time of loading is much larger than consolidation time. However, it is possible to imagine situations with much smaller loading times, where coupling between pore air and soil skeleton plays a paramount role. This is the case of fluidized granular beds, just to mention a particular example of industrial interest.

Bishop in 1973 [Bis73] describes the case of Jupille flowslide, which happened in Belgium in February 1961. A tip of uncompacted fly ash located in the upper part of a narrow valley collapsed, and the subsequent flowslide travelled for about 600 m at very high speeds (130 km/h) until it stopped. Triggering mechanism was suggested to be ”collapse due to undermining of a steep, partly saturated and slightly cohesive face”. Bishop referred to Calembert and Dantinne [Dan], who in 1964 pointed out the role of the entrapped air. The mechanism of pore air consolidation can explain the ”sort of fog” which formed above the flowing material, as warmer air met the colder winter air in the exterior. The ”honeycomb” like structure of soil in the tip was responsible of its sudden collapse when movement started.

3.3 Limitations of the $u - p_w$ model

The displacement-pressure model described above presents a series of limitations, which in some cases results on a deterioration of the quality of the predictions.

We will describe next the most relevant.

3.3.1 Numerical diffusion and dispersion

As many displacement based finite elements, the proposed model presents numerical damping and dispersion. The former consists on an artificial damping of the amplitude of travelling waves, and the latter on numerical velocities of propagation which depend on the relative wave length Λ, i.e., the ratio between the wave length λ and the mesh size $\Delta x, \Lambda = \lambda/\Delta x$.

To illustrate the problem, we show in fig.6 the results of the propagation of a elastic wave on a shear layer (drained material).

The shape of the velocity wave at $x = L/4$ presents trailing oscillations, caused by waves of short wavelengths which travel with smaller velocity.

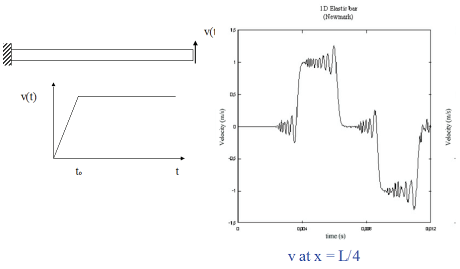

Figure 6: Wave propagation along a shear layer

3.3.2 Volumetric locking and mesh alignment effects

Volumetric locking is presented in materials approaching incompressibility conditions. In the case of coupled problems, it implies that permeability is close to zero. The problem consists on an artificial stiffness which makes the numerical model of the structure to deform much less than it theoretically should. In the case of plastic materials, flow rule imposes an additional condition on the volumetric plastic strain, which results on much higher failure loads. Volumetric locking is present in all displacement based finite elements, but specially in lower order elements. The solution to this problem consists of choosing higher order interpolation polynomials for the displacement field. The problem of mesh alignment consists on a spurious dependence of the failure mechanism on both the type of elements and the way they are arranged in the mesh. To illustrate it, we will consider a vertical cut on a perfect plastic Von Mises material. A load is applied trough a rough footing, as depicted in fig.7.

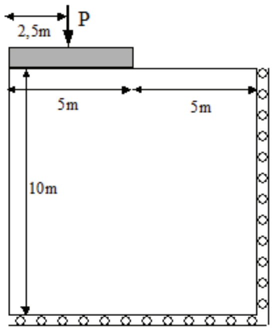

Figure 7: Footing on vertical slope

The material properties for both the soil and the footing are shown in table 1:

We will consider the two linear triangles finite element meshes depicted in Fig. 8

Table 1: Material properties for the soil and footing

	Material type	E(Pa)	υ	σ_y (Pa)
Soil	Von Mises	1.0E5	0.35	200.0
Footing	Linear elastic	1.0E8	0.35	

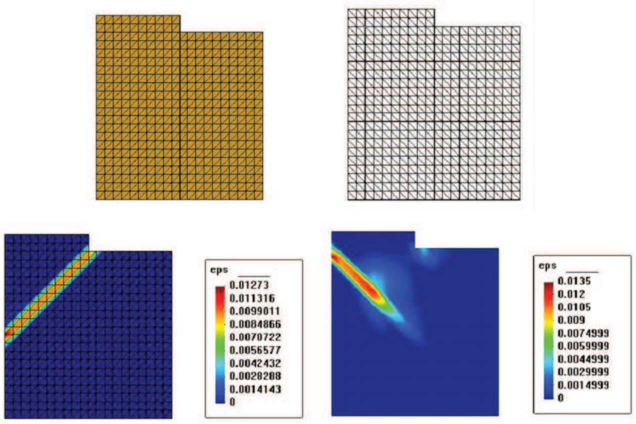

Figure 8: Mesh alignment effects on the failure mechanism of a vertical cut

The results are plotted in the same figure, where we have plotted the isolines of equivalent plastic strain. We can see how different alignments result on completely different mechanisms. The problem of alignment is related to the accuracy of the finite elements, and elements which behave well in bending do not exhibit important alignment effects, as happens in the enhanced strain quadrilaterals (Simo-Rifai elements) [SJ90].

3.3.3 Choice of the interpolation spaces for displacements and pore pressures

Soil dynamics problems often involve a large number of time steps and meshes with a large number of nodes which results on large times of computation. Time can be saved by using explicit schemes when possible, and elements with a low order of interpolation, such as triangles in 2D an tetrahedra in 3D.

If such elements are used, the displacement (or the velocity) field will be approximated using linear functions, and so the pore pressures will be approximated using the same shape functions.

Another very much interesting element is the Simo Rifai quadrilateral with bilinear pore pressures [P.M03].

Such equal order of interpolation elements present severe oscillations in the pore pressure field when the material has very small permeability and both the solid particles and the pore fluid have small compressibility. The situation is of similar nature to that found when using mixed formulations in Solid and Fluid Dynamics. The reason is that these mixed elements with equal interpolation do not satisfy the Babuska-Brezzi [Bab73], [Bre74] condition which is necessary to ensure stability or the much simpler patch test proposed by Zienkiewicz et al. [OS86] for mixed formulations. It is important to note that the latter is a necessary but not a sufficient condition for stability. The interested reader can find in the text of Bathe [Bat96] a detailed description. Allowed elements are for instance, quadrilaterals Q8P4 with quadratic approximation of the displacements and bilinear for the pore pressure, or the T6P3 triangles, both in 2D.

In order to use the simple linear triangles or tetrahedras for computational efficiency circumventing the limitations imposed by the Babuska-Brezzi conditions, special stabilization techniques have to be used. The problem has attracted the attention of numerous researchers from Fluid, Solid and Soil Mechanics in the past years. In the context of Fluid Dynamics, it is worth mentioning the work of Brezzi and Pitkaranta [BP84], Hughes, Franca and Balestra [THB86], Hafez and Soliman [HS91], Zienkiewicz and Wu [ZW91], just to mention a few.

These methods have been extended to Soil Dynamics problems by Zienkiewicz et al. [OS93] and to Soil Mechanics problems by Pastor et al. [PFM97], [PM99].

One of the most simple yet effective ways of stabilization is the fractional step algorithm, which was introduced by Chorin [Cho68] as a device to allow the use of standard time integration techniques in fluid dynamics problems. Among the several alternative formulations some forms were found later to provide the required stabilization for elements with equal order of interpolation of velocities and pressures. The discovery was first made by Schneider, Rathby and Yovanovich [GM95] and Kawahara and Ohmiya [M.K85] and later justified by R.Codina, M.Vázquez and O.C.Zienkiewicz [RO95].

The method has been extended to Solid Dynamics by Zienkiewicz et al. [OM98] and Quecedo et al. [QM00], and to Soil Dynamics problems by Pastor et al [PM99], Li et al [XL03] and Mabssout et al. [M.M06]. It is also worth noticing the work of Mira et al. [P.M03] for enhanced strain elements based on Simo-Rifai element technology, providing a very interesting alternative in geomechanical simulations.

4 Numerical Model: mixed stress-velocity-pressure finite element formulations

So far we have discussed formulations based on the second order equation, but it is also possible to extend the solid dynamics model based on the system of first order equations to the case of saturated geomaterials (Mabssout et al 2006). This formulation presents the following advantages:

(i) Low order elements such as triangles and tetrahedral can be used even in bending dominated situations. Cost of computation is much smaller in these low order elements.

(ii) Oscillations during the propagation of shocks in fast dynamics problems are much smaller than in the case of classical second order algorithms

(iii) Provide a very good accuracy in dynamic localization problems.

Elements with the same order of interpolation of displacements and pressures present severe instabilities in the incompressible undrained limit. The problem is similar to those found in incompressible solid and fluid dynamics, and requires the use of the special stabilization techniques described in the preceding Section.

We will describe here the case of viscoplastic materials which has been considered by Mabssout et al. [M.M06].

The method is based on two techniques:

(i) a Taylor Galerkin scheme which ensures good accuracy in bending dominated situations, good damping and numerical dispersion properties, and very small dependence on mesh alignment

(ii) A fractional step technique allowing equal order of interpolation of pressures and velocities.

The elements used were linear triangles, having stresses, velocities and pore pressures as nodal variables.

4.1 Taylor Galerkin for solid dynamics

Concerning the **Taylor Galerkin** algorithm, it can be consider as an extension of the Lax Wendroff finite differences scheme, where a Taylor series expansion in time is followed by a space discretization. In the case of the Taylor Galerkin scheme, spacial discretization is done using finite elements in space (simple linear triangles and tetrahedras).

Taylor Galerkin method was independently proposed by [RLZ84] and [Don84].

Here we will present a simple 2 step explicit Taylor Galerkin algorithm formulated in terms of velocities and stresses as primary variables. This two step algorithm has been widely used for advection dominated problems in Fluid Dynamics [Per86] [ZT00]. We will present next the algorithm for completeness.

We will start by writing the momentum and constitutive equations as:

$$\frac{\partial}{\partial t}\begin{bmatrix}\sigma_{11}\\ \sigma_{22}\\ \sigma_{33}\\ v_1\\ v_2\end{bmatrix} - \frac{\partial}{\partial x}\begin{bmatrix}D_{11}v_1\\ D_{12}v_1\\ D_{33}v_2\\ \frac{\sigma_{11}}{\rho}\\ \frac{\sigma_{12}}{\rho}\end{bmatrix} - \frac{\partial}{\partial y}\begin{bmatrix}D_{12}v_2\\ D_{22}v_2\\ D_{33}v_1\\ \frac{\sigma_{12}}{\rho}\\ \frac{\sigma_{22}}{\rho}\end{bmatrix} = \begin{bmatrix}0\\ 0\\ 0\\ 0\\ 0\end{bmatrix} \tag{32}$$

where D_{ij} are the components of the elastic matrix $\mathbf{D}^e$.

Above equation can be written in conservation form as

$$\frac{\partial \bar{\phi}}{\partial t} + \frac{\partial F_x}{\partial x} + \frac{\partial F_y}{\partial y} = \bar{S} \tag{33}$$

where we have introduced the vectors of unknowns $\bar{\phi}$, fluxes F_x and F_y, and source $\bar{S}$.

The Taylor-Galerkin algorithm for solving the conservation equation (33)

$$\frac{\partial \bar{\phi}}{\partial t} + div\mathbf{F} = \bar{S} \tag{34}$$

where **F** is the advective flux tensor and $\bar{S}$ is the vector of sources, starts from a second order expansion in time

$$\bar{\phi}^{n+1} = \bar{\phi}^n + \Delta t \left.\frac{\partial \bar{\phi}}{\partial t}\right|^n + \frac{1}{2}\Delta t^2 \left.\frac{\partial^2 \bar{\phi}}{\partial t^2}\right|^n \tag{35}$$

where the first order time derivative of the unknowns can be calculated using equation (33) as

$$\left.\frac{\partial \bar{\phi}}{\partial t}\right|^n = \left(\bar{S} - div\,\mathbf{F}\right)^n \tag{36}$$

To obtain the second order time derivative, the Two-Step Taylor-Galerkin procedure considers an intermediate step between t^n and t^{n+1}. The aim of this first time step is to calculate the solution at a time t$^{n+1/2}$. This step is followed by a second one that brings the solution to t^{n+1}.

In this way, the first step results in

$$\bar{\phi}^{n+1/2} = \bar{\phi}^n + \frac{\Delta t}{2}\left(\bar{S} - div\,\mathbf{F}\right)^n \tag{37}$$

which allows the calculation of $\mathbf{F}^{n+1/2}$ and $\bar{S}^{n+1/2}$.

Considering now a Taylor series expansion of the flux and source terms,

$$\mathbf{F}^{n+1/2} = \mathbf{F}^n + \left(\frac{\partial \mathbf{F}}{\partial t}\right)^n \frac{\Delta t}{2}$$

$$\bar{S}^{n+1/2} = \bar{S}^n + \left(\frac{\partial \bar{S}}{\partial t}\right)^n \frac{\Delta t}{2}$$

where the values of $\mathbf{F}^{n+1/2}$ and $\bar{\mathrm{S}}^{n+1/2}$ are calculated using $\bar{\phi}^{n+1/2}$, the flux and sources time derivatives are

$$\begin{aligned}\left(\frac{\partial \mathbf{F}}{\partial t}\right)^{n} &= \frac{2}{\Delta t}\left(\mathbf{F}^{n+1/2} - \mathbf{F}^{n}\right)\\ \left(\frac{\partial \bar{S}}{\partial t}\right)^{n} &= \frac{2}{\Delta t}\left(\bar{S}^{n+1/2} - \bar{S}^{n}\right)\end{aligned}$$

Incorporating these expressions into the second order time derivative

$$\left.\frac{\partial^2 \bar{\phi}}{\partial t^2}\right|^{n} = \frac{\partial}{\partial t}\left(\bar{S} - div\,\mathbf{F}\right)^{n}$$

results in

$$\left.\frac{\partial^2 \bar{\phi}}{\partial t^2}\right|^{n} = \frac{2}{\Delta t}\left(\bar{S}^{n+1/2} - \bar{S}^{n} - div\left(\mathbf{F}^{n+1/2} - \mathbf{F}^{n}\right)\right) \tag{38}$$

Substituting now the expressions obtained for the first (36) and second (38) order time derivatives in the Taylor series expansion (35) results in

$$\bar{\phi}^{n+1} = \bar{\phi}^{n} + \Delta t\left(\bar{S}^{n+1/2} - div\,\mathbf{F}^{n+1/2}\right)$$

This equation is discretized in space using the conventional Galerkin weigthing to finally result in the system of equations to be solved to obtain the unknown increments in the variables at the time step. The resulting system of equations is:

$$\underline{M}\,\Delta\phi = \Delta t\int_{\Omega}\underline{\mathbf{N}}\,\mathbf{S}^{n+1/2}d\Omega - \int_{\Gamma_N}\underline{N}\left(\mathbf{F}^{n+1/2}\cdot\bar{n}\right)d\gamma + \int_{\Omega}\mathbf{F}^{n+1/2}\,grad\,\underline{\mathbf{N}}\,d\Omega \tag{39}$$

The system of equations to be solved during each time step is of the type

$$\underline{\mathbf{M}}\mathbf{x} = \mathbf{f}$$

and can be economically solved using a Jacobi iteration scheme [Per86]

$$\mathbf{x}^{(k+1)} = \mathbf{x}^{(k)} + M_L^{-1}(f - \underline{M}\mathbf{x}^{(k)})$$

where the superscript k is an iteration counter, if an approximate inverse matrix, M_L^{-1}, is known in advance. As in the case of equation (39) an approximate inverse of the system matrix, $\underline{M}$, is the lumped mass matrix, the equation system (39) can be solved using this algorithm. Typically, less than six iterations are enough to obtain an accurate solution.

4.2 An introduction to Fractional step

Regarding the **fractional step**, we will come back to the stress-velocity-pore pressure equations

$$\begin{aligned}\rho\frac{dv}{dt} &= \text{div }\sigma' - \text{grad }p_w + \rho b\\ \frac{1}{Q^*}\frac{dp_w}{dt} &= \text{div }(k\text{ grad }p_w) - \text{div }v\\ \sigma &= \sigma' - p_w I\\ d\sigma' &= D^{ep}d\varepsilon\end{aligned} \tag{40}$$

We will rewrite the first equation as:

$$\rho\frac{v^* - v^n}{\Delta t} = \text{div }\sigma' + \rho b|^n \tag{41}$$

$$\rho\frac{v^{n+1} - v^*}{\Delta t} = -\text{ grad }p_w|^{n+\theta_2} = -\text{ grad }(p_w + \theta_2\Delta p_w) \tag{42}$$

where we have introduced an intermediate velocity v^* and the increment of pore pressure

$$p_w^{n+1} = p_w^n + \Delta p_w \tag{43}$$

We will choose usually $\theta_2 = 1/2$ in Eqn 42 as

$$\frac{1}{Q^*}\frac{\Delta p_w}{\Delta t} = \text{div}\,(k\text{ grad }p_w)|^n - \text{div }v^{n+1} \tag{44}$$

Now, the velocity v^{n+1} can be obtained from 42 as:

$$v^{n+1} = v^* - \frac{\Delta t}{\rho}\text{grad }(p_w + \theta_2\Delta p_w) \tag{45}$$

After substituting in 44, we obtain:

$$\left(\frac{1}{Q^*} - \frac{\Delta t^2\theta_2}{\rho}\nabla^2\right)\frac{\Delta p_w}{\Delta t} = \text{grad }(k\text{ div }p_w)|^n - \text{div }v^* + \Delta t\,\nabla^2 p_w^n \tag{46}$$

Summarizing, the fractional step method consist on performing the time step computations as follows:

(i) First of all, obtain the intermediate velocity field v^* using 41:

$$v^* = v^n + \frac{\Delta t}{\rho}\left(\text{div }\sigma' + \rho b\right)^n \tag{47}$$

(ii) Solve implicitly 46 to obtain Δp_w and

$$p_w^{n+1} = p_w^n + \Delta p_w \tag{48}$$

(iii) Finally, obtain the velocity field at time n+1 using 45

Equations 45, 47 and 48 can be discretized using a standard Galerkin finite element technique. It is important to notice that the time step is limited for the dry solid skeleton response, as the pore pressure laplacian equation has been solved implicitly.

4.3 The stabilized $\sigma' - v - p_w$ model

In the case of elasto-viscoplastic materials the $\sigma' - v - p_w$ model, the equations are:

$$\begin{aligned} \rho \frac{\partial v}{\partial t} &= \text{div } \sigma' - \text{grad } p_w + \rho b \\ \frac{\partial \sigma}{\partial t} &= D^e \, \text{grad}^s \, v - D^e \dot{\varepsilon}^{vp} \\ \frac{1}{Q^*} \frac{dp_w}{dt} &= \text{div } (k \text{ grad } p_w) - \text{div } v \end{aligned} \tag{49}$$

where $\text{grad}^s \, v$ is the rate of deformation tensor with components

$$d_{ij} = \frac{1}{2} \left(\frac{\partial v_i}{\partial x_j} + \frac{\partial v_j}{\partial x_i} \right)$$

The fractional step algorithm consists of:

(i) A first step where equations 49(a) and (b) are solved up to an intermediate state *:

$$\begin{aligned} \frac{\sigma'^* - \sigma'^n}{\Delta t} &= \frac{\Delta \sigma'^*}{\Delta t} = D^e \, \text{grad}^s \, v - D^e \dot{\varepsilon}^{vp} \big|^n \\ \frac{v^* - v^n}{\Delta t} &= \frac{\Delta v^*}{\Delta t} = \text{div } \sigma' + \rho b \big|^n \end{aligned} \tag{50}$$

(ii) A second step where the pore pressure is evaluated at time n+1 (see eqn.46)

$$\left(\frac{1}{Q^*} - \frac{\Delta t^2 \theta_2}{\rho} \nabla^2 \right) \frac{\Delta p_w}{\Delta t} = \text{div } (k \text{ grad } p_w) \big|^n - \text{div } v^* + \Delta t \nabla^2 p_w^n \tag{51}$$

(iii) a third step where velocities and stresses at time n+1 are evaluated

$$\begin{aligned} \frac{\sigma'^{n+1} - \sigma'^*}{\Delta t} &= \frac{\Delta \sigma'^{**}}{\Delta t} = \left. \frac{\partial p_w}{\partial t} \right|^{n+1} \\ \rho \frac{v^{n+1} - v^*}{\Delta t} &= \rho \frac{\Delta v^{**}}{\Delta t} = - \text{grad } p_w \big|^{n+1} \end{aligned} \tag{52}$$

Nodal variables are velocities, stresses and pore pressures.

Above equations are solved as follows:

(a) Eqns. 50 are solved using the Taylor Galerkin method, combined with a Runge Kutta algorithm for the source terms which has been used by Quecedo et al [Que04] and Mabssout et al [M.M06]. We obtain σ'^{*} and v^{*}

(b) The pore pressure laplacian 51 is solved, obtaining p_w^{n+1}

(c) Finally, stresses and velocities are obtained at time n+1 using eqn 52.

5 Stabilized stress-velocity-pressure algorithm: Examples and applications

5.1 Shock propagation in a one dimensional soil layer

The purpose of this example is to show the advantages of the first order formulation in fast dynamics problems exhibiting shocks. The main advantage (Mabssout and Pastor 2002 [M.M02]) in dynamics is the better performance of the first order algorithm with much lower numerical diffusion and dispersion than the second order approach. This result on sharper shocks with much smaller oscillations. In this example we will consider the propagation of a shock wave on a 1D elastic bar of 1 m length. The left boundary is a fixed end, while the velocity is prescribed at the right boundary. The velocity is given by:

$$v(L,t) = 0 \quad t < 0 \qquad \text{and} \quad v(L,t) = 1 \quad t \geq 0$$

The analytical solution consists on a wave travelling to the left which reflects on the fixed boundary, doubling the amplitude of the stress and inverting its sign. In Figure 9 we provide a comparison between the results provided by the Taylor Galerkin and the Newmark schemes. It can be seen how the oscillations accompanying the shock, which indicate numerical dispersion (small wave lengths travel with smaller speed), are larger in the Newmark scheme

5.2 Dynamic localization on a clay specimen

We will analyze here the case of a bidimensional saturated soil subjected to a constant surface loading applied to its upper face, which is applied dynamically. The soil behavior is assumed to be described by a viscoplastic Perzyna law with Modified Cam Clay yield surface. The problem has been sketched in Figure 10a, and it consists of a square of side 1 m. For symmetry reasons only one half will be considered in the analysis

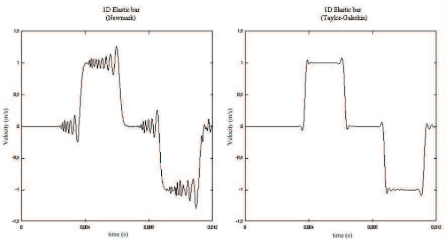

Figure 9: Shock propagation on a elastic bar: Newmark (left) versus Taylor-Galerkin algorithms (Mabssout and Pastor 2002 [M.M02])

The analysis has been performed using the fractional step, Taylor Galerkin algorithm proposed by Mabssout et al (2006). The mesh used in the calculation is shown in Figure 10b and the applied boundary conditions are the following:

(i) On the bottom, both the velocity and the pore water flux are assumed to be zero.

(ii) On the left vertical boundary, the horizontal component of the velocity is zero, the vertical component of the normal surface force is zero, and the pore water flux is zero.

(iii) on the rigth boundary, the normal component of the surface force is set to zero, the flux of water being zero.

(iv) on the upper boundary, the horizontal component of the velocity is zero, and the vertical component is taken as 1 m/s.

The soil has been assumed to be viscoplastic, with the modified Cam Clay yield surface and hardening/softening rule. The Young's modulus has been taken as E = 8.107 Pa, $\nu = 0.3$, $\rho = 1700\ kg/m^3$. The parameters of Perzyna's model are $\gamma = 20\ s^{-1}$ and $N = 1$. The modified Cam Clay model parameters are: $M = 1.0$, $\lambda = 0.1$ and $\kappa = 0.01$.

The initial effective stress of the specimen and the initial velocity and pressure are set equal to zero in the whole domain. The calculation is carried out in the undrained incompressible limit, i.e. $Q^* \to \infty$ and $\kappa_w \to 0$.

Figure 11 shows (a) the effective plastic strain contours, (b) the velocity vectors and (c) the deformed mesh. The mesh is unstructured in order to avoid possible aligment effects due to the mesh orientation. It can be observed in Figure 11 a good definition of the shear band, and the wave is reflected at the bottom, hereafter, the stress doubles, the stress path crosses the yield surface, and the strain localizes in the form of a shear band which is incepted at the bottom-right corner of the specimen. Again the wave reflects on the left boundary and a reflection shear band propagates from there up to the right-top corner

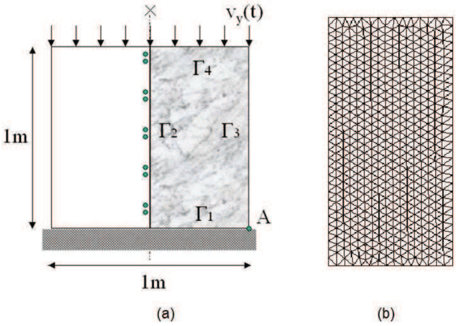

Figure 10: Strain localization in 2D (a) Problem layout (b) Finite element mesh

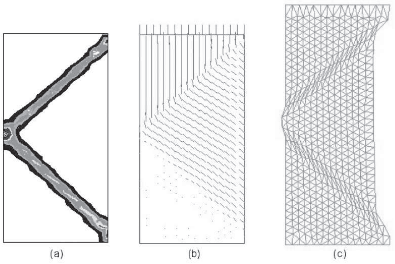

Figure 11: Localization in a saturated specimen: (a) Equivalent plastic strain contours (b) velocity vectors, (c) deformed mesh (After Mabssout et al. 2006)

6 Conclusions

We will conclude this Chapter by recalling the main topics we have discussed here.

(i) For a given coupled problem, there exist a series of different alternative mathematical models with different ranges of application. The $u - p_w$ formulation provides accurate results in many geotechnical applications of interest.

(ii) Regarding $u - p_w$ mixed models, the formulation used for the solid phase presents the same advantages and limitations that in structural problems, therefore, 8 noded quadrilaterals and, specially, enhanced strain elements of the Simo Rifai type are strongly recommended. They have to be stable, either by selecting a suitable space for pore pressure interpolation, or by using stabilization techniques.

(iii) When more accuracy is needed in special situations, stress-velocity-pore pressure formulations provide it. They allow the use of lower order elements.

References

[And67] Jackson R Anderson, T.B. Fluid mechanical description of fluidized beds. equations of motion. *Ind. Eng. Chem. Fundam*, 6:527–539, 1967.

[Bab73] I. Babŭska. The finite element method with lagrange multipiers. *Num. Math*, (20):179–192, 1973.

[Bat96] K.J Bathe. Finite element procedures. *Prentice Hall, New Jersey*, 1996.

[Bio41] M.A. Biot. General theory of three-dimensional consolidation. *J. Appl. Phys.*, 155(12), 1941.

[Bio55] M.A. Biot. Theory of elasticity and consolidation for a porous anisotropic solid. *J. Appl. Phys.*, 182(26), 1955.

[Bis73] A.W. Bishop. The stability of tips and spoil heaps. *Quart.J.Eng.Geol.*, (6):335–376, 1973.

[Boe00] R. De Boer. Theory of porous media: Highlights in historical development and current state. 2000.

[Bow76] R.M. Bowen. Theory of mixtures, part i. *In: Eringen, A.C. (ed.) Continuum physics III*, 1976.

[BP84] F. Brezzi and J. Pitkaranta. On the stabilization of finite element approximations of the stokes problem. efficient solutions of elliptic problems, notes on numerical fluid mechanics. *W. Hackbusch (Eds.)*, pages 11–19, 1984.

[Bre74] F. Brezzi. On the existence, uniqueness and approximation of saddle point problems arising from lagragian multipliers. *RAIRO 8-R2.*, pages 129–151, 1974.

[Cho68] AJ. Chorin. Numerical solution of incompressible flow problems. *Studies in Numerical Analysis*, (2):64–71, 1968.

[Cou95] O. Coussy. Mechanics of porous continua. 1995.

[Dan] Calembert & Dantinne. The avalanche of ash at jupille (liege) on february 3rd, 1961. from:The commemorative volume dedicated to Professeur F.Campus, journal = W. Hackbusch (Eds.), year = 1964, pages = 41-57,.

[Don84] J. Donea. A taylor-galerkin method for convection transport phenomena. *Int. J. Num. Meth. Engng*, (20):101–119, 1984.

[GM95] G.D.Raithby G.E.Schneider and M.M.Yovanovich. F.e. in environmental engineering: Coupled thermo-hydro-mechanical processes in porous media including pollutant transport. *Arch. Comput. Methods Eng.*, (2):1–54, 1995.

[Gre60] Adkins J.E. Green, A.E. Large elastic deformations and nonlinear continuum mechanics. 1960.

[Gre69] Naghdi P.M. Green, A.E. On basic equations for mixtures. *Q. J. Mech. Appl. Math.*, (22):427–438, 1969.

[HS91] M. Hafez and M. Soliman. Numerical solution of the incompressible navier-stokes equations in primitive variables on unstaggered grids. *Proc. AIAA Conf. 91-1561-CP.*, pages 368–379, 1991.

[Lew98] Schrefler B.A. Lewis, R.W. The finite element method in the static and dynamic deformation and consolidation of porous media. *J.Wiley.*, 1998.

[Li90] Zienkiewicz O.C. Xie Y.M. Li, X. A numerical model for immiscible two-phase fluid flow in a porous medium and its time domain solution. *Int. J. Numer. Methods Eng.*, (30):1195–1212, 1990.

[M.K85] K.Ohmiya M.Kawahara. Finite element analysis of density flow using velocity correction method. *Int. J. Num. Meth. Fluids*, (5):981–993, 1985.

[M.M02] M.Pastor M.Mabssout. A taylor–galerkin algorithm for shock wave propagation and strain localization failure of viscoplastic continua. *Comp. Meth. Appl. Mech. Eng.*, (192):955–971, 2002.

[M.M06] M.Pastor M.Mabssout, M.I.Herreros. Wave propagation and localization problems in saturated viscoplastic geomaterials. *International J. for Numerical Methods in Engineering.*, (68):425–447, 2006.

[MO55] M.G.Katona and O.C.Zienkiewicz. A unified set of single-step algorithms, part 3: the beta-m method, a generalisation of the newmark scheme. *Int.J.Num.Meth:eng.*, (21):1345–1359, 1955.

[OM98] R.L.Taylor O.C.Zienkiewicz, J.Rojek and M.Pastor. Triangles and tetrahedra in explicit dynamic codes for solids. *Int.J.Numer.Meth.Eng.*, (43):565–583, 1998.

[OS86] R.L.Taylor O.C.Zienkiewicz, S.Qu and S.Nakazawa. The patch test for mixed formulations. *Int.J.Numer.Meth.Eng.*, (23):1873–1883, 1986.

[OS93] J.Wu O.C.Zienkiewicz, M.Huang and S.Wu. A new algorithm for the coupled soil-pore fluid problem",shock and vibration. (1):3–14, 1993.

[OZ91] R.L. Taylor O.C. Zienkiewicz. *The Finite Element Method, Vol. 2, 4th-ed.* McGraw-Hill, 1991.

[Per86] J. Peraire. *A Finite Element Method for Convection Dominated Flows.* PhD thesis, University of Wales, Swansea, 1986.

[PFM97] Li Tongchun Pastor, M and J.A. Fernández Merodo. Stabilized finite elements for harmonic soil dynamics problems near the undrained-incompressible limit. *Soil Dynamics and Earthquake Engineering*, (16):161–171, 1997.

[PM99] Li T Liu X Huang M. Pastor M, Zienkiewicz OC. Stabilized finite elements with equal order of interpolation for soil dynamics problems. *Archives of Computational Methods in Engineering*, (6):3–33, 1999.

[P.M03] T.Li y X.Liu P.Mira, M.Pastor. A new stabilized enhanced strain element with equal order of interpolation for soil consolidation problems. *Comp.Methods Appl.Mech.Engrg*, (192):4257–4277, 2003.

[QM00] Zienkiewicz OC Quecedo M, Pastor M. Application of a fractional step method to localization problems. computers and structures. *Int.J.Numer.Meth.Eng.*, (74):535–545, 2000.

[Que04] Pastor M. Herreros M.I. Fernández Merodo J.A. Quecedo, M. Numerical modelling of the propagation of fast landslides using the finite element method. *Int. J. Numer. Methods Eng.*, (59):755–794, 2004.

[RLZ84] K. Morgan R.L. Lohner and O. C. Zienkiewicz. The solution of non-linear hyperbolic equation systems by the finite element method. *Int. J. Num. Meth. Fluids.*, (4):1043–1063, 1984.

[RO95] M.Vázquez R.Codina and O.C.Zienkiewicz. *Proc.Int.Conf. on Finite Elements in Fluids-New trends and applications, Venezia, 15-21 Oct*, chapter A fractional step method for compressible flows: boundary conditions and incompressible limit, pages 409–418. M.Morandi Cecchi, K.Morgan, J.Periaux, B.A.Schrefler and O.C.Zienkiewicz (Eds), 1995.

[Sch95] B.A. Schrefler. F.e. in environmental engineering: Coupled thermo-hydro-mechanical processes in porous media including pollutant transport. *Arch. Comput. Methods Eng.*, (2):1–54, 1995.

[SJ90] Rifai M.S Simo J.C. A class of mixed assumed strain methods and the method of incompatible modes. *Int. J. Numer. Methods Eng.*, 6(8):1595–1638, 1990.

[THB86] L.P. Franca T.J.R. Hughes and M. Balestra. A new finite element formulation for fluid dynamics. v. circumventing the babuska-brezzi condition: A stable petrov-galerkin formulation of the stokes problem accommodating equal order interpolation. *Comp. Meth. Appl. Mech. Eng.*, (59):85–99, 1986.

[XL03] Pastor M. Xikui L, Xianhong H. An iterative stabilized fractional step algorithm for finite element analysis in saturated soil dynamics. *Computer Methods in Applied Mechanics and Engineering*, (192):3845–3859, 2003.

[Zie80] Chang C.T. Bettess P. Zienkiewicz, O.C. Drained, undrained, consolidating and dynamic behaviour assumptions in soils. *Géotechnique.*, (30):385–395, 1980.

[Zie84] Shiomi T. Zienkiewicz, O.C. Dynamic behaviour of saturated porous media; the generalized biot formulation and its numerical solution. *Int. J. Numer. Anal. Methods Geomech.*, (8):71–96, 1984.

[Zie90a] Chan A.H.C. Pastor M. Paul D.K. Shiomi T. Zienkiewicz, O.C. Static and dynamic behaviour of soils: A rational approach to quantitative solutions. *Proc. R. Soc. A Math. Phys. Eng. Sci.*, (429):285–309, 1990.

[Zie90b] Xie Y.M. Schrefler B.A. Ledesma A. Bicanic N. Zienkiewicz, O.C. Static and dynamic behaviour of soils: A rational approach to quantitative solutions. ii. semi-saturated problems. *Proc. R. Soc. A Math. Phys. Eng. Sci.*, (429):311–321, 1990.

[ZS99] Chan A.H.C. Pastor M. Schrefler B.A. Zienkiewicz, O.C. and T. Shiomi. Computational geomechanics. *John Wiley & Sons Ltd.*, 1999.

[ZT00] O. C. Zienkiewicz and R. L. Taylor. *The Finite Element Method*. Butterworth-Heinmann, 2000.

[ZW91] O.C. Zienkiewicz and J. Wu. Incompressibility without tears. how to avoid restrictions of mixed formulations. *Int. J. Numer. Meth. Eng.*, (32):1184–1203, 1991.

Hydraulic Fracture

B.A. Schrefler, P. Rizzato, S. Secchi

Department of Civil, Environmental and Architectural Engineering
University of Padova, Italy

Simulation of 2D and 3D hydraulic fracturing in fully saturated porous media is presented. The discrete fractures are driven by the fluid pressure. A cohesive fracture model is adopted. In the 3D case the fracture follows the face of the element around the fracture tip which is closest to the normal direction of the maximum principal stress at the tip, while in the 2D setting the fracture follows directly the direction normal to the maximum principal stress. No predetermined fracture path is needed. This requires continuous updating of the mesh around the crack tip to take into account the evolving geometry. The updating of the mesh is obtained by means of an efficient mesh generator based on Delaunay tessellation. The governing equations are written in the framework of porous media mechanics and are solved numerically in a fully coupled manner. Numerical examples deal with well injection in a geological setting and hydraulic fracture in a concrete dam. Pressure and displacement jumps are evidenced and an explanation is given.

1 Introduction

Fluid-driven fracture propagating in porous media is a common problem in geomechanics. It is used to enhance the recovery of hydrocarbons from underground reservoirs or to make geothermal reservoirs with high temperatures or temperature gradients but low permeability economically exploitable. Another application of importance is related to the overtopping stability analysis of dams.

Contributions to the mathematical modelling of fluid-driven fractures have been made continuously since the sixties, beginning with stationary analytical solutions in the frame of linear fracture mechanics by [Per61], [Ric76], [Cle78], [Hua85a,b] and [Det91]. Numerical models appeared from the nineties on. [Boo90] presented a numerical model in the context of linear fracture mechanics which allows for fluid leakage in the medium surrounding the fracture and assumes a moving crack depending on the applied loads and material properties. [Car00] showed a fully 3D hydraulic fracture model which neglects the fluid continuity equation in the medium surrounding the fracture. [Sch06], [Sec08] and [Sec12] used Standard Galerkin Finite Elements with space and time adaptivity in a 2D and 3D setting taking into account also the flow in the domain. Extended Finite Elements (XFEM) have been applied to hydraulic fracturing by [Rét08], [Moh13a,b], [Mes15]. Partition of unity finite elements are used for 2D mode I crack propagation in saturated ionized porous media by [Kra13] and zero thickness interface elements by [Car12]. [Irz14] used isogeometric elements. Phase field models were applied by [Whe14] and [Mik15]. All the published numerical results, except those of [Sch06], [Sec08] and [Sec12] and [Kra13] are smooth while the physical behavior shows stepwise advancement and pressure drop in case of hydraulic fracturing and pressure rise in case of mechanical loading ([Tzs95], [Piz13], [Sec14] and [Sol14]). The origin of the stepwise advancement observed in [Kra13] is believed to be numerical.

In [Sch06] we have shown for the first time numerically in a 2D setting that in case of hydraulic fracturing the fracture advances stepwise. The same has been reconfirmed for the 3-D case in [Sec12]. The reason for this is that the flow effect due to pumping is transmitted to the solid through the pressure coupling term in the effective stress; the solid is loaded and upon rupture produces an increase of the volumetric strain which in turn produces a drop in pressure. During periods of pressure increase the crack does not advance because the solid is partially unloaded; the crack propagates suddenly when the limit stress in the solid is reached. The stepwise advancement does not appear in other time dependent coupled solutions involving cohesive fracture, as e.g. the thermoelastic one of [Sim03]. It is recalled that in this last case the fracture lips are stress free while in case of hydraulic fracturing they are not stress free because of the fluid pressure. The model used to obtain the physically observed behavior in hydraulic fracturing will now be described in more detail, following [Sch06] and [Sec08].

2 The numerical model

In the framework of discrete crack models, the mechanical behaviour of the solid phase at a distance from the process zone is assumed to obey a Green-elastic or hyperelastic material behaviour [Sch06].

For the fracture itself we use the cohesive fracture model shown in figure 1: between the real fracture apex which appears at macroscopic level and the apex of a fictitious fracture there is the process zone where cohesive forces act. For mode I crack opening, following [Bar59], [Dug60] and [Hil76], the cohesive law with monotonically increasing opening is

$$\sigma = \sigma_0 \left(1 - \frac{\delta_\sigma}{\delta_{\sigma cr}}\right) \tag{1}$$

σ_0 being the maximum cohesive traction (closed crack), δ_σ the current relative displacement normal to the crack, $\delta_{\sigma cr}$ the maximum opening with exchange of cohesive tractions and $G = \sigma_0 \times \delta_{\sigma cr}/2$ the fracture energy. If after some opening $\delta_{\sigma 1} < \delta_{\sigma cr}$

the crack begins to close, tractions obey a linear unloading as

$$\sigma = \sigma_0 \left(1 - \frac{\delta_{\sigma 1}}{\delta_{\sigma cr}}\right) \frac{\delta_\sigma}{\delta_{\sigma 1}} \tag{2}$$

When the crack reopens, equation (2) is reversed until the opening $\delta_{\sigma 1}$ is recovered, then tractions obey again equation (1).

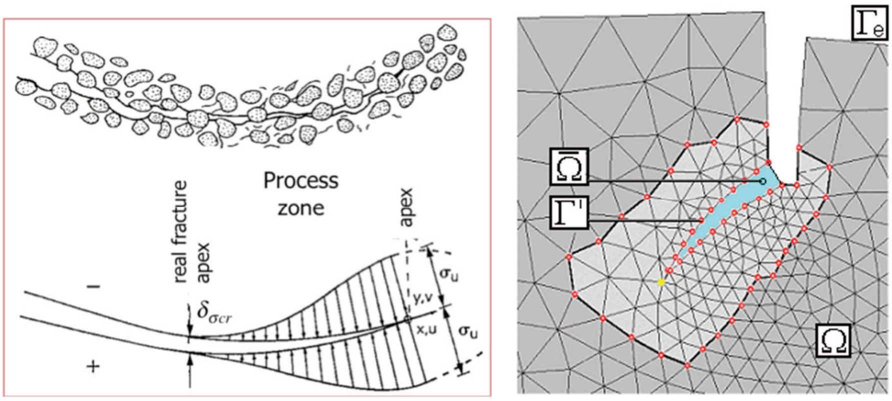

Figure 1: Definition of cohesive crack geometry, reprinted from [Sec12], Copyright (2012), with permission from Springer; and hydraulic fracture domain, reprinted from [Sch06], Copyright (2006), with permission from Elsevier.

When tangential relative displacements of the sides of a fracture in the process zone cannot be disregarded, mixed mode crack opening takes place. This is usually the case of a crack moving along an interface separating two solid components. In fact, whereas the crack path in a homogeneous medium is governed by the principal stress direction, the interface has an orientation that is usually different from the principal stress direction. The mixed cohesive mechanical model involves the simultaneous activation of normal and tangential displacement discontinuity and corresponding tractions. For the pure mode II, the relationship between tangential tractions and displacements is

$$\tau = \tau_0 \frac{\delta_\sigma}{\delta_{\sigma cr}} \frac{\delta_\tau}{|\delta_\tau|} \tag{3}$$

τ_0 being the maximum tangential stress (closed crack), δ_τ the relative displacement parallel to the crack and $\delta_{\sigma cr}$ the limiting value opening for stress transmission. The unloading/loading from/to some opening $\delta_{\sigma 1} < \delta_{\sigma cr}$ follows the same behavior as for mode I.

For the mixed mode crack propagation, the interaction between the two cohesive mechanisms is treated as in [Cam96]. By defining an equivalent or effective opening displacement δ and the scalar effective traction t as

$$\delta = \sqrt{\beta^2 \delta_\tau^2 + \delta_\sigma^2} \qquad t = \sqrt{\beta^{-2} \tau^2 + \sigma^2} \tag{4}$$

the resulting cohesive law is

$$\mathbf{t} = \frac{t}{\delta}\left(\beta^2 \delta_\tau + \delta_\sigma\right) \tag{5}$$

β being a suitable material parameter that defines the ratio between the shear and the normal critical components. For more details see [Sch06].

2.1 The governing equations

Taking into account the cohesive forces and the symbols of figure 1, the linear momentum balance of the mixture, discretized in space, is written as

$$\mathbf{M}\,\mathbf{v} + \int_\Omega \mathbf{B}^\mathbf{T} \boldsymbol{\sigma}'' d\Omega - \mathbf{Qp} \; - \mathbf{f}^{(1)} - \int_{\Gamma'} (\mathbf{N}^u)^\mathbf{T} \mathbf{c} \, d\Gamma' = \mathbf{0} \tag{6}$$

where Γ' is the boundary of the fracture and process zone and **c** the cohesive traction acting in the process zone as defined above.

The fully saturated medium surrounding the fracture has constant absolute permeability while for the permeability within the crack the Poiseuille or cubic law is assumed. This permeability is not dependent on the rock type or stress history, but is defined by crack aperture only. Deviation from the ideal parallel surfaces conditions causes only an apparent reduction in flow and can be incorporated into the cubic law, which reads as [Wit80]

$$k_{ij} = \frac{1}{f}\frac{w^3}{12} \tag{7}$$

w being the fracture aperture and f a coefficient in the range 1.04-1.65 depending on the solid material. In the following, this parameter will be assumed as constant and equal to 1.0. Incorporating the Poiseuille law into the weak form of the water mass balance equation within the crack and discretizing in space by means of the finite element method results in

$$\mathbf{H}\,\mathbf{p} \; + \mathbf{S}\,\mathbf{p} \; + \int_{\Gamma'} (\mathbf{N}^p)^\mathbf{T} \overline{\mathbf{q}}^w d\Gamma' = \mathbf{0} \tag{7a}$$

with

$$\mathbf{H} = \int_{\overline{\Omega}} \left(\nabla \mathbf{N}^{p}\right)^{\mathbf{T}} \frac{w^{2}}{12\mu_{w}} \nabla \mathbf{N}^{p} d\overline{\Omega} \tag{7b}$$

$$\mathbf{S} = \int_{\overline{\Omega}} \left(\mathbf{N}^{p}\right)^{\mathbf{T}} \frac{1}{Q^{*}} \mathbf{N}^{p} d\overline{\Omega} \tag{7c}$$

The last term of equation (7a) represents the leakage flux into the surrounding porous medium across the fracture borders and is of paramount importance in hydraulic fracturing techniques. This term can be represented by means of Darcy's law using the medium permeability and pressure gradient generated by the application of water pressure on the fracture lips. No particular simplifying hypotheses are hence necessary for this term. This equation can be directly assembled at the same stage as the following equation (8), because both have the same structure: only the parameters have to be changed in the appropriate elements depending whether they belong to the fracture or to the surrounding medium.
The discretized mass balance equation for the porous medium surrounding the fracture is

$$\mathbf{Q}\mathbf{u} + \mathbf{H}\mathbf{p} + \mathbf{S}\mathbf{p} - \mathbf{f}^{(2)} - \int_{\Gamma'} (\mathbf{N}^{p})^{\mathbf{T}} \overline{\mathbf{q}}^{w} d\Gamma' = \mathbf{0} \tag{8}$$

where $\overline{q}_{w}$ represents the water leakage flux along the fracture toward the surrounding medium of equation (7). This term is defined along the entire fracture, i.e. the open part and the process zone. It is worth mentioning that the topology of the domain Ω changes with the evolution of the fracture. In particular, the fracture path, the position of the process zone and the cohesive forces are unknown and must be regarded as products of the mechanical analysis.

Discretization in time is then performed with time Discontinuous Galerkin approximation following [LiW96] and [Sec08]. Denoting with $I_n = (t_n^-, t_{n+1}^+)$ a typical incremental time step of size $\Delta t = t_{n+1} - t_n$, the weighted residual forms are

$$\begin{aligned} &\int_{In} \delta\mathbf{v}^{\mathbf{T}} (\mathbf{M}\,\mathbf{v} + \mathbf{K}\mathbf{u} - \mathbf{Q}\mathbf{p} - \mathbf{f}^{(1)}) dt + \int_{In} \delta\mathbf{u}^{\mathbf{T}} \mathbf{K}(\dot{\mathbf{u}} - \mathbf{v}) dt + \\ &+ \delta\mathbf{u}^{\mathbf{T}}\Big|_{t_n} \mathbf{K}(\mathbf{u}_n^{+} - \mathbf{u}_n^{-}) dt + \delta\mathbf{v}^{\mathbf{T}}\Big|_{t_n} \mathbf{M}(\mathbf{v}_n^{+} - \mathbf{v}_n^{-}) = \mathbf{0} \end{aligned} \tag{9}$$

$$\begin{aligned} &\int_{In} \delta\mathbf{p}^{\mathbf{T}} (\mathbf{Q}^{\mathbf{T}}\mathbf{v} + \mathbf{S}\mathbf{s} + \mathbf{H}\mathbf{p} - \mathbf{f}^{(2)}) dt + \int_{In} \delta\mathbf{p}^{\mathbf{T}} \mathbf{S}(\dot{\mathbf{p}} - \mathbf{s}) dt + \\ &+ \delta\mathbf{p}^{\mathbf{T}}\Big|_{t_n} \mathbf{S}(\mathbf{p}_n^{+} - \mathbf{p}_n^{+}) dt = \mathbf{0} \end{aligned} \tag{10}$$

with the constraint conditions

$$\begin{aligned}\dot{\mathbf{u}} - \mathbf{v} &= \mathbf{0}\\ \dot{\mathbf{p}} - \mathbf{s} &= \mathbf{0}\end{aligned} \tag{11}$$

Subscripts -/+ indicate quantities immediately before and after the generic time station. Field variables and their first time derivatives at time $t \in [t_n, t_{n+1}]$ are interpolated by linear time shape functions and the following discretized equations are obtained

$$\begin{aligned}\mathbf{u}_n &= \mathbf{u}_n^- + \frac{\Delta t}{2}(\mathbf{v}_n - \mathbf{v}_{n+1})\\ \mathbf{u}_{n+1} &= \mathbf{u}_n^- + \frac{\Delta t}{2}(\mathbf{v}_n + \mathbf{v}_{n+1})\\ \mathbf{s}_n &= \frac{1}{\Delta t}(\mathbf{p}_{n+1} + 3\mathbf{p}_n - 4\mathbf{p}_n^-)\\ \mathbf{s}_{n+1} &= \frac{1}{\Delta t}(\mathbf{p}_{n+1} + 3\mathbf{p}_n + 2\mathbf{p}_n^-)\end{aligned} \tag{12}$$

$$\begin{aligned}&\left(\frac{1}{2}\mathbf{M} - \frac{5}{36}\Delta t^2\mathbf{K}\right)\mathbf{v}_n + \left(\frac{1}{2}\mathbf{M} + \frac{1}{36}\Delta t^2\mathbf{K}\right)\mathbf{v}_{n+1} + \frac{\Delta t}{3}\mathbf{Q}\mathbf{p}_n +\\ &+ \frac{\Delta t}{6}\mathbf{Q}\mathbf{p}_{n+1} = -\frac{\Delta t}{2}\mathbf{K}\mathbf{u}_n^- + \mathbf{M}\mathbf{v}_n^- + \int_{I_n} N_1(t)\mathbf{f}_n^{(1)}\,dt\\ &\left(-\frac{1}{2}\mathbf{M} - \frac{7}{36}\Delta t^2\mathbf{K}\right)\mathbf{v}_n + \left(\frac{1}{2}\mathbf{M} + \frac{5}{36}\Delta t^2\mathbf{K}\right)\mathbf{v}_{n+1} + \frac{\Delta t}{6}\mathbf{Q}\mathbf{p}_n +\\ &+ \frac{\Delta t}{3}\mathbf{Q}\mathbf{p}_{n+1} = -\frac{\Delta t}{2}\mathbf{K}\mathbf{u}_n^- + \int_{I_n} N_2(t)\mathbf{f}^{(1)}\,dt\\ &\frac{\Delta t}{3}\mathbf{Q}^{\mathrm{T}}\mathbf{v}_n + \frac{\Delta t}{6}\mathbf{Q}^{\mathrm{T}}\mathbf{v}_{n+1} + \left(\frac{1}{2}\mathbf{S} + \frac{\Delta t}{3}\mathbf{H}\right)\mathbf{p}_n + \left(\frac{1}{2}\mathbf{S} + \frac{\Delta t}{6}\mathbf{H}\right)\mathbf{p}_{n+1} =\\ &= \mathbf{S}\mathbf{p}_n^- + \int_{I_n} N_1(t)\mathbf{f}^{(2)}\,dt\end{aligned} \tag{13}$$

$$\begin{aligned}&\frac{\Delta t}{6}\mathbf{Q}^{\mathrm{T}}\mathbf{v}_n + \frac{\Delta t}{3}\mathbf{Q}^{\mathrm{T}}\mathbf{v}_{n+1} + \left(-\frac{1}{2}\mathbf{S} + \Delta t\mathbf{H}\right)\mathbf{p}_n + \left(\frac{1}{2}\mathbf{S} + \frac{\Delta t}{3}\mathbf{H}\right)\mathbf{p}_{n+1} =\\ &= \int_{I_n} N_2(t)\mathbf{f}^{(2)}\,dt\end{aligned}$$

The nodal displacement, velocity, and pressure, $\mathbf{u}_n^-, \mathbf{v}_n^-, \mathbf{p}_n^-$ for the current step coincide with the unknowns at the end of the previous one, hence are known in the time marching scheme and coincide with the initial condition for the first time step. The system of algebraic equations is solved with a monolithic approach using an optimized non- symmetric-sparse-matrix algorithm. The number of unknowns is doubled with respect to the traditional trapezoidal method.

The submatrices of the above equations are the usual ones of soil consolidation [Lew98], except for

$$\mathbf{f}^{(1)} = \int_{\Omega} \left(\mathbf{N}^u\right)^{\mathbf{T}} \rho \mathbf{b} d\Omega + \int_{\Gamma_t} \left(\mathbf{N}^u\right)^{\mathbf{T}} \overset{\underline{\mathbf{g}}}{\mathbf{t}} d\Gamma + \int_{crack} \left(\mathbf{N}^u\right)^{\mathbf{T}} \mathbf{c} d\Gamma \qquad (14)$$

where **c** is the cohesive traction and is different from zero only if the element has a side on the lips of the fracture Γ'within the process zone. Given that the liquid phase is continuous over the whole domain, leakage flux along the opened fracture lips is accounted for through the **H** matrix together with the flux along the crack. Finite elements are in fact present along the crack, as shown in figure 1, which account only for the pressure field and have no mechanical stiffness. In the present formulation, non-linear terms arise through cohesive forces in the process zone and permeability along the fracture.

Because of the continuous variation of the domain as a consequence of the propagation of the cracks, see below, also the boundary Γ' and the related mechanical conditions change. Along the formed crack edges and in the process zone, boundary conditions are the direct result of the field equations while the mechanical parameters have to be updated. The adopted remeshing technique accounts for all these changes [Sec03].

2.2 Fracture nucleation and advancement algorithm

A fracture arises when the Rankine criterion is not satisfied at a point. At the interior this point is substituted by four points, two in the direction of the normal to the maximum principal stress at a spacing of the fracture tip advancement Δs and two normal to this direction at a much smaller spacing. Along a boundary or in case of branching the points reduce to three.

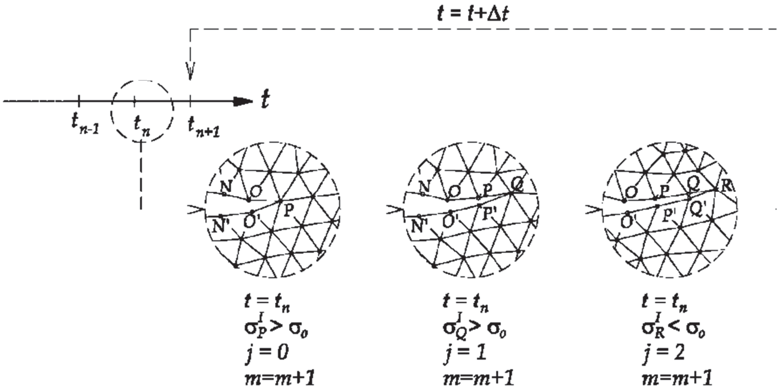

Figure 2: Multiple advancing fracture step at the same time station. Reprinted from [Sec12], Copyright (2012), with permission from Springer.

As far as the fracture advancement is concerned the procedure for 2D and 3D situations differs: in 2D the fracture follows directly the direction normal to the maximum principal stress while in 3D the fracture follows the face of the element around the fracture tip which is closest to the normal direction of the maximum principal stress; the fracture tip becomes a curve in space (front). If during the advancement a new node is created at the front the resulting elements for the filler are tetrahedral. If an internal node along the process zone advances, a new wedge element results in the filler [Sec12].

At each time station t_n, all the necessary spatial refinements are made, i.e. j successive tip (front) advancements are possible within the same time step (figure 2). Their number in general depends on the chosen time step increment Δt, the adopted crack length increment Δs, and the variation of the applied loads. From numerical experiments it appears however that j is rather limited. The advancement algorithm requires continuous remeshing with a consequent transfer of nodal vectors from the old to the continuously updated mesh by a suitable operator $\mathbf{V}_m(\Omega_{m+1}) = \aleph\left(\mathbf{V}_m(\Omega_m)\right)$ [Sec07]. The solution is then repeated with the quantities of mesh m but re-calculated on the new mesh $m+1$ before advancing the crack tip to preserve as far as possible energy and momentum. Note that the advancement algorithm allows for displacement jumps within a time step, i.e. the advancement algorithm is decoupled from the time stepping algorithm. This is of paramount importance as shown below.

2.3 Refinement

Three types of refinement are needed to obtain satisfactory results: the refinement in space in general, the satisfaction of an element threshold number over the process zone and a refinement in time. For refinement and de-refinement in space the Zienkiewicz-Zhu error estimator is used [Zhu88]. Fluid lag, i.e. negative fluid pressures at the crack tip may arise if the speed at which the crack tip advances is sufficiently high so that for a given permeability water cannot flow in fast enough to fill the created space. It can be obtained numerically only if an element threshold number is satisfied over the process zone. It is given by the number of elements over process zone and can be estimated in advance from the problem at hand and the expected process zone length. Hence a sort of object oriented refinement is needed locally which is extensively dealt with in [Sch06]. Adaptivity in time can be obtained by means of the adopted Discontinous Galerkin Method in the time domain (DGT). The error of the time-integration procedure can be defined through the jump of the solution

$$\begin{aligned} \llbracket \mathbf{u}_n \rrbracket &= \mathbf{u}_n - \mathbf{u}_n^- \\ \llbracket \mathbf{v}_n \rrbracket &= \mathbf{v}_n - \mathbf{v}_n^- \\ \llbracket \mathbf{p}_n \rrbracket &= \mathbf{p}_n - \mathbf{p}_n^- \end{aligned} \tag{15}$$

at each time station, i.e. the difference between the final point of time step *n-1* and the first point of time step *n.* By adopting the total energy norms as error measure, we define the following terms

$$\begin{gathered} \|\mathbf{e}_\mathrm{u}\|_\mathrm{n} = \left(\llbracket \mathbf{v}_\mathrm{n} \rrbracket^\mathrm{T} \mathbf{M} \llbracket \mathbf{v}_\mathrm{n} \rrbracket + \llbracket \mathbf{u}_\mathrm{n} \rrbracket^\mathrm{T} \mathbf{K} \llbracket \mathbf{u}_\mathrm{n} \rrbracket \right)^{1/2} \\ \|\mathbf{e}_\mathrm{u,p}\|_\mathrm{n} = \left(\llbracket \mathbf{u}_\mathrm{n} \rrbracket^\mathrm{T} \mathbf{Q} \llbracket \mathbf{p}_\mathrm{n} \rrbracket \right)^{1/2} \\ \|\mathbf{e}_\mathrm{p}\|_\mathrm{n} = \left(\llbracket \mathbf{p}_\mathrm{n} \rrbracket^\mathrm{T} \mathbf{Q}^\mathrm{T} \llbracket \mathbf{u}_\mathrm{n} \rrbracket + \llbracket \mathbf{p}_\mathrm{n} \rrbracket^\mathrm{T} \mathbf{H} \llbracket \mathbf{p}_\mathrm{n} \rrbracket \, \Delta\mathrm{t} + \llbracket \mathbf{p}_\mathrm{n} \rrbracket^\mathrm{T} \mathbf{P} \llbracket \mathbf{p}_\mathrm{n} \rrbracket \right)^{1/2} \end{gathered} \tag{16}$$

$$\|\mathbf{e}\|_n = max\left\{ \|\mathbf{e}_u\|_n , \|\mathbf{e}_{u,p}\|_n , \|\mathbf{e}_p\|_n \right\}$$

Error measures defined in equation (16) account at the same time for the cross effects among the different fields and the ones between space and time discretizations. The relative error is defined as in [LiW96]

$$\eta_n = \frac{\|\mathbf{e}\|_n}{\|\mathbf{e}\|_{\max}} \tag{17}$$

where $\|\mathbf{e}\|_{\max}$ is the maximum total energy norm

$$\|\mathbf{e}\|_{\max} = max(\|\mathbf{e}\|_i), \qquad 0 < i < n$$

When $\eta > \eta_{toll}$ the time step Δt_n is modified and a new $\Delta t_n^{'} < \Delta t_n$ is obtained according to

$$\Delta t_n^{'} = \left(\frac{\theta \, \eta_{tol}}{\eta} \right)^{1/3} \Delta t_n \tag{18}$$

where $\theta < 1.0$ is a safety factor. If the error is smaller than a defined value $\eta_{toll,min}$ the step is increased using a rule similar to equation (18).

As it stands, the refinements in space and time are carried out sequentially, starting with the space refinement, followed by the element threshold number and then the refinement in time. An eye is kept on the satisfaction of the discrete maximum principle of [Ran83] which states that it is not possible to refine in time below a certain limit depending on the material properties without also refining in space. A proper functional would be needed to link all the three refinements necessary.

3 Examples

The first application deals with a hydraulically driven fracture due to a fluid pumped at constant flow rate in 2D conditions (plane strain). Figure 3 shows the geometry of the problem together with the finite element discretization. A notch with a sharp tip is present along the symmetry axis of the analyzed area.

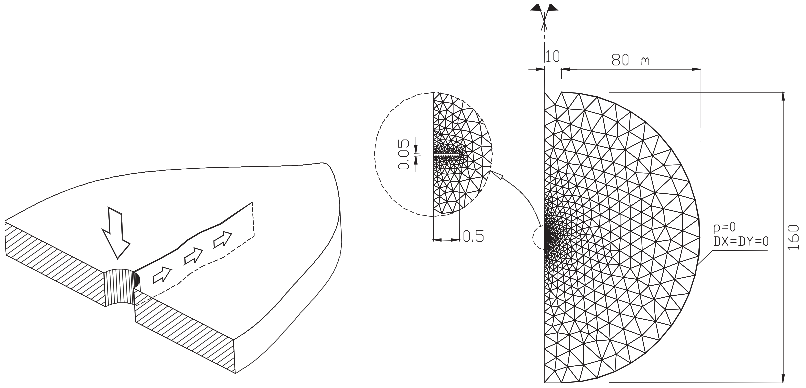

Figure 3: Problem geometry for water injection benchmark and overall discretization. Reprinted from [Sec07], by permission of John Wiley & Sons Limited.

The mouth pressure evolution in time is shown in figure 4 for the case of permeable and impermeable domain surrounding the fracture. Oscillations can clearly be seen as well as pressure jumps. The pressure jumps correspond to the mechanism outlined in the introduction while the oscillations in between the jumps are of numerical origin and would require a smaller time step (now 0.02 sec).

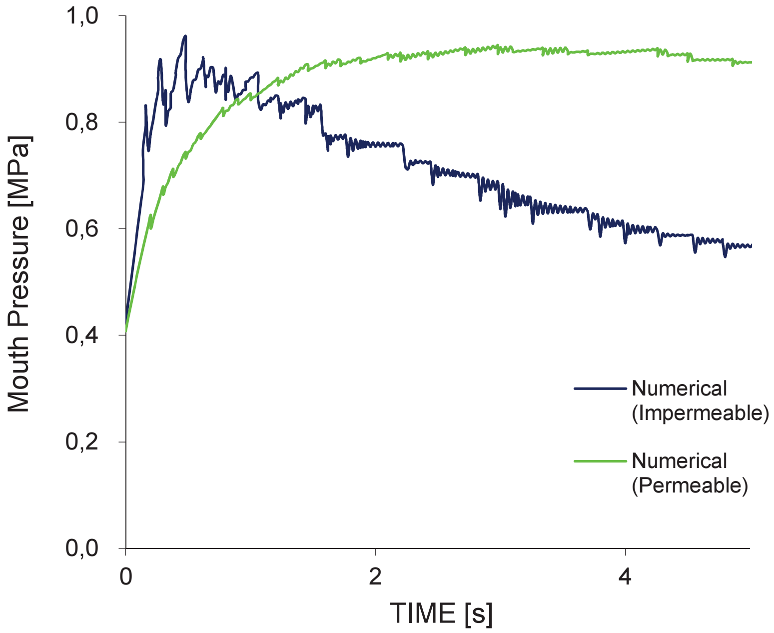

Figure 4: Mouth pressure versus time.

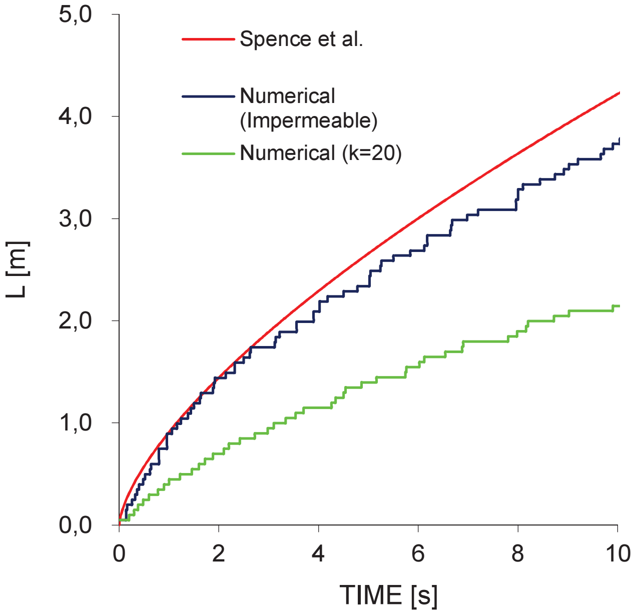

Figure 5: Crack length versus time.

The crack length versus time is shown in figure 5. Clearly a stepwise advancement can be observed for both numerical solution while the asymptotic one of [Spe85] under the hypothesis of incompressible fluid, impermeable fracture and adoption of LEFM is smooth.

By superimposing the solutions for the evolution of pressure and crack length the mechanism outlined in the introduction becomes clear: the pressure jumps correspond to the crack jumps. Between two pressure jumps the pressure builds slowly up due to pumping until the strength threshold is reached and the crack advances with a jump followed by a quiescent period for the crack.

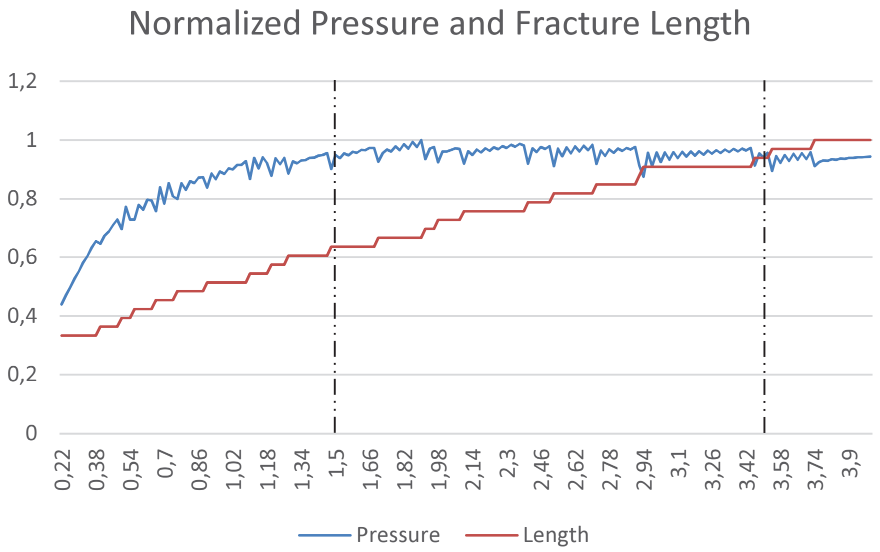

Figure 6: Comparison between normalized pressure evolution and fracture length.

The second case deals with the benchmark exercise A2 proposed by [ICO99]. The benchmark consists in the evaluation of failure conditions as a consequence of overtopping wave acting on a concrete gravity dam of figure 7. We show in figure 8 the 2D solution when the water height is 78 m and the fracture has reached a length of 3.5 m. In the right insert in figure 7 it can be seen that two different values of dynamic viscosity of the fluid result in different fracture paths.

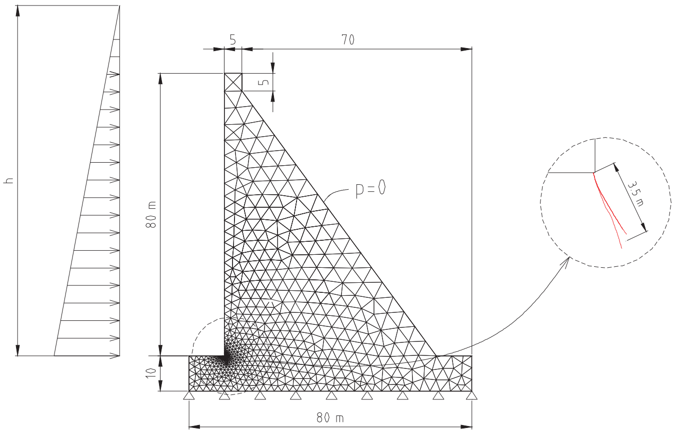

Figure 7: Problem geometry for ICOLD benchmark and calculated crack positions. Reprinted from [Sch06], Copyright (2006), with permission from Elsevier.

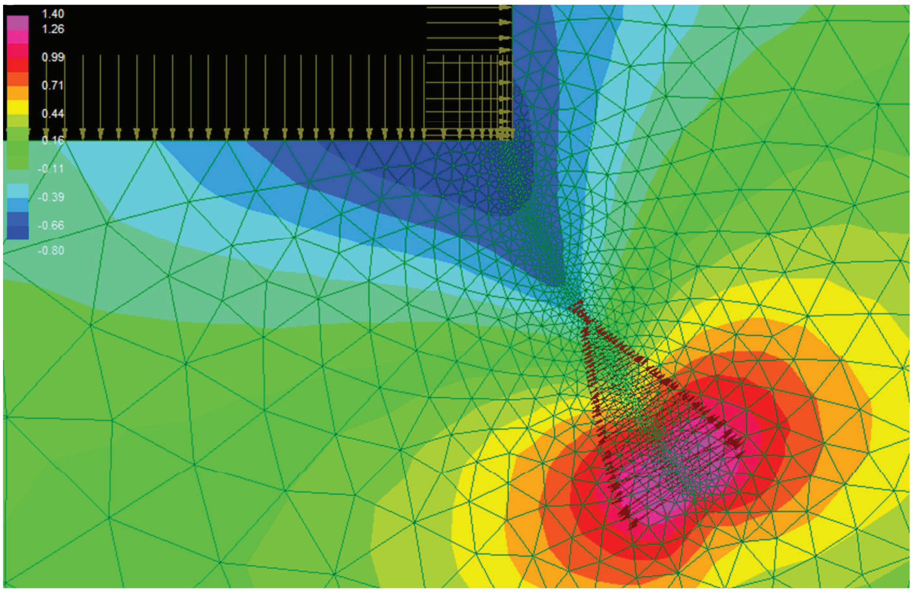

Figure 8: Fracture position with cohesive forces for a water height of 78 m. Reprinted from [Sch06], Copyright (2006), with permission from Elsevier.

Figure 9: Pressure distribution within the crack at water height of 78 m. Fluid lag at the crack tip can be noticed. Reprinted from [Sch06], Copyright (2006), with permission from Elsevier.

The pressure distribution in the crack is shown in figure 9 for a water height behind the dam of 78 m. Negative water pressure (fluid lag) can be noticed at the crack tip. Without a sufficient number of elements over the process zone, the fluid lag is missed. Finally, the steps of the crack mouth opening displacement are shown in figure 10.

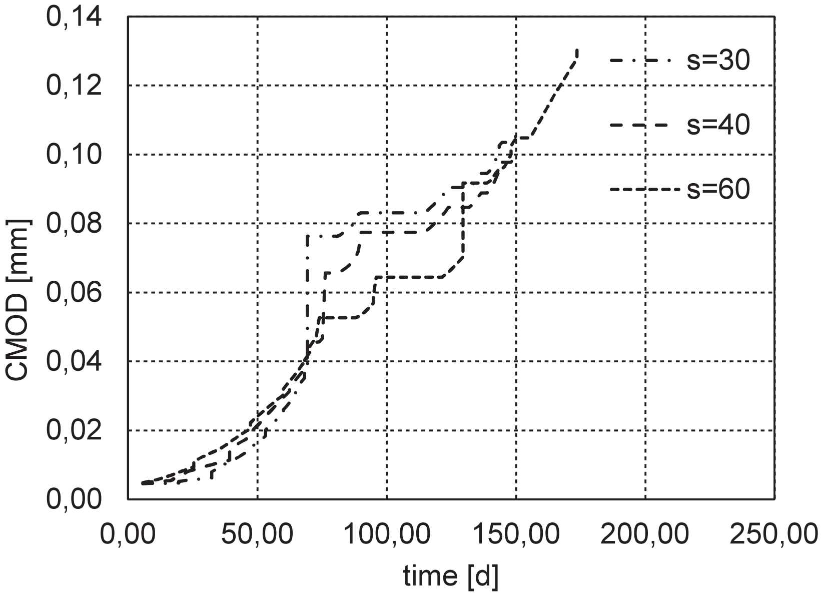

Figure 10: Crack mouth opening displacement versus time for different crack tip advancements Δs in mm. Reprinted from [Sch14], Copyright (2014).

4 Conclusions

Fracture propagation in fluid saturated porous media requires particular attention because of the interaction of three velocities (and their respective length scales): the crack tip advancement velocity and the velocities of the fluid in the crack itself and the seepage velocity around the crack tip. This interaction produces a peculiar behavior resulting in stepwise advancement and pressure jumps. The mechanism in case of hydraulically driven fracture has been evidenced here and produces pressure drop when the fracture advances. In case of mechanical loading, not shown here, the mechanism is different, i.e. there is pressure rise instead of pressure drop: the fluid being incompressible or nearly incompressible takes first all the perturbation (load step or fracture advancement) and discharges the solid. The pressure then dissipates in time and reloads the solid which breaks once the fracture toughness is reached again. This is an interpretation of what appears in the experiment of [Piz13]. An algorithm capable of simulating the pressure jumps must allow for displacement jumps and must avoid interference between crack tip advancement scheme and time discretization. Beyond our own the only other procedure known up to now adapted to simulate the observed jumps, is an XFEM procedure with such small elements that the enrichment part is substantially downplayed with respect to the standard FE part, [Riz14]. Both procedures have in common that the crack can propagate over more elements within one time step, i.e. that jumps are possible and the above mentioned interference between the velocities is avoided. Other published algorithms show more time steps elapsed before an element is crossed by the crack and the observed phenomena have been missed. A review of these algorithms can be found in [Sim14].

References

[Bar59] G.I. Barenblatt. The formation of equilibrium cracks during brittle fracture: General ideas and hypotheses. Axially-symmetric cracks. *J. Appl. Math. Mechanics,* 23:622-636, 1959.

[Boo90] T.J. Boone and A.R. Ingraffea. A numerical procedure for simulation of hydraulically driven fracture propagation in poroelastic media. *Int. J. Num. Anal. Methods in Geomechanic*s, 14:27-47, 1990.

[Cle78] M.P. Cleary. Moving singularities in elasto-diffusive solids with applications to fracture propagation. *Int. J. Solids and Structures,* 14:81-97, 1978.

[Cam96] G.T. Camacho and M. Ortiz. Computational modelling of impact damage in brittle materials. *Int. J. of Solids and Structures,* 33:2899-2938, 1996.

[Car00] B.J. Carter, J. Desroches, A.R. Ingraffea and P.A. Wawrzynek. *Simulating fully 3-D hydraulic fracturing*. In Modeling in Geomechanics, Zaman, Booker and Gioda (eds.), 525-567. Wiley, Chichester, 2000.

[Det91] E. Detournay and A.H. Cheng. Plane strain analysis of a stationary hydraulic fracture in a poroelastic medium. *Int. J. Solids and Structures,* 27:1645-1662, 1991.

[Dug60] D.S. Dugdale. Yielding of steel sheets containing slits. *J. Mech. Phys. Solids,* 8:100-104, 1960.

[Hil76] A. Hilleborg, M. Modeer and P.E. Petersson. Analysis of crack formation and crack growth in concrete by means of fracture mechanics and finite elements. *Cement and Concrete Research,* 6:773-782, 1976.

[Hua85a] N.C. Huang and S.G. Russel. Hydraulic fracturing of a saturated porous medium – I: General theory. *Theoretical and Applied Fracture Mechanics,* 4:201-213, 1985.

[Hua85b] N.C. Huang and S.G. Russel. Hydraulic fracturing of a saturated porous medium – II: Special cases. *Theoretical and Applied Fracture Mechanics,* 4:215-222, 1985.

[ICO99] ICOLD Fifth International Benchmark Workshop on Numerical Analysis of dams: Theme A2, Denver, Colorado, 1999.

[Irz14] F. Irzal, J.J.C. Remmers, C.V. Verhoosel and R. de Borst. An isogeometric analysis Bézier interface element for mechanical and poromechanical fracture problems. *Int. J. Num. Methods in Engineering,* 97:608-628, 2014.

[Kra09] F. Kraaijeveld: *Propagating discontinuities in ionized porous media*. Ph.D. Thesis, Eindhoven University of Technology, October 6, 2009.

[Kra13] F. Kraaijeveld, J.M.R.J. Huyghe, J.J.C. Remmers and R. de Borst: 2-D mode one crack propagation in saturated ionized porous media using partition of unity finite elements. Olivier Coussy Memorial issue, *J. Applied Mech. Trans. ASME,* 80(2):020907, 2013.

[Lew98] R.W. Lewis and B.A. Schrefler. *The Finite Element Method in the Static and Dynamic Deformation and Consolidation of Porous Media*, Wiley, Chichester 1998.

[LiW98] X.D. Li and N.E. Wiberg. Implementation and adaptivity of a space-time finite element method for structural dynamics. *Comp. Methods Appl. Mech. Engrg,* 156:211-229, 1998.

[Mes15] G. Meschke and D. Leonhart. A Generalized Finite Element Method for hydro-mechanically coupled analysis of hydraulic fracturing problems using space-time variant enrichment functions, *Comput. Methods Appl. Mech. Engrg.,* 290:438-465, 2015.

[Mik15] A. Mikelic, M. F. Wheeler and T. Wick. A phase-field method for propagating fluid- filled fractures coupled to a surrounding porous medium, *SIAM Multiscale Modeling and Simulation,* 13(1):367–398, 2015.

[Moh13a] T. Mohammadnejad and A.R. Khoei. Hydromechanical modelling of cohesive crack propagation in multiphase porous media using extended finite element method. *Int. J. Num. Anal. Methods in Geomechanics*, 37:1247–1279, 2013.

[Moh13b] T. Mohammadnejad and A.R. Khoei. An extended finite element method for hydraulic fracture propagation in deformable porous media with the cohesive crack model. *Finite Elements in Analysis and Design,* 73:77–95, 2013.

[Per61] T.K. Perkins and L.R. Kern. Widths of hydraulic fractures. *SPE Journal*, 222:937-949, 1961.

[Piz13] F. Pizzocolo, J.M.R.J. Huyghe and K. Ito. Mode I crack propagation in hydrogels is stepwise. *Engineering Fracture Mechanics,* 97:72-79, 2013.

[Ran83] E. Rank, C. Katz and H. Werner. On the importance of the discrete maximum principle in transient analysis using finite element methods. *Int. J. Num. Methods in Engineering,* 19:1771-1782, 1983.

[Rét08] J. Réthoré, R. de Borst and M.A. Abellan. A two-scale model for fluid flow in an unsaturated porous medium with cohesive cracks. *Computational Mechanics,* 42:227-238, 2008.

[Ric76] J.R. Rice and M.P. Cleary. Some basic stress diffusion solutions for fluid saturated elastic porous media with compressible constituents. *Rev. Geophs. Space physics,* 14:227-241, 1976.

[Riz14] P. Rizzato. *Mesh independence study of X-FEM simulations on fracture propagation in porous media*. Master Thesis, Department of Civil Environmental and Architectural Engineering. Padua, Italy: University of Padua, 2014.

[Sec03] S. Secchi and L. Simoni. An improved procedure for 2-D unstructured Delaunay mesh generation. *Advances in Engineering Software,* 34:217-234, 2003.

[Sch06] B.A. Schrefler, S. Secchi and L. Simoni. On adaptive refinement techniques in multifield problems including cohesive fracture. *Comp. Methods Appl. Mech. Engrg*., 195:444-461, 2006.

[Sec14] S. Secchi and B.A. Schrefler. Hydraulic fracturing and its peculiarities, *Asia Pacific J. on Comput. Engineering,* 1:8 doi:10.1186/2196-1166-1-8, 2014.

[Sec07] S. Secchi, L. Simoni and B.A. Schrefler. Numerical procedure for discrete fracture propagation in porous materials. *Int. J. Num. Anal. Methods in Geomechanics,* 31:331-345, 2007.

[Sec08] S. Secchi, L. Simoni and B.A. Schrefler. Numerical difficulties and computational procedures for thermo-hydro-mechanical coupled problems of saturated porous media. *Computational Mechanics,* 43:179-189, 2008.

[Sec12] S. Secchi and B.A. Schrefler. A method for 3-D hydraulic fracturing simulation. *Int. J. Fracture,* 178:245-258, 2012.

[Sim14] L. Simoni and B.A. Schrefler. Multi Field Simulation of Fracture. In Stéphane P.A. Bordas, editor: *Advances in Applied Mechanics*, Vol. 47, AAMS, UK: Academic Press, pages 367-519, 2014.

[Sim03] L. Simoni and S. Secchi. Cohesive fracture mechanics for a multi-phase porous medium. *Engrg. Comput.*, 20:675-698, 2003.

[Sol15] M.Y. Soliman, M. Wigwe, A. Alzahabi, E. Pirayesh and N. Stegent. Analysis of Fracturing Pressure Data in Heterogeneous Shale Formations. *Hydraulic Fracturing Journal*, 1(2):8-12, 2014.

[Spe85] D.A. Spence and P. Sharp. Self-similar solutions for elastohydrodynamic cavity flow*, Proc. R. Soc. London,* 400:289–313, 1985.

[Tzs95] F. Tzschichholz and H.J. Herrmann. Simulations of pressure fluctuations and acoustic emission in hydraulic fracturing. *Physical Review E,* 5:1961-1970, 1995.

[Wit80] P.A. Witherspoon, J.S.Y. Wang, K. Iwai and J.E. Gale. Validity of cubic law for fluid flow in a deformable rock fracture. *Water Resources Research*, 16:1016-1024, 1980.

[Whe14] M.F. Wheeler, T. Wick and W. Wollner. An augmented-Lagrangian method for the phase-field approach for pressurized fractures. *Comp. Methods Appl. Mech. Engrg*., 271:69–85, 2014.

[Zhu88] J.Z. Zhu and O.C. Zienkiewicz. Adaptive techniques in the finite element method. *Comm. Appl. Num. Methods*, 4:197-204, 1988.

Finite element analysis of non-isothermal multiphase porous media in dynamics

L. Sanavia[1], **T. D. Cao**[1,2]

[1]*Department of Civil, Environmental and Architectural Engineering, University of Padova, Italy*

[1,2]*Department of Mechanical Engineering, Technische Universität Darmstadt, Germany*

This work presents a mathematical and a numerical model for the analysis of the thermo-hydro-mechanical (THM) behavior of multiphase deformable porous materials in dynamics. The fully coupled governing equations are developed within the Hybrid Mixture Theory. To analyze the THM behavior of soil structures in the low frequency domain, e.g. under earthquake excitation, the u-p-T formulation is advocated by neglecting the relative acceleration of the fluids and their convective terms. The standard Bubnov-Galerkin method is applied to the governing equations for the spatial discretization, whereas the generalized Newmark scheme is used for the time discretization. The final non-linear and coupled system of algebraic equations is solved by the Newton method within the monolithic approach. The formulation and the implemented solution procedure are validated through the comparison with other finite element solutions or analytical solutions.

1 Introduction

The analysis of the dynamic response of multiphase porous media has many applications in civil engineering. Onset of landslides due to earthquakes or rainfall and the seismic behavior of dams are examples where inertial forces cannot be neglected. Moreover, there are situations where it is important to consider also the effect of temperature variation. It is the case of catastrophic landslides, where the mechanical energy dissipated in heat inside the slip zone may lead to vaporization of the pore water creating a cushion of zero friction, which may accelerate the movement of the landslides [Var02]. Another interesting case is the seismic analysis of deep nuclear waste disposal.

Many authors have developed models for the analysis of the dynamic behavior of multiphase porous media in isothermal conditions. A state of art can be found in Zienkiewicz et al. [Zie99] and Schanz [Sch09]. Recently, Nenning and Schanz [Nen10] presented an infinite element for wave propagation problems; Heider et al. [Hei11] analyzed a numerical solution of dynamic wave propagation problems in infinite half spaces with incompressible constituents and Albers [Alb10] analyzed wave propagation problems in saturated and partially saturated porous media.

This work presents a formulation of a fully coupled model for deformable multiphase geomaterials in dynamics including thermal effects.
The model is derived introducing the u-p-T (displacements, pressures, temperature) formulation in the multiphase model developed in Lewis and Schrefler [Lew98], in which the relative acceleration of the fluids and their convective terms have been neglected following [Cha88], [Zie99]. This reduced model is valid for low frequency problems, as in earthquake engineering, [Cha88], [Zie99]. The standard Galerkin method is applied to the governing equations for the spatial discretization, while the generalized Newmark scheme is used for the time discretization. The final nonlinear set of equations is solved by the Newton method with a monolithic approach.
The model has been implemented in the finite element code COMES-GEO, [Gaw96], [Lew98], [San06], [San08], [San09], [Gaw09], [Gaw10], [San12] and has been validated through the comparison with analytical or finite element quasi-static or dynamic solutions.

2 Macroscopic balance equations

The full mathematical model necessary to simulate the thermo-hydro-mechanical behavior of partially saturated porous media in dynamics was developed within the Hybrid Mixture Theory (HMT) by Lewis and Schrefler [Lew98], using averaging theories according to Hassanizadeh and Gray [Has79a], [Has79b], [Has80], [Gra91]. This model can be derived from the more advanced averaging theory TCAT - Thermodynamically Constrained Averaging Theory (see the chapter of this book from Gray and Miller or [Gra14] and its references listing the journal papers on this topic).

The variably saturated porous medium is treated as a multiphase system composed of solid skeleton (s) with open pores filled with liquid water (w) and gas (g). The latter, is assumed to behave as an ideal mixture of dry air (non-condensable gas, ga) and water vapor (condensable gas, gw). At the macroscopic level the porous material is modeled by a substitute continuum of volume B with boundary ∂B that simultaneously fills the entire domain, instead of the real fluids and the solid which fill only a part of it. In this substitute continuum each constituent π has a reduced density which is obtained through the volume fraction $\eta^{\pi}(\boldsymbol{x},t) = dv^{\pi}(\boldsymbol{x},t) / dv(\boldsymbol{x},t)$, where dv is the volume of the average volume element (representative elementary volume, REV) of the porous medium and dv^{π} is the volume occupied by the constituent π in dv. $\boldsymbol{x}$ is the vector of the spatial coordinates and t the current time.

The solid is deformable and non-polar and the fluids, solid and thermal effects are coupled. All fluids are in contact with the solid phase. In the model, heat conduction and heat convection, vapor diffusion, (liquid) water flow due to pressure gradients or capillary effects and water phase change (evaporation and condensation) inside the pores are taken into account.

In the partially saturated zones the liquid water is separated from its vapor by a concave meniscus (capillary water). Due to the curvature of this meniscus, the sorption equilibrium equation [Gray91] gives the relationship $p^c=p^g-p^w$ between the capillary pressure $p^c(\boldsymbol{x},t)$ (also known as matrix suction), gas pressure $p^g(\boldsymbol{x},t)$ and liquid water pressure $p^w(\boldsymbol{x},t)$. This expression is approximated in dynamics; it is used here because of lack of experimental results. In the following, pore pressure is defined as compressive positive for the fluids, while stress is defined as tension positive for the solid phase.

The state of the medium is described by gas pressure p^g, capillary pressure p^c, temperature T and displacements of the solid matrix $\boldsymbol{u}$ [San06]. The balance equations are developed in geometrically linear framework and are written here at the macroscopic level.

For sake of completeness the equations of the model are only summarized in this chapter; the interested reader is refereed to [San15] for more details regarding the development of the mathematical model and its finite element implementation. Direct notation is adopted. Boldface letters denote vector or tensors and lightface italic letters are used for scalar quantities.

After neglecting the relative velocity and acceleration of the fluids in the governing equations of Lewis and Schrefler [Lew98], a set of balance equations for the whole multiphase medium is obtained as follows.

The linear momentum balance equations of the mixture in term of the generalized effective Cauchy's stress $\boldsymbol{\sigma}'(\boldsymbol{x},t)$ [Lew98], [Nut08] takes the form

$$div\left(\boldsymbol{\sigma}' - \left[p^g - S_w p^c\right]\mathbf{1}\right) + \rho\mathbf{g} = \rho\mathbf{a}^s \tag{1}$$

where $\rho = [1-n]\rho^s + nS_w\rho^w + nS_g\rho^g$ is the mass density of the overall medium, $S_w(\boldsymbol{x},t)$ is the degree of saturation of the liquid water $n(\boldsymbol{x},t)$ is the porosity and $S_g(\boldsymbol{x},t)$ is the degree of saturation of the gas, with $S_w+S_g=1$. $\rho^s(\mathbf{x},t)$ is the density of the solid grain, $\rho^w(\mathbf{x},t)$ is the density of liquid water and $\rho^g(\mathbf{x},t)$ is the density of the gas phase. $\mathbf{g}$ is the gravity acceleration vector, $\mathbf{1}$ is the second order identity tensor and $\mathbf{a}^s(\mathbf{x},t)$ the acceleration of the solid phase. The form of Eq. (1) assumes incompressible grains, which is common in soil mechanics. In order to consider compressible grains, the Biot coefficient should be set in front of the solid pressure (this becomes important when dealing with rock and concrete). The total stress of equation (1), using saturation as weighting functions for the partial pressures, was introduced in [Sch84] using volume averaging for the bulk materials and is thermodynamically consistent, e.g. [Gra91].

The mass balance equations for the dry air and the liquid water and its vapor are, respectively:

$$\begin{aligned}&\operatorname{div}\left(\rho^{ga}\frac{k^{rg}\boldsymbol{k}}{\mu^{g}}\left[-\operatorname{grad}p^{g}+\rho^{g}\boldsymbol{g}\right]\right)+\operatorname{div}\left(\rho^{g}\frac{M_{a}M_{w}}{M_{g}^{2}}\boldsymbol{D}_{g}^{ga}\operatorname{grad}\left(\frac{p^{gw}}{p^{g}}\right)\right)\\&+\rho^{ga}S_{g}\operatorname{div}\boldsymbol{v}^{s}+nS_{g}\dot{\rho}^{ga}-\rho^{ga}n\dot{S}_{w}-\rho^{ga}\beta_{s}\left(1-n\right)S_{g}\dot{T}=0\end{aligned}\tag{2}$$

and

$$\begin{aligned}&\operatorname{div}\left(\rho^{w}\frac{k^{rw}\boldsymbol{k}}{\mu^{w}}\left(-\operatorname{grad}p^{w}+\rho^{w}\boldsymbol{g}\right)\right)+\operatorname{div}\left(\rho^{gw}\frac{k^{rg}\boldsymbol{k}}{\mu^{g}}\left(-\operatorname{grad}p^{gw}+\rho^{gw}\boldsymbol{g}\right)\right)\\&-\operatorname{div}\left(\rho^{g}\frac{M_{a}M_{w}}{M_{g}^{2}}\boldsymbol{D}_{g}^{gw}\operatorname{grad}\left(\frac{p^{gw}}{p^{g}}\right)\right)+\left[\rho^{w}S_{w}+\rho^{gw}S_{g}\right]\operatorname{div}\boldsymbol{v}^{s}+\rho^{w}\frac{nS_{w}}{K_{w}}\left[\dot{p}^{g}-\dot{p}^{c}\right]\\&-\left[\rho^{w}\beta_{sw}+\rho^{gw}\beta_{s}\left(1-n\right)S_{g}\right]\dot{T}+\left[n\rho^{w}-n\rho^{gw}\right]\dot{S}_{w}+nS_{g}\dot{\rho}^{gw}=0\end{aligned}\tag{3}$$

where **k** ($\boldsymbol{x}$,t) = $k(\boldsymbol{x},t)\mathbf{1}$ is the intrinsic permeability tensor of the porous matrix in water saturated condition [m^2], which is assumed to be isotropic, $k^{r\pi}(\boldsymbol{x},t)$ is the fluid relative permeability parameter and $\mu^{\pi}(\boldsymbol{x}, t)$ is the dynamic viscosity of the fluid [Pa s], with $\pi = w, g$. K_w is the bulk modulus of the liquid water. β_{sw} = [1-n]$\beta_s[S_g\rho^{gw} + \rho^w S_w]$, with $\beta_s(\boldsymbol{x}, t)$ the cubic thermal expansion coefficient of the solid. $\mathbf{D}_g^{gw}(\boldsymbol{x})$ is the effective diffusivity tensor of water vapor in the gas phase contained within the pore space, and M_a, M_w and $M_g(\boldsymbol{x},t)$ are the molar mass of dry air, liquid water and the gas mixture $M_g=\left[\frac{\rho^{gw}}{\rho^{g}}\frac{1}{M_w}+\frac{\rho^{ga}}{\rho^{g}}\frac{1}{M_a}\right]^{-1}$, respectively. These equations contain the mass balance equation of the solid phase, which has been introduced to eliminate the time derivative of the porosity.

The enthalpy balance equation for the multiphase medium is:

$$\begin{aligned}&-\operatorname{div}\left(\rho^{w}\frac{k^{rw}\mathbf{k}}{\mu^{w}}\left[-\operatorname{grad}\left(p^{w}\right)+\rho^{w}\mathbf{g}\right]\right)\Delta H_{vap}-\operatorname{div}\left(\chi_{eff}\operatorname{grad}T\right)-\rho^{w}S_{w}\operatorname{div}\mathbf{v}^{s}\Delta H_{vap}\\&+\left[C_{p}^{w}\rho^{w}\frac{k^{rw}\mathbf{k}}{\mu^{w}}\left[-\operatorname{grad}\left(p^{w}\right)+\rho^{w}\mathbf{g}\right]+C_{p}^{g}\rho^{g}\frac{k^{rg}\mathbf{k}}{\mu^{g}}\left[-\operatorname{grad}p^{g}+\rho^{g}\mathbf{g}\right]\right]\cdot\operatorname{grad}T\\&+\left(\rho C_{p}\right)_{eff}\dot{T}-\rho^{w}\frac{nS_{w}}{K_{w}}\dot{p}^{w}\Delta H_{vap}+\beta_{sw}\dot{T}\Delta H_{vap}-n\left[\rho^{w}-\rho^{gw}\right]\dot{S}_{w}\Delta H_{vap}=0\end{aligned}\tag{4}$$

where $\left(\rho C_p\right)_{eff}(\boldsymbol{x},t)$ is the effective thermal capacity of the porous medium, $C_p^w(\boldsymbol{x},t)$ and $C_p^g(\boldsymbol{x},t)$ are the specific heat of water and gas, respectively, and $\chi_{eff}(\boldsymbol{x},t)$ is the effective thermal conductivity of the porous medium. The RHS term of Equation (4) considers the contribution of the evaporation and condensation. In equations (2)-(4) the advective fluxes have been described using Darcy's law for liquid water and gas, while the diffusion of vapor in the gas phase has been modeled with Fick's law. A recent development of a model which considers the air dissolved in the liquid water and its desorption at lower water pressures in quasi-statics loading conditions is presented in [Gaw09].

3 Constitutive relationships

For the gaseous mixture of dry air and water vapour, the ideal gas law is introduced. The equation of state of perfect gas (Clapeyron's equation) and Dalton's law are applied to dry air (ga), water vapor (gw) and moist air (g).

$$p^{ga} = \rho^{ga} TR / M_a, \quad p^{gw} = \rho^{gw} TR / M_w, \quad p^g = p^{ga} + p^{gw}, \quad \rho^g = \rho^{ga} + \rho^{gw} \qquad (5)$$

In the partially saturated zones, the equilibrium water vapor pressure $p^{gw}(\boldsymbol{x},t)$ can be obtained from the Kelvin-Laplace equation, where the water vapor saturation pressure, $p^{gws}(\boldsymbol{x},t)$, depending only upon the temperature, can be calculated from the Clausius-Clapeyron equation or from an empirical correlation. The saturation degree $S_{\mathrm{w}}(\boldsymbol{x},t)$ and the relative permeability $k^{\mathrm{r}\pi}(\boldsymbol{x},t)$ are experimentally determined functions dependent on capillary pressure and temperature (e.g. [Fra08] for S_{w}). The bulk density of liquid water that is dependent on the temperature is modeled using the relationship proposed by Furbish [Fur97]. The liquid water viscosity, dry air and water vapor viscosity, and the latent heat of evaporation are also temperature dependent relationships.

The solid skeleton is assumed elastic or elasto-plastic, homogeneous and isotropic in the numerical simulations described in Section 5. Its mechanical behavior is described within the classical rate-independent elasto-plasticity theory for geometrically linear problems. For the third numerical example, the yield function restricting the effective stress state $\boldsymbol{\sigma}'(\boldsymbol{x},t)$ is developed in the form of Drucker-Prager model for simplicity, with linear isotropic softening and non-associated plastic flow to take into account the post-peak and dilatant behavior of dense sands, respectively. The return mapping and the consistent tangent operator for the Jacobian matrix, equations (9), is developed in [San06], where the singular behavior of the Drucker-Prager yield surface in the zone of the apex is solved by using the multi-surface plasticity theory (following the formulation developed in [San02] for isotropic linear hardening/softening and volumetric-deviatoric non-associative plasticity in case of large strain elasto-plasticity).

The Drucker-Prager yield function with linear isotropic hardening/softening has been used in the form

$$F\left(p,\mathbf{s},\xi\right)=3\alpha_F p+\left\|\mathbf{s}\right\|-\beta_F\sqrt{\tfrac{2}{3}}\left[c_0+h\xi\right] \tag{6}$$

in which $p=\frac{1}{3}\left[\boldsymbol{\sigma}':\mathbf{1}\right]$ is the mean effective Cauchy pressure, $\left\|\mathbf{s}\right\|$ is the L_2 norm of the deviator effective Cauchy stress tensor $\boldsymbol{\sigma}'$, c_0 is the initial apparent cohesion, α_F and β_F are two material parameters related to the friction angle ϕ of the soil,

$$\alpha_F=2\frac{\sqrt{\frac{2}{3}}\sin\phi}{3-\sin\phi}\qquad \beta_F=\frac{6\cos\phi}{3-\sin\phi} \tag{7}$$

h the hardening/softening modulus and ξ the equivalent plastic strain.
To take into account the effect of capillary pressure and temperature on the evolution of the yield surface, the interested reader can refer, for example, to the chapter by Manzanal et. al of this book and [Fra08] for capillary dependent constitutive relationships in isothermal or non-isothermal conditions, respectively.

4 Spatial and time discretization

The finite element model is derived by applying the Galerkin procedure for the spatial integration and the generalized Newmark method for the time integration of the weak form of the balance equations (1)-(4) [Lew98], [Zie99], [Zie00].
In particular, after spatial discretization within the isoparametric formulation, the following non-symmetric, non-linear and coupled system of equations is obtained:

$$\begin{cases}\boldsymbol{C}_{gg}\dot{\overline{\boldsymbol{p}}}^g+\boldsymbol{C}_{gc}\dot{\overline{\boldsymbol{p}}}^c-\boldsymbol{C}_{gT}\dot{\overline{\boldsymbol{T}}}+\boldsymbol{C}_{gu}\dot{\overline{\boldsymbol{u}}}+\boldsymbol{K}_{gg}\overline{\boldsymbol{p}}^g-\boldsymbol{K}_{gc}\overline{\boldsymbol{p}}^c-\boldsymbol{K}_{gT}\overline{\boldsymbol{T}}=\boldsymbol{f}_g\\ \boldsymbol{C}_{cg}\dot{\overline{\boldsymbol{p}}}^g+\boldsymbol{C}_{cc}\dot{\overline{\boldsymbol{p}}}^c+\boldsymbol{C}_{cT}\dot{\overline{\boldsymbol{T}}}+\boldsymbol{C}_{cu}\dot{\overline{\boldsymbol{u}}}-\boldsymbol{K}_{cg}\overline{\boldsymbol{p}}^g+\boldsymbol{K}_{cc}\overline{\boldsymbol{p}}^c+\boldsymbol{K}_{cT}\overline{\boldsymbol{T}}=\boldsymbol{f}_c\\ -\boldsymbol{C}_{Tg}\dot{\overline{\boldsymbol{p}}}^g-\boldsymbol{C}_{Tc}\dot{\overline{\boldsymbol{p}}}^c+\boldsymbol{C}_{TT}\dot{\overline{\boldsymbol{T}}}-\boldsymbol{C}_{Tu}\dot{\overline{\boldsymbol{u}}}-\boldsymbol{K}_{Tg}\overline{\boldsymbol{p}}^g+\boldsymbol{K}_{Tc}\overline{\boldsymbol{p}}^c+\boldsymbol{K}_{TT}\overline{\boldsymbol{T}}=\boldsymbol{f}_T\\ \boldsymbol{M}_{uu}\ddot{\overline{u}}+\int\boldsymbol{B}^T\boldsymbol{\sigma}'dW-\boldsymbol{K}_{ug}\overline{\boldsymbol{p}}^g+\boldsymbol{K}_{uc}\overline{\boldsymbol{p}}^c=\boldsymbol{f}_u\end{cases} \tag{8}$$

where the displacements of the solid skeleton $\mathbf{u}(\boldsymbol{x},t)$, the capillary pressure $p^{c}(\boldsymbol{x},t)$, the gas pressure $p^{g}(\boldsymbol{x},t)$ and the temperature $T(\boldsymbol{x},t)$ are expressed in the whole domain by global shape function matrices $\mathbf{N}_u(\boldsymbol{x})$, $\mathbf{N}_c(\boldsymbol{x})$, $\mathbf{N}_g(\boldsymbol{x})$, $\mathbf{N}_T(\boldsymbol{x})$ and the nodal value vectors $\overline{\boldsymbol{u}}\left(t\right),\overline{\boldsymbol{p}}^c\left(t\right),\overline{\boldsymbol{p}}^g\left(t\right),\overline{\boldsymbol{T}}\left(t\right)$.
Following the Generalized Newmark Method, equations (8) are rewritten at time $t_{(n+1)}$. The elements of the matrices $\boldsymbol{C}_{ij}$, $\boldsymbol{K}_{ij}$ and the vectors $\boldsymbol{f}_i$ are given in [San15].
In this study, the generalized Newmark time integration scheme [Zie00] is applied to the non-linear equation system (8) and a non-linear system of algebraic equations is

obtained, in which the unknowns are $\boldsymbol{x} = \left[\Delta\dot{\bar{p}}^g\,,\ \Delta\dot{\bar{p}}^c\,,\ \Delta\dot{\bar{T}}\,,\ \Delta\ddot{\bar{\boldsymbol{u}}} \right]$. The non-linear system is solved by Newton-Raphson method, thus obtaining the equation system that can be solved numerically (written below in a compact form) as:

$$\left.\frac{\partial \mathbf{G}}{\partial \mathbf{X}}\right|_{\mathbf{X}^i_{n+1}} \Delta\mathbf{X}^{i+1}_{n+1} \cong -\mathbf{G}\left(\mathbf{X}^i_{n+1}\right) \tag{9}$$

with the symbol $(\bullet)^{i+1}_{n+1}$ to indicate the current iteration (i+1) in the current time step (n+1) and where $\partial\mathbf{G}/\partial\mathbf{X}$ is the Jacobian matrix.

Owing to the strong coupling between the mechanical, thermal and the pore fluids fields, a monolithic solution of (9) is preferred.

5 Finite element simulations

This section addresses the numerical validation of the model previously derived and presents an application studying a biaxial strain localization test.

Different tests have been simulated and presented in [San15], aiming to validate: a) the wave propagation in a solid material (equation (1) restricted to single phase solid material), b) the isothermal water saturated model (equations (1) and (3) with S_w=1), c) the isothermal variably saturated model (equations (1), (2) and (3)) and d) the non-isothermal water saturated model (equations (1), (3) and (4) with Sw=1). Analytical solutions are available in [Slu92] and [Boe93] for the first two tests respectively, while the numerical results from tests c) and d) have been compared with the numerical solution of the corresponding quasi-static models because of the lack of analytical solutions. Some representative results of tests c) and d) are illustrated here.

5.1 Drainage of liquid water from initially water saturated soil column

This numerical test is based on an experiment performed by Liakopoulos [Lia65] on a column 1 meter high (Figure 1) of Del Monte sand and instrumented to measure the moisture tension at several points along the column during its desaturation due to gravitational effects. Before the start of the experiment, water was continuously added from the top and was allowed to drain freely at the bottom through a filter, until uniform flow conditions were established. Then the water supply was ceased and the tensiometer readings were recorded. The finite element simulation is performed with the two-phase flow model in isothermal conditions. For the numerical calculation, a two-dimensional problem in plane strain conditions is solved; the spatial domain of the column is divided into 20 eight-node isoparametric finite elements of equal size. Furthermore, nine Gauss integration points were used. The material parameters are listed in [Gaw96] or [San15], as well as the description of the boundary conditions and the equations for the saturation-capillary pressure and the relative permeability of water-capillary pressure relationships.

This problem has been solved considering single or two-phase flow mainly in quasi-static condition (e.g. [Gaw96]); a finite element solution in dynamics was presented in [Sch98]. The initial hydro-mechanical equilibrium state is obtained via a preliminary quasi-static solution.

The comparison between the dynamic and the quasi-static solution is plotted in Figures 2 to 4, where the profiles for liquid water pressure, liquid water saturation and vertical displacement along the column are plotted. Since the inertial loads are negligible in the experiment, the finite element solution in dynamics gives almost the same results of the quasi-static model [Gaw96], [Gaw09].

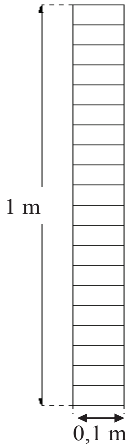

Figure 1: Geometry and finite element discretization of the sand column.

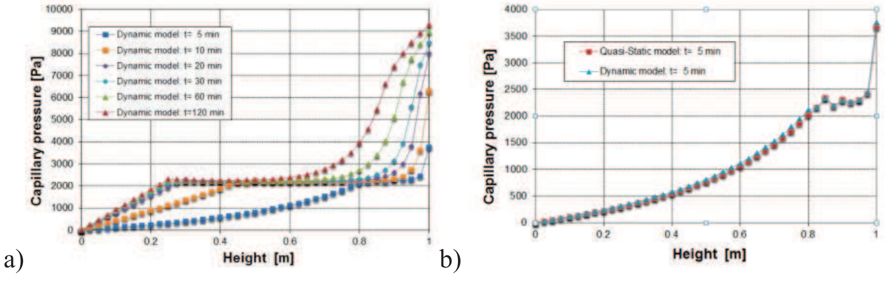

Figure 2: Profiles of capillary pressure versus height: a) dynamic solution; b) comparison between the quasi-static and the dynamic solution.

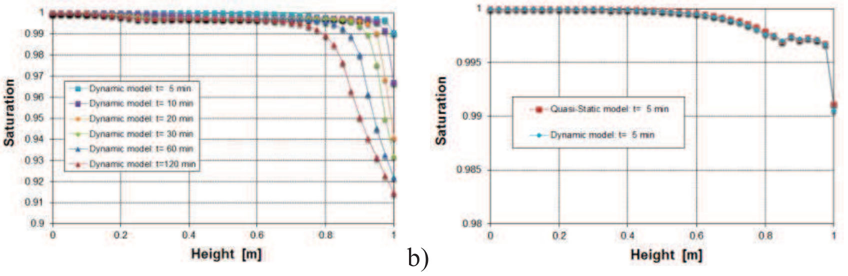

a) b)

Figure 3: Profiles of liquid water saturation degree versus height: a) dynamic solution; b) comparison between the quasi-static and the dynamic solution.

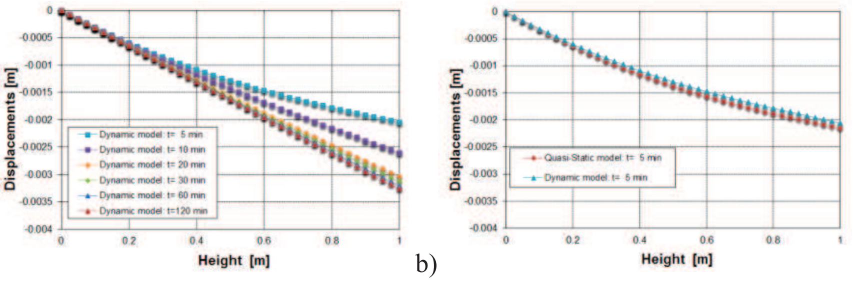

a) b)

Figure 4: Profiles of vertical displacement versus height: a) dynamic solution; b) comparison between the quasi-static and the dynamic solution.

5.2 Numerical validation of the non-isothermal water saturated model

This problem deals with a water saturated thermo-elastic consolidation [Abo85], simulating a column, 7 m high and 2 m wide, of a linear elastic material subjected to an external surface load of 10 kPa and to a surface temperature jump of 50 K above the initial temperature of 293.15 K (Figure 5). The material parameters used in the computation are summarized in [San08]. The liquid water and the solid grain are assumed incompressible for the quasi-static analysis, whereas the compressibility of the liquid water is taken into account in the dynamic analysis. The initial and boundary conditions are described in [San08] and [San15]. Plane strain condition is assumed. The spatial domain is discretized with eight-node isoparametric elements; nine Gauss points are used.

The solution of the finite element model presented in this work is compared with the quasi-static solution [San08] and is plotted in Figures 6 and 7. The results show that the dynamic solution is faster than the quasi-static one at the beginning of the analysis, and that the dynamic solution reaches the quasi-static one at the steady-state.

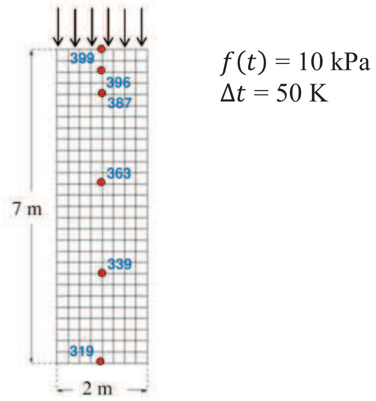

Figure 5: Description of the non-isothermal water saturated test.

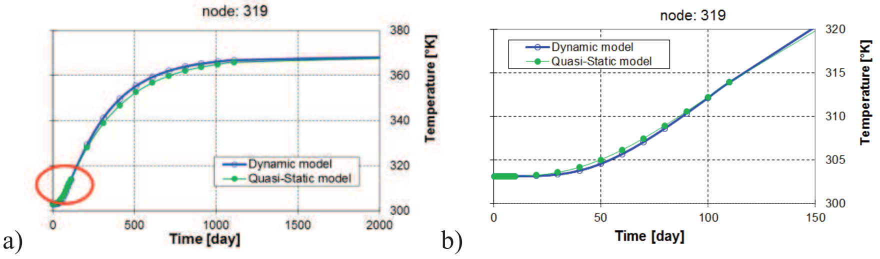
a) b)

Figure 6: Temperature time history for node 319 up to the steady state solution (a) and in the first period (b) highlighted in a).

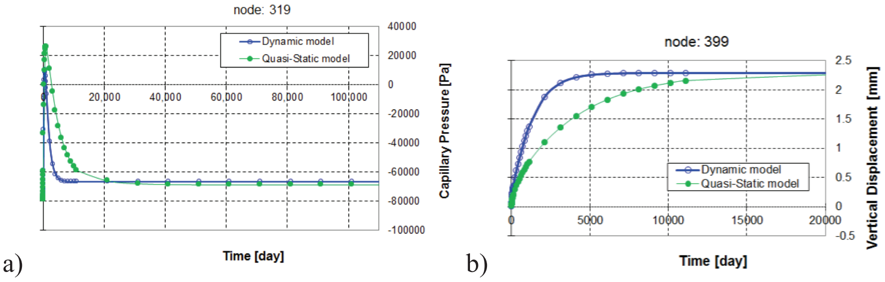
a) b)

Figure 7: a) Capillary pressure time history for node 319 and b) vertical displacement time history for node 399.

5.3 Globally undrained biaxial compression test

A plane strain compression test of initially water saturated dense sand in globally undrained conditions is simulated here with the model developed in the previous sections. This case was solved in [San06] in quasi-static conditions and is inspired by the experimental work of Mokni and Desrues [Mok98], in which cavitation of the liquid water was experimentally observed at localization.

A sample of 34 cm height and 10 cm width is compressed with imposed vertical displacement applied to the top surface at a velocity of 3.6 mm/s (Figure 8). Vertical and horizontal displacements are constrained at the bottom surface; the boundary of the sample is impervious and adiabatic.

The mechanical behavior of the solid skeleton is simulated using the elasto-plastic Drucker-Prager constitutive model (with isotropic linear softening and non-associated plastic flow) summarized in Section 3. At time t= 0 seconds, the initial conditions for the domain are the hydrostatic water pressure, the gas pressure at atmospheric value and a temperature of 293.15 K. Gravity acceleration is taken into account; the initial stress state in equilibrium with the initial conditions and thermo-hydro boundary conditions is computed with the corresponding quasi-static model [San06]. The geomechanical characteristics of the dense sand are given in [San06].

Figures 9 and 10 show the contour plots at 13 seconds of the following thermo-hydro-mechanical variables: equivalent plastic strain, volumetric strain, capillary pressure, liquid water saturation and relative humidity. Positive volumetric strains are observed inside the dilatant shear bands (Figure 9b), inducing a liquid water pressure drop up to the development of capillary pressures (Figure 10a) desaturating the plastic zones (Figure 10b) because of the phase change of the liquid water into vapor due to cavitation (Figure 10c).

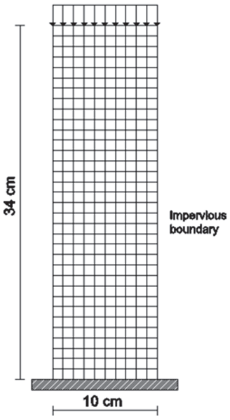

Figure 8: Finite element discretization and boundary conditions of the biaxial compression test.

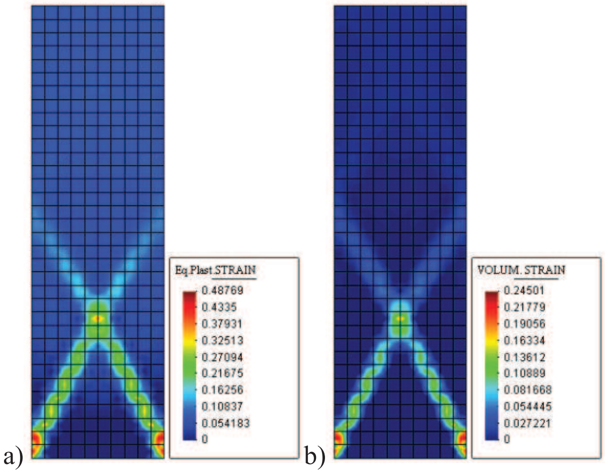

Figure 9: Numerical solution at 13 s: a) equivalent plastic strain, b) volumetric strain.

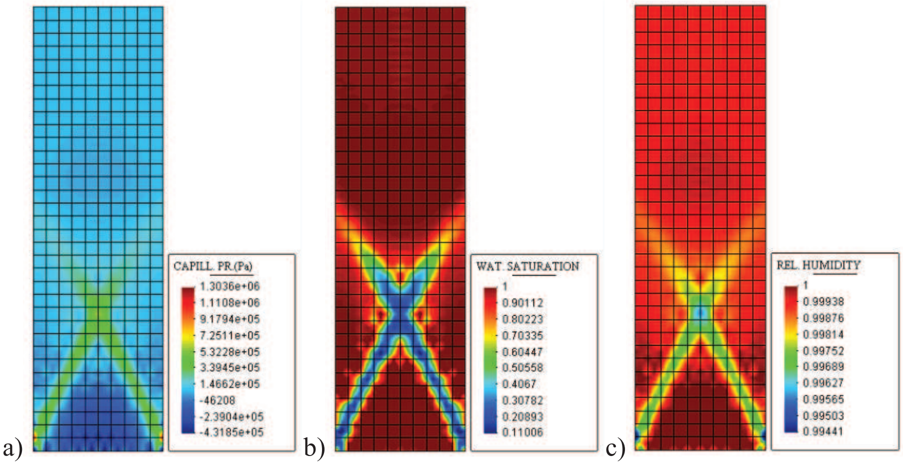

Figure 10: Numerical solution at 13 s: a) capillary pressure, b) liquid water saturation, c) relative humidity.

To study the independence of shear band width from the finite element size in dynamics, e.g. [Sch96], [Sch99], [Zha99] and [Sch06], test runs with meshes of 85, 340 and 1360 elements have been carried out. In this case, the analysis of the finite element results [Cao15] shows that the shear band width is reasonably mesh independent, while the peak value of the equivalent plastic strain and, as a consequence, of the volumetric strain, the capillary pressure, the water vapor pressure and the relative humidity are sensitive to mesh refinement and a regularization scheme would be needed as expected (e.g. [Zha99], [Sch99] and [Sch06]), because the internal length scale given by the liquid water motion [Zha99] is not sufficient to regularize the numerical solution.

6 Conclusions

A model for the analysis of the thermo-hydro-mechanical behavior of porous media in dynamics was developed. Starting from the generalized mathematical model developed in [Lew98] for deforming porous media in non-isothermal conditions, the u-p-T formulation was derived following [Zie99]. The validity of such an approximation is limited to low frequencies problems [Zie99], as in earthquake engineering. In this formulation, the relative accelerations of the fluids and the convective terms related to these accelerations are neglected.

The numerical model was derived within the finite element method: the standard Bubnov-Galerkin procedure [Zie00] was adopted for the discretization in space, while the implicit and unconditionally stable generalized Newmark procedure was applied for the discretization in time [Zie00].

The model was implemented in the finite element code Comes-Geo [Lew98], [Gaw96], [San06], [San08], [San09], [Gaw09], [Gaw10]. The formulation and the implemented solution procedure were validated through the comparison with literature benchmarks, finite element solutions or analytical solutions. In this work, comparison between the finite element solution in dynamics and the corresponding quasi-static solution is presented by studying the non-isothermal consolidation in a water saturated column and the drainage of liquid water in an initially water saturated soil column.

This work extends the model developed in [Sch98] to non-isothermal conditions and removes the passive air phase assumption of the multiphase porous media model in dynamics developed in [Zie99] and [Gaw98].

Acknowledgements. The authors would like to thank the 7th Framework Programme of the European Union (ITN MuMoLaDe project 289911) and University of Padova (CPDR121149) for the financial support.

References

[Abo85] Aboustit, B. L., Advani, S. H. and Lee, J. K. Variational principles and finite element simulations for thermo-elastic consolidation. *Int. J. Numer. Anal. Methods Geomech.* 9: 49-69, 1985.

[Alb10] Albers, B. *Modeling and numerical analysis of wave propagation in saturated and partially saturated porous media*. Habilitation Thesis, Technischen Universität Berlin n.48, Shaker Verlag, 2010.

[Boe93] de Boer R, Ehlers W, Liu Z. One-dimensional transient wave propagation in fluid-saturated incompressible porous media. *Archive of Applied Mechanics,* 63(1): 59-72, 1993.

[Cao15] Cao T.d, Sanavia L., Schrefler BA. A thermo-hydro-mechanical model for multiphase geomaterials in dynamics with application to strain localization simulation. *Int. J. Num. Meth. Engng.*, in revision.

[Cha88] Chan, A.H.C. *A unified finite element solution to static and dynamic in geomechanics*. Ph.D. Thesis, University College of Swansea, 1988.

[Fra08] François, B. and Laloui, L. ACMEG-TS: A constitutive model for unsaturated soils under non-isothermal conditions. *Int. J. Numer. Anal. Methods Geomech* 32:1955-1988, 2008.

[Fur97] Furbish DJ. *Fluid Physics in Geology: An Introduction to Fluid Motions on Earth's Surface and within Its Crust*. Oxford University Press, 1997.

[Gaw09] Gawin, D., Sanavia, L. A unified approach to numerical modelling of fully and partially saturated porous materials by considering air dissolved in water. *CMES: Computer Modeling in Engineering & Sciences*, 53: 255-302, 2009.

[Gaw10] Gawin, D., Sanavia, L. Simulation of cavitation in water saturated porous media considering effects of dissolved air. *Transport in Porous Media*, 81: 141-160, 2010.

[Gaw96] Gawin, D., Schrefler, B.A. Thermo-hydro-mechanical analysis of partially saturated porous materials. *Engineering Computations,* 13: 113-143, 1996.

[Gaw98] Gawin, D., Sanavia, L., Schrefler, B.A. Cavitation modelling in saturated geomaterials with application to dynamic strain localisation, *International Journal for Numerical Methods in Fluids*, 27: 109-125, 1998.

[Gra13] Gray WG, Miller CT, Schrefler BA. Averaging theory for description of environmental problems: What have we learned, *Advances in Water Resources*; 51: 123–138, Doi.org/10.1016/j.advwatres.2011.12.005, 2013.

[Gra14] Gray WG, Miller CT. *Introduction to the Thermodynamically Constrained Averaging Theory for porous medium systems*, Springer, 2014.

[Gra91] Gray WG, Hassanizadeh M. Unsaturated flow theory including interfacial phenomena. *Water Resources Research,* 27: 1855-1863, 1991.

[Has79a] Hassanizadeh, M., Gray, W.G. General conservation equations for multiphase system: 1. Averaging technique. *Advances in Water Resources,* 2:131-144, 1979.

[Has79b] Hassanizadeh, M., Gray, W.G. General conservation equations for multiphase system: 2. mass, momenta, energy and entropy equations. *Advances in Water Resources*, 2: 191-201, 1979.

[Has80] Hassanizadeh M, Gray WG. General conservation equations for multiphase systems: 3. Constitutive theory for porous media flow. *Advances in Water Resources,* 3(1): 25-40, 1980.

[Hei11] Heider, Y., Markert, B., Ehlers, W. Dynamic wave propagation in infinite saturated porous media half spaces. *Computational Mechanics* 49: 319-336, 2011.

[Lew98] Lewis, R.W. and Schrefler, B.A. *The finite element method in the static and dynamic deformation and consolidation of porous media*. Wiley, 1998.

[Lia65] Liakopoulos, A.C. *Transient flow through unsaturated porous media. PhD thesis*, University of California, Berkeley, USA, 1965.

[Mok98] Mokni, M., Desrues, J. Strain localisation measurements in undrained plane-strain biaxial tests on hostun RF sand. *Mechanics of Cohesive-frictional Materials*, 4, 419 – 441, 1998.

[Nen10] Nenning, M., Schanz, M. Infinite elements in a poroelastodynamic FEM. *Int. J. Numer. Anal. Methods Geomech.* 35: 1774-1800, 2010.

[Nut08] Nuth, M., Laloui, L. Effective stress concept in unsaturated soils: Clarification and validation of a unified approach. *Int. J. Numer. Anal. Methods Geomech.* 32:771-801, 2008.

[San02] Sanavia, L., B.A. Schrefler, and P. Steinmann, A formulation for an unsaturated porous medium undergoing large inelastic strains, *Computational Mechanics, 28*: 137-151, 2002

[San06] Sanavia, L., Pesavento, F., Schrefler, B.A. Finite element analysis of non-isothermal multiphase geomaterials with application to strain localization simulation. *Computational Mechanics*, 37: 331-348, 2006.

[San08] Sanavia, L., François, B., Bortolotto, R., Luison, L. and Laloui, L. Finite element modelling of thermo-elasto-plastic water saturated porous materials. *Journal of Theoretical and Applied Mechanics,* 38:7-24, 2008.

[San09] Sanavia, L. Numerical modelling of a slope stability test by means of porous media mechanics. *Engineering Computations,* 26: 245-266, 2009.

[San15] Sanavia L., Cao T.D A model for non-isothermal variably saturated porous media in dynamics, in preparation.

[Sch06] Schrefler, B.A., Zhang, H.W. and Sanavia, L. Interaction between different internal length scales in fully and partially saturated porous media – The 1-D case, *Int. J. Numer. Anal. Methods Geomech.,* 30: 45-70, 2006.

[Sch09] Schanz, M. Poroelastodynamics: linear models, analytical solutions, and numerical methods. *Applied Mechanics Reviews,* 62: 1-15, 2009.

[Sch84] Schrefler, B.A. *The Finite Element Method in Soil Consolidation (with applications to Surface Subsidence)*. PhD. Thesis, University College of Swansea, C/Ph/76/84, Swansea UK, 1984.

[Sch96] Schrefler BA, Sanavia L., Majorana CE. A multiphase medium model for localization and post localization simulation in geomaterials. *Mechanics of Cohesive-Frictional Materials*, 1:95-114, DOI: 10.1002/(SICI)1099-1484(199601)1:1<95::AID-CFM5>3.0.CO;2-D, 1996.

[Sch98] Schrefler, B.A., Scotta, R. A fully coupled dynamic model for two-phase fluid flow in deformable porous media. *Computer Methods in Applied Mechanics and Engineering,* 190: 3223-3246, 1998.

[Sch99] Schrefler, B.A., Zhang, H.W., Sanavia, L. Fluid-structure interaction in the localisation of saturated porous media. *ZAMM Zeitschrift für Angewandte Mathematik und Mechanik (Journal of Applied Mathematics and Mechanics. Z. Angew. Math. Mech.)*, 79: 481-484, 1999.

[Slu92] Sluys, L.J. *Wave propagation, localization and dispersion in softening solids*, Ph.D. Dissertation, Delft University of Technology, 1992.

[Var02] Vardoulakis, I. Dynamic thermo-poro-mechanical analysis of catastrophic landslides. *Géotechnique*, 52: 157-171, 2002.

[Zha99] Zhang H.W., Sanavia L, Schrefler B.A. An interal length scale in dynamic strain localization of multiphase porous media. *Mechanics of Cohesive-frictional Materials,* 4(5): 443-460, 1999.

[Zie00] Zienkiewicz, O.C. and Taylor, R.L. *Finite element method* (5th edition) volume 1 - the basis. Elsevier, 2000.

[Zie99] Zienkiewicz, O.C., Chan, A.H., Pastor, M., Schrefler, B.A. and Shiomi, T. *Computational geomechanics with special reference to earthquake engineering*. Wiley, 1999.

Numerical modelling of a Municipal Waste Disposal as a Bio- Chemo- Thermo- Hydro-Mechanical problem

F. Collin[1], **J. Hubert**[1,2], **X.F. Liu**[3], **B. Cerfontaine**[1]

[1]*Department ArGEnCo, University of Liège, Belgium ;*

[2]*FRS-FNRS, Fonds National de la Recherche Scientifique, Belgium ;*

[3]*Centre for Geotechnical and Materials Modelling, Faculty of Engineering and Built Environment, The University of Newcastle, Australia*

This paper considers the Municipal Solid Waste (MSW) as a multi-physics porous medium, where Bio-Chemo-Thermo-Hydro-Mechanical phenomena have a dominant effect on the long term behavior. Considering MSW in a bioreactor landfill provides a perfect application for coupled and multiphysics phenomena. A two-stage anaerobic biochemical model based on McDougall's formulation is considered accounting for the progressive degradation of the organic matter. In presence of water, this latter decomposition is an exothermic reaction leading to an increase of the temperature, a generation of by-products as gases and chemical species, and finally compaction of the waste. The proposed model couples McDougall's formulation with an unsaturated flow model, a thermal model including a source term for heat generation from the biodegradation of organic matter and finally a mechanical model. As proposed by [Hue97], the constitutive law is a modified Camclay model allowing biochemical hardening/softening. The fully coupled model is implemented into the `LAGAMINE` *multi-physics finite element code. Numerical simulations are performed to study the couplings between all the phenomena and to propose a prediction for the long-term settlement of a bioreactor landfill. The first part of this paper introduces the main features of the BCHTM model. The second part deals with its application to the fully coupled modelling of a 1D column of waste. Each physical phenomenon is introduced sequentially in order to understand its effect on the evolution of the waste column. Analytical solutions are provided for each simplified physical problem in order to validate the numerical results and to isolate the influence of the main parameters.*

1 Introduction

The need for more efficient landfill management has led to the development of new generation ”bioreactor landfills” [RMT02]. They are characterized by water injection or recirculation of generated leachate to accelerate the biodegradation of the organic fraction [KCM11]. It leads to rapid stabilization of waste, better control over biogas production, gain of landfill space and overall shorter and cheaper monitoring and maintenance [RAY96, Bea00, YWSM01]. One of the keys to properly operate bioreactor landfills is the ability to accurately predict the settlements. It is a great challenge because of the inherent complexity of the landfill system. The whole process is governed by the biodegradation of organic waste coupled with thermal, hydraulic and mechanical phenomena [McD07, CZL14]. The first models trying to predict the settlement were empirical time dependent models with or without taking into account waste degradation such as [GL61, Sow75, ER90, Oli03]. They were useful due to their simplicity but lacked the ability to accurately predict long term settlements. More recently, the focus has been brought on the necessity of integrated analysis which would include biodegradation model into ”classical” mechanical and hydraulic models used in geomechanics [HMTH07, McD07, RRW11, CXZ12, WB13, CZL14]. This would allow to capture every fundamental phenomenon and merge them into multiphysics models able to better estimate long term behavior. It is, then, an absolute necessity to understand the main biochemical reactions occuring during biodegradation [PK00, AJ00, Rod05, BBH$^+$10] and to translate them into usable mathematical models. There are mostly two types of biodegradation models : multi-phase degradation using Monod kinetic [EFFL96, HHO$^+$01, WRR03] and two stage anaerobic digestion model [McD07, RRW11, GED08, CGLZ15]. The latter became increasingly popular because of its ability to represent the whole process in a simplified manner whereas the former requires lots of parameters whose values are not always easily determined. Most integrated models do not take into account the thermal effects on biological reactions despite important temperature variation during the decomposition of organic content. Although some [KCM11, GED08, EFFL96] consider the thermal aspect of the process, their thermo-hydro-biological models are unable to calculate landfill settlements. Also, few models [McD07] use sophisticated constitutive models within elasto-plastic framework to describe the chemo-mechanical behavior of solid waste.

The objective of this work is to present an example of multiphysical couplings in geomechanics. It aims at describing in a logical sequence how to manage each physical problem separately and how to couple it with the other phenomena. The biochemo-thermo-hydro-mechanical (BCTHM) modelling of a column of waste is a perfect case study for that purpose.

The two-stage anaerobic biodegradation model adopted by [McD07] is implemented into a fully coupled thermo-hydro-mechanical framework for unsaturated porous media, which has been developed in the `LAGAMINE` code over the last three decades [Cha07, Col03]. Details of the implementation as well as the main parameters can be found in [HLC15]. The biodegradation model is linked to both the governing mass balance equations (for VFA and methanogen biomass) and the energy balance equa-

tion through source term. The mechanical model adopted is a simplified version of the chemo-hydro-mechanical (CHM) model presented by [LBL$^+$05].
The physical phenomena are considered sequentially, from the simple flow model to the fully coupled BC-THM model. Numerical results are presented and compared with a closed-form solution of each independent problem. This aims at both validating the results and emphasizing the importance of the main parameters. This procedure provides a better understanding of the physical phenomena and their couplings.

2 BC-THM behavior of Municipal Waste

Municipal wastes are porous media, where highly coupled mutliphysical phenomena take place. In addition to the hydromechanical behavior classically observed in geomaterials, bio-chemical processes responsible for the organic matters degradation make the coupled behavior of the waste much more complex. In the following, the model formulation is described for the different physical phenomena.

2.1 Bio-chemical model

The microbiological activity within the landfills is responsible for the mineralization of the organic content and the production of biogas. This process modifies the hydromechanical properties of the waste and has to be considered in a detailed analysis of the MSW long term behavior. The biodegradation can be split into two main stages [Rod05], which are briefly described in the following sections.

Aerobic stage The aerobic phase is the first step of the biodegradation and begins just after the wastes are landfilled. It lasts at most a few weeks since the deposit of subsequent layers of waste will deprive the previous ones of any oxygen and will cut the aerobic stage short. During this process, the organic content (Org) is degraded into macromolecules by bacteria. It is a very exothermal reaction leading to an important temperature raise sometime reaching over 60 °C.

Anaerobic stage The anaerobic stage begins as soon as the aerobic one ends. It can last up to 40 or 50 years. This stage consists of the four reactions defined below [Rod05]

- Hydrolysis: the macromolecules are decomposed by hydrolytic bacteria into smaller molecules (lipid into fatty acid ; polysaccharide into monosaccharide ; protein into amino acid).
- Acidogenesis: the products of the hydrolysis are transformed into ethanol, organic acid and Volatile Fatty Acid (VFA).

- Acetogenesis: the products of the hydrolysis are consumed and transformed into acetyl acid and hydrogen.
- Methanogenesis: during this last step, the acetyl acid is consumed to produce carbon dioxide and the hydrogen is consumed to produce first methanogen biomass in a liquid phase that will transform into methanogen biogas and carbon dioxide in a second step.

The two-stage biochemical model described by [McD07] is adopted here to describe the hydrolysis/acidogenesis and methanogesis reactions. McDougall's formulation neglects the aerobic stage but since the aerobic waste decomposition represents a minor part of the landfill lifetime it is, therefore, less significant than anaerobic decomposition [ZB04]. This formulation is used to determine the growth/decay term for the internal variables characterizing the biodegradation,

- Org $[kg.m^{-3}]$ the organic content,
- c $[g.m^{-3}]$ the VFA concentration in water,
- m $[g.m^{-3}]$ the methanogen biomass in water.

McDougall's model provides the formulation of the biochemical model and the governing mass balance equations for these three chemical species, presented in the following sections. These equations describe the reaction rate and are expressed in $(g.m^{-3}_{aqueous}.s^{-1})$. This unit highlights the dependency of the reaction on the moisture content.

2.1.1 Hydrolysis and acidogenesis

Hydrolysis and acidogenesis is the first stage of the biodegradation, which represents the depletion of the organic content and its transformation into VFA. These latter intermediate products serve as a precursor for methanogen biomass. However, high VFA concentration has inhibitory effects on those reactions [GED08], which is also taken into account in the model through an inhibitor factor.

The modified enzymatic hydrolysis equation is proposed by [McD07] and mathematically describes the reaction rate

$$r_g = b\theta_e\phi P, \tag{1}$$

where four governing factors are taken into account

- $\theta_e = (\theta - \theta_{res})/(\theta_{sat} - \theta_{res})$ [-] is the effective water content (in volume, $\theta = n.S_{r,w}$), θ_{res} [-] is the residual water content and θ_{sat} [-] is the water content at saturation.
- b $[g.m^{-3}_{aqueous}.s^{-1}]$ is the maximum VFA growth rate under the most favorable environmental conditions, which normally occurs at the early stage of hydrolysis reaction.

- $\phi = 1 - (1 - Org/Org_0)^{\xi}$ [-] is the relative digestibility decreasing with the organic matter depletion, where Org_0 $[kg.m^{-3}]$ is the initial organic content and ξ [-] is a parameter.
- $P = \exp(-k_{VFA}.c)$ [-] is the inhibition factor accounting for the inhibitory effect of high VFA concentration, in which k_{VFA} $[g.m^{-3})^{-1}]$ is an inhibition constant.

2.1.2 Acetogenesis and methanogenesis

The second stage of the biochemical reactions occurring in the MSW transforms the VFA generated from the hydrolysis/acidogenesis reactions to methanogen biomass. Note that the biogas is not taken into account in current model for the sake of simplicity. The methanogen biomass production rate r_j is calculated through a Monod kinetic equation [BC10] and the VFA consumption rate r_h is directly linked to the methanogen biomass accumulation through a substrate yield coefficient Y,

$$r_j = \frac{k_0.c/\theta}{k_{MC} + c/\theta}.\frac{m}{\theta}, \tag{2}$$

$$r_h = r_j/Y, \tag{3}$$

where k_0 $[s^{-1}]$ is the maximum specific growth rate, k_{MC} $[g.m^{-3}_{aqueous}]$ is the half saturation constant.

2.1.3 Methanogen decay

The methanogen biomass decay over time r_k is given by the first order decay equation as follow:

$$r_k = k_2.\frac{m}{\theta}, \tag{4}$$

where k_2 $[s^{-1}]$ is the methanogen death coefficient.

2.1.4 Governing balance equations

The degradation rate of organic matter and accumulation rate of VFA and methanogen biomass can be incorporated as sink or source terms into classical advection-dispersion equations. They lead to advection-dispersion-reactive transport models, respectively written per m^3 of waste, for VFA (c) , methanogen biomass (m) and organic matter (Org),

$$\mathrm{div}\,(\underline{u}.c) - \mathrm{div}\left(\underline{\underline{D_h}}.\bigtriangledown c\right) + [r_g - r_h].\theta = \frac{\partial c}{\partial t}, \tag{5}$$

$$\mathrm{div}\,(\underline{u}.m) - \mathrm{div}\left(\underline{\underline{D_h}}.\bigtriangledown m\right) + [r_j - r_k].\theta = \frac{\partial m}{\partial t}, \tag{6}$$

$$-Z.r_g.\theta = \frac{\partial Org}{\partial t}, \tag{7}$$

where $\underline{u} = \underline{q}_l/(S_{r,w}.n_e)$ is the actual average velocity of the liquid flow, $S_{r,w}$ [-] is the water saturation degree, n_e [-] is the effective porosity, $\underline{q}_l$ is the water Darcy's velocity and Z [-] a substrate yield coefficient.

On the left side of equations (5) and (6), the first terms represent advective flux, linked to the actual average velocity of liquid flow $\underline{u}$. The second terms describe diffusive flux, which combines mechanical dispersion and molecular diffusion and the thirds are the source terms describing the generation or degradation of VFA or methanogen biomass. The terms on the right side are the storage term of VFA and methanogen biomass, respectively. Mass balance equation for organic matter (7) does not include any transport terms because the organic matter is considered as a part of solid skeleton and no erosion of organic matter occurs during the leachate recirculation or water injection.

It is worth noticing that the above reactive transport models were derived with no consideration of immobile water phase. These models are more suitable for the MSW with low organic matter content while not for the MSW with high organics matter content.

2.2 Hydraulic model

In municipal waste disposal, the materials are under unsaturated conditions and the temperature increases generated by the waste decomposition induce production of water vapour. Each fluid phase of the medium (liquid and gaseous) constitutes a mixture of two components, which are dry air and water vapour for the gas phase and liquid water and dissolved air for the liquid phase.

The variables chosen for the description of the flow problem are liquid water pressure, gas pressure and temperature. As a first approach and for sake of simplicity, the gas pressure variations are not considered in the following. That is the reason why the gas mass balance equation will not be expressed.

2.2.1 Water mass balance equation

The compositional approach [PC89, OCGA94, LS87] is used here to write balance equations, *i.e.* we assume that the conservation mass of each chemical species (water and air). The phase exchange term is cancelled in balance equations,

$$\underbrace{\frac{\partial}{\partial t}\left(\rho_w \cdot n \cdot S_{r,w}\right) + \operatorname{div}\left(\underline{f}_w\right)}_{\text{Liquid water}} + \underbrace{\frac{\partial}{\partial t}\left(\rho_v \cdot n \cdot S_{r,g}\right) + \operatorname{div}\left(\underline{f}_v\right)}_{\text{Water vapour}} - Q_w = 0 \tag{8}$$

where n is the porosity of the medium, ρ_w is the liquid water density, ρ_v is the water vapour density, $\underline{f}_w$ et $\underline{f}_v$ are the mass flows respectively for water and water vapour, $S_{r,g} = 1 - S_{r,w}$ is the gas saturation degree and Q_w is water source term.

The mass flows have two contributions, taking into account the advection of each phase (Darcean flow) and the diffusion of the different components within the phase (Fickean flow). Given the small amount of dissolved gas, liquid water diffusion within the liquid phase will be neglected.

The mass flows used in equation (8) are expressed as

$$\underline{f}_w = \rho_w \cdot \underline{q}_l, \tag{9}$$

$$\underline{f}_v = \rho_v \cdot \underline{q}_g + \underline{i}_v, \tag{10}$$

where $\underline{q}_l$ et $\underline{q}_g$ are the advection flow of the liquid and gas phases, $\underline{i}_v$ is the diffusive flow of water vapour within the gaseous phase. The expression of each terms are described in the following.

2.2.2 Advection of the liquid phase

In unsaturated conditions, Darcy's law remains valid provided that the permeability is modified as a function of the saturation degree. The water permeability is usually expressed as the product of the intrinsic permeability K_{int}^{sat} (measured in saturated conditions) by a relative permeability coefficient $k_{r,w}$ depending on the water saturation degree:

$$\underline{\underline{K}}_w(S_{r,w}) = \underline{\underline{K}}_{int}^{sat} \cdot k_{r,w}(S_{r,w}). \tag{11}$$

The generalized Darcy's law becomes

$$\underline{q}_l = \frac{-\underline{\underline{K}}_{int}^{sat} \cdot k_{r,w}(S_{r,w})}{\mu_w}\left[\underline{grad}(p_w) + g \cdot \rho_w \cdot \underline{grad}(z)\right], \tag{12}$$

where $\underline{\underline{K}}_{int}^{\mathrm{sat}}$ is the intrinsic permeability tensor (independent from the nature of the fluid), $k_{r,w}$, the water relative permeability and μ_w, the water dynamic viscosity.

It is worth noting that in equation (12), the fluid properties would have been those of the liquid phase (mixture of liquid water and dissolved air), and not those of liquid water. However, given the small amount of dissolved gas, its influence on the liquid viscosity and the liquid density is neglected.

2.2.3 Diffusion within the gaseous phase

The gas phase is a mixture of water vapour and dry air. Even if gas phase flows are neglected, a binary diffusion of each component within the phase is possible. Thus, the diffusive flows of water vapour and dry air in the gas phase are given by the Fick's law following

$$\underline{i}_v = -n \cdot (1 - S_{r,w}) \cdot \tau \cdot D_{v/a} \cdot \rho_a \tag{13}$$

where $D_{v/a}$ is the diffusion coefficient of water vapour in dry air.

2.3 Thermal Model

Due to the exothermal nature of the early stage of biodegradation reactions (so-called aerobic reactions) and the general heat transfer associated with boundary conditions, a significant temperature increase normally takes place in bioreactor landfills [BBLR07]. In order to simulate the temperature evolution within the landfill, a source term related to the heat generation due to the biodegradation reaction is introduced into a classic governing energy balance equation, leading to the following heat transport equation

$$\frac{\partial S_T}{\partial t} + \operatorname{div}\left(\underline{V}_T\right) - Q_T = 0, \tag{14}$$

where S_T is the heat storage, V_T is the heat flux and Q_T is the heat production term.

In equation (14), the heat storage term is given by the sum of each components contribution,as follows

$$\begin{aligned} S_T = {} & n.S_{r,w}.\rho_w c_{p,w}.(T - T_0) + n.S_{r,g}.\rho_a c_{p,a}(T - T_0) \\ & + (1-n)\rho_s c_{p,s}(T - T_0) + n.S_{r,g}.\rho_v c_{p,v}(T - T_0) \\ & + n.S_{r,g}.\rho_v.L \end{aligned} \tag{15}$$

in which $c_{p,i}$ $[J.kg^{-1}.K^{-1}]$ is specific heat of the component i, ρ_s $[kg.m^{-3}]$ is the solid waste density, ρ_a $[kg.m^{-3}]$ is the dry air density, L $[J.kg^{-1}]$ is the latent heat of water vaporization, T_0 is the initial temperature and T is the temperature.

The heat flux consists of a conduction term proportional to the thermal conductivity of the MSW and a convective term related to the heat transported by water flows

$$\begin{aligned} V_T = {} & -\Gamma \nabla T + c_{p,w} \varrho_w \underline{q}_l (T - T_0) + c_{p,v}\left(\rho_v \cdot \underline{q}_g + \underline{i}_v\right)(T - T_0) \\ & + \left(\rho_v \cdot \underline{q}_g + \underline{i}_v\right) L \end{aligned} \tag{16}$$

where Γ $[W.kg^{-1}.K^{-1}]$ is the thermal conductivity of the waste. The thermal conductivity of the MSW is estimated by summing the thermal conductivities of different phase components of the MSW, including the water, air and the solid phase.

The heat production term (Q_T) is derived by empirical consideration of the energy release from exothermal biochemical reactions occurring in the MSW, which is similar to the formulation proposed by [EFFL96],

$$Q_T = \frac{\partial Org(t)}{\partial t} H_m, \tag{17}$$

where H_m $[J/kg]$ is the quantity of heat produced by the degradation of one kilogram of organic matter.

2.4 Mechanical model

McDougall's work suggests that the total settlement can be calculated based on three contributions: elastic and plastic load induced strain, creep and biodegradation strain. It is proposed to implement these contributions (except creep) within a simplified version of the chemo-hydro-mechanical (CHM) model presented by [LBL$^+$05] which is based on previous works of [Hue92, Hue97, HLG02].

The CHM model has been originally developed to simulate the behavior of unsaturated clay in presence of chemicals in the pore fluid. A concentration parameter (Ω [-]) is included in the model to express the modification of properties with chemicals as well as computing the (elastic or plastic) strains induced by concentration changes. In this study, the concentration parameter is related to organic matter content such that

$$\Omega = 1 - \frac{Org}{Org_0}. \tag{18}$$

The lowest the organic matter content, the lowest the strength of the waste.

The constitutive model is thus written in terms of effective stress tensor and the concentration parameter. Bishop's effective stress has been chosen to describe the stress-strain relation

$$\sigma'_{ij} = \sigma_{ij} - p_g \delta_{ij} + S_{r,w}(p_g - p_w)\delta_{ij}, \tag{19}$$

where σ'_{ij} is the effective stress tensor, σ_{ij} is the total stress tensor, p_g is the gas pressure (constant and equal to the atmospheric pressure) and δ_{ij} is Kronecker's tensor.

2.4.1 Constitutive equations

The equations relate the strain to the stress and the organic content - through the concentration factor, Ω. The strain rate is the sum of an elastic reversible part and a plastic irreversible part. The elastic part is also decomposed into mechanical and chemical components.

$$\dot{\epsilon}_{ij} = \dot{\epsilon}^{e}_{ij} + \dot{\epsilon}^{p}_{ij} = \dot{\epsilon}^{(e,m)}_{ij} + \dot{\epsilon}^{(e,\Omega)}_{ij} + \dot{\epsilon}^{(p,m)}_{ij} \tag{20}$$

The three main strain components are presented as follows

1. The elastic strain-stress law is a classical Hooke's law;
2. The chemical elastic strain is defined according to the formulation in [Hue97]

   $$\dot{\epsilon}_{ij}^{(e,c)} = -1/3\beta\dot{\Omega}\delta_{ij}, \tag{21}$$

   where β [-] is a parameter depending on the waste and the concentration;
3. The plastic strain rate is defined within a classical elastoplastic framework.

Three plastic yielding mechanisms are implemented into the chemo-hydro-mechanical (CHM) model by [LBL$^+$05]: pore collapse, frictional-cohesive failure and tensile failure. They are represented respectively by the following equations

$$f_1 \equiv q^2 + M^2(p+p_s)(p-p_0) = 0, p \geq (p_0 - p_s)/2 \tag{22}$$

$$f_2 \equiv q - M(p-p_s) = 0, \sigma_t < p \leq (p_0 - p_s)/2 \tag{23}$$

$$f_3 \equiv p + \sigma_t = 0, \tag{24}$$

where p_0 [Pa] is the pre-consolidation pressure, p_s [Pa] is a parameter related to the cohesion, M [-] is a parameter defining the slope of the frictional cohesive failure in the deviatoric plane, σ_t [Pa] is the limit tensile strength, $p = \sigma_{kk}/3$ and $q = \sqrt{3/2 s_{ij} s_{ij}}$ are the stress invariants and s_{ij} is the deviatoric part of the stress tensor.

2.4.2 Chemical hardening/softening

The large deformation due to the biodegradation of organic matter fraction of MSW is considered in our proposed constitutive model by introducing chemical softening, controlled by the concentration parameter (Ω). This parameter varies from zero to one with degradation of the organic matter from initial content to zero.

This concentration parameter (Ω) influences both the pre-consolidation pressure and the cohesion parameter in order to describe the biodegradation effect on pore collapse mechanism and frictional-cohesive failure mechanism, respectively.

1. Effect on pore collapse mechanism: the preconsolidation pressure is a decreasing function of the concentration parameter,

   $$p_0(\Omega) = p_0^* S(\Omega), \tag{25}$$

   where p_0^* is the pre-consolidation pressure for initial organic content ($\Omega = 0$) and $S(\Omega) = \exp(-a\Omega)$ is the chemical softening function, where a [-] stands for a constant governing the decrease of the pre-consolidation pressure with the increase in concentration parameter.
2. Effect on frictional cohesive failure mechanism: the parameter p_s [Pa], controlling the cohesion, is assumed to vary as a linear function of the concentration parameter (Ω)

   $$p_s = p_s^* + k_\Omega \Omega \tag{26}$$

   where p_s^* [Pa] is the value of the parameter for initial organic content (Ω=0) and k_Ω is a model constant.

3 Application of the BC-THM model to a municipal waste disposal

The multiphysical processes occurring during the lifetime of a municipal waste disposal are simplified into a one-dimensional problem. Initial and boundary conditions of a 30 meter high column are depicted in Figure 1. A one meter thick drain is located at the base of the column.
In the sequel, the different physical processes are introduced progressively, highlighting their impact and respective couplings. At each step, a simplified analytical solution is proposed in order to emphasize the main parameters describing the physical phenomena. This solution is compared with the fully coupled numerical computations obtained from the implementation of the model previously described in `LAGAMINE` [CLRC02, HLC15].

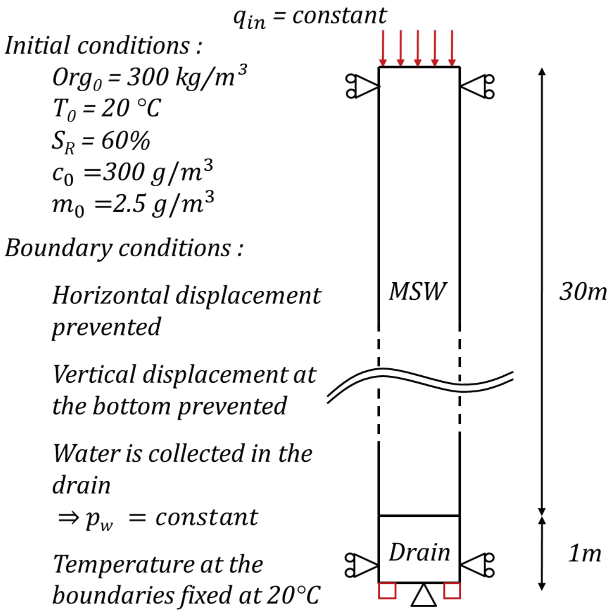

Figure 1: Initial and boundary conditions

3.1 Flow model

During the exploitation period of the disposal, a water influx q_{in} is imposed at the top boundary (negative in case of injection). This flow is either a rainfall infiltration rate or a water injection rate in case of active management of the disposal as a bioreactor. For the sake of simplicity, the retention curve is defined as

$$S_{r,w} = \exp\left(\frac{-p_c}{4A}\right) \leq 1, \tag{27}$$

where $p_c = p_g - p_w$ is the capillary pressure. In turn the relative permeability is defined as

$$k_{r,w} = \left(S_{r,w}\right)^4. \tag{28}$$

3.1.1 Hydraulic analytical approach

It is proposed to provide a closed-form solution of the water mass balance equation (8) for steady-state conditions. Considering an incompressible fluid and a uniform temperature of 20 °C (the water vapour contribution can be neglected), this equation is rewritten in one dimension as

$$\frac{\partial}{\partial z}\left(q_{l,z}\,\rho_w\right) = 0. \tag{29}$$

The obtained solution imposes that $q_{l,z}\,\rho_w = q_{in}$, which is constant all along the waste column since the considered solution is stationary.

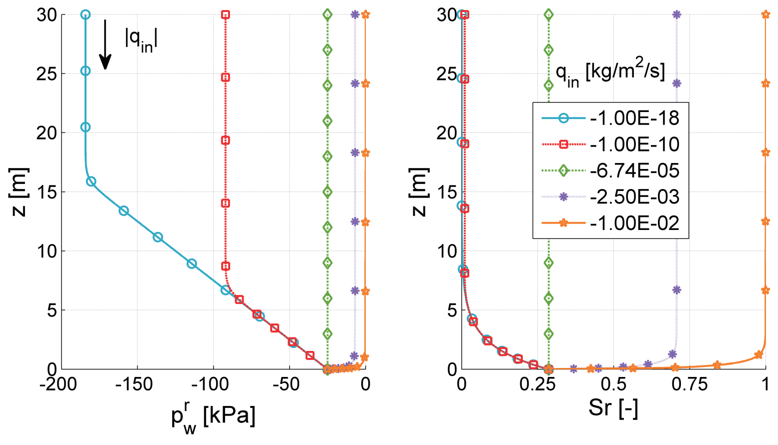

Figure 2: Profile of relative water pressure (a) and saturation (b) as a function of incoming water flow $|q_{in}|$ (Analytical solution).

Injecting equations (12) and (28) into equation (29) leads to

$$\frac{\partial p^r_w}{\partial z} + \frac{q_{in}\,\mu_w}{\rho_w\,K^{sat}_{int}} \exp\left(-\frac{p^r_w}{A}\right) = -\rho_w g, \tag{30}$$

where $p_w^r = -p_c$ is the relative water pressure. Substituting the expression $j = \exp(-p_w^r/A)$ into equation (30) reads

$$\frac{\partial j}{\partial z} = \beta\, j^2 + \gamma j \tag{31}$$

where $\beta = (q_{in}\, \mu_w)/(\rho_w\, K_{int}^{sat}\, A)$ and $\gamma = \rho_w g/A$ which has the form of the Verhulst equation. It is solved by the subtitution $u = 1/j$ and finally provides the profile of relative water pressure

$$p_w^r(z) = A\, \ln\left[C_1\, \exp(-\gamma\, z) - \frac{\beta}{\gamma}\right], \tag{32}$$

where C_1 is an integration constant determined from the boundary condition, p_0^r in $z = 0$, yielding to

$$C_1 = \frac{\beta}{\gamma} + \exp\left(\frac{p_0^r}{A}\right). \tag{33}$$

The profile of relative water pressure and saturation degree along the soil column are provided in Figure 2. It illustrates the influence of water injection at the top of the column.

3.1.2 Hydraulic numerical approach

The numerical model described in section 2.2 considers the transient response of the waste, as well as the contribution of the water vapour. Figure 3 shows that the steady-state is actually reached after 30 days and corresponds to the analytical solution. Therefore it can be concluded that the water vapour phase is negligible at 20°C.

3.2 Bio-Chemo-Hydraulic model

The evolution of the VFA (c), the methanogen biomass (m) and the organic matter (Org) are linked to the flow problem since the water content directly controls the biochemical reactions. This introduces a first coupling and the column waste disposal is considered as a bio-reactor described in section 2.1.

3.2.1 BC-H Analytical approach

The analytical approach focuses only on the degradation of the organic matter since it is coupled with the thermal and mechanical problems. The equation of the decomposition of the organic content reads

$$\frac{\partial org}{\partial t} = -\theta\, Z\, b\, \theta_e\, \exp(-k_{vfa}\, c)\left[1 - \left(\frac{org_0 - org}{org_0}\right)^{\xi}\right], \tag{34}$$

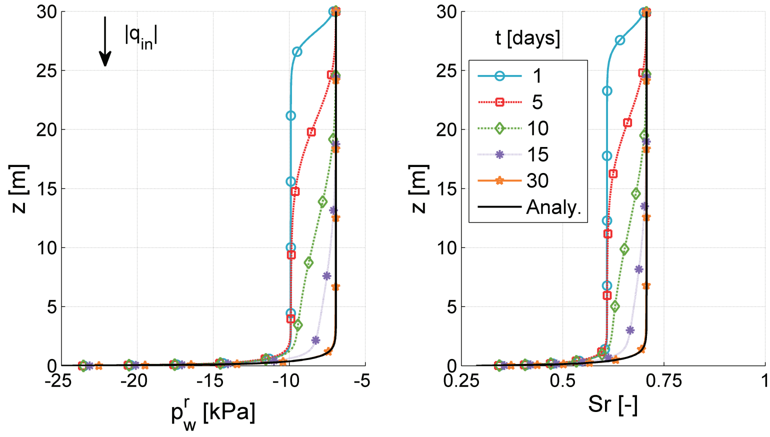

Figure 3: Profile of water pressure (a), p_w, and saturation degree (b) at different time steps (Numerical results).

where variable c is constant and θ is equal to its stationary value. The equation (34) is recast as a function of the concentration variable Ω

$$\frac{\partial \Omega}{\partial t} = C\,\left(1 - \Omega^{\xi}\right), \tag{35}$$

where $C = \theta\, Z\, b\, \theta_e\, \exp\left(-k_{vfa}\, c\right)/org_0$ is a time constant. This equation is solved using Mathematica leading to the approximated series solution

$$t = \frac{\Omega}{C} \sum_{n=1}^{\infty} \frac{(1)_n \left(\frac{1}{\xi}\right)_n}{\left(1+\frac{1}{\xi}\right)_n} \frac{\Omega^{n\xi}}{n!}, \tag{36}$$

where t is the time variable and

$$(x)_n = x\,(x+1)\,(x+2)\ldots(x+n-1). \tag{37}$$

Figure 4(b) illustrates the influence of the C constant on the evolution of Ω. This parameter is mainly a function of the water content and maximal degradation rate b. It explains why the degradation can spend over several dozen of years.

3.2.2 BC-H Numerical approach

Numerical results take into account the full bio-chemical couplings equations (5)-(7) and a transport term linked to the water flow. Figure 4(a) depicts the evolution of

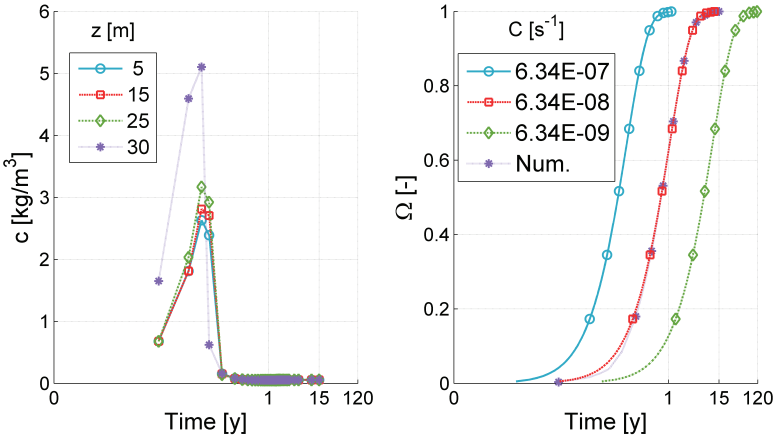

Figure 4: (a) Time evolution of the VFA at different depth (Numerical results) and (b) concentration variable Ω for different C values (Analytical results).

the VFA concentration with time. The VFA is a product of the first stage reaction and is simultaneously consumed by the second stage reaction generating methanogen biomass. At first, the VFA concentration increases quite a lot because of the injected water inducing important organic matter degradation and thus VFA production. Then, the VFA consumption dominates its production due to the high value of VFA concentration reached, leading to an important inhibitory effect on the depletion of organic matter and in turn of the VFA production. Consequently, it quickly decreases to an equilibrium state, where rates on VFA production and consumption are equal, as shown by [McD07]. This is confirmed by the profile of the VFA concentration at different times depicted in Figure 5(a).

Figure 5(b) exhibits an almost uniform organic matter degradation. It is slightly slower near the drain layer, where the water saturation degree is lower. The analytical solution well captures the numerical results, as shown in Figure 4(b). Indeed the flow and VFA concentration are stationary during the main lifetime of the waste disposal. Therefore approximating a constant VFA concentration and water content is a good approximation.

3.3 Bio-Chemo-Thermo-Hydraulic model

The first coupling is due to the exothermic nature of the bio-chemical reactions. Therefore the temperature within the waste disposal varies with the bio-degradation processes. The second coupling arises from the dependency on the bio-chemical reactions to the water saturation degree. Finally the heat produced is transferred either by thermal conduction or flow convection. One coupling effect has been neglected in our

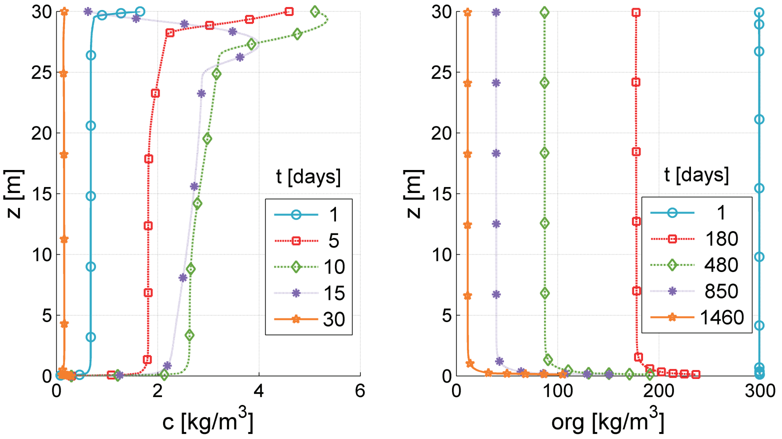

Figure 5: Profile of the VFA concentration and the organic matter content (Numerical results).

formulation: the BC reaction rates do not depend on the temperature.

3.3.1 BC-TH Analytical approach

The general heat balance equation (14) is simplified, discarding the convection terms and the water vapour contribution. The one-dimensional equations is then written as

$$\frac{\partial \mathrm{T}(z,t)}{\partial t} - \alpha \, \frac{\partial^2 \mathrm{T}(z,t)}{\partial z^2} = \mathrm{Q}(z,t), \tag{38}$$

where $\mathrm{T}(z,t)$ is the temperature, α [m/s^2] is the thermal diffusivity and $\mathrm{Q}(z,t)$ is a source term.

Following equation (17), the heat production is related to the degradation rate of the organic matter. Assuming a time decreasing exponential function of the organic matter, $(\Omega = exp(-\zeta t))$, the source term is expressed as follows

$$\mathrm{Q}(z,t) = \underbrace{\frac{H_m \, \zeta}{\rho \, c}}_{\delta} \, \exp(-\zeta t). \tag{39}$$

Let us assumed a column of soil at the initial temperature T_0 of 20 degrees, the final solution reads

$$\mathrm{T}(z,t) = \mathrm{T}_0 + \sum_{n=1}^{\infty} \sin\left(\frac{n\pi}{L} z\right) \int_0^t \mathrm{B}_n(s) \, \exp\left(-\alpha \, \lambda_n \, (t-s)\right) \, \mathrm{d}s, \tag{40}$$

where $\lambda_n = (n\pi/L)^2$ and

$$\mathrm{B}_n(s) \quad = \quad \frac{2}{L}\int_0^L \delta \exp\left(-\zeta s\right) \sin\left(\frac{n\pi}{L}z\right) \mathrm{d}z \tag{41}$$

$$= \begin{cases} \dfrac{4\delta}{n\pi} \exp\left(-\zeta\, s\right) & n\,\mathrm{odd} \\ 0 & n\,\mathrm{even} \end{cases} . \tag{42}$$

Introducing equation (42) into (40) leads to

$$\mathrm{T}(z,t) = \mathrm{T}_0 + \sum_{n=1,2}^{\infty} \frac{4\delta}{n\pi} \frac{1}{-\zeta + \alpha\lambda_n} \sin\left(\frac{n\pi}{L}z\right) \left[\exp\left(-\zeta t\right) - \exp\left(-\alpha\lambda_n t\right)\right] \tag{43}$$

Observed profiles of temperature result from the competition of two distinct effects: heat generation and heat diffusion. It is clear in Figure 6 that the heating is fast with respect to the heat diffusivity. Therefore the temperature evolves almost constantly over most part of the waste column. Afterwards, heat is progressively dissipated through the upper and lower boundaries.

3.3.2 BC-TH Numerical approach

Numerical model for heat transfer enables us to study the influence of different effects: heat generation, heat diffusion and heat convection. In order to evidence their influence, three numerical simulations are performed. The water vapour is shown to have no influence on the results and is not considered. In the following, $Case1$ corresponds to the modelling without convection (equivalent to the analytical solution). $Case2$ and $Case3$ refer to the solution of the problem taking into account heat convection for two distinct water flows, respectively q_{in} and $q_{in}/100$.

Figure 6 depicts that the analytical solution well captures numerical results for mean and long term predictions. The observed short-term discrepancies are related to the assumption we took on the evolution of the organic matter as a decreasing exponential function.

$Case2$ and $Case3$ exhibit the influence of the convection. In the first case the temperature does not increase significantly because the heat loss due to convection is high at the bottom of the column. In the second case, the temperature profile becomes progressively non symmetric (and non-parabolic) due to convection.

3.4 Bio-Chemo-Thermo-Hydraulic-Mechanical model

The biodegradation reactions degrade the properties of the waste: the apparent preconsolidation pressure is a decreasing function of the concentration variable Ω. The

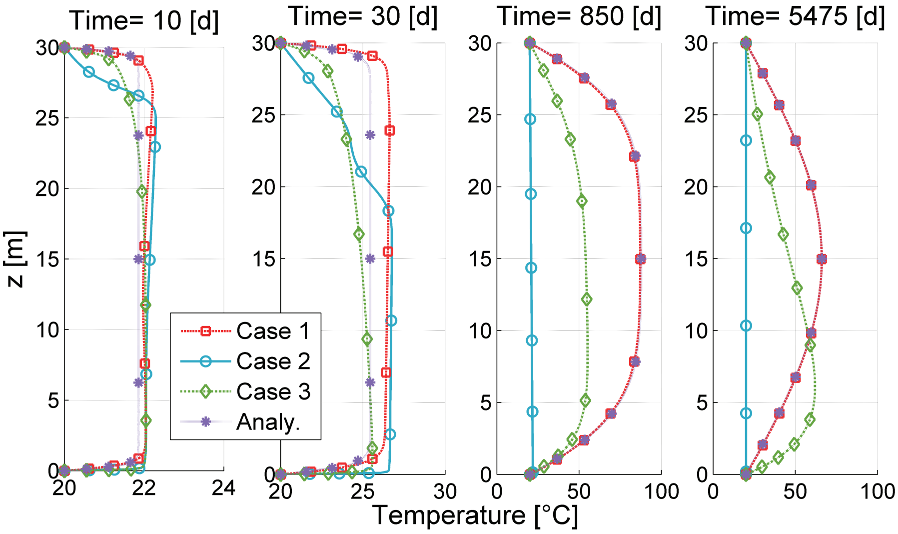

Figure 6: Profile of temperature for different time steps (Analytical and numerical results).

biochemical reactions firstly lead to a chemical softening of the waste and secondly to a mechanical hardening, as far as the stress state remains constant. Therefore the increase of the concentration variable induces a plastic compaction of the waste column.

3.4.1 BC-THM Analytical approach

First, we only consider the plastic volumetric deformation due to the bio-chemical couplings, in the frame of the constitutive model described in section 2.4. Under the assumption of a constant effective stress state, the consistency condition reads

$$\frac{\partial f}{\partial \Omega}.d\Omega + \frac{\partial f}{\partial p_0^*}\, dp_0^* = 0. \tag{44}$$

In addition, the hardening function in a CamClay model is classically defined as

$$\mathrm{d}p_0^* = \frac{1+e_0}{\lambda - \kappa}\, p_0^*\, \mathrm{d}\epsilon_v^p. \tag{45}$$

Combining these two latter equations with equation (22), the relation between the plastic volumetric strain and the variation of the concentration variable is written as

$$\mathrm{d}\epsilon_v^p = \frac{\lambda - \kappa}{1+e_0}\,(-a)\, d\Omega \tag{46}$$

where a is the constant governing the decrease of the pre-consolidation pressure with the decomposition.

3.4.2 BC-THM Numerical approach

Figure 7 presents first the evolution of the concentration variable at different locations. It is observed that the degradation is actually proportional to the water saturation degree. Indeed, the shift of the results in this figure is due to the difference of saturation with depth near the drain (low depth). The plastic volumetric strains follow the evolution of the degradation. Figure 7 shows that the analytical solution provides an upper-bound estimation of the numerical response.

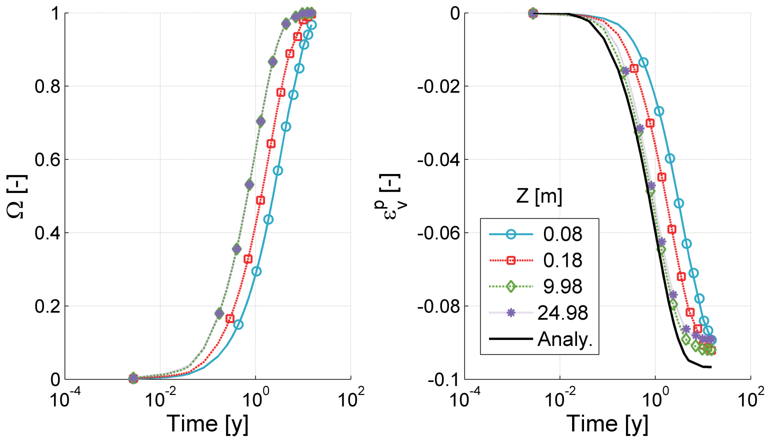

Figure 7: Profile of concentration content (a) and plastic volumetric strain (b) for different time steps (Analytical and numerical results).

4 Conclusions

This paper presents the formulation of a biochemo-thermo-hydro-mechanical model for the study and analysis of long term behavior of bioreactor landfill. The particularity of the BC-THM model formulation is the multi-physics coupling accounting for the inherent complexity of the bioreactor landfill system. The two stage anaerobic biodegradation model proposed by McDougall [McD07] is adopted as biochemical sub-model to reproduce the biodegradation of organic matter. It is incorporated into the thermo-hydro-mechanical framework of the `LAGAMINE` code. Furthermore, the effect of the biodegradation on mechanical behavior is taken into account using a simplified version of the chemo-mechanical model developed by [Hue97]. The hydraulic model is based on Darcy's law for water flow in unsaturated soils. Finally the thermal model is a classical energy balance equation with a source term taking into account the heat generated by the degradation of organic matter.

Then, an application of the BC-THM model on a one-dimensional problem is presented and the different physical processes are introduced progressively, in order to highlight the impact of each process and their respective couplings. For each step, an analytical solution is proposed in order to explain the physical phenomenon.

References

[AJ00] O Aguilar-Juarez. *Analyse et modélisation des réactions biologiques aérobies au cours de la phase d'exploitation d'un casier d'un centre d'enfouissement technique*. PhD thesis, Thèse de doctorat, Institut des Sciences Appliquées de Toulouse, 2000.

[BBH$^+$10] M Barlaz, C Bareither, A Hossain, J Saquing, I Mezzari, CH Benson, T Tolaymat, and R Yazdani. Performance of north american bioreactor landfills. ii: Chemical and biological characteristics. *Journal of Environmental Engineering*, 2010.

[BBLR07] CH Benson, M Barlaz, DT Lane, and JM Rawe. Practice review of five bioreactor/recirculation landfills. *Waste Management*, 27(1):13–29, 2007.

[BC10] J Bear and AH-D Cheng. *Modeling groundwater flow and contaminant transport*, volume 23. Springer Science & Business Media, 2010.

[Bea00] RP Beaven. *The hydrogeological and geotechnical properties of household waste in relation to sustainable landfilling.* PhD thesis, University of London, Department of Civil Engeering, Queen Mary and Westfield College, 2000.

[CGLZ15] YM Chen, RY Guo, YC Li, and LT Zhan. A model for anaerobic degradation of municipal solid waste. *Multilevel Modeling of Secure Systems in QoP-ML*, page 365, 2015.

[Cha07] R Charlier. Approche unifiée de quelques problèmes non linéaires de mécanique des milieux continus par la méthode des éléments finis (grandes déformations des métaux et des sols, contact unilatéral de solides, conduction thermique et écoulements en milieu poreux). 2007.

[CLRC02] F Collin, X-L Li, J-P Radu, and R Charlier. Thermo-hydro-mechanical coupling in clay barriers. *Engineering Geology*, 64(2):179–193, 2002.

[Col03] F Collin. *Couplages thermo-hydro-mécaniques dans les sols et les roches tendres partiellement saturés*. PhD thesis, Thèse de doctorat, Faculté des Sciences Appliquées, Université de Liège, 2003.

[CXZ12] YM Chen, XB Xu, and LT Zhan. Analysis of solid-liquid-gas interactions in landfilled municipal solid waste by a bio-hydro-mechanical coupled model. *Science China Technological Sciences*, 55(1):81–89, 2012.

[CZL14] Y Chen, T Zhan, and Y Li. Biochemical, hydraulic and mechanical behaviours of landfills with high-kitchen-waste-content msw. In *In A.Bouazza, S.T.S Yuen, B. Brown, eds. 7th International congress on Environmental Geotechnics*, pages 232–259, Melbourne, Australia, 2014.

[EFFL96] M El-Fadel, AN Findikakis, and JO Leckie. Numerical modelling of generation and transport of gas and heat in landfills i. model formulation. *Waste management & research*, 14(5):483–504, 1996.

[ER90] TB Edi and VJ Ranguette. Wuellner, ww," settlement of municipal refuse. *Geotechnics of waste fills: Theory and practice*, 1070:225, 1990.

[GED08] S Gholamifard, R Eymard, and C Duquennoi. Modeling anaerobic bioreactor landfills in methanogenic phase: Long term and short term behaviors. *water research*, 42(20):5061–5071, 2008.

[GL61] RE Gibson and KY Lo. *A theory of consolidation for soils exhibiting secondary compression*. Norges tekniske vitenskapsakademi, 1961.

[HHO$^+$01] A Haarstrick, DC Hempel, L Ostermann, H Ahrens, and D Dinkler. Modelling of the biodegradation of organic matter in municipal landfills. *Waste management & research*, 19(4):320–331, 2001.

[HLC15] J Hubert, X Liu, and F Collin. Numerical modeling of the long term behavior of municipal solid waste in a bioreactor landfill. *Computers and Geotechnics*, 2015.

[HLG02] T Hueckel, B Loret, and A Gajo. Swelling clays as reactive deformable, two-phase materials: basic concepts and options. *Chemo-mechanical Coupling in Clays*, pages 105–120, 2002.

[HMTH07] H Hettiarachchi, J Meegoda, J Tavantzis, and P Hettiaratchi. Numerical model to predict settlements coupled with landfill gas pressure in bioreactor landfills. *Journal of hazardous materials*, 139(3):514–522, 2007.

[Hue92] T Hueckel. Water-mineral interaction in hygromechanics of clays exposed to environmental loads: a mixture-theory approach. *Canadian Geotechnical Journal*, 29(6):1071–1086, 1992.

[Hue97] T Hueckel. Chemo-plasticity of clays subjected to stress and flow of a single contaminant. *International journal for numerical and analytical methods in geomechanics*, 21(1):43–72, 1997.

[KCM11] S Kumar, C Chiemchaisri, and A Mudhoo. Bioreactor landfill technology in municipal solid waste treatment: An overview. *Critical reviews in biotechnology*, 31(1):77–97, 2011.

[LBL$^+$05] Z Liu, N Boukpeti, X Li, F Collin, J-P Radu, T Hueckel, and R Charlier. Modelling chemo-hydro-mechanical behaviour of unsaturated clays: a feasibility study. *International journal for numerical and analytical methods in geomechanics*, 29(9):919–940, 2005.

[LS87] RW Lewis and BA Schrefler. The finite element method in the deformation and consolidation of porous media. 1987.

[McD07] J McDougall. A hydro-bio-mechanical model for settlement and other behaviour in landfilled waste. *Computers and Geotechnics*, 34(4):229–246, 2007.

[OCGA94] S Olivella, J Carrera, A Gens, and EE Alonso. Nonisothermal multiphase flow of brine and gas through saline media. *Transport in porous media*, 15(3):271–293, 1994.

[Oli03] F Olivier. *Tassement des déchets en CSD de classe II: du site au modèle*. PhD thesis, Université Joseph-Fourier-Grenoble I, 2003.

[PC89] S Panday and MY Corapcioglu. Reservoir transport equations by compositional approach. *Transport in Porous Media*, 4(4):369–393, 1989.

[PK00] F Pohland and J Kim. Microbially mediated attenuation potential of landfill bioreactor systems. *Water Science and Technology*, 41(3):247–254, 2000.

[RAY96] DR Reinhart and AB Al-Yousfi. The impact of leachate recirculating landfills : Case studies. *Waste Management & Research*, 14(4):347–365, 1996.

[RMT02] DR Reinhart, PT McCreanor, and T Townsend. The bioreactor landfill: Its status and future. *Waste Management & Research*, 20(2):172–186, 2002.

[Rod05] C Rodriguez. *Activité biologique dans les centres d'enfouissement technique de déchets ménagers: biodisponibilité de la cellulose et modélisation*. PhD thesis, PhD thesis, Université de Liege, Centre Wallon de Biologie Industrielle, 2005.

[RRW11] M Robeck, T Ricken, and R Widmann. A finite element simulation of biological conversion processes in landfills. *Waste management*, 31(4):663–669, 2011.

[Sow75] GF Sowers. Settlement of waste disposal fills: Conference. session four. 6f, 1t, 3r. proc. eighth int. conf. on soil mech. found. engng. moscow, v2. 2, 1973, p207–210. In *International Journal of Rock Mechanics and Mining Sciences & Geomechanics Abstracts*, volume 12, pages 57–58. Pergamon, 1975.

[WB13] JK White and RP Beaven. Developments to a landfill processes model following its application to two landfill modelling challenges. *Waste management*, 33(10):1969–1981, 2013.

[WRR03] JK White, Q Ren, and JP Robinson. A framework to contain a spatially distributed model of the degradation of solid waste in landfills. *Waste management & research*, 21(4):330–345, 2003.

[YWSM01] STS Yuen, QJ Wang, JR Styles, and TA McMahon. Water balance comparison between a dry and a wet landfill—a full-scale experiment. *Journal of Hydrology*, 251(1):29–48, 2001.

[ZB04] AI Zacharof and AP Butler. Stochastic modelling of landfill leachate and biogas production incorporating waste heterogeneity. model formulation and uncertainty analysis. *Waste management*, 24(5):453–462, 2004.

INPG – 3SR
46 avenue Félix Viallet
BP 53
38041 GRENOBLE CEDEX 9
FRANCE

ISBN 978-2-9542517-6-9

Fon: +33 (0) 456 528 621
Fax: +33 (0) 476 827 043
president@alertgeomaterials.eu
http://alertgeomaterials.eu

ALERT Doctoral School 2015
Coupled and multiphysics phenomena

Editors: B.A. Schrefler, L. Sanavia, F. Collin

P. Delage

Thermo-hydro-mechanical issues in geomaterials: physical mechanisms and experimental determination

J.M. Huyghe

General theory of mixtures. Physical chemistry of mixtures and swelling

J.M. Huyghe

Finite deformation poromechanics with application to heart muscle and blood perfusion

W.G. Gray, C.T. Miller

Thermodynamically Constrained Averaging Theory (TCAT) to model the coupled behavior of multiphase porous systems

D. Manzanal, M. Pastor, J.A. Fernández-Merodo, P. Mira, M. Martín Stikle, A. Yagüe, Y. Javanmardi

Generalized Plasticity modelling of geomaterials: the role of dilatancy

M. Pastor, P. Mira, J.A. Fernández-Merodo, M. Martín Stickle, D. Manzanal, A. Yagüe

An introduction to numerical modelling of coupled problems in geomechanics

B.A. Schrefler, P. Rizzato, S. Secchi

Hydraulic Fracture

L. Sanavia, T. D. Cao

Finite element analysis of non-isothermal multiphase porous media in dynamics

F. Collin, J. Hubert , X.F. Liu, B. Cerfontaine

Numerical modelling of a Municipal Waste Disposal as a Bio- Chemo-Thermo- Hydro-Mechanical problem

ISBN 978-2-9542517-6-9